The Stability of Multi-Layer Curtain Coating

by

Dominic James Dougal Henry

A thesis submitted to
The University of Birmingham
for the degree of
Doctor of Philosophy

School of Mathematics
The University of Birmingham
April 2016

Abstract

Coating flows have a vast array of applications, whereby a thin liquid film coats the surface of a solid substrate. Curtain coating is a lucrative method due to being able to coat multiple layers at the same time in one process. Combining many different components of fluid mechanics into one industrial process, fully understanding all the mechanisms involved in curtain coating is essential to fully utilise its potential of efficiently and uniformly coating multiple layers simultaneously. This thesis considers two of these components; film flow along an inclined plane and the stability of a liquid curtain, including both during and after curtain break-up, combining experimental and theoretical studies. An experimental investigation of the flow down the inclined plane of the coating die is presented, for a wide range of physical properties and parameters, with the results compared to a simple mathematical model derived from multi-layered film flow along an inclined surface. Furthermore, a mathematical model of a free-falling surfactant laden liquid curtain under gravity is derived. Incorporating the effect of an insoluble surfactant is found to alter steady state profiles, as well as stabilizing the curtain to small perturbations about the steady state. An experimental study into the liquid curtain during break-up is then presented, investigating the hysteresis phenomenon of curtain stability, as well as the origins of break-up and the speed of sheet retraction. Finally, a mathematical model of the spacing between the array of liquid jets that is formed after the curtain disintegrates is developed.

Acknowledgements

First of all, I would like to thank my supervisor Jamal Uddin for his constant support and advice throughout my time at The University of Birmingham. I'll be forever indebted for his efforts in my education and upbringing over the years.

I'd also like to thank Jeremy Marston, for his supervision of the experimental work presented in this thesis, and support of my overall study. Teaching me that perseverance is key when it comes to experimental work has also held true in many other aspects.

Thanks to Sigurdur Thoroddsen for inviting and hosting me to work at his high-speed fluids lab at King Abdullah University of Science and Technology, and the team there for making me feel so welcome on each of my research visits.

My friends and family deserve many thanks for their support of my postgraduate studies.

Thanks to the EPSRC for the funding of my PhD studies.

Last, but by no means least, my parents unwavering backing of my studies has been a constant source of strength. Without them I would have never got this far.

List of Publications

Several parts of the thesis presented has been published in peer-reviewed journals. These are given by the following (in chronological order):

1. J.O. Marston, S.T. Thoroddsen, J. Thompson, M.G. Blyth, D. Henry and J. Uddin (2014) Experimental investigation of hysteresis in the break-up of liquid curtains. *Chemical Engineering Science*, 117:248–263

2. D. Henry, J. Uddin, J.Thompson, M.G. Blyth, S.T. Thoroddsen and J.O. Marston (2014) Multi-layer film flow down an inclined plane: experimental investigation. *Experiments in Fluids*, 55:1859

3. D. Henry, J. Uddin, J.O. Marston and S.T. Thoroddsen (2016) Stability of an unsupported multi-layer surfactant laden liquid curtain under gravity. *Journal of Engineering Mathematics*, 99:119–136

Chapters 2 and 3 are entirely based upon the works of the publications 2 and 3 listed. Chapter 4 originates from the work carried out in publication 1. It is noted here that all experimental work and analysis presented in this thesis was conducted by the author.

Contents

List of Symbols

Despite every effort to be consistent with notation throughout this thesis, this was not always possible due to the mixed nature of theoretical and experimental work. The meaning of each new symbol that is introduced throughout the thesis is made clear. Listed here are the symbols that are consistent throughout.

Symbol	**SI unit**	**Meaning**
σ	Nm^{-1}	surface tension
ρ	kgm^{-3}	density
$\mathbf{T}$	Pa	stress tensor
μ	Pa.s	dynamic viscosity
Q	$\mathrm{m}^2\mathrm{s}^{-1}$	flow rate per unit width
Γ		surfactant concentration
∇_s	–	surface gradient operator
We	–	Weber number
Ca	–	capillary number
Re	–	Reynolds number
Fr	–	Froude number
Oh	–	Ohnesorge number
$\mathcal{R}$	–	modified Reynolds number
$\mathcal{B}$	–	modified surface activity number
$\mathcal{C}$	–	modified capillary number

Chapter 1

Introduction

Coating flows have been a source of scientific interest for many decades, with the ability to understand the many fluid mechanical elements occurring in these processes being critical to the development of new industrial methods [118]. Recently, one such method, known as "curtain coating" has received much interest from the coating community due to its potential of efficiently coating multiple layers simultaneously [85].

In coating methods, a liquid impinges upon a solid (or liquid) substrate, so that the solid-gas interface becomes a liquid-gas interface. Often the liquid applied will contain solids to be dried, and thus the resulting product is a solid layer. These processes have a vast array of applications, such as traditional practices in the paper industry [3], whereby photographic paper is coated with a light-sensitive chemical formula 'emulsion' layer. More modern applications include touchscreen technology; in some cases a thin conductive layer is coated to one side of the screen as a sensor, or in anti-fingerprint applications [120]. A final example given here is in biomedical applications, where hydrophilic coatings are applied to many medical materials [69]. In essence, coating a thin film upon a solid substrate can radically change the surface properties of the solid that is covered. This change can be used to enhance the surface properties that are desirable.

The processes of coating flows can generally be split into two classes, self-metered and

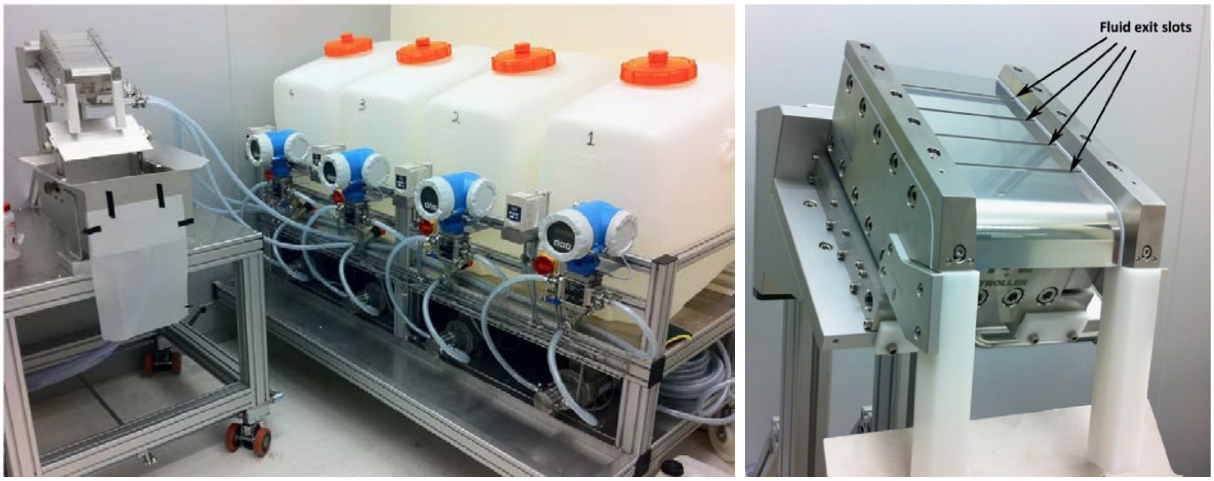

(a) (b)

Figure 1.1: Photographs of the curtain coating equipment. Subfigure (a) shows both the "pumping station" (to the right) and the "coating station" (to the left); (b) shows the slide-die with the four fluid layer exit slots labelled.

premetered methods. Self-metered coating processes (for example, blade [107] and roll [30] coating) are simpler, involving the application of one layer at a time. The properties of the fluid and the web speed (speed of the solid substrate to be coated) govern how thick the coated layer will be. Despite being more complex, premetered processes, where the film thickness of the coated layer is predetermined by the specification of the flow rate, offer a more efficient way of coating. Curtain coating is one such premetered method.

The advantages of curtain coating include the ability to apply thin liquid layers to irregular surfaces and the capability of coating at very high speeds [85]. However, the most lucrative advantage of curtain coating is the ability to coat multiple layers, comprising of different fluids, simultaneously. This saves the cost of coating and drying each layer individually, which comes at a greater cost and a slower production time.

Figure 1.1 (a) shows a picture of the equipment used during the curtain coating procedure. To the right of this picture is the "pumping station", whereby the working fluids are held (in the tanks marked 1–4) and connected to fluid pumps to be fed to the coating die, in this case a slide-die, which is to the left of Figure 1.1 (a). The slide-die is shown

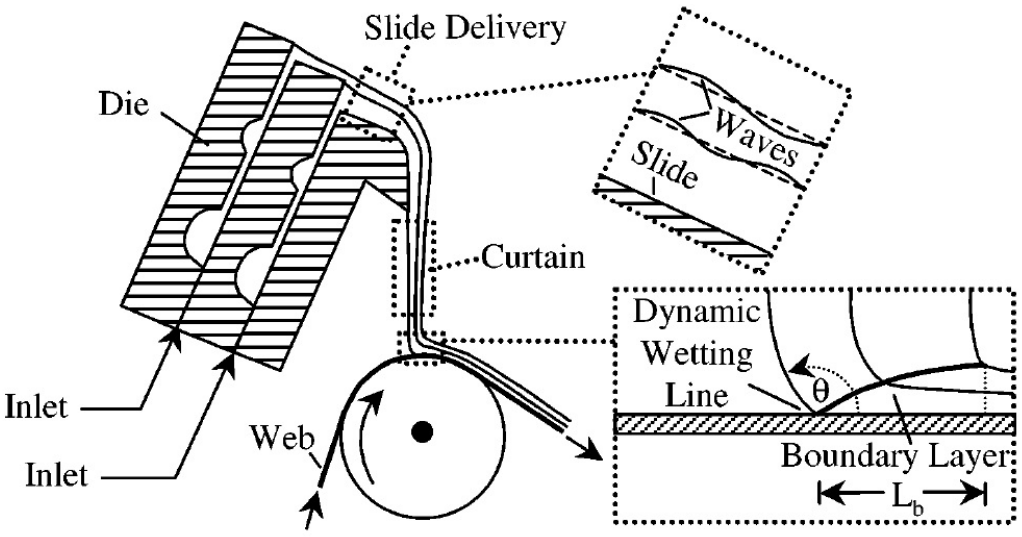

Figure 1.2: Schematic of the curtain coating process (from [118]).

in more detail in Figure 1.1 (b), with the four fluid exit slots labelled, where each fluid layer exits to be prepared for coating.

The slide-die set-up is depicted in more detail in Figure 1.2, showing a cross-sectional schematic of the curtain coating process, taken from [118]. Figure 1.3 shows an altered version of Figure 1.2, labelling parts of the slide-die referred to throughout this thesis. The liquids to be coated are pumped into the die via inlets on the slide-die, using high-precision flowmeters to determine the flow rate (and ultimately the layer thickness) of each layer. From here, the fluids flow through the internal geometry of the slide-die, containing at least one cavity to ensure an even distribution of liquid across the die [71, 72]. The liquid then exits the slide die at the fluid exit slots, with the layers flowing down the inclined plane of the die face, being 'stacked' on top of one another to form a multi-layer film. This multi-layer inclined plane flow, with a free surface and several liquid-liquid interfaces, may be susceptible to perturbations in which waves propagate on these interfaces [79, 91, 123], which can affect the constant thickness of the applied layer.

When producing a coating formed of n-layers, an n-layered film is produced (in the region labelled 'slide delivery' in Figure 1.2) ready for the formation of an n-layered liquid

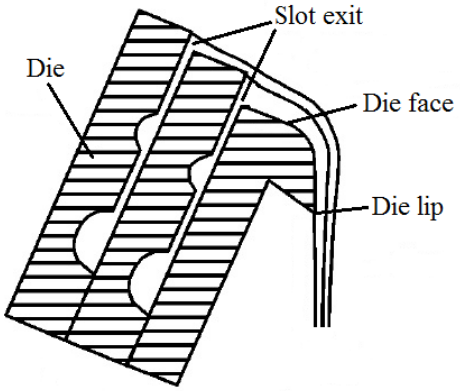

Figure 1.3: Schematic of the slide-die from the curtain coating process (modified from [118]).

curtain, after leaving the slide die at the die lip (see Figure 1.3). The free-falling liquid curtain (or sheet), typically 5-20 cm in length [54], is kept at a uniform width via the use of vertical edge guides. A major disruption to the coating process can be caused by the instability of the liquid curtain. To apply thin coatings, the flow rate is correspondingly reduced. However, there will be a critical flow rate at which point the curtain will rupture, and the fluid will instead leave the die as an array of liquid jets (clearly unsuitable for coating) [48]. The stability of a liquid sheet has been shown [20] to be determined by the ratio between the inertia and surface tension of the fluid, and thus characterised by the Weber number. A simple stability criterion based on this dimensionless number has been calculated in the literature, both in the single layer [74], and multi-layer case [41].

The final stage of the curtain coating process sees the liquid curtain impinge upon the substrate to be coated, labelled the 'web' in Figure 1.2. This region of wetting can cause problems for a variety of reasons. For example, the dynamic contact line can get pushed back (in the opposite direction to the moving substrate) forming a heel of fluid [81]. This can be due to a low substrate speed or a high flow rate, and is problematic for a few reasons - including potential recirculation of fluid, inducing bubbles to leave potential 'coating streaks'. As well as this, the heel may prove to be unstable, potentially causing

a loss of uniformity. Conversely, if the substrate speed is too fast and the flow rate is low, the dynamic contact line will get dragged under the vertical curtain and air pockets will be entrained in the coating layer [13, 15].

This thesis studies the components of the curtain coating process associated with the film flow along the inclined plane of the die face and the liquid curtain. A more in-depth introduction to these aspects is presented at the beginning of each respective chapter.

In collaboration with King Abdullah University of Science and Technology (KAUST), Saudi Arabia, Chapter 2 is focused on imaging and analyzing the thin film flow down the inclined plane of the coating die in an experimental study. The author learned and performed all the experiments at KAUST, before undertaking the image processing and data analysis. Despite much theoretical attention (see, for example, [58, 115, 123]), there is a lack of experimental results in the literature to support even simple mathematical models. In Chapter 2 we describe the experimental techniques adopted, an interesting subject in its own right. This is followed by a derivation of a simple mathematical model, the Newtonian case of the model of Weinstein [116], of inclined plane film flow consisting of n-layers. The experimental results are then analysed, comparing film thicknesses and velocity profiles to the aforementioned theory.

The next aspect of the curtain coating process considered in this thesis is the free-falling liquid curtain. In Chapter 3, we investigate the linear stability of an unsupported two-layer liquid curtain containing insoluble surfactants in both liquids. By making a thin film approximation, the governing equations are simplified, from which equations describing the steady state profiles are obtained. These are solved numerically, enabling the plotting of cross-sectional curtain profiles. The effect that varying the parameters, in particular with the introduction of surfactant, has on these profiles is investigated. The response of the curtain to perturbations about this steady state is then examined, identifying a new stability criterion, extending the work of Brown [20] and Dyson *et*

al. [41].

Following this theoretical work on the stability of a liquid curtain, an experimental investigation into the liquid sheet is conducted. Similar to Chapter 2, this was again in collaboration with KAUST, with all experiments and analysis conducted by the author. The difference between the flow rate required to form a stable curtain and the flow rate at which the curtain disintegrates is considered, with this range in flow rates defining a hysteresis window. The size of the hysteresis window as a function of different fluid properties, such as surface tension and viscosity, is explored. Also studied is the location of where curtain break-up originates. Before completely disintegrating, a small hole (or puncture) in the curtain forms, and grows. The location of this initial puncture is sited, finding that the geometry of the edge guides (vertical or tapered slightly inwards) has a considerable effect. Finally, the speed at which this hole grows is calculated for a range of different liquid properties, and compared to theoretical speeds of liquid sheet retraction, such as the Taylor-Culick speed.

Chapter 5 derives a theoretical model of the liquid film falling from the coating die after curtain break-up, when a series of liquid jets are formed. Noted previously from experiments, these jets are found to have a uniform spacing. Comparing to the Rayleigh-Taylor wavelength of a liquid film falling from the underside of a horizontal solid provides a poor match. This is due to a number of possible reasons, such as the lack of a 'fresh supply' (in the form of an incoming flow rate) or the effect of surfactant. This chapter investigates how tilting the horizontal solid at a small angle allows for the model to account for the incoming flow rate, and incorporates the effect of an insoluble surfactant, similar to Chapter 3. By considering this thin film flow on the underside of an inclined plane for single and two-layer films with surfactant, the beginnings of an extension to the results of Brun *et al.* [21] are presented.

Chapter 2

Multi-layer Film Flow Down an Inclined Plane: Experimental Investigation

2.1 Introduction

In Chapter 1 the industrial process of curtain coating was introduced. The initial stages of the curtain coating process involves the liquids being pumped from the holding tanks through to the inlets of the slide die. High-precision flow-meters control the flow rate to several inlets that evenly distribute the liquid across an exit slot onto the surface of the slide die. Each separate liquid layer then flows down the inclined plane due to gravity, with the merging of liquid layers occurring at each exit slot. This forms a multi-layered film, whereby the liquid layers are each piled on top of one another, in preparation for the formation of a multi-layered liquid curtain. It is the flow of the liquid film down the inclined plane of the coating die that is the interest of the experimental study conducted in this chapter. Figure 2.1 shows a cross-sectional schematic of the flow examined herein.

During the inclined plane flow, there is the formation of a free-surface and several

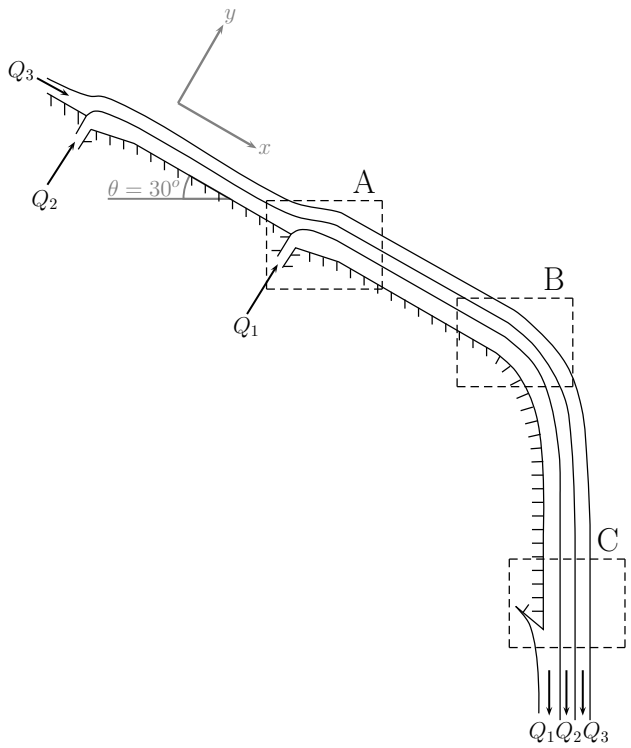

Figure 2.1: Cross-sectional schematic of the slide die for a three-layer film flow. The dashed boxes mark the different viewing regions where experimental images were taken as follows: (A) the exit slot region of layer 1, (B) the curvature of the die and (C) the lip where the film forms a curtain.

liquid-liquid interfaces with the layers stacked upon one another. The exact number of liquid-liquid interfaces depends on the number of liquid layers within the film (a film comprising of n-layers will have $n-1$ liquid-liquid interfaces and a free surface). This flow is susceptible to perturbations with waves being able to propagate along these interfaces and the free surface. Because these perturbations can affect the thickness of the applied liquid layer, potentially resulting in a non-uniform coating, a greater understanding of the slide delivery process will be valuable to the curtain coating industry.

The film flow of a single fluid down a plane inclined by an angle θ to the horizontal, considered in two-dimensions as in the schematic shown in Figure 2.2, has already been subject to considerable study. It is well known that a trivial solution exists to the 2-D governing equations and boundary conditions, known as the Nusselt solution, named after Nusselt's pioneering work on the laminar film condensation on a vertical plate [90]. This

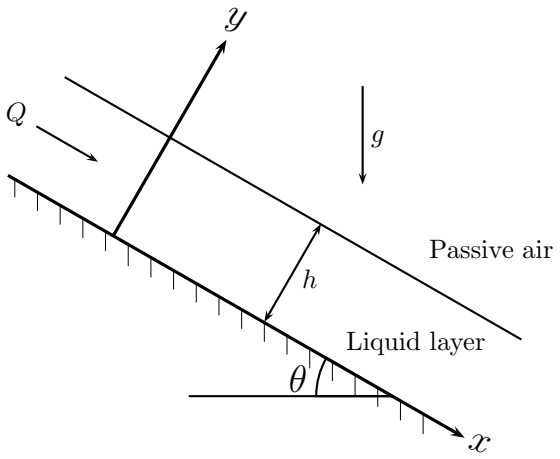

Figure 2.2: Schematic of a single-layer film flowing down an inclined plane, that has the Nusselt [90] solution given by (2.1.1) and (2.1.2).

was built upon by Jeffreys [57], with the steady solution having a unidirectional velocity given by

$$u(y) = \frac{\rho g \sin\theta}{2\mu} y\,(2h - y)\,, \tag{2.1.1}$$

with the constant film thickness given by

$$h = \left(\frac{3\mu Q}{\rho g \sin\theta}\right)^{1/3}. \tag{2.1.2}$$

where ρ is the density of the liquid, μ the dynamic viscosity, Q the flow rate per unit width and g the acceleration due to gravity. Jeffreys also noted how the flow is characterised by the Reynolds number, $Re = \rho Q/\mu$, observing turbulent flow down a vertical plane when $Re > 300$.

Many subsequent works focussed on the propagation and growth of free surface waves on a single layer fluid film. Since the observation that as the Reynolds number decreases the flow becomes laminar, there was a belief at the time that there existed a critical Reynolds number, below which the flow was entirely stable with no observable waves. The original work carried out by Kapitza [65] estimated this critical Reynolds number to be 5.8. Subsequently, Yih gave the first detailed theoretical handling of the stability of the uniform laminar flow of a single fluid down an inclined plane [122]. Yih solved

the Orr-Sommerfeld equation via a power series in the wavenumber multiplied by the Reynolds number, before numerically computing a critical Reynolds number of 1.5.

Experimental work continued in the same vein, concerned with obtaining the Reynolds number below which waves cannot be observed. Examples include the work of Friedman and Miller [46], who observed no waves below $Re = 6.25$, and Grimley [51], who similarly observed no waves below $Re = 6.2$. Theoretical research into the stability of a homogeneous Newtonian fluid flowing down an inclined plane continued with Benjamin arguing analytically that such a critical Reynolds number does not exist for the particular case of uniform flow down a vertical plane [11]. This was supported by the experimental work of Binnie [12], who provided wave speeds that matched well with Benjamin's theoretical study.

In a later paper by Yih [123] a more definitive argument was presented, both mathematically and physically, acknowledging the mistakes of his previous work [122]. Based upon the power series expansion used in his original work, a simpler perturbation procedure was used to analyse stability. Concluding that neutral disturbances exist for small Reynolds numbers right up to the case of $Re = 0$ for all film flows down an inclined plane, the critical Reynolds number was redefined as being the corresponding Reynolds number above which there exists free surface waves that will be amplified. This was given as $Re_c = \frac{5}{6}\cot\theta$.

Through a series of papers by Kao, subsequent work from the single layer case focussed on extending the study of film flow on an inclined plane to the two-layer case [62, 63, 64]. The stratification of both density and viscosity were examined, posing the central question: does the stability of a two-layer system behave the same as the homogeneous case with the same depth and at the same inclined angle? A key feature of this study involved the use of a relative stability index, defined as the ratio of the critical depths of two-layer and one-layer flows.

It was established that in the case of the lower layer having a larger density, the effect of stratification is to increase stability, with the larger the difference in densities, the more stabilising the effect. As expected, in the reverse situation the flow is destabilised. Having confirmed the major role a second mode located at the fluid-fluid interface (as opposed to the free surface) plays in the stability, Kao concluded that the presence of an upper layer has a destabilising effect, in comparison with a homogeneous fluid of the same total depth. The reader is referred to reference [64] for the conclusions on viscosity stratification, which are too involved for the introduction of this chapter.

The study of film flow down an inclined plane was further advanced with the extension to the study of wave motion in an n-layered film [4]. The wave speed of the interfacial mode was found to be much smaller than that of the free-surface mode; with the interfaces seeming to oscillate in phase for the free surface mode, but either in or out of phase for the interfacial modes. This work was followed by a linear stability analysis of this wave motion [115], providing a comprehensive study on how differing ratios of densities, viscosities and layer thicknesses affect interfacial mode instabilities at the liquid-liquid interfaces and the free surface.

The work mentioned so far has remained confined to considering Newtonian fluids, yet it is clear that a non-Newtonian system will change the features of the flow due to the change in constitutive equations, whilst being relevant to industry due to the wide use of non-Newtonian fluids. Weinstein [116] studied the effect of the rheology of a shear-thinning fluid, applying the Carreau model to the constitutive equations. The film thicknesses were considered as a dependent variable, as holds true in a premetered coating method, since the thicknesses of the liquid layers are not known *a priori*. The film thicknesses are dependent on variables such as the flow rate and the inclination angle. In the shear-thinning layer, there will be a range of viscosities, dependent on the strain rate. For instance, at the free surface the strain rate will be zero, so that the fluid here will show

the Newtonian viscosity, whereas at high strain rates (e.g. at the solid boundary of the incline) the viscosity will be lower. Weinstein showed that free-surface waves propagate as in a Newtonian system, the viscosity behaving as some average of the changing viscosities across the shear-thinning layer. On the other hand, interfacial waves are largely affected by local interfacial viscosities, not by some average Newtonian viscosity. The growth of these waves can be either increased or decreased compared with the Newtonian case.

Moreover, Weinstein determined the film thicknesses and velocity profiles in each layer, numerically using a finite difference method. Considering a comparison with a Newtonian fluid having the maximum viscosity exhibited in the shear-thinning layer, the shear-thinning velocities were found to be larger and the film thickness smaller. Compared to the corresponding Newtonian fluid with the minimum viscosity exhibited in the shear-thinning layer, the result is vice versa.

Experimentally, numerous studies have utilised particle image velocimetry (PIV) techniques to visualise small-scale liquid film flows. Alekseenko *et al.* [5] applied PIV to the flow of a single-layer film down an inclined cylinder, showing that the underside film flow obeyed the Nusselt solution. Adomeit and Ritz [2] employed both PIV and fluorescence to study the film thickness and wave motion of an inclined single-layer film. Wierschem *et al.* [119] applied laser doppler velocimetry to measure the velocity in falling films.

Of particular relevance to curtain coating, multi-layer film flows have been investigated by the work of Schweizer, documenting a technique to visualise small-scale film flows [103]. Photographs captured the cross-sectional liquid film profile along a slide die, showing liquid interfaces as well as internal features of the flow using hydrogen bubbles and dye injection to visualise streamlines. This study included the formation of vortices under certain flow conditions, and visualising the liquid film being coated onto a moving substrate in a slide-die coating configuration. The experimental results were used as boundary conditions in a finite element method conducted by Christodoulou and Scriven

[25], successfully matching with the experimental results. Despite this, no attention was given to measuring the velocity field or the film thicknesses of the flow along the inclined plane of the die.

Much concentration has remained experimentally on the various aspects of visualisation techniques, with the reader referred to [67] for a summary of the innovative experimental methods carried out. However, Jiang *et al.* provide some experimental data for three-layer flows of gelatine solution, though the emphasis remained on stability and wave-like structures rather than the film thicknesses [58]. In addition, Noakes *et al.* refined the original imaging technique of Schwiezer to study two-layer flows for a range of slide die geometries, comparing the experimental free surface profiles and streamlines to those derived from their numerical simulations, showing good agreement [89].

A liquid film flowing down an inclined plane continues to be an active research topic in the literature. For example, the more recent studies conducted by Dietze *et al.* [37, 38] theoretically and experimentally study the flow separation that takes place in the capillary wave region of falling films, obtaining film thickness and velocity measurements. A simple visualisation technique was used by Njifenju *et al.* [88], to study single-layer films, with emphasis on wave speeds for low-viscosity water films.

Despite this, the numerous theoretical and experimental works carried out have primarily been focussed on wave formation and the onset of turbulence. There are also various works outlining novel visualisation techniques that are applicable to coating flows, though there has been little utilisation of these techniques to experimentally verify even the simple theory carried out in the past. It is the aim of this chapter to bridge this evident gap by conducting an experimental investigation to test the validity of the film thicknesses given by, in the single layer case Nusselt [90], and in the multi-layer case the Newtonian version of Weinstein's work [116].

Moreover, does a multi-layer film behave in the same way as a single layer film? For

example, if we have a film comprising of two layers, both of the same fluid, with the flow rates (per unit width) of each layer being 1.5 $\mathrm{cm^2 s^{-1}}$ and 0.5 $\mathrm{cm^2 s^{-1}}$, does this film exhibit the same total film thickness and velocity profile as the single layer film with a flow rate of 2 $\mathrm{cm^2 s^{-1}}$? This question also motivates the study conducted in this chapter, and leads us to analyse whether the "1-layer approximation" for the total film height

$$h_T = \left(\frac{3\mu_1 Q_T}{\rho_1 g \sin\theta} \right)^{1/3}, \tag{2.1.3}$$

where μ_1 is the first layer's viscosity, Q_T the total flow rate per unit width and ρ_1 the bottom layer's density, can accurately predict the total film height of a multi-layer film.

Whilst these experiments were carried out, observations of capillary ridges and dimples were made near the regions where two layers merge (near the fluid slot exits). This phenomenon has been studied theoretically by the works of Kalliadasis *et al.* [61] and Bontozoglou and Serifi [18]. These works investigated the behaviour of a liquid film when flowing over topography, such as a dip (a 'step-in') or a rise (a 'step-out') in the solid interface on which the film flows. The study conducted in this chapter reports experimental evidence of similar features, which is lacking in the literature.

The experimental set-up is described before we derive a theoretical model of a multi-layer film flowing down an inclined plane, similar to Weinstein [116]; the differences being in our case the consideration of Newtonian fluids only and the numerical method employed. This theoretical model is then compared to the experimental results, having conducted experiments using two methods. A laser-induced fluorescence technique is used to measure the total film thickness and the change in film thickness from a simple one-layer flow to that of two and three-layers. In addition, particle image velocimetry (PIV) is conducted via a hydrogen bubble technique to obtain velocity profiles to compare to the theoretical model derived. Finally, the observed capillary ridge phenomenon is investigated.

2.2 Experimental set-up

2.2.1 Slide die geometry

For these experiments, a custom-built 4-layer slide die (TSE Troller AG, Switzerland) was used. A pumping station consisting of four 200-litre tanks to hold the fluid for each layer respectively, pumps and manually controlled flow-meters, was linked beside the coating station where the slide-die was situated (see Figure 1.1). A photograph of the general experimental set-up is shown in Figure 2.3. Below the die is an angled plate (shown at the bottom of Figure 2.3) to deflect liquid emanating from the die into a stainless steel catch pan. This meant the liquid could then be pumped back into the holding tanks to re-use. However, when conducting multi-layer experiments where the film comprised of different liquids, the liquid retained by the catch pan could not be recycled, due to the unknown composition of the resultant mix of liquids.

The pumps were able to deliver flow rates from 0.25 up to 7 litres/min, with the exact flow rate for each individual layer determined by the flowmeter (Proline Promag series 50H, Switzerland). These flow rates were then converted into a flow rate per unit width. The fluid was delivered to each layer through a feed line located at the bottom of the slide die and distributed through the width of the cavities. Then the layers would exit on the top face of the die, as described in Chapter 1.

The die is 12 cm wide and is fixed at an incline of 30 degrees from the horizontal. The exit region of each slot is approximately 5.5 mm in total length from the back of the exit slot. This geometry, shown in Figure 2.4, is referred to as a "Chamfered" exit slot [89] and was chosen specifically for its ability to produce laminar flows and to prohibit the inclusion of recirculation zones as seen in [103]. In addition, the die face easily wets to all fluids used in this study, with a very low surface roughness ($R_a = 0.1$ μm, $R_{t,max} = 1.2$ μm).

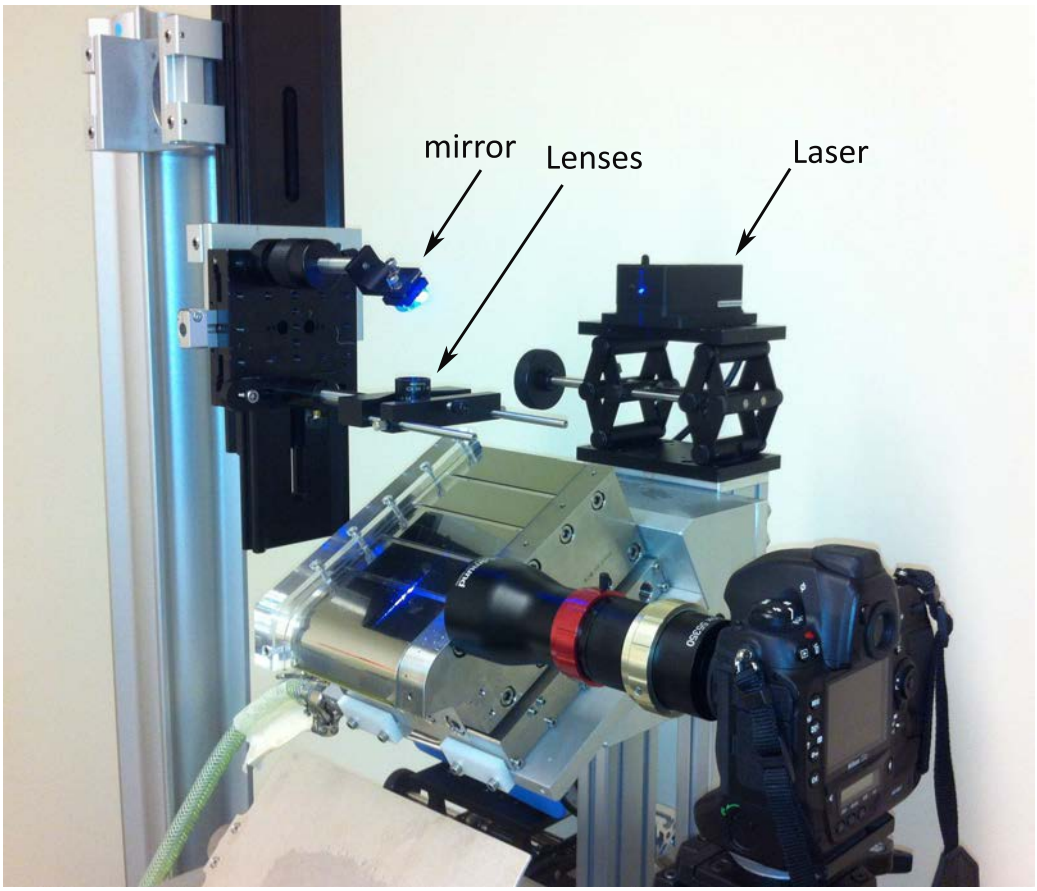

Figure 2.3: Photograph of the experimental setup, showing the die face illuminated by a blue laser passed through optics to create a light sheet.

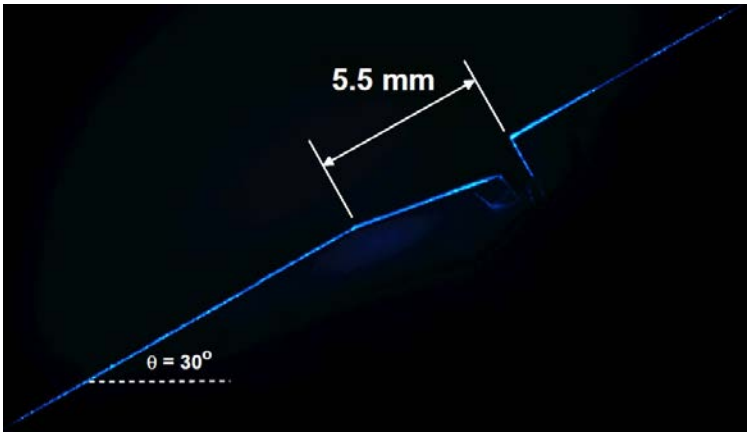

Figure 2.4: The geometry of the fluid exit slots. The edge of the die has been illuminated by the blue laser light sheet.

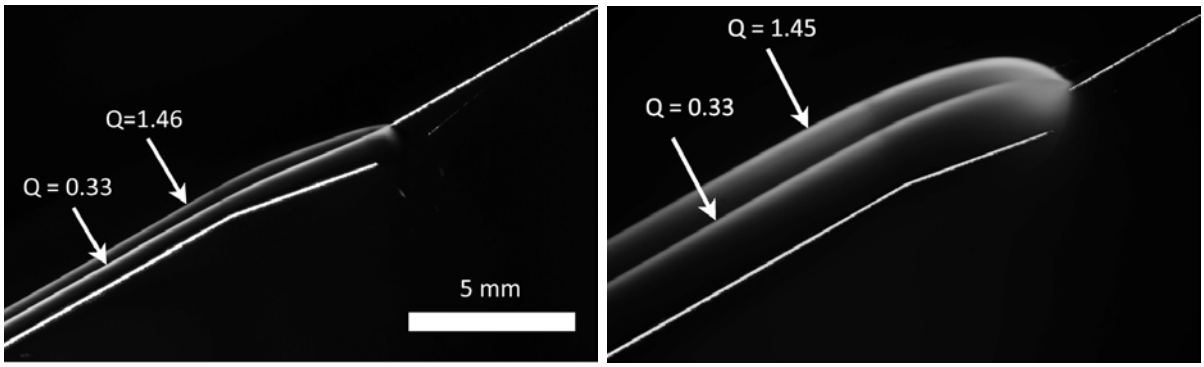

(a) (b)

Figure 2.5: Free surface profiles taken using the fluorescein imaging technique, for (a) 50% glycerol and (b) 90% glycerol. The flow rates are given in the figures (with units cm^2s^{-1}), along with a reference scale bar. The die face has been superimposed on the images.

2.2.2 Flow visualisation

In order to gain quantitative information from the flow, we need to use appropriate flow visualisation techniques. Reviews on this subject are given by Schweizer [67, 103] and herein we use a similar method of optical sectioning to image a single plane near the centre of the die to minimize edge effects. In our experiments, two different methods were used for capturing information about the flow.

Fluorescein technique

For obtaining the total film thickness, we used a laser-induced fluorescence technique, whereby the fluid contains fluorescein dye excited by the blue laser light (475 nm) with peak emission at 520 nm. Still photographs were captured by a high-resolution digital camera (Nikon D3X) at a pixel resolution of 6048 by 4032.

A reference image of the die face is taken, as in Figure 2.4, whereby the die face is illuminated by the blue laser sheet. An image of the flow is then superimposed onto the reference image, to produce an image such as those given in Figure 2.5. The total film thickness can be measured from these images, using the technique described in the next section.

In many previous studies (see, for example, [40, 92, 100]) measuring the instantaneous film thickness was complicated by the formation of free surface waves for low-viscosity fluids. Since the film thickness would be fluctuating, a time-averaging filter was used to circumvent this problem. In our study, we use long exposure times[1] (up to 1 s) without observing any blurring motion, thus indicating that there are no waves present. However, as discussed in detail in Section 2.7, we do observe stationary capillary ridges.

Hydrogen bubble technique

For obtaining the velocity fields, the hydrogen bubble technique was adopted as used in the works of Schweizer [103] and Noakes *et al.* [89] in combination with a high-speed camera (Photron Fastcam SA-3) at frame rates of 1000 fps. The same blue laser light from the fluorescein technique was used, with a mirror and lens assembly (shown in Figure 2.3) to render a light sheet angled down onto the face of the die.

A schematic of the experimental set-up of the hydrogen bubble technique is provided in Figure 2.6. The schematic is from the view-point of the camera, i.e. taking a cross-sectional view of the liquid film. The main points of the hydrogen bubble technique are as follows: an electrical circuit incorporating the liquid film is created by using a DC power supply with a fine platinum wire (75 μm in diameter) as the negative electrode and the die itself as the positive electrode. When the wire is lowered into the liquid film, hydrogen bubbles are created and swept along with the flow of the film, thus acting as tracer particles. Since this method relies on the conductivity of the liquid, a small amount of salt (sodium chloride) is added to the fluid and the voltage selected using guidelines from [103]. In all cases, we carefully lowered the wire into the exit slot cavity to ensure

[1]The exposure time (equivalent to the shutter speed) refers to the amount of time that the digital sensor of the camera is exposed to light. Hence, too long an exposure time can result in an image being overly bright (known as overexposure), and too short an exposure time can result in an image being overly dark (underexposure). This also means when capturing moving objects, a longer exposure time will produce a blurred image following the motion (for example, a streak of light following a car's headlights).

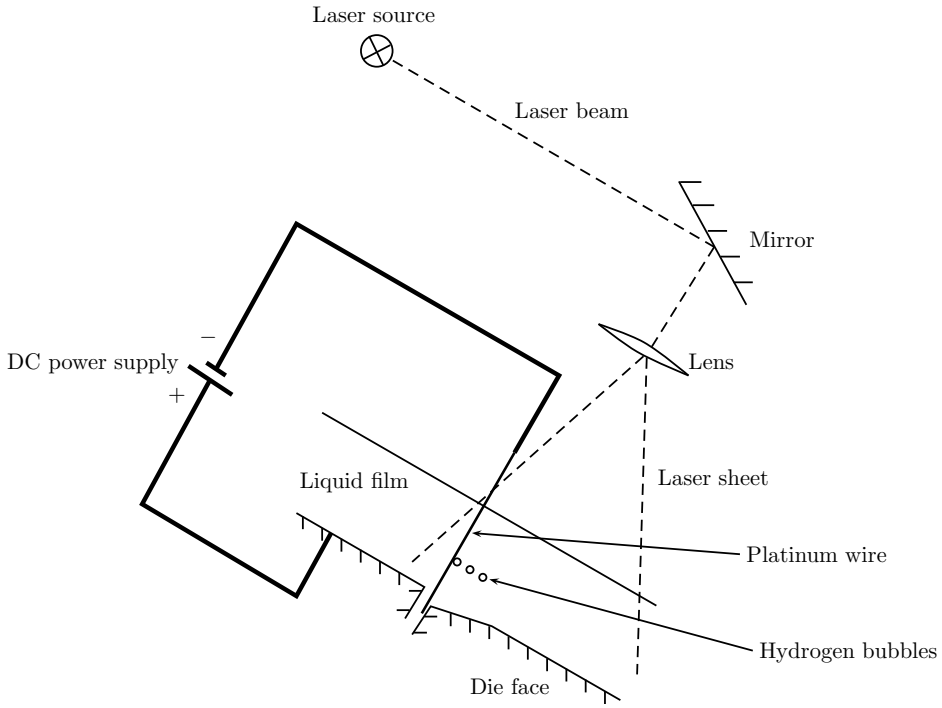

Figure 2.6: A schematic of the experimental set-up of the hydrogen bubble technique.

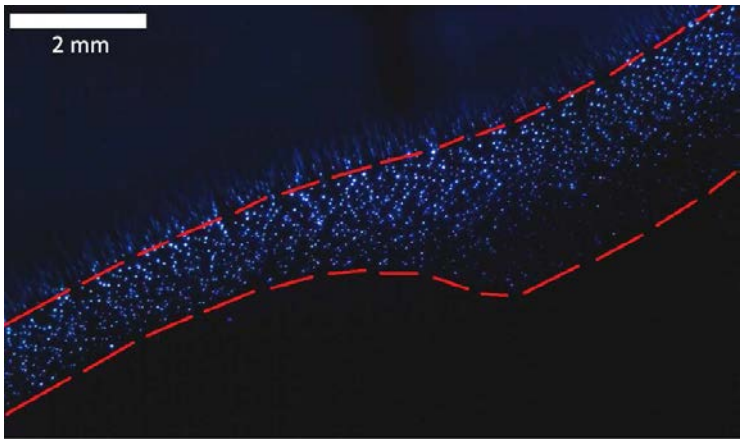

Figure 2.7: An example frame from a high-speed video sequence taken at 1000 fps for a 2-layer 5% CMC solution, with $Q_1 = 0.67$ cm^{2}s^{-1} and $Q_2 = 0.5$ cm^{2}s^{-1}. The dashed red line indicates the free surface and lower interface of the top layer, since there are hydrogen bubbles within the top layer only.

the full height of the liquid layer(s) is seeded with the tracer bubbles.

The bubbles were then illuminated with the same blue laser light sheet and, due to the highly reflective nature of the bubbles, they were easily captured by the high-speed camera with shutter speeds of 1/3000 sec to minimize streaking. Figure 2.7 shows an example frame from the high-speed videos taken. This figure highlights another feature of the hydrogen-bubble technique, that a liquid-liquid interface can also be located within a multi-layer film. For all 2-layer experiments, the second (top) layer was seeded with hydrogen bubbles. This enabled the liquid-liquid interface to be located, as well as the velocity field in the top layer. For all 3-layer experiments, the second and third (top two) layers were seeded with hydrogen bubbles. This enabled the liquid-liquid interface between the first (bottom) and second (middle) layer to be located, as well as the velocity field in the second and third layers.

The diameter of the wire, d_w, was chosen using the criterion $d_w < 40 \left(\frac{3(\mu/\rho)^4}{g \sin\theta Q^2} \right)^{1/3}$. This formula was empirically postulated by Clutter and Smith [28], whereby the effect of the wire is negligible when the Reynolds number is less than 40, using d_w as the length scale and the average velocity of the film calculated from the Nusselt solution (2.1.1) and

(2.1.2) as the velocity scale. Also, with reference to [103], the bubbles produced with this diameter wire are small enough (the bubbles having a diameter of ≈ 35 μm) that we can neglect the buoyancy force experienced throughout the flow of the film and thus expect them to faithfully follow the flow.

To obtain a cross-sectional profile as the fluid emanates from the exit slot and flows along the inclined plane, all still photographs and high-speed video sequences were taken from the side of the slide die with a telecentric lens which is focused into the plane of the laser sheet. The edge guides on the top face of the die, used primarily to constrain the fluid to the die face, were transparent and induced an upwards facing meniscus, thus rendering easy optical access to the centre of the die face where the laser sheet was positioned. This technique is also detailed in [103]. The laser sheet is rendered by reflecting a horizontal beam at an angle off a mirror and then passing through a combination of an elliptical and cylindrical lens onto the face of the die. Before taking a set of images, a reference image with no flow is captured, such as that shown in Figure 2.4. This allows us, in the analysis, to superimpose the reference image with an image of the free surface when there is film flow, meaning the film thickness and contact line position can be resolved.

2.2.3 Fluid properties

The fluids used in this study were simple water-glycerol mixtures and aqueous solutions of carboxymethyl cellulose (CMC), with an average molecular weight of 90,000 g/mol and degree of substitution (DS) of 0.7. The concentration of glycerol in the water-glycerol mixtures range from 50 - 90%, exhibiting Newtonian behaviour. Sodium dodecyl sulfate (SDS) is added to samples of the 60% and 80% solutions, at both 0.05% and 0.2% concentrations, as a surfactant to test the effect of varying the surface tension. The CMC solutions exhibited shear-thinning properties that were best described by the Cross

Glycerol conc. ($\%_{v/v}$)	Surfactant conc. ($\%_{w/w}$)	Viscosity μ (mPa.s)	Density ρ (kg/m^3)	Surface tension σ (mN/m)
50	-	8.4	1146	66.9
60	-	15.3	1171	65.7
70	-	30	1196	64.7
80	-	72	1218	63.7
90	-	219	1241	62.3
∼60	0.05 SDS	16.6	1171	48.5
∼60	0.2 SDS	16.6	1171	39.9
∼80	0.05 SDS	77	1218	55.8
∼80	0.2 SDS	77	1218	48.2

Table 2.1: Physical properties of the glycerol-based fluids used in the experiments. The stated values were measured at the ambient temperature of the laboratory during the experiments (21 ^{o}C).

model[2] [10], given by

$$\frac{\mu - \mu_\infty}{\mu_0 - \mu_\infty} = \frac{1}{1 + [\lambda\dot{\gamma}]^{(1-n)}} \tag{2.2.1}$$

where μ is the apparent viscosity for a given shear rate $\dot{\gamma}$, μ_0 and μ_∞ are the asymptotic values of viscosity at zero and infinite shear rates, λ is a constant with units of time and n is a rate index constant.

The surface tensions were measured using a du Nouy ring tensiometer (K100, Kruss GmbH, Germany), whilst viscosity measurements made using a cone-and-plate geometry on a rotational rheometer (Ares G2, TA Instruments, USA). The physical properties of the glycerol mixtures are listed in Table 2.1, whilst the rheological and physical properties of the CMC solutions are listed in Table 2.2.

2.3 Theoretical model for multiple layers

In this section we consider a mathematical model of a liquid film comprising of n-layers flowing down an inclined plane, at an angle θ to the horizontal. A schematic is shown in Figure 2.8. This model is a similar, albeit simpler, case of the model of Weinstein [116]

[2]At low shear rates, a fluid that follows the Cross model exhibits Newtonian behaviour. At high shear rates the fluid behaves as a power-law fluid.

CMC conc. ($\%_{w/w}$)	μ_0 mPa.s	λ $\times 10^{-3}$ s	n -	Surface tension mN/m
2	37	0.12	0.03	69.8
3	137	0.33	0.223	69.6
4	407	0.93	0.346	69.9
5	926	2.58	0.422	68.2

Table 2.2: Rheological and physical properties of the CMC solutions used. For all solutions, a value of $\mu_\infty = 0.001$ Pa.s was assumed for fitting to equation (2.2.1). The stated values were measured at the ambient temperature of the laboratory during the experiments (21 ^{o}C).

whereby shear-thinning fluids were considered and the steady, uniform film problem solved using a finite difference method. In the theory presented here, we consider Newtonian fluids and solve the system numerically via Newton's method.

The x-axis is taken to be parallel with the inclined plane (so that the line $y = 0$ corresponds to the die face), with the y-axis perpendicular to this. The dimensional equations that govern the flow of each layer are given by the Navier-Stokes and continuity equations

$$\rho_k \left(\frac{\partial \mathbf{u}_k}{\partial t} + (\mathbf{u}_k \cdot \nabla) \mathbf{u}_k \right) = -\nabla p_k + \mu_k \nabla^2 \mathbf{u}_k + \rho_k g \left(\sin\theta \mathbf{i} - \cos\theta \mathbf{j} \right), \tag{2.3.1}$$

$$\nabla \cdot \mathbf{u}_k = 0, \tag{2.3.2}$$

where the subscript $k \in [1, n]$ refers to the layer being considered, with $\mathbf{i}$ and $\mathbf{j}$ denoting the unit vectors in the increasing x and y-direction respectively. It has been assumed each layer is a Newtonian liquid that is incompressible.

To solve equations (2.3.1) and (2.3.2), boundary conditions are imposed at the solid boundary, each liquid-liquid interface and the free surface. First, the no-slip and impermeability condition is given by

$$\mathbf{u}_1 = 0, \tag{2.3.3}$$

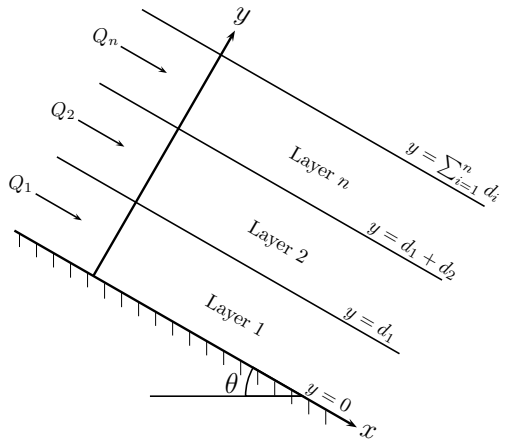

Figure 2.8: A schematic of the theory derived in this section.

at $y = 0$. At each liquid-liquid interface, there are the normal and tangential stress conditions

$$[\mathbf{n}_k \cdot \mathbf{T}_j \cdot \mathbf{n}_k]_{j=k}^{j=k+1} = \sigma_k \mathbf{n}_k \left(\nabla \cdot \mathbf{n}_k\right), \tag{2.3.4}$$

and

$$[\mathbf{n}_k \cdot \mathbf{T}_j \cdot \mathbf{t}_k]_{j=k}^{j=k+1} = 0, \tag{2.3.5}$$

at $y = \sum_{i=1}^{k} d_i$, where $k \in [1, n-1]$. The outward facing unit normal and tangent vectors at $y = \sum_{i=1}^{k} d_i$ are given by $\mathbf{n}_k$ and $\mathbf{t}_k$, whilst σ_k is the surface tension of the interface at $y = \sum_{i=1}^{k} d_i$. Moreover, $\mathbf{T}$ is the stress tensor, given by

$$\mathbf{T}_{ij} = -p\delta_{ij} + \mu\left(\frac{\partial u_i}{\partial x_j} + \frac{\partial u_j}{\partial x_i}\right),$$

where, in this equation only, the subscript i and j are used as part of suffix notation. The kinematic condition and continuity of velocity conditions are also imposed at each liquid-liquid interface

$$\frac{\partial h_k}{\partial t} + u_k \frac{\partial h_k}{\partial x} = v_k, \tag{2.3.6}$$

where $h_k = \sum_{i=1}^{k} d_i$, and

$$\mathbf{u}_k = \mathbf{u}_{k+1}, \tag{2.3.7}$$

at $y = \sum_{i=1}^{k} d_i$, where $k \in [1, n-1]$. The final boundary conditions are given at the free surface, where we assume the air is passive and has no effect on the flow. These are the normal and tangential stress conditions, and the kinematic condition

$$\mathbf{n}_n \cdot \mathbf{T}_n \cdot \mathbf{n}_n = -\sigma_n \mathbf{n}_n \left(\nabla \cdot \mathbf{n}_n\right), \tag{2.3.8}$$

$$\mathbf{n}_n \cdot \mathbf{T}_n \cdot \mathbf{t}_n = 0, \tag{2.3.9}$$

and

$$\frac{\partial h_n}{\partial t} + u_n \frac{\partial h_n}{\partial x} = v_n, \tag{2.3.10}$$

where $h_n = \sum_{i=1}^{n} d_i$, at $y = \sum_{i=1}^{n} d_i$. Next, the governing equations, (2.3.1) and (2.3.2), and boundary conditions, (2.3.3) – (2.3.10), are non-dimensionalised and solved in the steady state assuming a waveless solution.

Since in coating flows, the film thickness is not known *a priori* it is convenient to use a length scale that does not involve the film thickness to non-dimensionalise the equations. Thus, following [58] and [116], the following scales are used:

$$y = d_s \overline{y}, \quad u = \frac{Q_T}{d_s} \overline{u}, \quad p = \frac{\rho_1 Q_T^2}{d_s^2} \overline{p}, \tag{2.3.11}$$

where bars denote dimensionless variables, and

$$d_s = \left(\frac{\mu_1 Q_T}{\rho_1 g \sin\theta}\right)^{1/3}, \quad N_k = \frac{\mu_k}{\mu_1}, \quad M_k = \frac{\rho_k}{\rho_1},$$

correspond to the length scale, viscosity ratio and density ratio respectively. The subscript k refers to which liquid layer is considered, with $k \in [1, n]$. The total flow rate, that is

the sum of the flow rate of each individual layer, is given by Q_T. In addition, we form the Reynolds number $Re = \rho_1 Q_T/\mu_1$, meaning that no dimensionless group is dependent on the unknown thickness.

Uni-directional ($\overline{v}_k = 0$, $\partial/\partial\overline{x} = 0$) and steady ($\partial/\partial\overline{t} = 0$) flow is now assumed. The Navier-Stokes equations (2.3.1) become in non-dimensional form

$$N_k \frac{\mathrm{d}^2\overline{u}_k}{\mathrm{d}\overline{y}^2} + M_k = 0, \tag{2.3.12}$$

$$-Re\tan\theta\frac{\mathrm{d}\overline{p}_k}{\mathrm{d}\overline{y}} - M_k = 0, \tag{2.3.13}$$

where $k \in [1, n]$, whilst the continuity equation (2.3.2) is automatically satisfied. Equations (2.3.12) and (2.3.12) are subject to the non-dimensional boundary conditions as follows.

The no-slip condition from (2.3.3):

$$\overline{u}_1 = 0, \tag{2.3.14}$$

at $\overline{y} = 0$. The normal stress, tangential stress and continuity of velocity conditions from (2.3.4), (2.3.5) and (2.3.7):

$$\overline{p}_k = \overline{p}_{k+1}, \tag{2.3.15}$$

$$N_k\frac{\mathrm{d}\overline{u}_k}{\mathrm{d}\overline{y}} = N_{k+1}\frac{\mathrm{d}\overline{u}_{k+1}}{\mathrm{d}\overline{y}} \tag{2.3.16}$$

$$\overline{u}_k = \overline{u}_{k+1}, \tag{2.3.17}$$

at $\overline{y} = \sum_{i=1}^{k}\overline{d}_i$ for $k \in [1, n-1]$. The normal and tangential stress conditions from (2.3.8) and (2.3.9):

$$\overline{p}_n = 0, \tag{2.3.18}$$

$$N_n \frac{\mathrm{d}\overline{u}_n}{\mathrm{d}\overline{y}} = 0, \tag{2.3.19}$$

at $\overline{y} = \sum_{i=1}^{n} \overline{d}_i$. The kinematic boundary conditions (2.3.6) and (2.3.10) are automatically satisfied.

We also have the condition for the flow rate

$$\frac{Q_k}{Q_T} = \overline{Q}_k = \int_{\sum_{i=0}^{k-1} \overline{d}_i}^{\sum_{i=0}^{k} \overline{d}_i} \overline{u}_k \, \mathrm{d}\overline{y}, \tag{2.3.20}$$

for $k \in [1, n]$. Integrating (2.3.12) twice, and using the boundary conditions (2.3.14), (2.3.16), (2.3.17) and (2.3.19) the solution for the velocity is obtained:

$$\overline{u}_k = \frac{1}{N_k} \left(a_k + c_k \overline{y} - \frac{1}{2} M_k \overline{y}^2 \right), \tag{2.3.21}$$

where

$$a_k = \sum_{i=1}^{k-1} \left[\left(\frac{N_k}{N_i} c_i - \frac{N_k}{N_{i+1}} c_{i+1} \right) \sum_{j=1}^{i} \overline{d}_j + \frac{1}{2} \left(\frac{N_k}{N_{i+1}} M_{i+1} - \frac{N_k}{N_i} M_i \right) \left(\sum_{j=1}^{i} \overline{d}_j \right)^2 \right], \tag{2.3.22}$$

$$c_k = M_n \sum_{i=1}^{n} \overline{d}_i + \sum_{i=k}^{n-1} \left[(M_i - M_{i+1}) \sum_{j=1}^{i} \overline{d}_j \right]. \tag{2.3.23}$$

The condition on the flow rate (2.3.20) is used to calculate the thickness of the k'th layer; using the coordinate transform

$$Y = \frac{1}{\overline{d}_k} \left(\overline{y} - \sum_{i=1}^{k-1} \overline{d}_i \right) \tag{2.3.24}$$

each fluid layer will have a domain $Y \in [0, 1]$, as opposed to an unknown domain (the film thickness). $Y = 0$ corresponds to the bounding interface closest to the inclined plane; $Y = 1$ corresponds to the upper bounding interface, and the condition on the flow rates

becomes

$$\overline{Q}_k = \int_0^1 \overline{u}_k\left(Y\right)\overline{d}_k \ \mathrm{d}Y. \tag{2.3.25}$$

Thus, for a fluid film consisting of n-layers, the solution for velocity in the k'th layer, u_k, is given by (2.3.21). Moreover, (2.3.25) provides a system of n equations in the n unknown film thicknesses, $\overline{d}_k$.

In the single-layer case, we have from (2.3.21)

$$\overline{u}_1 = \overline{d}_1\overline{y} - \frac{1}{2}\overline{y}^2,$$

and from the transformation (2.3.24) and flow rate condition (2.3.25)

$$\begin{aligned}
1 &= \int_0^1 \overline{u}_1\left(Y\right)\overline{d}_1 \ \mathrm{d}Y \\
&= \int_0^1 \left(\overline{d}_1^2 Y - \frac{1}{2}\overline{d}_1^2 Y^2\right)\overline{d}_1 \ \mathrm{d}Y \\
&= \overline{d}_1^3\left[\frac{1}{2}Y^2 - \frac{1}{6}Y^3\right]_0^1 \\
&= \frac{1}{3}\overline{d}_1^3.
\end{aligned}$$

Since for a single layer film, from the non-dimensionalisation, $\overline{Q}_1 = 1$. From this, we obtain

$$\overline{d}_1 = 3^{1/3}.$$

Converting these equations back into their dimensional form, we obtain the solutions for the velocity and the film thickness

$$u = \frac{\rho g \sin\theta}{2\mu} y\left(2d_1 - y\right), \qquad d_1 = \left(\frac{3\mu Q}{\rho g \sin\theta}\right)^{1/3},$$

which matches with the Nusselt solution (2.1.1) and (2.1.2), as expected.

In the two-layer case, we find using (2.3.21)

$$\overline{u}_1 = \frac{1}{N_1}\left(c_1\overline{y} + a_1 - \frac{1}{2}M_1\overline{y}^2\right),$$
$$\overline{u}_2 = \frac{1}{N_2}\left(c_2\overline{y} + a_2 - \frac{1}{2}M_2\overline{y}^2\right),$$

where a_1, a_2, c_1 and c_2 are calculated using (2.3.22) and (2.3.23). From this and (2.3.25), we have that

$$\overline{Q}_1 = \frac{\overline{d}_1^2}{N_1}\left(\frac{1}{3}M_1\overline{d}_1 + \frac{1}{2}M_2\overline{d}_2\right),$$
$$\overline{Q}_2 = \frac{\overline{d}_2}{N_2}\left(\frac{1}{2}\frac{N_2}{N_1}M_1\overline{d}_1^2 + \frac{N_2}{N_1}M_2\overline{d}_1\overline{d}_2 + \frac{1}{3}M_2\overline{d}_2^2\right).$$

Using Newton's method with set parameter values for the flow rates, densities and viscosities, a solution for the film thicknesses $\overline{d}_1$ and $\overline{d}_2$ can be found from these two equations. These are considered as

$$f_1\left(\overline{d}_1, \overline{d}_2\right) = 0,$$
$$f_2\left(\overline{d}_1, \overline{d}_2\right) = 0.$$

Using an initial 'guess', $\mathbf{x}_0 = (1, 1)$ for $\overline{d}_1$ and $\overline{d}_2$, the iterative procedure is given by

$$\mathbf{x}_i = \mathbf{x}_{i-1} - \left(J\left(\mathbf{x}_{i-1}\right)\right)^{-1}\mathbf{F}\left(\mathbf{x}_{i-1}\right),$$

where $i = 1, 2, 3\ldots$, and

$$\mathbf{x} = \left(\overline{d}_1, \overline{d}_2\right)^T,$$

$$\mathbf{F}\left(\mathbf{x}\right) = \left(f_1, f_2\right)^T,$$

$$J(\mathbf{x}) = \begin{pmatrix} \frac{\partial f_1}{\partial \bar{d}_1}(\mathbf{x}) & \frac{\partial f_1}{\partial \bar{d}_2}(\mathbf{x}) \\ \frac{\partial f_2}{\partial \bar{d}_1}(\mathbf{x}) & \frac{\partial f_2}{\partial \bar{d}_2}(\mathbf{x}) \end{pmatrix}.$$

This process is computed numerically via Matlab. A similar procedure will solve the film thicknesses for more than two layers.

For clarification on the terms used in the next sections of this chapter, when comparing the experimental results to theory, the "single-layer theory" refers to the Nusselt solution, (2.1.1) and (2.1.2), which we have shown to be identical to the single-layer theory of this section. Any use of the term "multi-layer theory" (or "n-layer theory") refers to the theory outlined in this section, where the velocities have been determined from (2.3.21) and the film thicknesses numerically computed via (2.3.25).

When considering multi-layer films, the "1-layer approximation" refers to equation (2.1.3). If the layers are comprised of the same fluid, the theory from this section matches exactly with the "1-layer approximation". That is, the total film height from (2.1.3) matches with the total film height computed from the theory in this section.

2.4 Total film thickness measurements

2.4.1 1-layer films

In Figure 2.9 we plot the film thickness measured for the CMC solutions at all different concentrations used. Here, the single layer Nusselt solution (2.1.2) used assumes the zero-shear viscosities (i.e. $\mu_0 = 37$, 137, 407 and 926 mPa.s) as the constant viscosity, which yields good agreement and thus indicates that the shear-thinning characteristics are minimal in the one-layer flow. Taking, as a first approximation, an average shear rate $\dot{\gamma} \approx U_s/h = O(10\ \mathrm{s}^{-1})$, and using equation (2.2.1) and values in Table 2.2, we see that the 5% CMC solutions viscosity may be reduced from $\mu_0 = 926$ mPa.s to $\mu = 825$ mPa.s, whilst the 4% CMC solutions viscosity may be reduced from $\mu_0 = 407$ mPa.s to $\mu = 389$

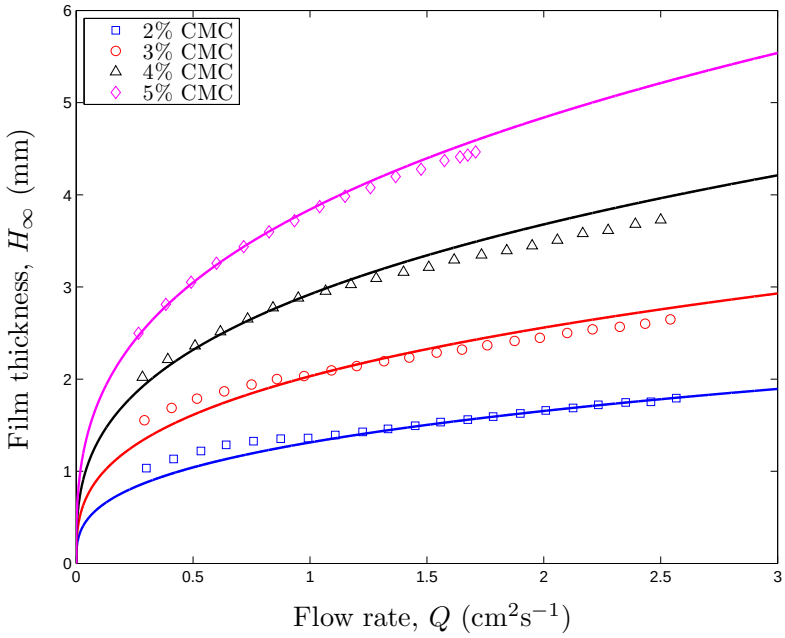

Figure 2.9: Film thickness versus flow rate for 2%, 3%, 4% and 5% CMC solutions. The data points correspond to experimental measurements, whilst the solid lines plot the predicted thickness from equation (2.1.2). $Re = 0.034 - 6.75$.

mPa.s. The reduction in the 2% and 3% CMC solutions is negligible. We see a slight overestimate from the theory, explained from the use of the zero-shear rate viscosity, whereas the actual viscosity will be slightly below this.

Figure 2.10 plots the normalised film thickness, i.e. the ratio of the experimental film thickness and the theoretical thickness from (2.1.2), H_∞/H_{theory}, against (a) viscosity and (b) surface tension, for four fixed flow rates. The entire range of glycerol-based and CMC-based fluids are included in Figure 2.10 (a), obtaining the full range of viscosities used in the experiments (note the viscosity scale is logarithmic thus spanning two orders of magnitude). As with Figure 2.9, we find good agreement between the measured and predicted values across the range of viscosities and surface tensions with a maximum difference of 22%.

Finally, in Figure 2.11, all of the data acquired from the 1-layer experiments is plotted, in the form of the experimental measurements for the film height versus the theoretical

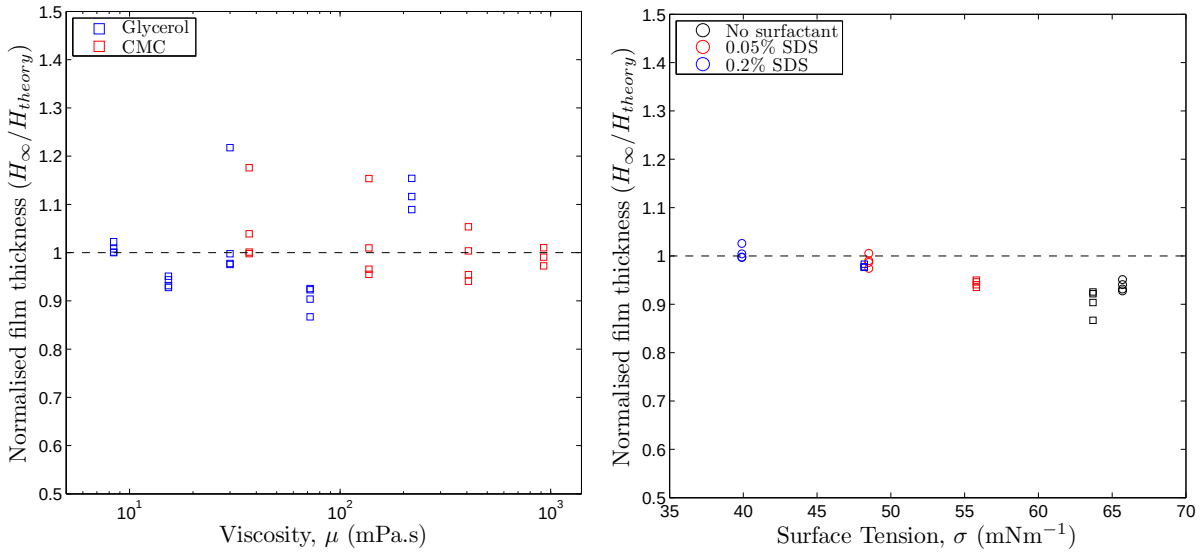

(a) (b)

Figure 2.10: Normalised film thickness plotted against (a) viscosity and (b) surface tension. In (a), all glycerol (without SDS) and all CMC solutions are plotted. In (b), all 60% (circles) and 80% (squares) glycerol are plotted, along with the corresponding concentrations with 0.05% and 0.2% SDS.

predictions of (2.1.2). This comprises a total of 262 experimental conditions, with the various flow rates, viscosities and densities of the single layer fluid. The data collected from the experiments agrees well with the theory, for all of the solutions used. Noting that these film thicknesses were taken downstream of the exit slot, this is to be expected as the film flow has reached a fully developed steady state.

2.4.2 2-layer films of the same fluid

When considering a 2-layer film, where both layers are comprised of the same fluid (so that the only difference between layers is the relative flow rate, i.e. differential motion), the mathematical description given in Section 2.3 predicts that the 2-layer film behaves as a 1-layer film. For example, this means that a 2-layer film with flow rates in the bottom and top layers given by $Q_1 = 1.5$ cm^{2}s^{-1} and $Q_2 = 0.5$ cm^{2}s^{-1} theoretically has the same total film thickness and velocity profile as that of a single layer with a flow rate

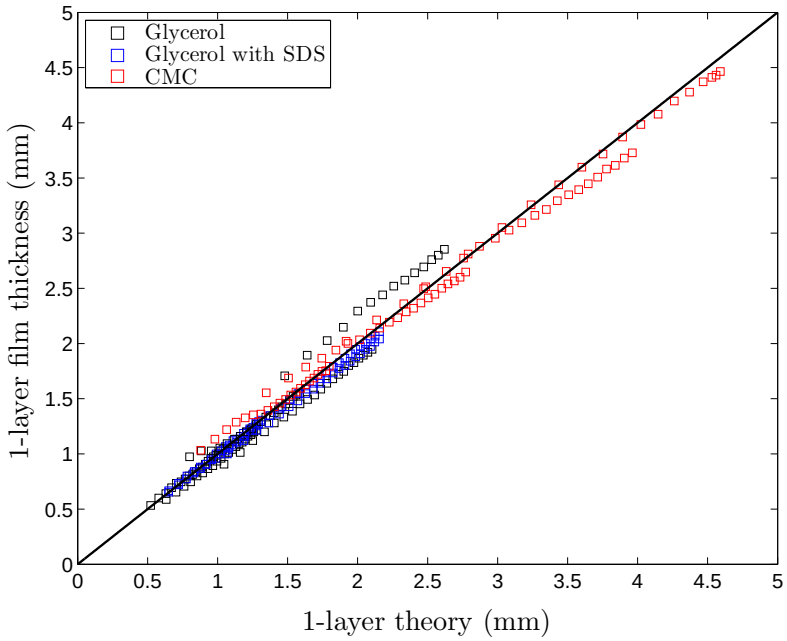

Figure 2.11: Comparison of film thickness measurements versus the 1-layer exact solution (2.1.2). The plot includes all 1-layer experiments, a total of 262 measurements with $Re = 0.034 - 34$.

$Q = 2$ cm^{2}s^{-1}. This implies that the 1-layer approximation given by equation (2.1.3) should predict the thickness of each film in this section exactly.

Figure 2.12 shows two example plots of the total flow rate plotted against total film thickness, where both layers are (a) 70% glycerol and (b) 4% CMC. The solid black line shows the simple 1-layer approximation (2.1.3), whilst the data points show a variety of different experimental data. Either the flow rate in the bottom layer was fixed and the flow rate in the top layer was varied or vice versa (see legend for details). In both cases, and for both fluids, it can be seen that the 1-layer approximation describes the thickness almost precisely across the whole range of flow rates.

In Figure 2.13 we plot all of the experimental data from the two-layer experiments (a total of 833 measurements) to compare against the 1-layer approximation. There is clearly a very good fit between the data and the theory, despite some slight discrepancies for the higher viscosity glycerol solutions with $h > 2$ mm.

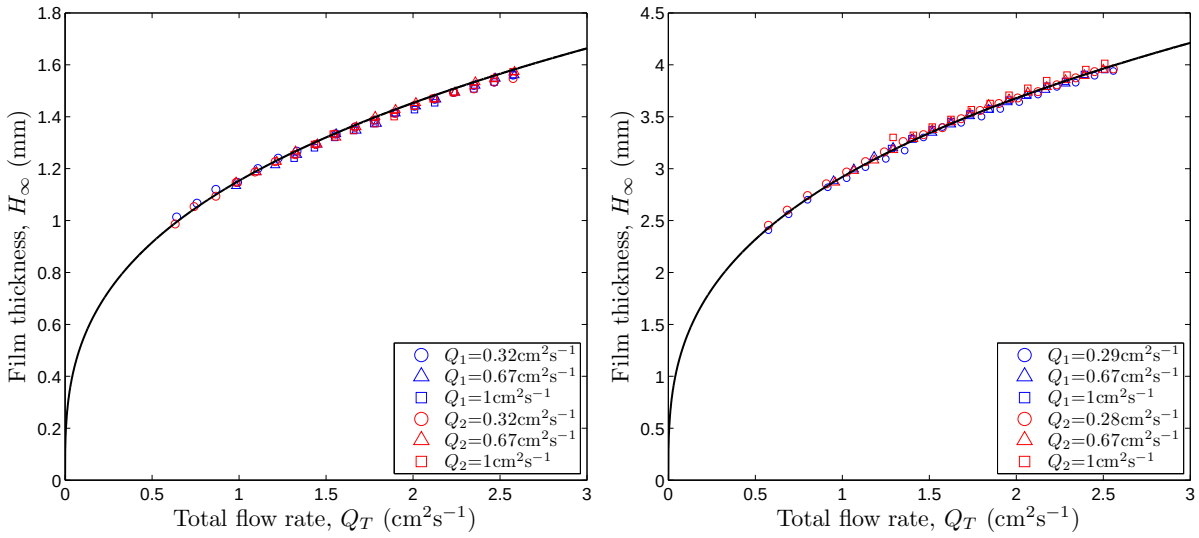

Figure 2.12: Total film thickness versus total flow rate for 2-layer film flows where both layers are (a) 70% glycerol and (b) 4% CMC. The legend indicates which layer had a fixed flow rate, whilst the other layer's flow rate was varied. The solid black curve shows the 1-layer approximation, equation (2.1.3). Reynolds numbers are (a) $Re = 2.4 - 10.4$ and (b) $Re = 0.15 - 0.64$.

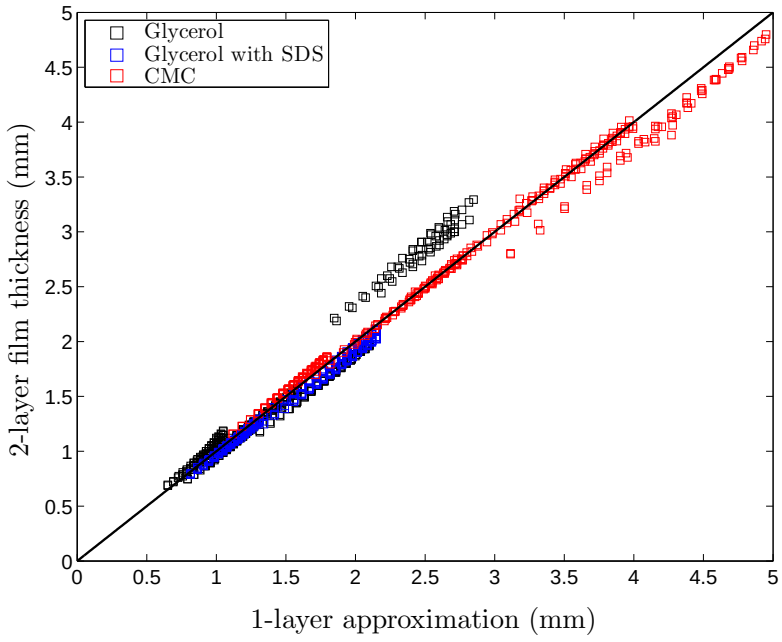

Figure 2.13: Comparison of film thickness measurements versus the 1-layer approximation (2.1.3). The plot includes all 2-layer experiments, a total of 883 measurements. $Re = \ 0.065 - 35$.

2.4.3 2-layer films of different fluids

For two-layer films of different fluids, we observe some discrepancies with the one-layer film approximation, depending on which fluid is in the bottom layer closest to the die face. This is evident with reference to Figures 2.14 and 2.15. Figure 2.14 shows the total film thicknesses measured for 2-layer films comprised of different fluids - namely 60% and 80% glycerol, both containing 0.2% SDS. In Figure 2.14(a), the flow rate Q_2 is varied whilst Q_1 is fixed (value in the legend), conversely in (b) Q_1 is varied whilst Q_2 is fixed. We note some differences between the 1-layer approximation (2.1.3) (plotted as dashed lines) and the theory computed numerically from (2.3.21) and (2.3.25) (solid lines). In particular, we find that the fit with the 1-layer approximation deteriorates with increasing flow rate in Figure 2.14 (a), whereas in Figure 2.14 (b) the fit improves with increasing flow rate. In contrast, the theory in both plots provides a good fit to the data across the whole range of flow rates tested, thus indicating that the 1-layer approximation may not be applicable to all flows of different liquids.

Since the 1-layer approximation (2.1.3) is based upon the properties of the first layer, the results of Figure 2.14 are to be expected. In (a), as the flow rate Q_2 increases, the 'effect' of the first (bottom) layer diminishes. The film becomes more similar to a single-layer film comprising of the liquid in the second (top) layer, thus the difference between the 1-layer approximation and the multi-layer theory increases as Q_2 increases. In (b), as Q_1 increases, the first layer 'dominates' the two-layer film. This means the difference between the 1-layer approximation and the multi-layer theory decreases as Q_1 increases.

In Figure 2.15 (a) we plot the raw values of film thicknesses for all 2-layer experiments with these fluids (60% and 80% glycerol) versus flow rate. In Figure 2.15 (b) the film thicknesses have been normalised with respect to both the 1-layer approximation (2.1.3) and the multi-layer theory from (2.3.21) and (2.3.25). Here, we can clearly see that regardless of which fluid is in the top or bottom layer, the 1-layer approximation deviates

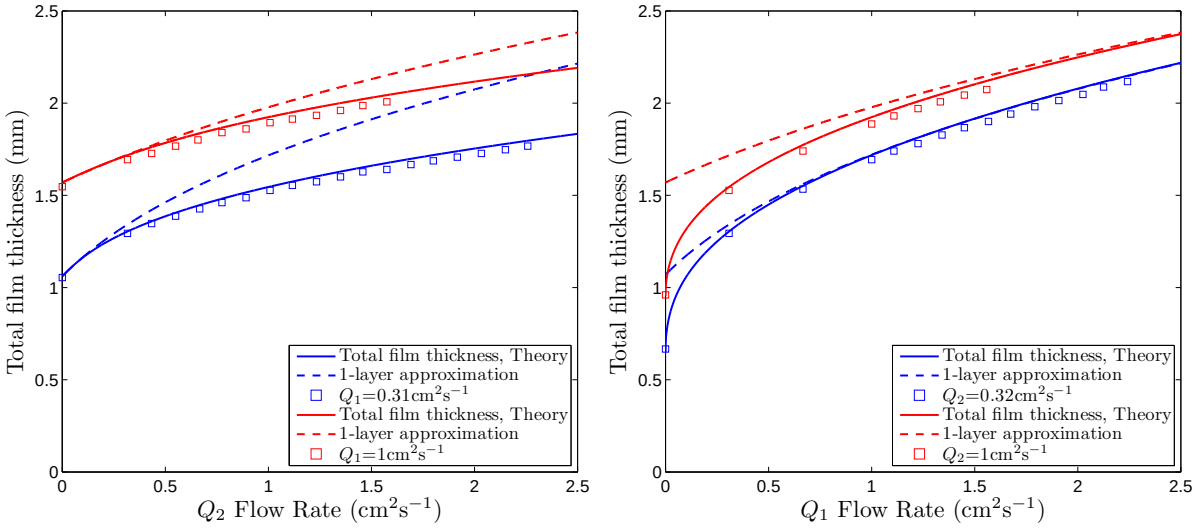

Figure 2.14: Total film thicknesses for two-layers of different fluids; The bottom layer is 80% glycerol and the top layer is 60% glycerol, both with 0.2% SDS. (a) Shows variation with increasing Q_2 and (b) shows variation with increasing Q_1. $Re = 1.0 - 4.4$.

from the experimental data up to a maximum of 20% for the highest flow rates. In contrast, for the values normalised by the multi-layer theory, we find $H_\infty/H_{theory} \approx 1$, indicating a good agreement in accordance with Figure 2.14. Figure 2.15 also shows there is a larger discrepancy when the more viscous fluid is in the bottom layer (i.e. blue data points) and with a higher flow rate in the top layer, which may also be in part due to streamwise developments in the flow for this case (see the discussion in Section 2.7 for more details).

2.5 Interface location for multi-layer films

In this section, we present data from the high-speed video sequences where the hydrogen bubble injection method was employed to visualize the flow. For 2-layer experiments, the top layer was seeded with bubbles so that the position of the liquid-liquid interface becomes clear. For 3-layer experiments, the top two layers were seeded with bubbles so that the position of the liquid-liquid interface between the bottom and middle layer

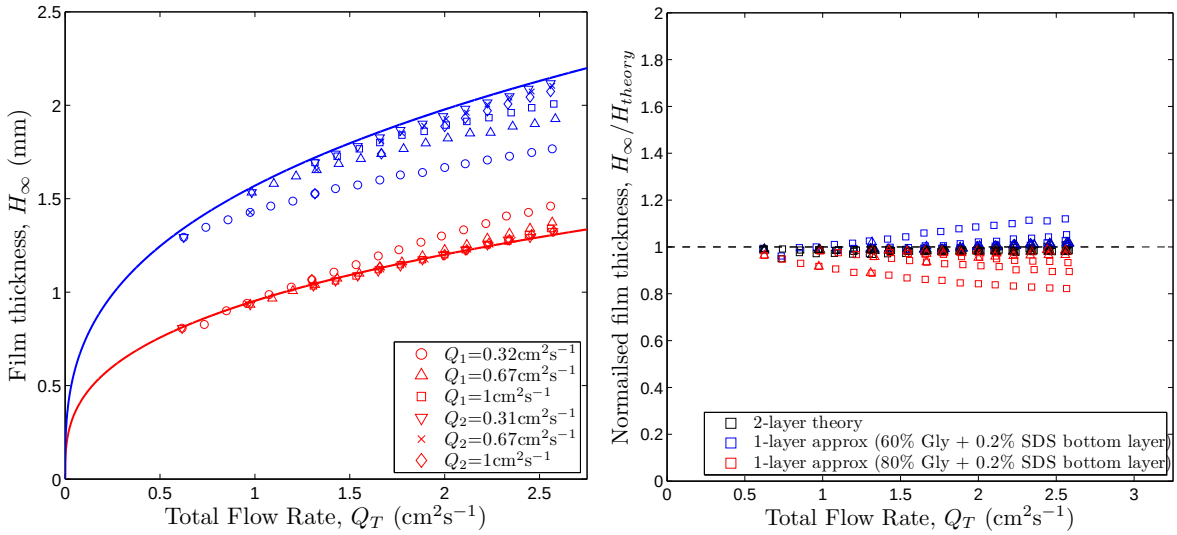

(a) (b)

Figure 2.15: All of the two-layer experiments plotted where one layer is 60% glycerol with 0.2% SDS, and the other is 80% glycerol with 0.2% SDS. (a) The red data points indicate when the 60% solution was the bottom layer; the blue when the 80% solution was the bottom layer. The layer that had a fixed flow rate is indicated in the legend. The solid lines show the predicted thickness from the 1-layer approximation. (b) Normalised film thickness versus total flow rate for all data in (a). The black data points indicate normalisation with respect to the two-layer theory, the blue (60% glycerol bottom layer) and red (80% glycerol bottom layer) data points with respect to the 1-layer approximation. $Re = 1.0 - 19.9$.

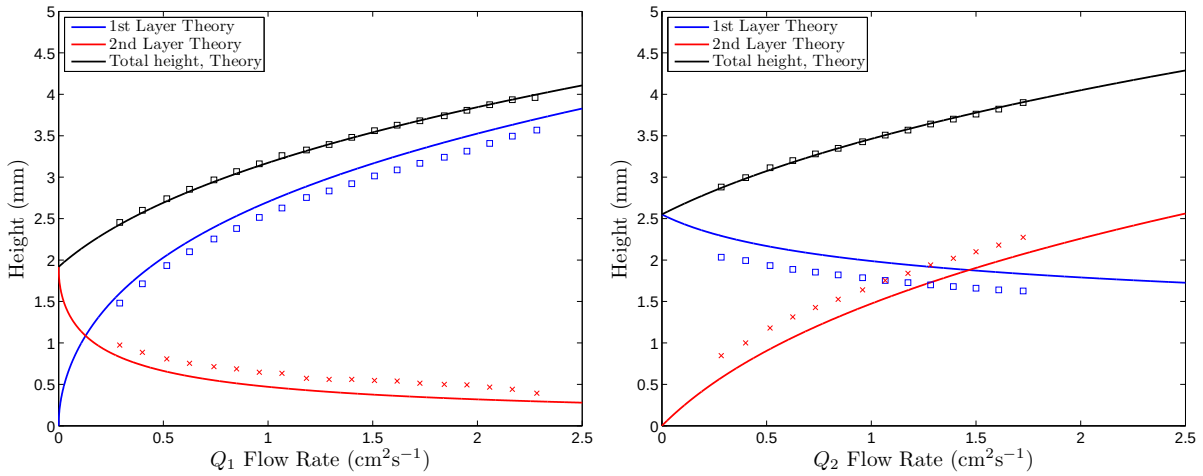

Figure 2.16: The theoretical heights of the bottom layer (blue line), top layer (red), and the total thickness (black), as well as the experimental data points. Each layer is 4% CMC; in (a) the top layer's flow rate is fixed at $Q_2 = 0.28$ cm^{2}s^{-1} as Q_1 is varied; In (b) the bottom layer's flow rate is fixed at $Q_1 = 0.67$ cm^{2}s^{-1} as Q_2 is varied. $Re = 0.12 - 0.61$.

becomes clear. Hence, using this technique the heights of individual layers are captured as well as the total film thickness, which can then be compared to the multi-layer theory in Section 2.3. Figure 2.16 plots both the theoretical, computed numerically from (2.3.21) and (2.3.25), and experimental values of the bottom layer, top layer and total thickness in a two-layer film. In (a), the flow rate Q_2 is fixed, whilst Q_1 is varied.

In Figure 2.16(b), we fix the flow rate Q_1, whilst varying Q_2. Similar to (a), the experimental data of the total film thickness matches well with the theory, though the theory for the thickness of the bottom layer provides a small overestimate (of less than 10%), due to the higher shear rates in the bottom layer leading to a decrease in the zero-shear rate viscosity.

The process of fixing the flow rate of one layer, whilst varying the other, in a two-layer film is further investigated in Figure 2.17. Here, we have included schematics above each column of figures to indicate which experimental procedure was used. In (a) and (c) Q_2 was varied whilst Q_1 was fixed, with this being reversed in (b) and (d).

As we can see from figures (b) and (d), the procedure whereby Q_1 is varied appears to have a more significant effect on the film thickness of both layers than when Q_2 is varied. This is evident from observing the change in absolute values of both h_1 and h_2 in (a) and (c) versus (b) and (d). For example, we observe that $h_1 : 1.1 \rightarrow 2.1$ mm as $Q_1 : 0.35 \rightarrow 0.9$ cm^{2}s^{-1} in Figure 2.17 (b), whereas $h_2 : 0.5 \rightarrow 1.1$ mm as $Q_2 : 0.35 \rightarrow 0.9$ cm^{2}s^{-1} in Figure 2.17(c). Irrespective of the experimental procedure, we obtain a good agreement between experiment and theory, showing that the simple theory in Section 2.3, that is solving (2.3.21) and (2.3.25) numerically, adequately describes both 1-layer and 2-layers film flows.

Figure 2.18 shows a similar analysis for a 3-layer flow of 4% CMC solution, where Q_1 and Q_2 are fixed and Q_3 varies. In this case, hydrogen bubbles were present in both the 2nd and 3rd layers so that we obtain film thicknesses of h_1 and $h_2 + h_3$. The difference between Figures 2.18 (a) and (b) is the value of the fixed flow rate Q_1. As with Figure 2.16 (for the same fluid), the multi-layer theory describes the change in the individual film heights reasonably well but slightly underestimates the bottom film height ($h_2 + h_3$), leading to an underestimate of the total film thickness.

In Figure 2.19 we see this same result for all of the 3-layer film experiments. The data points normalised with respect to the 3-layer theory are all consistently clustered around the parity line ($H_\infty / H_{theory} = 1$).

2.6 Flow Velocity Measurements

An example velocity field, determined as per the method outlined in Section 2.2, is shown in Figure 2.20 for a 90% glycerol solution (see caption for details). In all cases, we observe qualitatively similar features, whereby the flow velocity exhibits a parabolic distribution normal to the die face, before the two layers merge; and thereafter the top layer assumes a more constant velocity. The distance downstream of the exit slot in order for the top

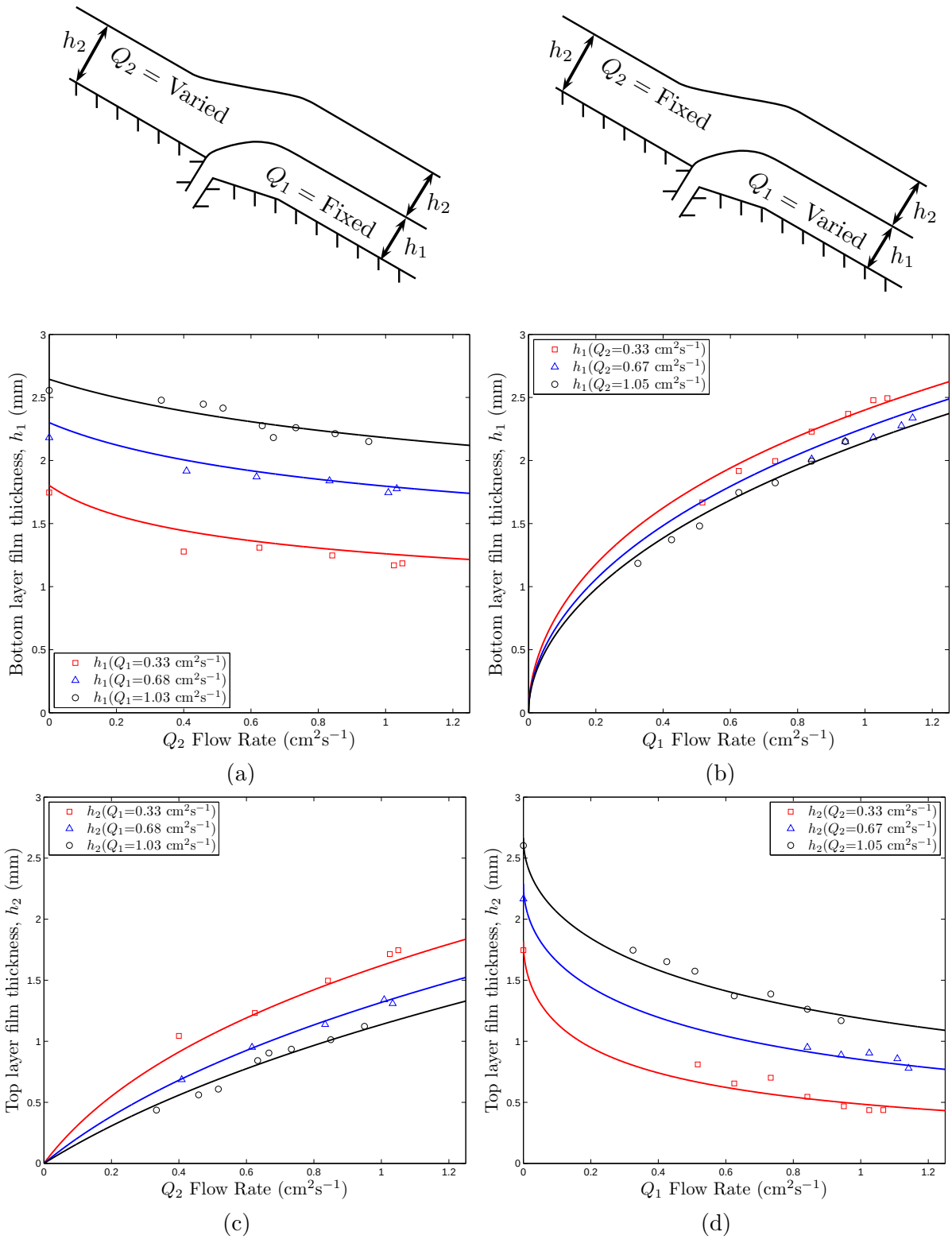

Figure 2.17: 2-layer experiments with 90% glycerol, where Q_2 was varied in (a) and (c), and Q_1 was varied in (b) and (d). The schematic above these plots depicts which layer was kept at a fixed flow rate. In all subfigures, the legends indicate the flow rate of the layer which was held constant. $Re = 0.08 - 0.29$.

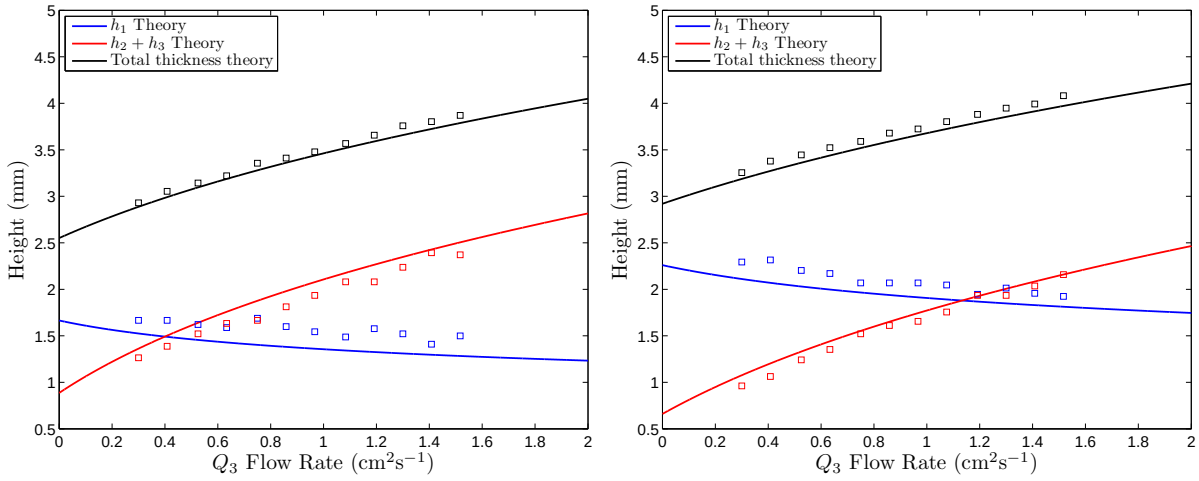

Figure 2.18: Plots of the film thicknesses, for 3-layer films, showing the bottom layer thickness (h_1, blue), the thickness of the top two layers ($h_2 + h_3$, red) as well as the total film thickness (black). All layers are 4% CMC; In (a) the fixed flow rates are $Q_1 = 0.33$ cm^{2}s^{-1} and $Q_2 = 0.33$ cm^{2}s^{-1}; In (b) the fixed flow rates are $Q_1 = 0.67$ cm^{2}s^{-1} and $Q_2 = 0.33$ cm^{2}s^{-1}. Q_3 is varied in both cases. $Re = 0.25 - 0.61$.

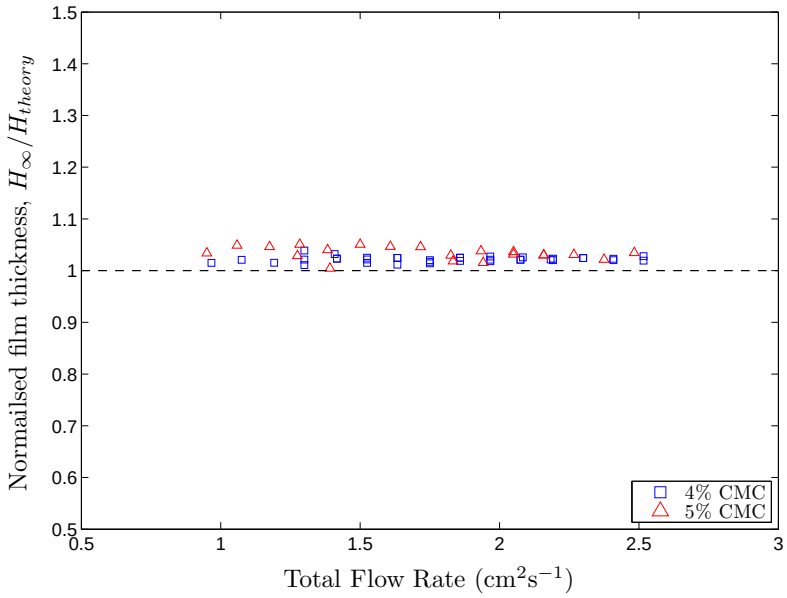

Figure 2.19: Normalised film thickness versus total flow rate for all 3-layer films. The squares correspond to all layers being 4% CMC, the triangles to all layers being 5% CMC. $Re = 0.1 - 0.61$.

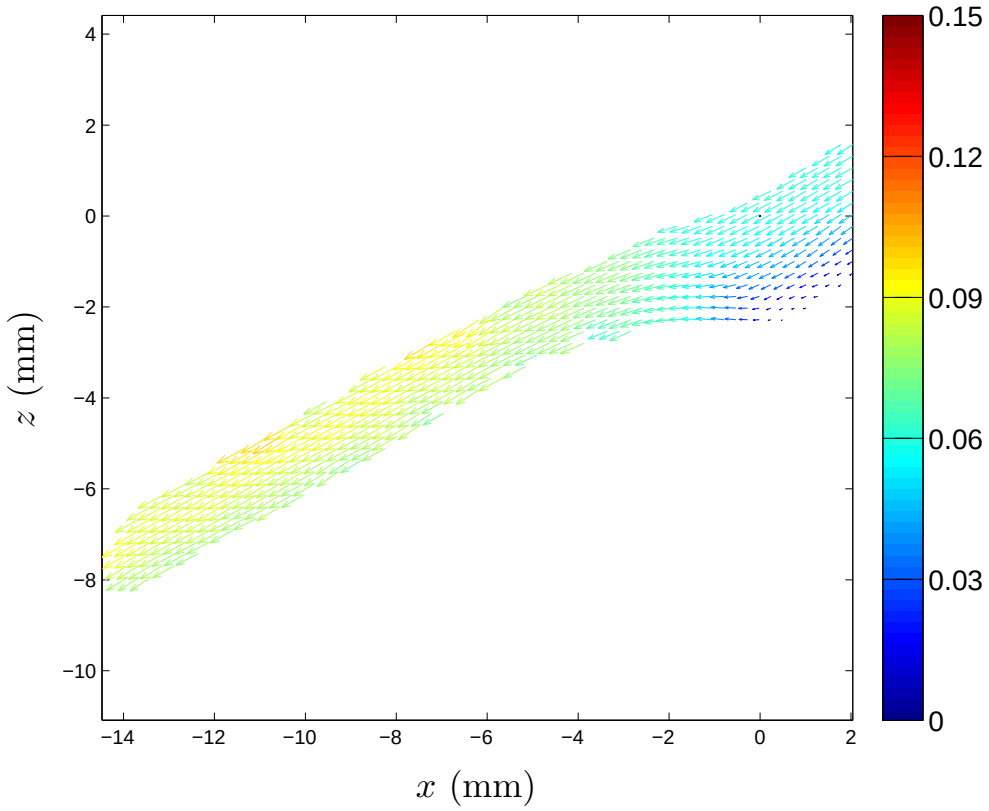

Figure 2.20: An example velocity field measured near the exit slot of layer 1 (location A in Figure 2.1). The velocity scale is in ms^{-1}. In this example, the film is comprised of two layers, both 90 % glycerol, with $Q_1 = 0.68$ $\mathrm{cm}^2\mathrm{s}^{-1}$ and $Q_2 = 1.01$ $\mathrm{cm}^2\mathrm{s}^{-1}$. With hydrogen bubbles present in the top layer only, this is where we see the velocity field, having analysed the high-speed video through PIV software.

layer to reach this constant velocity is approximately 5 - 7 mm for most cases. In the remainder of this section, we present measurements of the surface velocity and velocity as a function of distance perpendicular to the die face.

Firstly, considering 2-layer films, Figure 2.21 shows four different experimental conditions. In each subfigure, (a)-(d), the vertical dashed lines correspond to the theoretical location of the fluid-fluid interface between the two layers (red) as well as the theoretical location of the free surface (blue). Since the flow is seeded with hydrogen bubbles only in the top layer, we would expect our measurements to coincide with these limits, which is indeed the case.

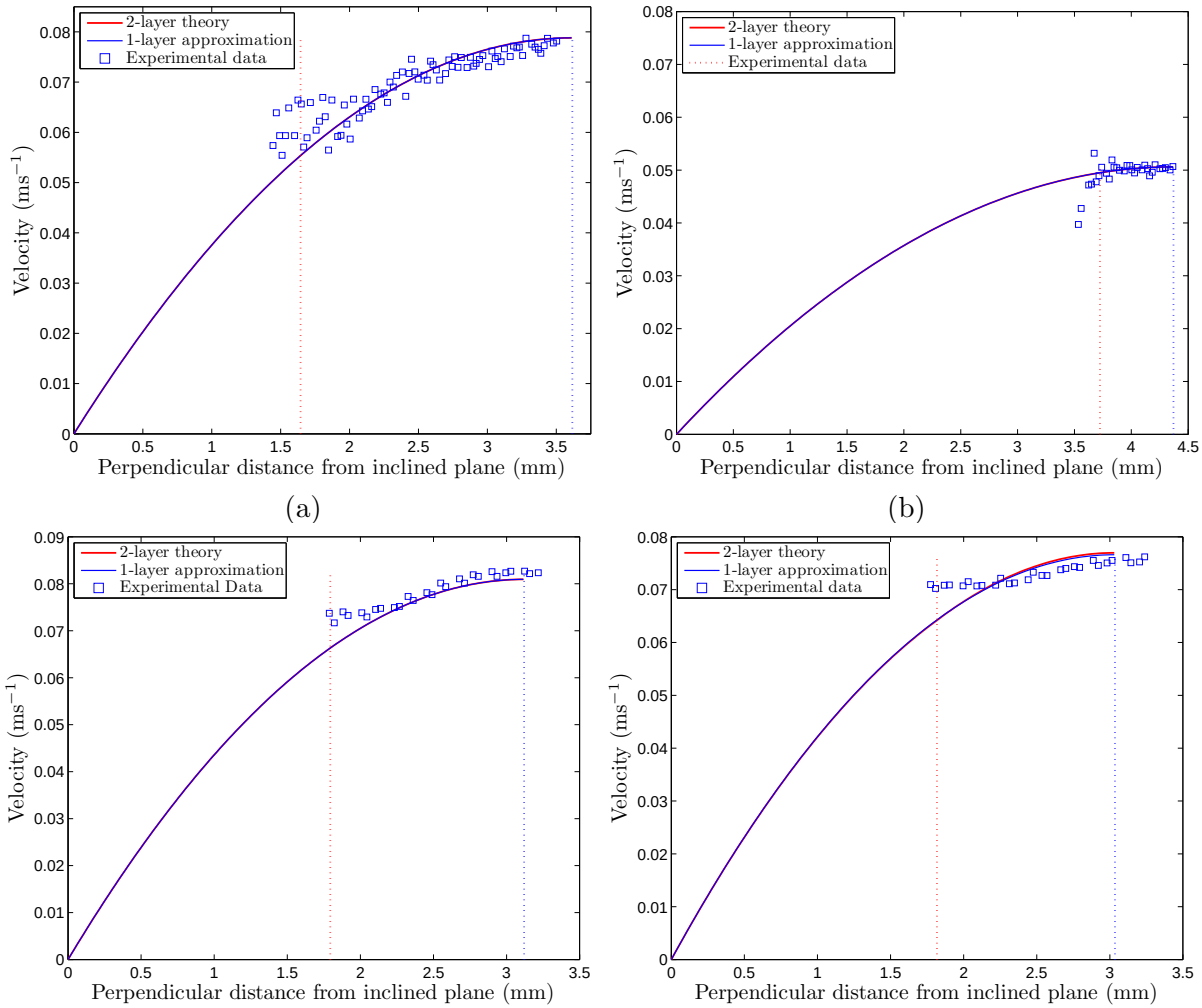

Figure 2.21: Plots of the perpendicular distance from the die face against velocity for 2-layer films. In (a) both layers are 4% CMC with $Q_1 = 0.5$ cm^{2}s^{-1}, $Q_2 = 1.4$ cm^{2}s^{-1} ($Re = 0.47$); In (b) both layers are 5% CMC with $Q_1 = 1.15$ cm^{2}s^{-1}, $Q_2 = 0.33$ cm^{2}s^{-1} ($Re = 0.16$); In (c) both layers are 90% glycerol with $Q_1 = 0.68$ cm^{2}s^{-1}, $Q_2 = 1.01$ cm^{2}s^{-1} ($Re = 0.96$); In (d) both layers are 90% glycerol with 0.05% SDS, with $Q_1 = 0.68$ cm^{2}s^{-1}, $Q_2 = 0.88$ cm^{2}s^{-1} ($Re = 0.87$).

In all cases, we find that despite the relatively small range of velocities, there is a favorable comparison between the theory (2.3.21) and experiments. Note that in Figure 2.21 (d) the two layers are *different* fluids; the bottom layer is 90% glycerol, and the top layer is 90% glycerol with 0.05% SDS, but there is no observable effect on the comparison between the multi-layer theory and 1-layer approximation in this case.

Furthermore, as well as determining the velocity profile along a line perpendicular to the die face, the free surface velocity can be extracted along the profile of the film that is imaged, both upstream and downstream of the exit slot. Figure 2.22 depicts this; upstream of the exit slot ($x > 0$) the film is a single layer, with the theoretical free surface velocity given by the lower dashed horizontal line. The two layers then merge to form a 2-layer film at $x = 0$, after which we observe an increase in free-surface velocity until approximately 6 mm downstream ($x = -6$) when the free-surface velocity plateaus around 4.7 cms^{-1} and 7.5 cms^{-1} in Figures 2.22 (a) and (b) respectively. Both of these values are similar to the theoretical free-surface velocities at this point (shown by the upper dot-dash lines in both plots).

To summarise, Figure 2.23 plots all measurements of the free-surface velocity for the two-layer experiments, where the measurements upstream (technically for single layer) have also been included. It is clear that the theory of Section 2.3 provides a valid description across the broad range of parameters ($Re = 0.03 - 1.8$) used herein.

The equivalent analysis for 3-layer films is shown in Figures 2.24 and 2.25, respectively. In Figure 2.24, we find that the multi-layer theory describes the experimental data well in both (a) and (b), though the theory does show a slight overestimate of the experimental data. These same trends are also displayed in the free surface velocities, measured as a function of distance upstream, or downstream, of the exit slot. This is shown in Figure 2.25, despite a consistent overestimate of the multi-layer theory, emphasised particularly in (b).

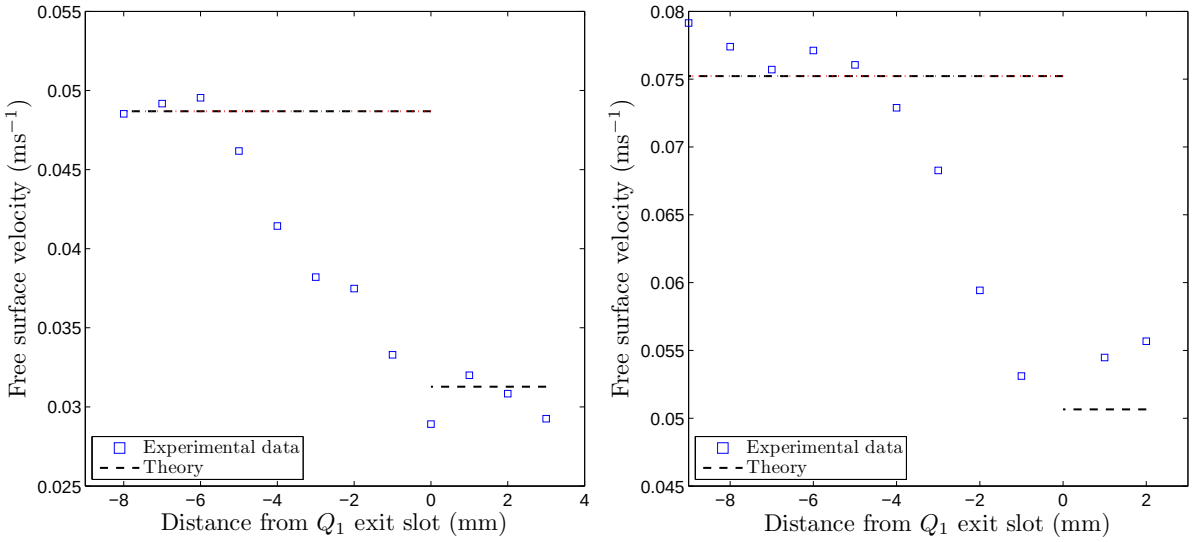

Figure 2.22: Plots of the horizontal distance from exit slot 1 against the free surface velocity for 2-layer flows. The dashed lines correspond to theoretical predictions, the data points to experiments. In (a) both layers are 5% CMC with $Q_1 = 0.68$ cm^{2}s^{-1}, $Q_2 = 0.72$ cm^{2}s^{-1} ($Re = 0.15$); In (b) both layers are 90% glycerol with $Q_1 = 0.68$ cm^{2}s^{-1}, $Q_2 = 0.83$ cm^{2}s^{-1} ($Re = 0.86$).

2.7 Capillary ridge formation

Throughout the course of these experiments, we observed a small ridge (or dimple) formation on the free-surface for the lowest viscosity fluids ($\mu = 8.4$ and 15.3 mPa.s). However, as mentioned in Section 2.2, we conclude that these are not waves as the images were captured with a sufficiently long exposure (1 s) so that any waves would not appear sharp, since the free surface velocity U_s has a magnitude of order cms^{-1}, meaning that the crest of the wave would travel several several centimetres during the exposure time. This is not the case in our images, as shown in Figure 2.26. In this image, a capillary ridge occurs just prior to the exit slot region, which is both preceded and followed by a dimple. This free surface profile formation has previously been observed in numerical studies for a film flow over a 'step-in' feature, described in detail by Bontozoglou and Serifi [18].

As shown in Figure 2.26, a reference picture can be superimposed onto a picture with

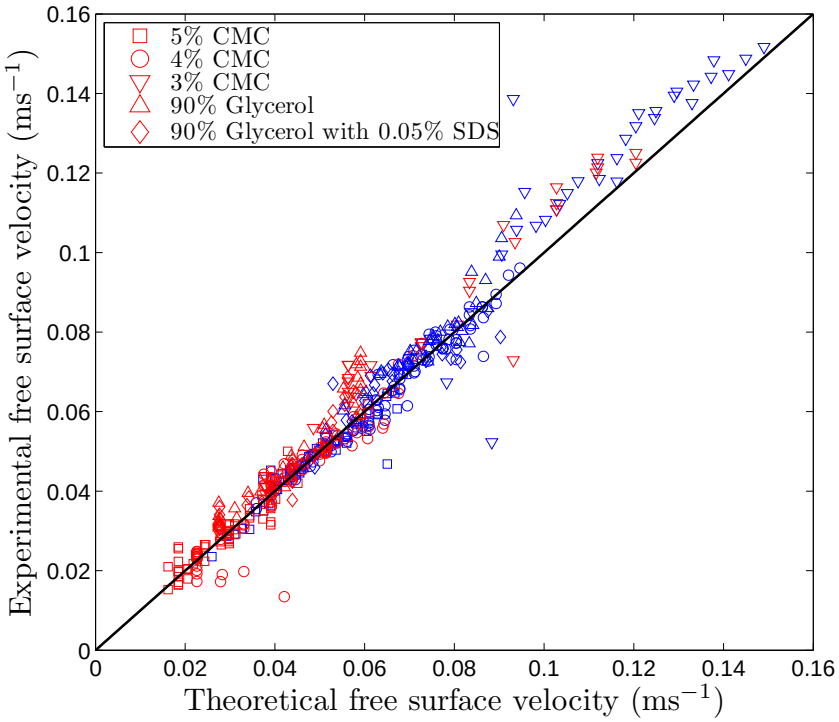

Figure 2.23: Theoretical prediction of the free surface velocity plotted against experimental values for all 2-layer film flows. Different symbols correspond to the different fluids. The red data points correspond to the single-layer film upstream of the exit slot, whilst the blue data points correspond to the two-layer film downstream of the exit slot. $Re = 0.03 - 1.8$.

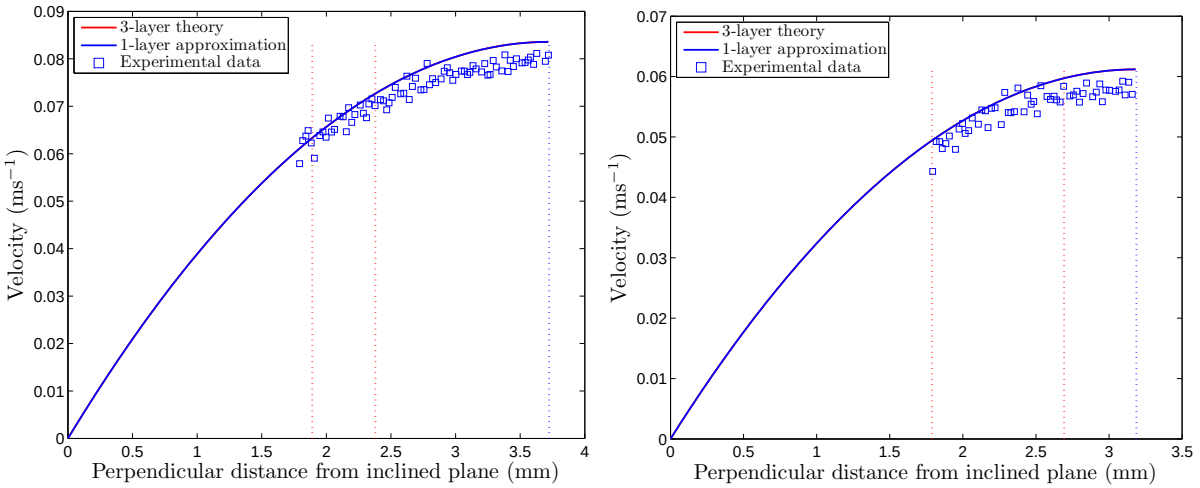

Figure 2.24: Plots of the perpendicular distance from the die face against velocity for 3-layer films. All layers are 4% CMC with (a) $Q_1 = 0.67$ cm^{2}s^{-1}, $Q_2 = 0.33$ cm^{2}s^{-1}, $Q_3 = 1.08$ cm^{2}s^{-1} ($Re = 0.51$); And (b) $Q_1 = 0.5$ cm^{2}s^{-1}, $Q_2 = 0.5$ cm^{2}s^{-1}, $Q_3 = 0.3$ cm^{2}s^{-1} ($Re = 0.32$).

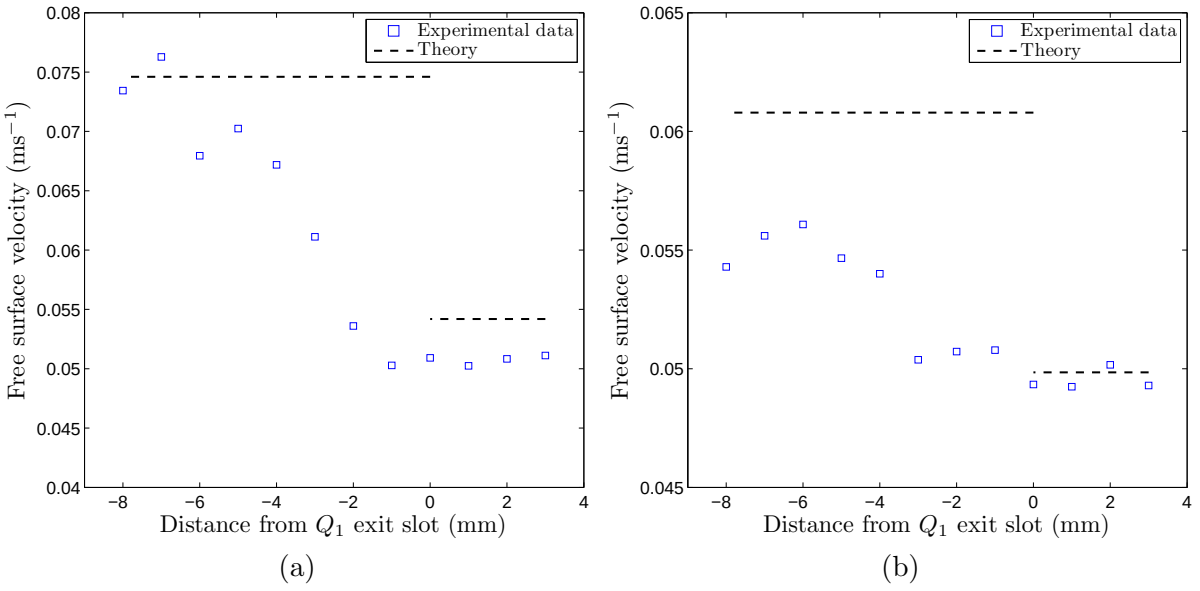

Figure 2.25: Plots of the horizontal distance from exit slot 1 against free-surface velocity for 3-layer films. In (a) all layers are 4% CMC with $Q_1 = 0.67$ cm^{2}s^{-1}, $Q_2 = 0.33$ cm^{2}s^{-1}, $Q_3 = 0.75$ cm^{2}s^{-1} ($Re = 0.43$); And (b) all layers are 5% CMC with $Q_1 = 0.5$ cm^{2}s^{-1}, $Q_2 = 0.5$ cm^{2}s^{-1}, $Q_3 = 0.94$ cm^{2}s^{-1} ($Re = 0.21$).

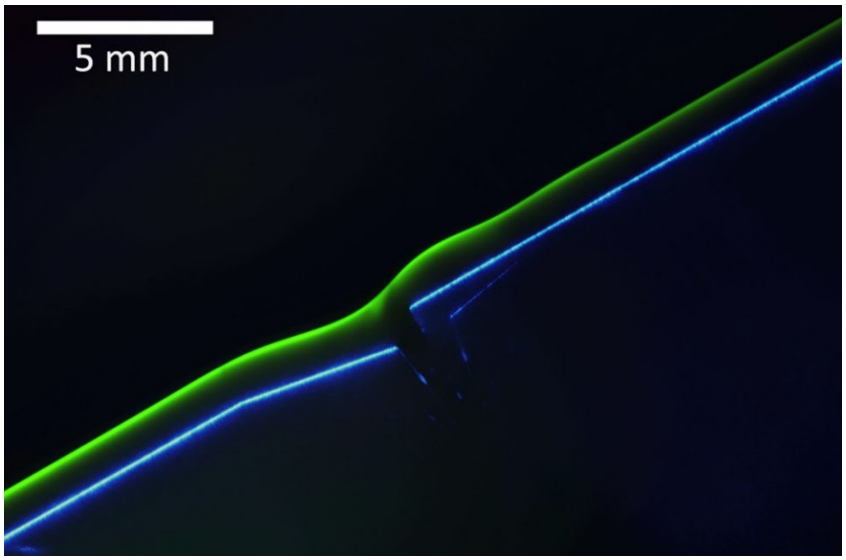

Figure 2.26: Raw experimental image showing the free-surface of a two-layer flow near the exit slot region of Q_1. The die face has been super-imposed on the image for reference. The flow rates here are $Q_1 = 0.31$ and $Q_2 = 2.25$ cm^{2}s^{-1}. $Re = 35$. Only the free surface is visible here, not the interface between the top and bottom layers. A capillary ridge can be seen before the layers meet.

flow. To digitize this raw experimental image, using the Matlab image processing toolbox, a black and white binary image of this is created, whereby any pixel with luminance greater than a level of 0.05 becomes a white pixel (and other pixels become black). Rotating this image 30 degrees clockwise, the free surface of the film is then located by starting at the top of the image, and tracing vertically down the image pixel-by-pixel until a white pixel is located. By doing this across each horizontal pixel, the free surface profile is digitized.

This process has been carried out on a number of different images, with the results shown in Figure 2.27. Free surface profiles for (a) and (b) 50%, (c) and (d) 60% and (e) and (f) 70% glycerol ($\mu = 8.4, 15.3$ and 30.0 mPa.s) have been plotted. These plots are all of 2-layer films, located at the first layer exit slot, that is where the top layer first meets the bottom layer and the transition from a single layer film to a two-layer film occurs (location A in Figure 2.1). The vertical black lines correspond to the location of the exit slot, with the origin (0 mm from the slot) defined as the point at which the exit slot begins. The film heights were measured as if the inclined plane was 30 degrees for the whole of the die face, without an exit slot region. This is shown in Figure 2.28, showing a schematic of a two-layer film; the exit slot region has a dashed line across where the film thickness (h_T) was measured. Thus the film thickness in between these vertical lines in Figure 2.27 is a measure of the film thickness as if the exit slot is not present, but remains plotted for completeness. The particular feature to note, however, is the ridge and/or dimple which occur before the exit slot, i.e. $x < 0$, which is most readily observed in Figure 2.27 (a).

In Figures 2.27, (a), (c) and (e) the bottom layer flow rate, Q_1, is fixed (at 0.31 or 0.32 cm^2s^{-1} in each case) and each plot indicates the difference when the top layer, Q_2, is varied. It can be seen, in particular for Figure 2.27(a), that before reaching the exit slot for layer 1, the free-surface exhibits a pronounced capillary ridge formation, whereby the free surface goes from being almost uniform 10 millimetres upstream, to having a wave-

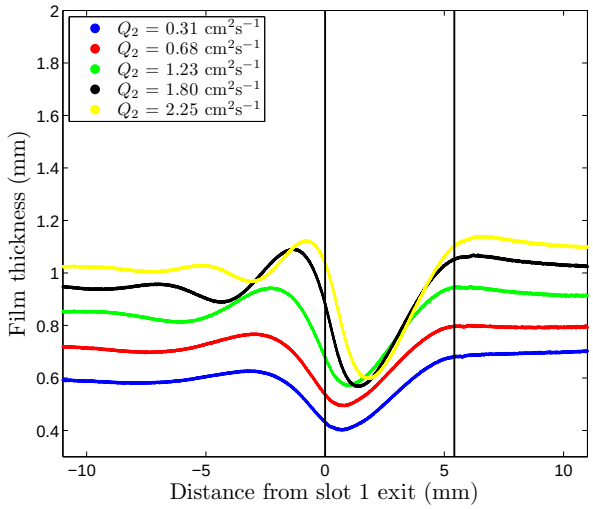

(a) 50% glycerol: $Q_1 = 0.31$ cm^{2}s^{-1} fixed

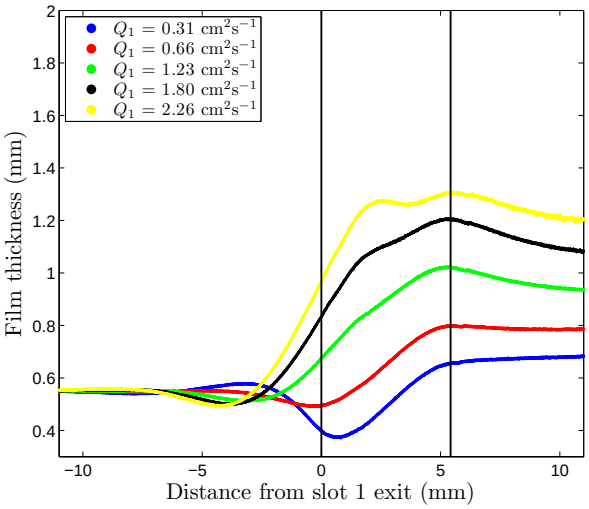

(b) 50% glycerol: $Q_2 = 0.31$ cm^{2}s^{-1} fixed

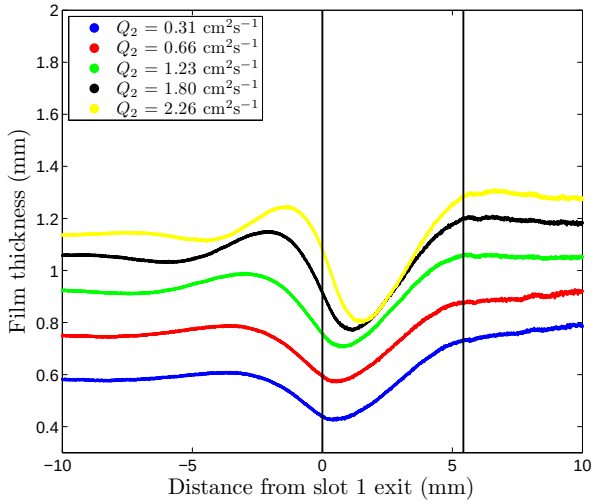

(c) 60% glycerol: $Q_1 = 0.32$ cm^{2}s^{-1} fixed

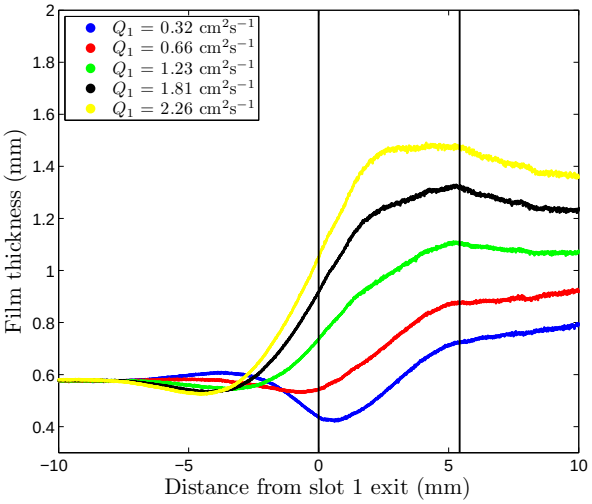

(d) 60% glycerol: $Q_2 = 0.31$ cm^{2}s^{-1} fixed

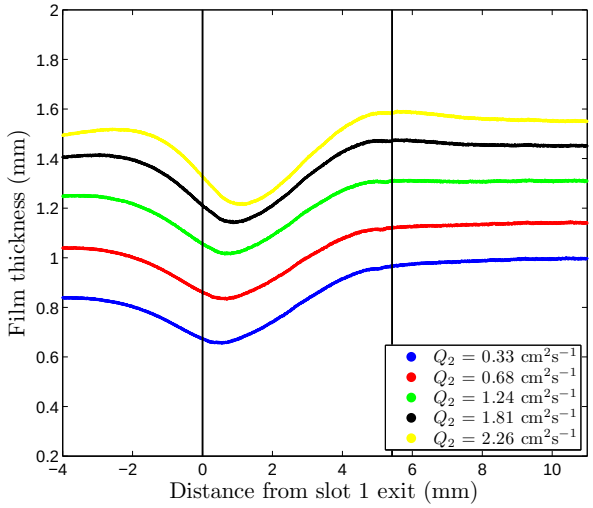

(e) 70% glycerol: $Q_1 = 0.32$ cm^{2}s^{-1} fixed

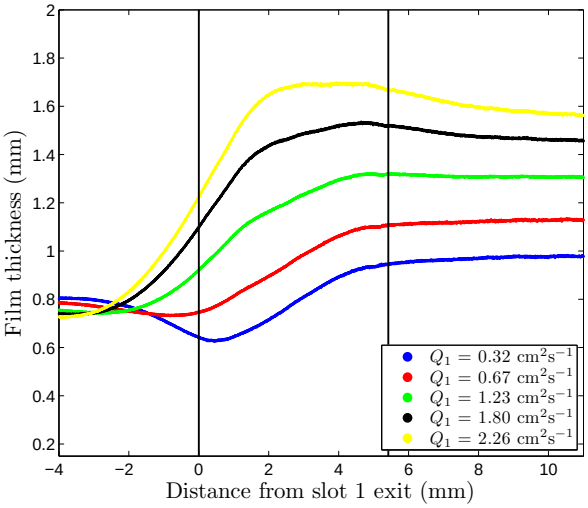

(f) 70% glycerol: $Q_2 = 0.32$ cm^{2}s^{-1} fixed

Figure 2.27: Total film height against distance from the exit slot of the first layer. All are 2-layer films comprised of the same liquid as indicated in the subcaption, with $Re = 2.4-34$.

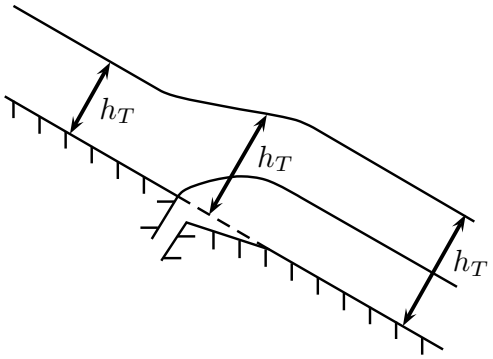

Figure 2.28: Cross-sectional schematic of the slide die for a two-layer film flow, showing how the film thickness was measured over the exit slot of the die. The dashed line across the exit slot indicates where the thickness was measured from, across the 'gap' of the exit slot in the inclined plane of the die face.

like pattern just a few millimetres from the exit slot. This effect is exaggerated when Q_2 is increased, due to an increase in the Reynolds number, as also described in [18]. In accordance with this, as the viscosity is increased, these disturbances are damped out as can be seen in the comparison between Figures 2.27 (a) and (c) or (e). After the exit slot region (approximately 5.5 mm downstream), the film now comprises of two-layers and returns to a more or less uniform thickness (discussed in more detail later).

In Figure 2.27 (b), (d) and (f), Q_2 is fixed (at either 0.31 or 0.32 cm^2s^{-1}) and Q_1 is varied as indicated in the legends. Focussing on Figure 2.27 (b), however, despite all profiles having the same uniform thickness upstream ($x \approx -10$ mm), a dimple formation appears at $x \approx -4$ mm for the highest flow rates ($Q_1 = 1.81$ or 2.26 cm^2s^{-1}), before rising to meet the flow coming from the exit slot. The location of the dimple occurs progressively closer to the exit slot as the flow rate decreases and, in particular, there is a transition from dimple to ridge as $Q_1 = 0.31$ cm^2s^{-1} followed by a dimple *inside* the exit slot region. Again, the magnitude of this effect is damped out as viscosity increases.

In our experiments, due to the geometry of the exit slot, we have an extension of the "step-in" capillary ridge formation for low flow rates in Q_1, described by Bontozoglou and Serifi [18]. For our geometry, when there is a low flow rate in Q_1, the flow from Q_2

essentially sinks down into the exit slot region, inducing a component of velocity normal to the free surface, which results in a small reduction in the streamwise velocity and thus a local high-pressure region, which would result in a pressure gradient back towards the direction of the incoming flow Q_2. As such, one would expect a small thickening of the film just prior to the exit region, which is precisely what we observe.

In contrast, for high-flow rates in Q_1 we essentially have an extension of the "step-out" [18], where the opposite would be true, inducing a dimple in the top layer before the two layers merge, which is again what we observe in the experimental profiles shown in Figure 2.27.

In the work of Bontozoglou and Serifi [18], the film flow over step-in or step-out features was vertical. They showed that the size of the capillary ridges initially grows with Reynolds number, but then diminishes. Two limits were identified as follows: a low Reynolds number limit, whereby the streamwise deformations are expected to follow the simple scaling law $l = L/H = Ca^{-1/3}$, where L is the streamwise scale of the deformation, H is the undisturbed film thickness and $Ca = \rho g H^2/\sigma$ is the capillary number. In the high Re-limit, where inertia dominates, the deformations are expected to follow the scaling $l = We^{-1/2} = (\rho H U^2/\sigma)^{-1/2}$. For example, Figure 2.27 (a) shows the streamwise lengthscale is of the order of 2 mm immediately prior to the step-in, the streamwise lengthscale being the total length of the ridge which resides above the upstream uniform thickness. In this high Reynolds number case ($Re = 30.7$), the predicted lengthscale is $L = H\,(\rho H U^2/\sigma)^{-1/2} = 3.5$ mm, showing a relatively large quantitative discrepancy. However, the orientation of the flow is different and, for our experiments, flow emanates from the exit slot, which was not the case in the study [18].

Furthermore, the predictions from the numerical study [18] for step-ins showed that as Re increases, the ridge is transformed into a series of damped stationary capillary waves. This certainly appears in the experiments; for example, in Figure 2.27 (a), as the flow rate

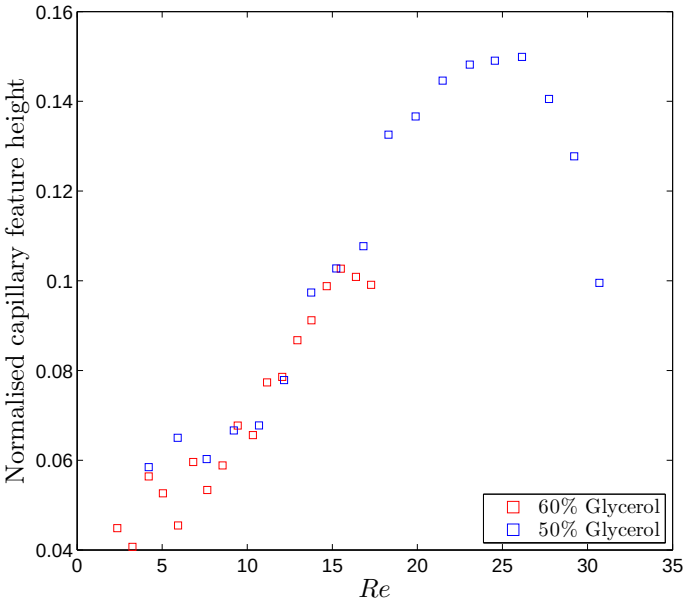

Figure 2.29: Normalised capillary feature (ridge) height versus Reynolds number.

is increased, we observe a progression from a single ridge ($Q = 0.31$ cm^{2}s^{-1}) to a series of stationary waves reaching further upstream ($Q = 1.8$ and 2.25 cm^{2}s^{-1}). In contrast to the situation where the flow is fully developed and steady state, for this particular feature, surface tension thus becomes important and a higher surface tension would act to increase the size of the capillary ridges or dimples.

Figure 2.29 plots the normalised ridge height, $(H_{ridge} - H)/H$, where H_{ridge} is the maximum height of the capillary ridge and H is the upstream uniform film thickness, against the Reynolds number in the top layer (i.e. $Re = \rho Q_2/\mu_2$). Both fluids (50 and 60% glycerol) exhibit an initial increase in ridge height as Re increases, but a definitive local maxima occurs at $Re \approx 25$. This non-monotonic dependence was reported by Bontozoglou and Serifi as being due to the distinction between regimes where viscosity dominates (low Re) and where inertia dominates (high Re), whereby the intermediate regime is where capillary forces dominate and results in a pronounced ridge.

As seen, the profiles tend to a uniform profile after the two layers merge. However, this

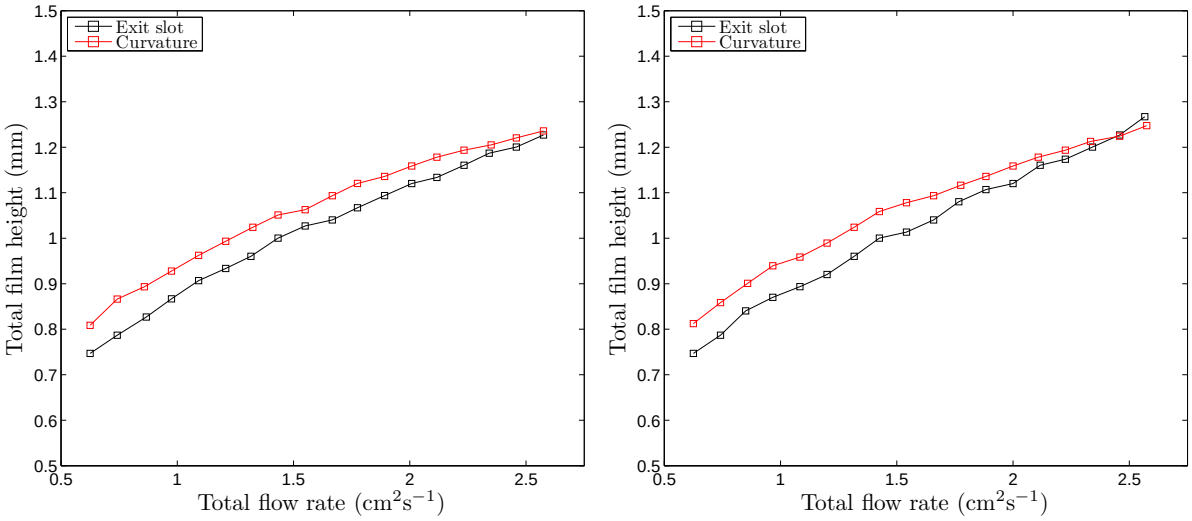

(a) (b)

Figure 2.30: A comparison of measuring the film heights at different positions along the die. Both (a) and (b) plot the total film height against total flow rate for a 2-layer film, both layers consisting of 60% glycerol, with $Q_1 = 0.32$ cm^{2}s^{-1} fixed in (a), and $Q_2 = 0.31$ cm^{2}s^{-1} fixed in (b). The film thickness was measured in two locations; just after the slot 1 exit (black; At location A in Figure 2.1) and further along the die face, just before the change from an inclined plane to a curved surface (red; At B in Figure 2.1). $Re = 4.6 - 19.9$.

behaviour does not occur until sufficiently far downstream (> 10 mm in some cases). As such, in Figure 2.30 we compare the film thickness measured in this location (location A in Figure 2.1) to those measured just before the curvature of the die (location B in Figure 2.1). That is, for a variety of flow rates, we plot the total film height at a distance of 10 mm downstream from the exit slot (the furthest distance downstream the film thickness was measured in Figure 2.27), as well as at the location of just before the inclined plane of the die becomes curved. Figure 2.30 does this for the cases of (c) and (d) in Figure 2.27, considered to see the most change in total film height after the exit slot region, from 5.5 mm to 10 mm downstream of the exit slot.

We see in these cases that the measurement of the film thickness just after the exit slot (location A) is consistently lower than the measurement taken just before the curvature (location B). However, the maximum difference, even for this low-viscosity fluid ($\mu =$

15.3 mPa.s) is always less than 0.08 mm ($< 11\%$ of the film thickness). This consistent thickening of the layer may be due in part to a streamwise development of the film flow after the layers merge at the exit slot of the bottom layer, imposing a Poiseuille-type velocity profile, which would interact with the upstream film. This appears to be supported by the free surface profiles, in particular, those shown in Figure 2.27 (c). Noting that the error in the experimental measurements is small ($\approx O(10)\,\mu m$) compared to the film thickness ($\approx O(100)\,\mu m$), we thus concede that this discrepancy is indeed due to a streamwise development of the flow.

2.8 Conclusions

In summary, we have completed an experimental study of both single and multi-layer film flows down an inclined plane in order to test the applicability of the one-layer approximation (2.1.3) for both film thicknesses *and* velocity profiles. In addition, we have provided a critical evaluation of this against the full, albeit simple, multi-layer theory of Section 2.3 over a range of physical properties and parameters, with $Re \approx 0.03 - 60$.

The film thicknesses measured for both single layer films and two-layer films of the same fluid were described accurately by the well-established one-layer approximation, with no difference between the one-layer approximation (2.1.3) and the full theoretical description of Section 2.3. However, this did not hold for two-layer films of different fluids, where the full theory, obtained numerically from (2.3.21) and (2.3.25), provided a much better description of the experimental observations, in particular when the bottom layer was more viscous than the top layer.

In addition to measurements of total film thicknesses, we provided extensive measurements of the change in heights of the individual layers for multi-layer films, where the experimental data was again described well by the simple theory of Section 2.3.

Using high-speed imaging, we extracted velocity profiles for both two and three-layer

films, measuring the velocity as a function of distance from the die face and the free-surface velocity. In the two and three-layer case there is again good agreement between theory and experiment; as expected, when the layers are all composed of the same fluid, theoretically the one-layer approximation (2.1.3) provides precisely the same total film thickness and velocity profile as the two and three-layer theory from Section 2.3.

For two-layer films of low viscosity fluids, we observed the formation of stationary capillary ridges and dimples along the free surface, just prior to the exit slot region where the two layers merge. These formations were described with reference to the work of Bontozoglou and Serifi [18] for film flows over step-ins and step-outs, whereby the qualitative observations from the present experiments matched accurately with their numerical study. The ridges were found to be most pronounced for low-viscosity, high-flow rates (i.e. higher Reynolds numbers), where the peak ridge is preceded by a series of dimples and ridges of diminishing amplitude.

By inspection of the film thickness profiles around the exit slot, we found that the two-layer films generally reach their equilibrium values approximately 11 mm downstream of the exit slot and comparison with the film thicknesses measured a further 40 mm downstream showed a maximum difference of 10%, attributed to a streamwise development in the flow.

To summarise and conclude this chapter, we have provided a validation of the one-layer approximation for a range of physical properties and parameters, when the layers are all comprised of the same fluid. However, when the layers are made up of different fluids the simple multi-layer theory provides a more accurate description. Understanding the flow in the region where layers merge, whereby a liquid-liquid interface is formed is crucial for the design of components in many coating processes and the data gained from these, and similar, experiments provide the motivation for future work in this area.

Chapter 3

Stability of an unsupported multi-layer surfactant laden curtain under gravity

3.1 Introduction

In the previous chapter an experimental study was conducted analysing the behaviour of a multi-layer film flowing down an inclined plane (the face of the slot die). The next stage of the curtain coating process occurs once the liquid film has reached the vertical die lip (position C of the schematic in Figure 2.1 in Chapter 2), whereby the film leaves the die, forming a liquid curtain falling due to gravity. As previously explained, the curtain maintains uniform width via the use of edge guides, before impinging upon the substrate to be coated.

By lowering the flow rate of the liquid layer(s), the thickness of the curtain will be reduced, resulting in a thin coating which can often be desired in industry. However, there will be a critical flow rate at which point the curtain will rupture, unable to maintain stability, causing a major disruption to the coating process. This disruption is one of

the major operating difficulties of the curtain coating method and thus a greater understanding of the curtain stability is key to ensuring an efficient operating process. The theoretical study of this free surface flow is investigated in this chapter.

Ever since the early work of G. I. Taylor [110] on the topic of a liquid sheet rupturing in 1959, there has been significant interest in this topic. Extending the work of Taylor, Brown [20] produced a criterion for the stability of a thin sheet of moving liquid based upon a force balance on the free edge of the fluid. Once there is a hole in the sheet, if the inertia is large enough relative to the surface tension, the hole will be swept away with the flow of the curtain. However if the surface tension is greater, the hole will grow upstream and disintegrate the curtain. In industrial applications, if the flow rate of the liquid(s) producing the curtain are not high enough, the disturbance will not get 'flushed' away with the flow of the curtain, but will instead be allowed to propagate upstream, where ultimately the sheet of fluid will rupture.

Using this heuristic argument, the stability is based upon the Weber number, corresponding to the ratio of inertia to surface tension. Indeed, upon following a linear stability analysis [74, 76], the local stability criterion for an unsupported single-layer liquid sheet falling under gravity is given by

$$We = \frac{\rho Q v_c}{2\sigma} > 1, \tag{3.1.1}$$

where ρ is the liquid density, Q the flow rate per unit width of the curtain, v_c the local curtain velocity and σ the surface tension, assumed to be constant. Equation (3.1.1) shows the critical Weber number, above which the curtain is stable, is unity.

Since the formulation of this criterion, much work has been carried out on perturbations and wave formation along a liquid curtain. It was shown by Crapper *et al.* [31] that viscosity does not influence the initial stages of wave development, whilst Lin *et al.* [75]

showed that the critical Weber number does not depend on the liquid-gas density ratio or the Reynolds number. De Luca and Costa [33] provide an explanation of the importance of considering the absolute or convective character of disturbances, taking gravity into account, to confirm this and present theoretical results on the behaviour of standing waves.

More recently, with the advent of multi-layer coating, Dyson *et al.* [41] extended criterion (3.1.1) to a multi-layered sheet, whereby the curtain comprises of n liquid layers. The equivalent criterion in this case is given by

$$\frac{v_c \sum_{j=1}^{n} \rho_j Q_j}{\sum_{j=0}^{n} \sigma_j} > 1, \tag{3.1.2}$$

where ρ_j and Q_j are the density and flow rate per unit width of each individual layer, with σ_0 the surface tension of the liquid-gas interface of the first layer, σ_1 the interfacial tension between layers 1 and 2 and so on. By substituting $n = 1$ into (3.1.2), the single layer criterion (3.1.1) is recovered.

It is important to note how criterion (3.1.2) should be perceived; it is a sufficient but not necessary condition for stability. As explained by Dyson *et al.* [41], this condition guarantees stability since any disturbance will be swept downstream with the flow of the liquid curtain, so that there is no chance of any disturbance propagating upstream where it may affect the stability.

Indeed, once a stable curtain is formed, it is often found that the flow rate may then be reduced below that which was required for initial stability, a phenomenon known as a hysteresis window [82]; the total flow rate may be lowered enough so that (3.1.2) is violated yet a stable curtain remains. Experimental work has shown that a stable curtain can exist over a broad range of conditions where $We < 1$, due to a number of explanations, including nonlinear effects as the curtain thins [45], and the additional mass on the rim

of a free edge [97].

Despite offering a pragmatic condition useful to industry, there are assumptions made in the formulation of (3.1.2), including that of constant surface tension. It is desirable that the properties of a working fluid satisfy (3.1.2) so that a stable curtain is formed at the required coating thickness. As this is not always possible, a common technique used in industry to overcome this issue is the addition of surfactants, to lower the surface tension. The effect of surfactants are well known [99]; the surface tension becomes a function of the local surfactant concentration, and for several reasons, including the propagation of free-surface waves, there will be regions where surfactants are swept away, causing concentration gradients along both free-surfaces, and therefore gradients in surface tension. This provides the motivating question of this chapter, how does the introduction of surfactants affect the profile and stability of a free-falling liquid curtain?

Surfactants are amphiphilic organic compounds, comprising of two particular parts; a hydrophilic 'head' and a hydrophobic 'tail', meaning that surfactants (when mixed into a fluid) will diffuse and convect to and along a fluid-air interface, so that the tail may position itself out of the fluid and the head within the fluid [1]. This alignment of surfactant along the interface will change the surface properties, namely the reduction in the surface tension. There is only a certain concentration of surfactant that can be adsorbed, beyond which molecular aggregates of surfactant form, known as micelles. This concentration is known as the critical micelle concentration (cmc), beyond which the surface tension will not be reduced.

Surfactants are extremely useful in industrial applications. For example, a fluid with a lower surface tension will be more wetting, a property which is useful as the surfactant concentration can then give a measure of control over how a fluid wets a solids surface. More generally, as well as acting as a wetting agent, surfactants are used widely as cleaning, emulsifying and foaming agents. Furthermore, the addition of surfactants will not

change the chemical composition of the fluid, clearly a useful asset. A much more in depth discussion of surfactants and their applications can be found in [1].

Surfactants characteristically have a stabilizing effect on free surface waves, as in the region of thinning the surfactant concentration will be reduced, with the Marangoni stresses counteracting the surface motion. Thus the capillary pressure acting to thin the liquid sheet is opposed by this Marangoni-type flow, creating a surface elasticity, acting against the growth of free surface waves.

De Luca and Meola [34] provide an experimental investigation into the different flow regimes observed of a liquid sheet containing surfactants, from varying slot-die configurations. With regards to sheet disintegration, they hypothesized the constant surface tension, σ, in (3.1.1) should be replaced by the surface pressure, Π, defined as $\Pi = \sigma_s - \sigma$, where σ_s is the surface tension of the solvent (the 'clean' fluid, with no surfactant present) and σ the surface tension of the solution with surfactant. A linear correlation between the momentum flux $\rho Q v_c$ and Π at sheet breakup was indeed found [34].

Despite these experimental results, there is a lack of theoretical study of a falling liquid curtain under the effect of surfactant. Thus the objective of this chapter is to present a mathematical model, extending the work of Dyson *et al.* [41], to incorporate the presence of surfactants. This is done via the introduction of an advection-diffusion equation governing the transport of insoluble surfactant, along with a linear equation of state relating the surface tension to the surfactant concentration. The boundary conditions are altered accordingly to compensate for the introduction of a surface tension gradient. The difference this makes to the cross-sectional curtain profile in the steady state will be investigated; the free surface with the higher surface tension 'pulls' the curtain in that direction, and with surfactants lowering the surface tension there can be a dramatic change in this pull. Following this, a stability analysis is conducted via a multiple scales formulation, to examine the convective stability of a two-layer curtain and how criterion

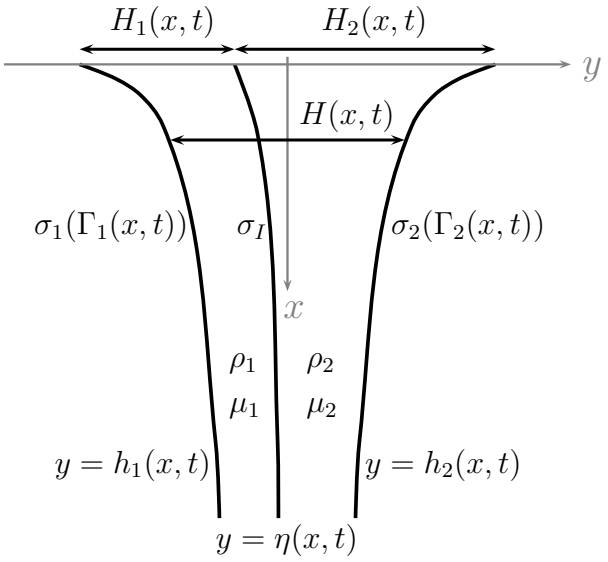

Figure 3.1: Schematic of the cross-section of a two-layer liquid curtain.

(3.1.2) is affected without the constant surface tension assumption. We then compare our criterion under various parameters with experiments.

3.2 Mathematical model

3.2.1 Problem statement

Following Dyson *et al.* [41] we begin by considering a cross-section of a two-layer liquid curtain, as shown in Figure 3.1. The coordinate system is such that the x-axis is pointing vertically downwards, with the y-axis perpendicular so that $x = 0$ is located at the top of the curtain and the original centre of mass of the curtain (i.e. the centre of mass at $x = 0$) is fixed at $y = 0$.

The viscosities (μ_1 and μ_2) and densities (ρ_1 and ρ_2) of each fluid layer are constant, whilst the surface tensions of the two fluid-gas interfaces, σ_1 and σ_2, are considered as a function of the local concentration of surfactant, Γ_1 and Γ_2 (with units mass of surfactant per unit of interfacial area), on each free-surface, $y = h_1$ and $y = h_2$. The interfacial tension σ_I at the liquid-liquid interface, $y = \eta$, is considered constant; since a surfactant molecule is amphipathic, they will favour residing on the free surface as opposed to liquid-

liquid interface at $y = \eta$. Thus we assume that the $y = \eta$ interface is free of surfactant.

By considering a cross-section of the liquid curtain, any edge effects from the vertical edge guides are neglected, and the model also neglects any effects from the coating die from which the curtain is created and the substrate on which the curtain impinges. Moreover, we only consider Newtonian fluids.

We consider the problem as a single fluid with variable density ρ and viscosity μ such that each convects with the flow

$$\frac{\partial \rho}{\partial t} + (\mathbf{u} \cdot \nabla)\, \rho = 0, \tag{3.2.1}$$

$$\frac{\partial \mu}{\partial t} + (\mathbf{u} \cdot \nabla)\, \mu = 0, \tag{3.2.2}$$

where $\mathbf{u} = (u, v)$ is the velocity in (x, y) coordinates. The flow is governed by the Navier-Stokes and continuity equations

$$\rho \frac{\mathrm{D}\mathbf{u}}{\mathrm{D}t} = \rho \left(\frac{\partial \mathbf{u}}{\partial t} + (\mathbf{u} \cdot \nabla)\, \mathbf{u} \right) = \nabla \cdot \mathbf{T} + \rho g \mathbf{i}, \tag{3.2.3}$$

$$\frac{\partial \rho}{\partial t} + \nabla \cdot (\rho \mathbf{u}) = 0, \tag{3.2.4}$$

where $\mathbf{T}$ is the stress tensor and $\mathbf{i}$ the unit vector in the direction of increasing x.

As we are considering a two-layer curtain, we have three interfaces to consider when formulating the boundary conditions, the two free surfaces, $y = h_j(x, t)$ (throughout this chapter, unless otherwise stated, a subscript j refers to the fluid layer being considered, i.e. $j = 1, 2$, numbered left to right), and the liquid-liquid interface at $y = \eta(x, t)$.

Considering the boundary conditions on the free surfaces, the local surfactant concentration, Γ_j, presents a new unknown in our model, with the surface tension, σ_j, becoming a function of this concentration, i.e. $\sigma_j = \sigma_j(\Gamma_j)$, noting how the surface tensions can be different (and can vary differently) on the two free surfaces. Due to variations in Γ_j,

a tangential shear stress arises along the interfaces, which is balanced by the jump in tangential components of the hydrodynamic stress at the interface. This is incorporated into our mathematical model, via the stress balance equation at $y = h_j$

$$\mathbf{T}_j \cdot \mathbf{n}_j = \nabla_{s,j}\sigma_j - \sigma_j \left(\nabla \cdot \mathbf{n}_j\right) \mathbf{n}_j. \tag{3.2.5}$$

where $\mathbf{n}_j$ is the unit outward facing normal and $\nabla_{s,j} = (\mathrm{I} - \mathbf{n}_j\mathbf{n}_j) \cdot \nabla$ is the gradient along the surface, with I being the identity matrix.

An additional requirement for the model is an equation that governs how the concentration of surfactant evolves over the changing free-surfaces. This is given by a time-dependent advection-diffusion equation [17, 106]

$$\frac{\partial \Gamma_j}{\partial t} + \nabla_{s,j} \cdot \left(\Gamma_j \mathbf{u}_{s,j}\right) + \Gamma_j \left(\nabla_{s,j} \cdot \mathbf{n}_j\right) \left(\mathbf{u} \cdot \mathbf{n}_j\right) = S\left(\Gamma_j, C_s\right) + D_s \nabla_s^2 \Gamma_j, \tag{3.2.6}$$

on $y = h_j(x,t)$, where $\mathbf{u}_{s,j} = (\mathrm{I} - \mathbf{n}_j\mathbf{n}_j) \cdot \mathbf{u}$ is the velocity along the surface $y = h_j$, S accounts for the absorption of surfactant from the free surface to the bulk of fluid (a function of the concentration of surfactant in the bulk phase C_s, as well as Γ_j) and D_s is the diffusivity of surfactant along the surface [70]. In our model, we account only for insoluble surfactants, as well as assuming that diffusivity is small. This simplifies (3.2.6) to

$$\frac{\partial \Gamma_j}{\partial t} + \nabla_{s,j} \cdot \left(\Gamma_j \mathbf{u}_{s,j}\right) + \Gamma_j \left(\nabla_{s,j} \cdot \mathbf{n}_j\right) \left(\mathbf{u} \cdot \mathbf{n}_j\right) = 0, \tag{3.2.7}$$

on $y = h_j(x,t)$.

The final extension for the surfactant model is an equation of state linking the surfactant concentration to the surface tension, in the form $\sigma_j = \sigma_j\left(\Gamma_j\right)$. In dilute concentrations, the relationship between σ_j and Γ_j can be modelled as linear, with the Frumkin

equation of state being [1, 47]

$$\sigma_j = \sigma_{s,j} - \Gamma_j RT, \tag{3.2.8}$$

where $\sigma_{s,j}$ is the surface tension of the solvent, R the gas constant and T the absolute temperature. For the linear form of the Frumkin equation of state (3.2.8) to hold, we require $\Gamma/\Gamma_\infty \ll 1$, where Γ_∞ is the maximum interface surfactant concentration. That is, we require the surfactant to be present in dilute concentrations. As described by Stone and Leal [106], a more complicated equation of state introduces more parameters needed to form a closed problem, explaining our restriction to (3.2.8). For a more in-depth discussion on the comparison between the nonlinear Frumkin equation of state with the linear form, the reader is referred to Leal [70].

The last condition on the free surface is the kinematic condition, unchanged with the introduction of surfactants, given by

$$\frac{\partial h_j}{\partial t} + u_j \frac{\partial h_j}{\partial x} = v_j. \tag{3.2.9}$$

To complete the model, we have the conditions on the liquid-liquid interface $y = \eta$. These are the stress balance

$$\left[\mathbf{T}_j \cdot \mathbf{n}\right]_1^2 = -\sigma_I \left(\nabla \cdot \mathbf{n}\right) \mathbf{n}, \tag{3.2.10}$$

the continuity of velocity across the interface

$$u_1 = u_2, \qquad v_1 = v_2, \tag{3.2.11}$$

and finally the kinematic condition

$$\frac{\partial \eta}{\partial t} + u \frac{\partial \eta}{\partial x} = v. \tag{3.2.12}$$

Thus we have our governing equations (3.2.3) and (3.2.4), with boundary and interfacial conditions (3.2.5), (3.2.7)-(3.2.11). Before non-dimensionalising these equations, it will help in the forthcoming analysis to derive integral equations from (3.2.3), (3.2.4), (3.2.5) and (3.2.9).

We first note that the unit normal vectors and curvature at the free surfaces are given by

$$\mathbf{n}_j = \frac{(-1)^j}{\left(1+\left(\frac{\partial h_j}{\partial x}\right)^2\right)^{1/2}} \begin{pmatrix} -\frac{\partial h_j}{\partial x} \\ 1 \end{pmatrix}, \tag{3.2.13}$$

$$\nabla \cdot \mathbf{n}_j = \frac{(-1)^{j+1}\frac{\partial^2 h_j}{\partial x^2}}{\left(1+\left(\frac{\partial h_j}{\partial x}\right)^2\right)^{3/2}}, \tag{3.2.14}$$

with the unit normal and curvature at the liquid-liquid interface given by

$$\mathbf{n} = \frac{1}{\left(1+\left(\frac{\partial \eta}{\partial x}\right)^2\right)^{1/2}} \begin{pmatrix} \frac{\partial \eta}{\partial x} \\ -1 \end{pmatrix}, \tag{3.2.15}$$

$$\nabla \cdot \mathbf{n} = \frac{\frac{\partial^2 \eta}{\partial x^2}}{\left(1+\left(\frac{\partial \eta}{\partial x}\right)^2\right)^{3/2}}. \tag{3.2.16}$$

Substituting these into the free surface stress condition (3.2.5), we obtain the two components

$$(-1)^{j+1}\frac{\partial h_j}{\partial x}T_{jxx} + (-1)^j T_{jxy} = \frac{\frac{\partial \sigma_j}{\partial x}}{\left(1+\left(\frac{\partial h_j}{\partial x}\right)^2\right)^{1/2}} - \frac{\sigma_j \frac{\partial^2 h_j}{\partial x^2}\frac{\partial h_j}{\partial x}}{\left(1+\left(\frac{\partial h_j}{\partial x}\right)^2\right)^{3/2}}, \tag{3.2.17}$$

$$(-1)^{j+1}\frac{\partial h_j}{\partial x}T_{jxy}+(-1)^{j}T_{jyy}=\frac{\frac{\partial \sigma_j}{\partial x}\frac{\partial h_j}{\partial x}}{\left(1+\left(\frac{\partial h_j}{\partial x}\right)^2\right)^{1/2}}+\frac{\sigma_j\frac{\partial^2 h_j}{\partial x^2}}{\left(1+\left(\frac{\partial h_j}{\partial x}\right)^2\right)^{3/2}},\tag{3.2.18}$$

on $y=h_j(x,t)$. Similarly, substituting the normal and curvature (3.2.15) and (3.2.16) into (3.2.10), we obtain the two components to the stress condition

$$\frac{\partial \eta}{\partial x}\left(T_{2xx}-T_{1xx}\right)+T_{1xy}-T_{2xy}=-\frac{\sigma_I\frac{\partial^2\eta}{\partial x^2}\frac{\partial \eta}{\partial x}}{\left(1+\left(\frac{\partial \eta}{\partial x}\right)^2\right)^{3/2}},\tag{3.2.19}$$

$$\frac{\partial \eta}{\partial x}\left(T_{2xy}-T_{1xy}\right)+T_{1yy}-T_{2yy}=\frac{\sigma_I\frac{\partial^2\eta}{\partial x^2}}{\left(1+\left(\frac{\partial \eta}{\partial x}\right)^2\right)^{3/2}},\tag{3.2.20}$$

on $y=\eta(x,t)$.

We are now in the position to calculate the net momentum balances. By the continuity equation (3.2.4)

$$\frac{\partial \rho}{\partial t}+\frac{\partial}{\partial x}\left(\rho u\right)+\frac{\partial}{\partial y}\left(\rho v\right)=0,$$

combining this with the x-component of the Navier-Stokes equations (3.2.3)

$$\rho\left(\frac{\partial u}{\partial t}+u\frac{\partial u}{\partial x}+v\frac{\partial u}{\partial y}\right)=\frac{\partial T_{xx}}{\partial x}+\frac{\partial T_{xy}}{\partial y}+\rho g,$$

we have

$$\frac{\partial}{\partial t}\left(\rho u\right)+\frac{\partial}{\partial x}\left(\rho u^2\right)+\frac{\partial}{\partial y}\left(\rho uv\right)=\frac{\partial T_{xx}}{\partial x}+\frac{\partial T_{xy}}{\partial y}+\rho g.\tag{3.2.21}$$

Likewise, combining the continuity equation with the y-component of the Navier-Stokes equations (3.2.3), we have

$$\frac{\partial}{\partial t}\left(\rho v\right)+\frac{\partial}{\partial x}\left(\rho uv\right)+\frac{\partial}{\partial y}\left(\rho v^2\right)=\frac{\partial T_{xy}}{\partial x}+\frac{\partial T_{yy}}{\partial y}.\tag{3.2.22}$$

To obtain integral relations representing the net momentum balances, we integrate

(3.2.21) and (3.2.22) with respect to y across the liquid curtain. The left-hand side of both equations can be directly integrated across the whole liquid curtain, from $y = h_1$ to $y = h_2$, since both the longitudinal and transverse velocities are continuous across $y = \eta(x,t)$. However, when considering the right-hand side, to integrate across the liquid curtain we must break the integral into two parts, from $y = h_1(x,t)$ to $y = \eta(x,t)$ and then from $y = \eta(x,t)$ to $y = h_2(x,t)$, since the jump in stresses across $y = \eta$ is not continuous. As described in the stress condition (3.2.10), the jump in normal stresses is balanced by the curvature times the interfacial tension and the balance in tangential stresses is balanced by gradients in interfacial tension (though in this model there is no gradient in interfacial tension at $y = \eta$, there is only a variation in the surface tension along the free surfaces).

Using Leibniz's Integration Rule

$$\int_a^b \frac{\partial}{\partial\beta} f(\alpha,\beta)\,\mathrm{d}\alpha = \frac{\mathrm{d}}{\mathrm{d}\beta}\int_a^b f(\alpha,\beta)\,\mathrm{d}\alpha - f(\alpha,\beta)|_{\alpha=b}\frac{\partial b}{\partial\beta} + f(\alpha,\beta)|_{\alpha=a}\frac{\partial a}{\partial\beta},$$

as well as (3.2.9), (3.2.17) and (3.2.19), we integrate (3.2.21) across the liquid curtain, establishing the integral form of the net momentum balance in the x-direction

$$\begin{aligned}\frac{\partial}{\partial t}\int_{h_1}^{h_2}\rho u\,\mathrm{d}y + \frac{\partial}{\partial x}\int_{h_1}^{h_2}\rho u^2\,\mathrm{d}y = \frac{\partial}{\partial x}\int_{h_1}^{h_2}T_{xx}\,\mathrm{d}y + \int_{h_1}^{h_2}\rho g\,\mathrm{d}y \\ - \frac{\sigma_1\frac{\partial^2 h_1}{\partial x^2}\frac{\partial h_1}{\partial x}}{\left(1+\left(\frac{\partial h_1}{\partial x}\right)^2\right)^{3/2}} - \frac{\sigma_I\frac{\partial^2\eta}{\partial x^2}\frac{\partial\eta}{\partial x}}{\left(1+\left(\frac{\partial\eta}{\partial x}\right)^2\right)^{3/2}} - \frac{\sigma_2\frac{\partial^2 h_2}{\partial x^2}\frac{\partial h_2}{\partial x}}{\left(1+\left(\frac{\partial h_2}{\partial x}\right)^2\right)^{3/2}} \\ + \frac{\frac{\partial\sigma_1}{\partial x}}{\left(1+\left(\frac{\partial h_1}{\partial x}\right)^2\right)^{1/2}} + \frac{\frac{\partial\sigma_2}{\partial x}}{\left(1+\left(\frac{\partial h_2}{\partial x}\right)^2\right)^{1/2}}.\end{aligned} \tag{3.2.23}$$

Similarly, integrating (3.2.22) across the liquid curtain, and using (3.2.9), (3.2.18) and

(3.2.20), we establish the integral form of the net momentum balance in the y-direction

$$\begin{aligned}\frac{\partial}{\partial t}\int_{h_1}^{h_2}\rho v\,\mathrm{d}y+\frac{\partial}{\partial x}\int_{h_1}^{h_2}\rho uv\,\mathrm{d}y=\frac{\partial}{\partial x}\int_{h_1}^{h_2}T_{xy}\,\mathrm{d}y\\ +\frac{\sigma_1\frac{\partial^2 h_1}{\partial x^2}}{\left(1+\left(\frac{\partial h_1}{\partial x}\right)^2\right)^{3/2}}+\frac{\sigma_I\frac{\partial^2 \eta}{\partial x^2}}{\left(1+\left(\frac{\partial \eta}{\partial x}\right)^2\right)^{3/2}}+\frac{\sigma_2\frac{\partial^2 h_2}{\partial x^2}}{\left(1+\left(\frac{\partial h_2}{\partial x}\right)^2\right)^{3/2}}\\ +\frac{\frac{\partial\sigma_1}{\partial x}\frac{\partial h_1}{\partial x}}{\left(1+\left(\frac{\partial h_1}{\partial x}\right)^2\right)^{1/2}}+\frac{\frac{\partial\sigma_2}{\partial x}\frac{\partial h_2}{\partial x}}{\left(1+\left(\frac{\partial h_2}{\partial x}\right)^2\right)^{1/2}}.\end{aligned}\tag{3.2.24}$$

Non-dimensionalisation

We non-dimensionalise our model using the following scales

$$u_j=U\widehat{u}_j,\quad v_j=\varepsilon U\widehat{v}_j,\quad x=l\widehat{x},\quad y=\varepsilon l\widehat{y},$$

$$t=\frac{l}{U}\widehat{t},\quad \mathbf{T}_j=\frac{\mu_1 U}{l}\widehat{\mathbf{T}}_j,\quad p_j=\frac{\mu_1 U}{l}\widehat{p}_j,\quad \Gamma_j=\Gamma_{in,1}\widehat{\Gamma}_j,\tag{3.2.25}$$

where we note again a subscript j refers to whether we are considering fluid 1 or 2 ($j=1$ or 2 accordingly). Hats denote dimensionless variables, with U being the typical curtain velocity at the exit slot (at $x=0$) and l the curtain length (the height of curtain above the substrate to be coated). Letting h_0 be the initial thickness of the curtain (at $x=0$), then $\varepsilon=h_0/l$ is the aspect ratio, which we take $\varepsilon\ll 1$. Moreover, $\Gamma_{in,1}$ corresponds to the concentration of surfactant on the surface $y=h_1$ at $x=0$, considered constant.

The density and viscosity are non-dimensionalised with respect to the properties of fluid 1, such that

$$\widehat{\rho}=\begin{cases}1 & \text{if } h_1\leqslant y<\eta\\ \frac{\rho_2}{\rho_1} & \text{if } \eta<y\leqslant h_2,\end{cases}\tag{3.2.26}$$

$$\widehat{\mu} = \begin{cases} 1 & \text{if } h_1 \leqslant y < \eta \\ \frac{\mu_2}{\mu_1} & \text{if } \eta < y \leqslant h_2. \end{cases} \tag{3.2.27}$$

We assume that we are dealing with a Newtonian incompressible fluid, meaning we have the constitutive equations

$$\mathbf{T}_{ij} = -p\delta_{ij} + \mu\left(\frac{\partial u_i}{\partial x_j} + \frac{\partial u_j}{\partial x_i}\right), \tag{3.2.28}$$

where, in this equation only, the subscript i and j are used as part of suffix notation. Substituting in our dimensionless variables from (3.2.25) and (3.2.27), we obtain the dimensionless version of (3.2.28)

$$\widehat{T}_{jxx} = -\widehat{p}_j + 2\frac{\mu_j}{\mu_1}\frac{\partial \widehat{u}_j}{\partial \widehat{x}}, \tag{3.2.29}$$

$$\widehat{T}_{jxy} = \frac{\mu_j}{\mu_1}\left(\frac{1}{\varepsilon}\frac{\partial \widehat{u}_j}{\partial \widehat{y}} + \varepsilon\frac{\partial \widehat{v}_j}{\partial \widehat{x}}\right), \tag{3.2.30}$$

$$\widehat{T}_{jyy} = -\widehat{p}_j + 2\frac{\mu_j}{\mu_1}\frac{\partial \widehat{v}_j}{\partial \widehat{y}}. \tag{3.2.31}$$

Substituting our non-dimensional scales (3.2.25), as well as our constitutive equation, into our governing equations (3.2.3) we obtain their non-dimensional form

$$\varepsilon^2 Re\left(\frac{\partial \widehat{u}_1}{\partial \widehat{t}} + \widehat{u}_1\frac{\partial \widehat{u}_1}{\partial \widehat{x}} + \widehat{v}_1\frac{\partial \widehat{u}_1}{\partial \widehat{y}}\right) = \frac{\partial^2 \widehat{u}_1}{\partial \widehat{y}^2} + \varepsilon^2\left(\frac{\partial^2 \widehat{u}_1}{\partial \widehat{x}^2} + \frac{Re}{Fr^2} - \frac{\partial \widehat{p}_1}{\partial \widehat{x}}\right), \tag{3.2.32}$$

$$\varepsilon^2 Re\left(\frac{\partial \widehat{v}_1}{\partial \widehat{t}} + \widehat{u}_1\frac{\partial \widehat{v}_1}{\partial \widehat{x}} + \widehat{v}_1\frac{\partial \widehat{v}_1}{\partial \widehat{y}}\right) = -\frac{\partial \widehat{p}_1}{\partial \widehat{y}} + \varepsilon^2\frac{\partial^2 \widehat{v}_1}{\partial \widehat{x}^2} + \frac{\partial^2 \widehat{v}_1}{\partial \widehat{y}^2}, \tag{3.2.33}$$

$$\varepsilon^2 Re\frac{\rho_2}{\rho_1}\left(\frac{\partial \widehat{u}_2}{\partial \widehat{t}} + \widehat{u}_2\frac{\partial \widehat{u}_2}{\partial \widehat{x}} + \widehat{v}_2\frac{\partial \widehat{u}_2}{\partial \widehat{y}}\right) = \frac{\mu_2}{\mu_1}\frac{\partial^2 \widehat{u}_2}{\partial \widehat{y}^2} + \varepsilon^2\left(\frac{\mu_2}{\mu_1}\frac{\partial^2 \widehat{u}_2}{\partial \widehat{x}^2} + \frac{Re}{Fr^2}\frac{\rho_2}{\rho_1} - \frac{\partial \widehat{p}_2}{\partial \widehat{x}}\right), \tag{3.2.34}$$

$$\varepsilon^2 Re\frac{\rho_2}{\rho_1}\left(\frac{\partial \widehat{v}_2}{\partial \widehat{t}} + \widehat{u}_2\frac{\partial \widehat{v}_2}{\partial \widehat{x}} + \widehat{v}_2\frac{\partial \widehat{v}_2}{\partial \widehat{y}}\right) = -\frac{\partial \widehat{p}_2}{\partial \widehat{y}} + \frac{\mu_2}{\mu_1}\left(\varepsilon^2\frac{\partial^2 \widehat{v}_2}{\partial \widehat{x}^2} + \frac{\partial^2 \widehat{v}_2}{\partial \widehat{y}^2}\right), \tag{3.2.35}$$

where $Re = \rho_1 Ul/\mu_1$ and $Fr = U/\sqrt{gl}$ are the dimensionless Reynolds number and Froude

number, based on the material properties of fluid 1.

The continuity equation (3.2.4), assuming incompressibility (since the density of each fluid layer is constant), remains unchanged

$$\frac{\partial \widehat{u}_j}{\partial \widehat{x}} + \frac{\partial \widehat{v}_j}{\partial \widehat{y}} = 0. \tag{3.2.36}$$

Non-dimensionalising the boundary conditions, the free surface stress condition (3.2.5) becomes

$$\widehat{\mathbf{T}}_j \cdot \mathbf{n}_j = \frac{1}{Ca} \nabla_{s,j} \left(\frac{\sigma_j}{\sigma_{s,1}} \right) - \frac{1}{Ca} \frac{\sigma_j}{\sigma_{s,1}} \left(\nabla \cdot \mathbf{n}_j \right) \mathbf{n}_j, \tag{3.2.37}$$

on $\widehat{y} = \widehat{h}_j$, where $Ca = \mu_1 U / \sigma_{s,1}$ is the capillary number based on fluid 1 and the normal and curvature are given by

$$\mathbf{n}_j = \frac{(-1)^j}{\left(1 + \varepsilon^2 \left(\frac{\partial \widehat{h}_j}{\partial \widehat{x}} \right)^2 \right)^{1/2}} \begin{pmatrix} -\varepsilon \frac{\partial \widehat{h}_j}{\partial \widehat{x}} \\ 1 \end{pmatrix},$$

$$\nabla \cdot \mathbf{n}_j = \frac{(-1)^{j+1} \varepsilon \frac{\partial^2 \widehat{h}_j}{\partial \widehat{x}^2}}{\left(1 + \varepsilon^2 \left(\frac{\partial \widehat{h}_j}{\partial \widehat{x}} \right)^2 \right)^{3/2}}.$$

The evolution equation for surfactant concentration on the free surface (3.2.7) remains unchanged

$$\frac{\partial \widehat{\Gamma}_j}{\partial \widehat{t}} + \nabla_{s,j} \cdot \left(\widehat{\Gamma}_j \widehat{\mathbf{u}}_{s,j} \right) + \widehat{\Gamma}_j \left(\nabla_{s,j} \cdot \mathbf{n}_j \right) \left(\widehat{\mathbf{u}} \cdot \mathbf{n}_j \right) = 0, \tag{3.2.38}$$

whilst the equation of state (3.2.8) linking the surface tension to the surfactant concentration becomes

$$\frac{\sigma_j}{\sigma_{s,1}} = \frac{\sigma_{s,j}}{\sigma_{s,1}} \left(1 - \frac{\Gamma_{in,1}}{\Gamma_{in,j}} \beta_j \widehat{\Gamma}_j \right), \tag{3.2.39}$$

where the surface tension of the free surface $\widehat{y} = \widehat{h}_j$ has been non-dimensionalised with respect to the constant surface tension of the 'clean' (surfactant-free) fluid of layer 1.

Here, we have also introduced the surface activity number [106], $\beta_j = RT\Gamma_{in,j}/\sigma_{s,j}$, which provides a measure of the sensitivity of the surface tension, σ_j, to the surfactant concentration, Γ_j. Due to the non-dimensionalisation of the surfactant concentration from (3.2.25), $\widehat{\Gamma}_j = \Gamma_{in,j}/\Gamma_{in,1}$ is constant on $\widehat{y} = \widehat{h}_j$ at $\widehat{x} = 0$, so that the surface tension is reduced to $\sigma_j = \sigma_{s,j}\,(1 - \beta_j)$ here. This shows that $0 \leqslant \beta_j < 1$, where a value of $\beta_j = 0$ corresponds to the surfactant having no effect on the surface tension ($\sigma_j = \sigma_{s,j}$), and a value of $\beta_j = 1$ corresponds to the surfactant reducing the surface tension to zero (clearly unphysical). As explained previously, for the linear form of the equation of state to hold, the surfactant concentration must be present in dilute concentrations. Thus we only consider small values of β_j in our model.

The kinematic condition (3.2.9) remains unchanged

$$\frac{\partial \widehat{h}_j}{\partial \widehat{t}} + \widehat{u}\frac{\partial \widehat{h}_j}{\partial \widehat{x}} = \widehat{v}. \tag{3.2.40}$$

From the interfacial conditions at the liquid-liquid interface; the stress condition (3.2.10) becomes

$$\left[\widehat{\mathbf{T}}_{\mathbf{j}} \cdot \mathbf{n}\right]_1^2 = -\frac{1}{Ca}\frac{\sigma_I}{\sigma_{s,1}}\left(\nabla \cdot \mathbf{n}\right)\mathbf{n}, \tag{3.2.41}$$

where

$$\mathbf{n} = \frac{1}{\left(1 + \varepsilon^2\left(\frac{\partial \widehat{\eta}}{\partial \widehat{x}}\right)^2\right)^{1/2}}\begin{pmatrix} \varepsilon\frac{\partial \widehat{\eta}}{\partial \widehat{x}} \\ -1 \end{pmatrix},$$

$$\nabla \cdot \mathbf{n} = \frac{\varepsilon\frac{\partial^2 \widehat{\eta}}{\partial \widehat{x}^2}}{\left(1 + \varepsilon^2\left(\frac{\partial \widehat{\eta}}{\partial \widehat{x}}\right)^2\right)^{3/2}},$$

whilst the kinematic condition (3.2.12) and the continuity of velocity (3.2.11) remain

unchanged

$$\frac{\partial \widehat{\eta}}{\partial \widehat{t}} + \widehat{u}\frac{\partial \widehat{\eta}}{\partial \widehat{x}} = \widehat{v}, \tag{3.2.42}$$

$$\widehat{u}_1 = \widehat{u}_2, \qquad \widehat{v}_1 = \widehat{v}_2. \tag{3.2.43}$$

The non-dimensional version of the net-momentum balance in the x-direction, (3.2.23), is given by

$$\begin{aligned}
\varepsilon Re\left(\frac{\partial}{\partial \widehat{t}}\int_{\widehat{h}_1}^{\widehat{h}_2} \widehat{\rho}\widehat{u}\,\mathrm{d}\widehat{y} + \frac{\partial}{\partial \widehat{x}}\int_{\widehat{h}_1}^{\widehat{h}_2} \widehat{\rho}\widehat{u}^2\,\mathrm{d}\widehat{y}\right) &= \varepsilon\frac{\partial}{\partial \widehat{x}}\int_{\widehat{h}_1}^{\widehat{h}_2} \widehat{T}_{xx}\,\mathrm{d}\widehat{y} + \frac{\varepsilon Re}{Fr^2}\int_{\widehat{h}_1}^{\widehat{h}_2} \widehat{\rho}\,\mathrm{d}\widehat{y} \\
&- \frac{\varepsilon^2}{Ca}\left(\frac{\left(1-\beta_1\widehat{\Gamma}_1\right)\frac{\partial^2\widehat{h}_1}{\partial\widehat{x}^2}\frac{\partial\widehat{h}_1}{\partial\widehat{x}}}{\left(1+\varepsilon^2\left(\frac{\partial\widehat{h}_1}{\partial\widehat{x}}\right)^2\right)^{3/2}} + \frac{\frac{\sigma_I}{\sigma_{s,1}}\frac{\partial^2\widehat{\eta}}{\partial\widehat{x}^2}\frac{\partial\widehat{\eta}}{\partial\widehat{x}}}{\left(1+\varepsilon^2\left(\frac{\partial\widehat{\eta}}{\partial\widehat{x}}\right)^2\right)^{3/2}} + \frac{\frac{\sigma_{s,2}}{\sigma_{s,1}}\left(1-\frac{\Gamma_{in,1}}{\Gamma_{in,2}}\beta_2\widehat{\Gamma}_2\right)\frac{\partial^2\widehat{h}_2}{\partial\widehat{x}^2}\frac{\partial\widehat{h}_2}{\partial\widehat{x}}}{\left(1+\varepsilon^2\left(\frac{\partial\widehat{h}_2}{\partial\widehat{x}}\right)^2\right)^{3/2}}\right) \\
&- \frac{1}{Ca}\left(\frac{\beta_1\frac{\partial\widehat{\Gamma}_1}{\partial\widehat{x}}}{\left(1+\varepsilon^2\left(\frac{\partial\widehat{h}_1}{\partial\widehat{x}}\right)^2\right)^{1/2}} + \frac{\frac{\sigma_{s,2}}{\sigma_{s,1}}\frac{\Gamma_{in,1}}{\Gamma_{in,2}}\beta_2\frac{\partial\widehat{\Gamma}_2}{\partial\widehat{x}}}{\left(1+\varepsilon^2\left(\frac{\partial\widehat{h}_2}{\partial\widehat{x}}\right)^2\right)^{1/2}}\right)
\end{aligned} \tag{3.2.44}$$

and in the y-direction, the non-dimensional version of (3.2.24) is given by

$$\begin{aligned}
\varepsilon Re\left(\frac{\partial}{\partial \widehat{t}}\int_{\widehat{h}_1}^{\widehat{h}_2} \widehat{\rho}\widehat{v}\,\mathrm{d}\widehat{y} + \frac{\partial}{\partial \widehat{x}}\int_{\widehat{h}_1}^{\widehat{h}_2} \widehat{\rho}\widehat{u}\widehat{v}\,\mathrm{d}\widehat{y}\right) &= \frac{\partial}{\partial \widehat{x}}\int_{\widehat{h}_1}^{\widehat{h}_2} \widehat{T}_{xy}\,\mathrm{d}\widehat{y} \\
&+ \frac{1}{Ca}\left(\frac{\left(1-\beta_1\widehat{\Gamma}_1\right)\frac{\partial^2\widehat{h}_1}{\partial\widehat{x}^2}}{\left(1+\varepsilon^2\left(\frac{\partial\widehat{h}_1}{\partial\widehat{x}}\right)^2\right)^{3/2}} + \frac{\frac{\sigma_I}{\sigma_{s,1}}\frac{\partial^2\widehat{\eta}}{\partial\widehat{x}^2}}{\left(1+\varepsilon^2\left(\frac{\partial\widehat{\eta}}{\partial\widehat{x}}\right)^2\right)^{3/2}} + \frac{\frac{\sigma_{s,2}}{\sigma_{s,1}}\left(1-\frac{\Gamma_{in,1}}{\Gamma_{in,2}}\beta_2\widehat{\Gamma}_2\right)\frac{\partial^2\widehat{h}_2}{\partial\widehat{x}^2}}{\left(1+\varepsilon^2\left(\frac{\partial\widehat{h}_2}{\partial\widehat{x}}\right)^2\right)^{3/2}}\right) \\
&- \frac{1}{Ca}\left(\frac{\beta_1\frac{\partial\widehat{\Gamma}_1}{\partial\widehat{x}}\frac{\partial\widehat{h}_1}{\partial\widehat{x}}}{\left(1+\varepsilon^2\left(\frac{\partial\widehat{h}_1}{\partial\widehat{x}}\right)^2\right)^{1/2}} + \frac{\frac{\sigma_{s,2}}{\sigma_{s,1}}\frac{\Gamma_{in,1}}{\Gamma_{in,2}}\beta_2\frac{\partial\widehat{\Gamma}_2}{\partial\widehat{x}}\frac{\partial\widehat{h}_2}{\partial\widehat{x}}}{\left(1+\varepsilon^2\left(\frac{\partial\widehat{h}_2}{\partial\widehat{x}}\right)^2\right)^{1/2}}\right),
\end{aligned} \tag{3.2.45}$$

completing the non-dimensionalisation of our model. Note how in the case of no surfactant being present, that is when $\widehat{\Gamma}_j = 0$, the dimensionless equations of Dyson *et al.* [41] are

recovered (see Appendix A). For clarity, all hats are now dropped from dimensionless variables.

3.2.2 Asymptotic analysis

We take the following orders of magnitude, which are typical in the coating industry [41],

$$\varepsilon Re = \mathcal{R} = O(1), \qquad Ca = O(1), \qquad Fr = O(1). \tag{3.2.46}$$

Since ε is our small parameter, we use the asymptotic expansions

$$\begin{aligned}&\{u_j, v_j, p_j, h_j, \eta, \Gamma_j\}\\ &\quad = \{u_{j,0}, v_{j,0}, p_{j,0}, h_{j,0}, \eta_0, \Gamma_{j,0}\} + \delta\{u_{j,1}, v_{j,1}, p_{j,1}, h_{j,1}, \eta_1, \Gamma_{j,1}\} + O(\delta^2),\end{aligned} \tag{3.2.47}$$

Substituting (3.2.47) into our governing equations, the x-component of the Navier-Stokes equations, (3.2.32) and (3.2.34), to leading order become

$$\frac{\partial^2 u_{0,j}}{\partial y^2} = 0. \tag{3.2.48}$$

The y-component of the Navier-Stokes equations, (3.2.33) and (3.2.35), to leading order become

$$-\frac{\partial p_{0,j}}{\partial y} + \frac{\mu_j}{\mu_1}\frac{\partial^2 v_{0,j}}{\partial y^2} = 0, \tag{3.2.49}$$

whilst the leading order of the continuity equation, (3.2.36), becomes

$$\frac{\partial u_{0,j}}{\partial x} + \frac{\partial v_{0,j}}{\partial y} = 0. \tag{3.2.50}$$

Moving onto the boundary conditions on $y = h_j$, we find from the leading order of the

first component of the stress condition (3.2.37):

$$\frac{\partial u_{0,j}}{\partial y} = 0.$$

This result shows that the leading order velocity $u_{0,j}$ is a function of x and t only. From this, the leading order x-component of the Navier-Stokes equations (3.2.48) is automatically satisfied. The second component of the stress condition (3.2.37) to leading order gives

$$-p_{0,j} + 2\frac{\mu_j}{\mu_1}\frac{\partial v_{0,j}}{\partial y} = 0. \tag{3.2.51}$$

Differentiating this equation with respect to y, and substituting into (3.2.49), we obtain

$$\frac{\partial^2 v_{0,j}}{\partial y^2} = 0. \tag{3.2.52}$$

The equation governing the evolution of surfactant concentration (3.2.38), to leading order, is given by

$$\frac{\partial \Gamma_{0,j}}{\partial t} + \frac{\partial}{\partial x}\left(u_{0,j}\Gamma_{0,j}\right) = 0, \tag{3.2.53}$$

whilst the equation of state (3.2.39) at leading order is given by

$$\frac{\sigma_j}{\sigma_{s,1}} = \frac{\sigma_{s,j}}{\sigma_{s,1}}\left(1 - \frac{\Gamma_{in,1}}{\Gamma_{in,j}}\beta_j\Gamma_{0,j}\right), \tag{3.2.54}$$

and the kinematic condition (3.2.40) at leading order

$$\frac{\partial h_{0,j}}{\partial t} + u_{0,j}\frac{\partial h_{0,j}}{\partial x} = v_{0,j}. \tag{3.2.55}$$

Along the fluid-fluid interface, the leading order boundary conditions for the stress condition (3.2.41) (the second component, since the first is automatically satisfied to leading order), the kinematic condition (3.2.42), and the continuity of velocity (3.2.43),

are given by

$$-p_{0,2} + 2\frac{\mu_2}{\mu_1}\frac{\partial v_{0,2}}{\partial y} + p_{0,1} - 2\frac{\partial v_{0,1}}{\partial y} = 0, \tag{3.2.56}$$

$$\frac{\partial \eta_0}{\partial t} + u_{0,j}\frac{\partial \eta_0}{\partial x} = v_{0,j}, \tag{3.2.57}$$

$$u_{0,1} = u_{0,2}, \quad v_{0,1} = v_{0,2}. \tag{3.2.58}$$

Having completed the substitution of the asymptotic expansions (3.2.47) into our mathematical model, obtaining the leading order system, all subscript zeros are now dropped for clarity. By directly integrating (3.2.52), we see that

$$v_1 = A(x,t)y + B(x,t), \tag{3.2.59}$$

$$v_2 = C(x,t)y + D(x,t), \tag{3.2.60}$$

where A, B, C and D are arbitrary functions of x and t that are a result of the integration.

Velocities are continuous across the fluid-fluid interface, from (3.2.58), telling us that $u_1(x,t) = u_2(x,t)$ on $y = \eta$; since u_1 and u_2 do not depend on y, this implies that

$$u_1(x,t) = u_2(x,t) = u(x,t).$$

Substituting this relation, as well as (3.2.59) and (3.2.60) into the leading order continuity equation (3.2.50), we obtain

$$\begin{aligned}
\frac{\partial u}{\partial x} + \frac{\partial v_1}{\partial y} &= \frac{\partial u}{\partial x} + A = 0, \\
\frac{\partial u}{\partial x} + \frac{\partial v_2}{\partial y} &= \frac{\partial u}{\partial x} + C = 0,
\end{aligned}$$

and subtraction of these equations shows that

$$A = C = -\frac{\partial u}{\partial x}. \tag{3.2.61}$$

Moreover, from (3.2.58) we have that $v_1 = v_2$ on $y = \eta$, implying from (3.2.59), (3.2.60) and (3.2.61):

$$-\frac{\partial u}{\partial x}\eta + B = -\frac{\partial u}{\partial x}\eta + D,$$

so that

$$B = D.$$

Thus our leading order solution for the velocity is given by

$$u_1 = u_2 = u(x,t), \tag{3.2.62}$$

$$v_1 = v_2 = -\frac{\partial u}{\partial x}y + D. \tag{3.2.63}$$

Substituting (3.2.63) into the leading order free surface stress condition (3.2.51) we have that

$$p_j = -2\frac{\mu_j}{\mu_1}\frac{\partial u}{\partial x}, \tag{3.2.64}$$

which we note also satisfies the leading order stress condition on the liquid-liquid interface (3.2.56).

From the leading order kinematic condition on each interface (from (3.2.55) and (3.2.57) respectively), (3.2.62) and (3.2.63) we have

$$\frac{\partial h_j}{\partial t} + u\frac{\partial h_j}{\partial x} = -\frac{\partial u}{\partial x}h_j + D,$$
$$\frac{\partial \eta}{\partial t} + u\frac{\partial \eta}{\partial x} = -\frac{\partial u}{\partial x}\eta + D,$$

implying

$$D(x,t) = \frac{\partial h_j}{\partial t} + \frac{\partial}{\partial x}\left(u h_j\right) = \frac{\partial \eta}{\partial t} + \frac{\partial}{\partial x}\left(u\eta\right).$$

Subtraction of these three equations gives us

$$\frac{\partial H_j}{\partial t} + \frac{\partial}{\partial x}\left(u H_j\right) = 0, \tag{3.2.65}$$

where $H_1 = \eta - h_1$ and $H_2 = h_2 - \eta$ are the thicknesses of layer 1 and 2 respectively; with $H = H_1 + H_2$ being the total curtain thickness (see Figure 3.1).

Thus we have our leading order system, but to find a solution to this the next terms in the expansion must be considered, since the leading order system alone is underdetermined. As explained by Dyson *et al.*, the net momentum balance equations we derived earlier, (3.2.44) and (3.2.45), provide an easier way of obtaining the closed system.

We substitute the first order solutions (3.2.62), (3.2.63) and (3.2.64) into the net-momentum balance in the longitudinal direction (3.2.44), and take the limit $\varepsilon \to 0$, to obtain the leading order equation

$$\mathcal{R}\left(\frac{\partial}{\partial t}\int_{h_1}^{h_2} \rho u \,\mathrm{d}y + \frac{\partial}{\partial x}\int_{h_1}^{h_2} \rho u^2 \,\mathrm{d}y\right) = \frac{\mathcal{R}}{Fr^2}\int_{h_1}^{h_2} \rho \,\mathrm{d}y - \frac{1}{Ca}\left(\beta_1 \frac{\partial \Gamma_1}{\partial x} + \frac{\sigma_{s,2}}{\sigma_{s,1}}\frac{\Gamma_{in,1}}{\Gamma_{in,2}}\beta_2 \frac{\partial \Gamma_2}{\partial x}\right).$$

Performing the integration, this becomes

$$\begin{aligned}
&\mathcal{R}\left(u\underbrace{\left(\frac{\partial H_1}{\partial t} + \frac{\partial}{\partial x}\left(u H_1\right)\right)}_{=0 \text{ by } (3.2.65)} + \frac{\rho_2}{\rho_1} u \underbrace{\left(\frac{\partial H_2}{\partial t} + \frac{\partial}{\partial x}\left(u H_2\right)\right)}_{=0 \text{ by } (3.2.65)} + \left(\frac{\partial u}{\partial t} + u\frac{\partial u}{\partial x}\right)\left(H_1 + \frac{\rho_2}{\rho_1}H_2\right)\right) \\
&\quad = \frac{\mathcal{R}}{Fr^2}\left(H_1 + \frac{\rho_2}{\rho_1}H_2\right) - \frac{1}{Ca}\left(\beta_1 \frac{\partial \Gamma_1}{\partial x} + \frac{\sigma_{s,2}}{\sigma_{s,1}}\frac{\Gamma_{in,1}}{\Gamma_{in,2}}\beta_2 \frac{\partial \Gamma_2}{\partial x}\right),
\end{aligned}$$

i.e.

$$\mathcal{R}\left(\frac{\partial u}{\partial t}+u\frac{\partial u}{\partial x}\right)\left(H_1+\frac{\rho_2}{\rho_1}H_2\right) = \frac{\mathcal{R}}{Fr^2}\left(H_1+\frac{\rho_2}{\rho_1}H_2\right)-\frac{1}{Ca}\left(\beta_1\frac{\partial \Gamma_1}{\partial x}+\frac{\sigma_{s,2}}{\sigma_{s,1}}\frac{\Gamma_{in,1}}{\Gamma_{in,2}}\beta_2\frac{\partial \Gamma_2}{\partial x}\right). \tag{3.2.66}$$

We similarly find the transverse equation by substituting the first order solutions (3.2.62), (3.2.63) and (3.2.64) into the net-momentum balance in the y-direction (3.2.45), letting $\varepsilon \to 0$ and evaluating the integrals. However, before doing so, it transpires to be easier to introduce the variable $\overline{y}$; representing the cross-sectional centre of mass, defined by

$$\int_{h_1}^{h_2}\rho y\,\mathrm{d}y=\widehat{\rho}H\overline{y}=\frac{(\eta^2-h_1^2)}{2}+\frac{\rho_2\,(h_2^2-\eta^2)}{2\rho_1},$$

where $\widehat{\rho}$ is the mean density defined by

$$\int_{h_1}^{h_2}\rho\,\mathrm{d}y=\widehat{\rho}H=H_1+\frac{\rho_2}{\rho_1}H_2.$$

From this, we have

$$\begin{aligned}\overline{y}&=\frac{1}{\widehat{\rho}H}\left(\frac{\eta^2-h_1^2}{2}+\frac{\rho_2}{\rho_1}\frac{h_2^2-\eta^2}{2}\right)\\&=\eta+\frac{\frac{\rho_2}{\rho_1}\left(h_2-\eta\right)^2-\left(\eta-h_1\right)^2}{2\left(H_1+\frac{\rho_2}{\rho_1}H_2\right)}.\end{aligned} \tag{3.2.67}$$

Letting $\varepsilon \to 0$ in (3.2.45), we obtain

$$\begin{aligned}\mathcal{R}\left(\frac{\partial}{\partial t}\int_{h_1}^{h_2}\rho v\,\mathrm{d}y + \frac{\partial}{\partial x}\int_{h_1}^{h_2}\rho uv\,\mathrm{d}y\right)&\\ = \frac{1}{Ca}\left(\left(1-\beta_1\Gamma_1\right)\frac{\partial^2 h_1}{\partial x^2} + \frac{\sigma_I}{\sigma_{s,1}}\frac{\partial^2\eta}{\partial x^2} + \frac{\sigma_{s,2}}{\sigma_{s,1}}\left(1-\frac{\Gamma_{in,1}}{\Gamma_{in,2}}\beta_2\Gamma_2\right)\frac{\partial^2 h_2}{\partial x^2}\right)&\\ - \frac{1}{Ca}\left(\beta_1\frac{\partial\Gamma_1}{\partial x}\frac{\partial h_1}{\partial x} + \frac{\sigma_{s,2}}{\sigma_{s,1}}\frac{\Gamma_{in,1}}{\Gamma_{in,2}}\beta_2\frac{\partial\Gamma_2}{\partial x}\frac{\partial h_2}{\partial x}\right).&\end{aligned} \tag{3.2.68}$$

We substitute our leading order solutions, (3.2.62), (3.2.63) and (3.2.64), into (3.2.68) and evaluate the integrals to see that the left-hand side becomes

$$\begin{aligned}&\mathcal{R}\left(\frac{\partial}{\partial t}\int_{h_1}^{h_2}\rho v\,\mathrm{d}y + \frac{\partial}{\partial x}\int_{h_1}^{h_2}\rho uv\,\mathrm{d}y\right)\\ &\quad= \mathcal{R}\left(\frac{\partial}{\partial t}\Big(\int_{h_1}^{\eta} -\frac{\partial u}{\partial x}y + D\,\mathrm{d}y + \int_{\eta}^{h_2}\frac{\rho_2}{\rho_1}\Big(-\frac{\partial u}{\partial x}y + D\Big)\,\mathrm{d}y\Big)\right.\\ &\qquad\left.+\frac{\partial}{\partial x}\Big(\int_{h_1}^{\eta} u\Big(-\frac{\partial u}{\partial x}y + D\Big)\,\mathrm{d}y + \int_{\eta}^{h_2}\frac{\rho_2}{\rho_1}u\Big(-\frac{\partial u}{\partial x}y + D\Big)\,\mathrm{d}y\Big)\right)\\ &\quad= \mathcal{R}\Big(H_1 + \frac{\rho_2}{\rho_1}H_2\Big)\Big(\frac{\partial}{\partial t}\Big(D - \frac{\partial u}{\partial x}\overline{y}\Big) + u\frac{\partial}{\partial x}\Big(D - \frac{\partial u}{\partial x}\overline{y}\Big)\Big),\end{aligned}$$

having used (3.2.65) and (3.2.67). Moreover, after some algebra, again using (3.2.65) and (3.2.67), we have that

$$D - \frac{\partial u}{\partial x}\overline{y} = \frac{\partial\overline{y}}{\partial t} + u\frac{\partial\overline{y}}{\partial x} = \frac{\mathrm{D}\overline{y}}{\mathrm{D}t},$$

where $\mathrm{D}/\mathrm{D}t$ is the material derivative. This means (3.2.68) becomes

$$\begin{aligned}\mathcal{R}\left(H_1 + \frac{\rho_2}{\rho_1}H_2\right)\frac{\mathrm{D}^2\overline{y}}{\mathrm{D}t^2} = \frac{1}{Ca}\left(\left(1-\beta_1\Gamma_1\right)\frac{\partial^2 h_1}{\partial x^2} + \frac{\sigma_I}{\sigma_{s,1}}\frac{\partial^2\eta}{\partial x^2} + \frac{\sigma_{s,2}}{\sigma_{s,1}}\left(1-\frac{\Gamma_{in,1}}{\Gamma_{in,2}}\beta_2\Gamma_2\right)\frac{\partial^2 h_2}{\partial x^2}\right)&\\ - \frac{1}{Ca}\left(\beta_1\frac{\partial\Gamma_1}{\partial x}\frac{\partial h_1}{\partial x} + \frac{\sigma_{s,2}}{\sigma_{s,1}}\frac{\Gamma_{in,1}}{\Gamma_{in,2}}\beta_2\frac{\partial\Gamma_2}{\partial x}\frac{\partial h_2}{\partial x}\right).&\end{aligned} \tag{3.2.69}$$

This equation represents a balance between momentum in the y-direction and surface tension forces.

3.2.3 Steady state solutions

We have six equations, (3.2.53), (3.2.65), (3.2.66) and (3.2.69), in the six unknowns $\Gamma_j(x,t)$, $H_j(x,t)$, $u(x,t)$, $\overline{y}(x,t)$. Initial conditions are imposed to solve these equations in the steady state, so that the variables are functions of x only, denoted with a superscript 0. From the non-dimensional scales (3.2.25), $u^0 = 1$ at $x = 0$, whilst the non-dimensional flux q_j of the fluid at the top of the curtain is prescribed, in both layers. Furthermore, we take the origin of our coordinate system to be the point where the centroid exits the slot, that is $\overline{y}^0 = 0$ at $x = 0$, and that the centroid $\overline{y}^0$ exits vertically. Finally, the initial concentration of surfactant on the free surfaces $y = h_j^0$ is determined from the non-dimensionalisation (3.2.25). Thus we have the following boundary conditions

$$u^0 = 1, \qquad u^0 H_j^0 = q_j, \qquad \overline{y}^0 = \frac{\mathrm{d}\overline{y}^0}{\mathrm{d}x} = 0, \qquad \Gamma_j^0 = \frac{\Gamma_{in,j}}{\Gamma_{in,1}}, \tag{3.2.70}$$

at $x = 0$.

The steady state equations are given by

$$\frac{\mathrm{d}}{\mathrm{d}x}\left(u^0 H_j^0\right) = 0, \tag{3.2.71}$$

$$\frac{\mathrm{d}}{\mathrm{d}x}\left(u^0 \Gamma_j^0\right) = 0, \tag{3.2.72}$$

$$\mathcal{R}u^0\frac{\mathrm{d}u^0}{\mathrm{d}x}\left(H_1^0 + \frac{\rho_2}{\rho_1}H_2^0\right) - \frac{\mathcal{R}}{Fr^2}\left(H_1^0 + \frac{\rho_2}{\rho_1}H_2^0\right) + \frac{1}{Ca}\left(\beta_1\frac{\mathrm{d}\Gamma_1^0}{\mathrm{d}x} + \frac{\sigma_{s,2}}{\sigma_{s,1}}\frac{\Gamma_{in,1}}{\Gamma_{in,2}}\beta_2\frac{\mathrm{d}\Gamma_2^0}{\mathrm{d}x}\right) = 0, \tag{3.2.73}$$

$$\mathcal{R}\left(H_1^0+\frac{\rho_2}{\rho_1}H_2^0\right)u^0\frac{\mathrm{d}}{\mathrm{d}x}\left(u^0\frac{\mathrm{d}\overline{y}^0}{\mathrm{d}x}\right)$$
$$=\frac{1}{Ca}\left(\left(1-\beta_1\Gamma_1^0\right)\frac{\mathrm{d}^2h_1^0}{\mathrm{d}x^2}+\frac{\sigma_I}{\sigma_{s,1}}\frac{\mathrm{d}^2\eta^0}{\mathrm{d}x^2}+\frac{\sigma_{s,2}}{\sigma_{s,1}}\left(1-\frac{\Gamma_{in,1}}{\Gamma_{in,2}}\beta_2\Gamma_2^0\right)\frac{\mathrm{d}^2h_2^0}{\mathrm{d}x^2}\right)$$
$$-\frac{1}{Ca}\left(\beta_1\frac{\mathrm{d}\Gamma_1^0}{\mathrm{d}x}\frac{\mathrm{d}h_1^0}{\mathrm{d}x}+\frac{\sigma_{s,2}}{\sigma_{s,1}}\frac{\Gamma_{in,1}}{\Gamma_{in,2}}\beta_2\frac{\mathrm{d}\Gamma_2^0}{\mathrm{d}x}\frac{\mathrm{d}h_2^0}{\mathrm{d}x}\right). \tag{3.2.74}$$

From (3.2.71), we obtain

$$u^0H_j^0=\text{constant},$$

and using the initial conditions (3.2.70), we have the solution

$$u^0H_j^0=q_j. \tag{3.2.75}$$

From (3.2.72), we obtain

$$u^0\Gamma_j^0=\text{constant},$$

and using the initial conditions (3.2.70), we have the solution

$$u^0\Gamma_j^0=\frac{\Gamma_{in,j}}{\Gamma_{in,1}}. \tag{3.2.76}$$

From the non-dimensionalisation we have that $q_1+q_2\equiv 1$, resulting in the solution for H_j^0

$$H_1^0=\frac{q_1}{u^0},\quad H_2^0=\frac{1-q_1}{u^0}, \tag{3.2.77}$$

and by differentiating the solution (3.2.76), we note that

$$\frac{\mathrm{d}\Gamma_j^0}{\mathrm{d}x}=-\frac{1}{u^{0^2}}\frac{\Gamma_{in,j}}{\Gamma_{in,1}}\frac{\mathrm{d}u^0}{\mathrm{d}x}. \tag{3.2.78}$$

Substituting in our solutions from (3.2.75), (3.2.76) and (3.2.78) into (3.2.73), we have

$$\left(\mathcal{R}\left(q_1+\frac{\rho_2}{\rho_1}\left(1-q_1\right)\right)-\frac{1}{Ca}\frac{1}{u^{0^2}}\left(\beta_1+\frac{\sigma_{s,2}}{\sigma_{s,1}}\beta_2\right)\right)\frac{\mathrm{d}u^0}{\mathrm{d}x}-\frac{\mathcal{R}}{Fr^2}\frac{1}{u^0}\left(q_1+\frac{\rho_2}{\rho_1}\left(1-q_1\right)\right)=0. \tag{3.2.79}$$

Likewise substituting in (3.2.75), (3.2.76) and (3.2.78) into (3.2.74), as well as performing the differentiation on the left hand side, we see

$$\begin{aligned}\mathcal{R}\left(q_1+\frac{\rho_2}{\rho_1}\left(1-q_1\right)\right)&\left(\frac{\mathrm{d}u^0}{\mathrm{d}x}\frac{\mathrm{d}\overline{y}^0}{\mathrm{d}x}+u^0\frac{\mathrm{d}^2\overline{y}^0}{\mathrm{d}x^2}\right)\\&=\frac{1}{Ca}\left(\left(1-\beta_1\frac{1}{u^0}\right)\frac{\mathrm{d}^2h_1^0}{\mathrm{d}x^2}+\frac{\sigma_I}{\sigma_{s,1}}\frac{\mathrm{d}^2\eta^0}{\mathrm{d}x^2}+\frac{\sigma_{s,2}}{\sigma_{s,1}}\left(1-\beta_2\frac{1}{u^0}\right)\frac{\mathrm{d}^2h_2^0}{\mathrm{d}x^2}\right)\\&\quad+\frac{1}{Ca}\frac{1}{u^{0^2}}\frac{\mathrm{d}u^0}{\mathrm{d}x}\left(\beta_1\frac{\mathrm{d}h_1^0}{\mathrm{d}x}+\frac{\sigma_{s,2}}{\sigma_{s,1}}\beta_2\frac{\mathrm{d}h_2^0}{\mathrm{d}x}\right).\end{aligned} \tag{3.2.80}$$

The relation between the two layer thicknesses, H_1 and H_2, and the three interfaces h_1, h_2 and η is given by $h_j=\eta+(-1)^jH_j$, as we have previously seen. Using this relation, (3.2.67) and (3.2.75) we have that

$$h_j^0=\overline{y}^0-\frac{\frac{\rho_2}{\rho_1}\left(1-q_1\right)^2-q_1^2}{2u^0\left(q_1+\frac{\rho_2}{\rho_1}\left(1-q_1\right)\right)}+\frac{1}{u^0}\left(\frac{1}{2}\left(1+(-1)^j\right)-q_1\right),$$

which can be differentiated to obtain expressions for $\mathrm{d}h_j^0/\mathrm{d}x$ and $\mathrm{d}^2h_j^0/\mathrm{d}x^2$ in terms of $\overline{y}^0$ and u^0 as the only unknown variables

$$\frac{\mathrm{d}h_j^0}{\mathrm{d}x}=\frac{\mathrm{d}\overline{y}^0}{\mathrm{d}x}-\frac{1}{u^{0^2}}\frac{\mathrm{d}u^0}{\mathrm{d}x}\left(\frac{q_1^2-\frac{\rho_2}{\rho_1}\left(1-q_1\right)^2}{2\left(q_1+\frac{\rho_2}{\rho_1}\left(1-q_1\right)\right)}+\frac{1}{2}\left(1+(-1)^j\right)-q_1\right),$$

$$\frac{\mathrm{d}^2h_j^0}{\mathrm{d}x^2}=\frac{\mathrm{d}^2\overline{y}^0}{\mathrm{d}x^2}+\frac{1}{u^{0^2}}\left(\frac{2}{u^0}\left(\frac{\mathrm{d}u^0}{\mathrm{d}x}\right)^2-\frac{\mathrm{d}^2u^0}{\mathrm{d}x^2}\right)\left(\frac{q_1^2-\frac{\rho_2}{\rho_1}\left(1-q_1\right)^2}{2\left(q_1+\frac{\rho_2}{\rho_1}\left(1-q_1\right)\right)}+\frac{1}{2}\left(1+(-1)^j\right)-q_1\right). \tag{3.2.81}$$

Similarly, (3.2.67) gives us an expression for $\mathrm{d}^2\eta^0/\mathrm{d}x^2$ in terms of $\overline{y}^0$ and u^0

$$\frac{\mathrm{d}^2\eta^0}{\mathrm{d}x^2} = \frac{\mathrm{d}^2\overline{y}^0}{\mathrm{d}x^2} + \frac{1}{u^{0^2}}\left(\frac{2}{u^0}\left(\frac{\mathrm{d}u^0}{\mathrm{d}x}\right)^2 - \frac{\mathrm{d}^2u^0}{\mathrm{d}x^2}\right)\left(\frac{q_1^2 - \frac{\rho_2}{\rho_1}(1-q_1)^2}{2\left(q_1 + \frac{\rho_2}{\rho_1}(1-q_1)\right)}\right). \tag{3.2.82}$$

From these, (3.2.80) becomes

$$\begin{aligned}
&\left(\mathcal{R}u^0\Big(q_1 + \frac{\rho_2}{\rho_1}(1-q_1)\Big) - \frac{1}{Ca}\left(\Big(1-\beta_1\frac{1}{u^0}\Big) + \frac{\sigma_I}{\sigma_{s,1}} + \frac{\sigma_{s,2}}{\sigma_{s,1}}\Big(1-\beta_2\frac{1}{u^0}\Big)\right)\right)\frac{\mathrm{d}^2\overline{y}^0}{\mathrm{d}x^2} \\
&+\frac{\mathrm{d}u^0}{\mathrm{d}x}\left(\mathcal{R}\Big(q_1 + \frac{\rho_2}{\rho_1}(1-q_1)\Big) - \frac{1}{Ca}\frac{1}{u^{0^2}}\Big(\beta_1 + \frac{\sigma_{s,2}}{\sigma_{s,1}}\beta_2\Big)\right)\frac{\mathrm{d}\overline{y}^0}{\mathrm{d}x} \\
&+\frac{1}{Ca}\frac{1}{u^{0^2}}\left(\frac{\mathrm{d}^2u^0}{\mathrm{d}x^2} - \frac{2}{u^0}\left(\frac{\mathrm{d}u}{\mathrm{d}x}\right)^2\right)\left(\Big(1-\beta_1\frac{1}{u^0}\Big)\Big(\frac{q_1^2 - \frac{\rho_2}{\rho_1}(1-q_1)^2}{2\big(q_1 + \frac{\rho_2}{\rho_1}(1-q_1)\big)} - q_1\Big)\right. \\
&\qquad\left. + \frac{\sigma_I}{\sigma_{s,1}}\Big(\frac{q_1^2 - \frac{\rho_2}{\rho_1}(1-q_1)^2}{2\big(q_1 + \frac{\rho_2}{\rho_1}(1-q_1)\big)}\Big) + \frac{\sigma_{s,2}}{\sigma_{s,1}}\Big(1-\beta_2\frac{1}{u^0}\Big)\Big(\frac{q_1^2 - \frac{\rho_2}{\rho_1}(1-q_1)^2}{2\big(q_1 + \frac{\rho_2}{\rho_1}(1-q_1)\big)} + 1 - q_1\Big)\right) \\
&+\frac{1}{Ca}\frac{1}{u^{0^4}}\left(\frac{\mathrm{d}u^0}{\mathrm{d}x}\right)^2\left(\beta_1\Big(\frac{q_1^2 - \frac{\rho_2}{\rho_1}(1-q_1)^2}{2\big(q_1 + \frac{\rho_2}{\rho_1}(1-q_1)\big)} - q_1\Big) + \frac{\sigma_{s,2}}{\sigma_{s,1}}\beta_2\Big(\frac{q_1^2 - \frac{\rho_2}{\rho_1}(1-q_1)^2}{2\big(q_1 + \frac{\rho_2}{\rho_1}(1-q_1)\big)} + 1 - q_1\Big)\right) = 0.
\end{aligned} \tag{3.2.83}$$

To simplify equation (3.2.79) we multiply through by

$$\frac{1}{\mathcal{R}\left(q_1 + \frac{\rho_2}{\rho_1}(1-q_1)\right)},$$

and let

$$\Theta = \frac{1 + \frac{\sigma_I}{\sigma_{s,1}} + \frac{\sigma_{s,2}}{\sigma_{s,1}}}{\mathcal{R}Ca\left(q_1 + \frac{\rho_2}{\rho_1}(1-q_1)\right)},$$

$$\Lambda = \frac{\beta_1 + \frac{\sigma_{s,2}}{\sigma_{s,1}}\beta_2}{\mathcal{R}Ca\left(q_1 + \frac{\rho_2}{\rho_1}(1-q_1)\right)},$$

$$\Phi = \frac{2\left(\left(\beta_1 + \frac{\sigma_{s,2}}{\sigma_{s,1}}\beta_2\right)\left(\frac{q_1^2 - \frac{\rho_2}{\rho_1}(1-q_1)^2}{2\left(q_1 + \frac{\rho_2}{\rho_1}(1-q_1)\right)}\right) - q_1\beta_1 + \frac{\sigma_{s,2}}{\sigma_{s,1}}(1-q_1)\beta_2\right)}{Fr^4\mathcal{R}Ca\left(q_1 + \frac{\rho_2}{\rho_1}(1-q_1)\right)},$$

$$\Psi = \frac{\left(1 + \frac{\sigma_I}{\sigma_{s,1}} + \frac{\sigma_{s,2}}{\sigma_{s,1}}\right)\left(\frac{q_1^2 - \frac{\rho_2}{\rho_1}(1-q_1)^2}{2\left(q_1 + \frac{\rho_2}{\rho_1}(1-q_1)\right)}\right) - q_1 + \frac{\sigma_{s,2}}{\sigma_{s,1}}(1-q_1)}{Fr^4\mathcal{R}Ca\left(q_1 + \frac{\rho_2}{\rho_1}(1-q_1)\right)},$$

so that equation (3.2.79) becomes

$$\left(1 - \frac{\Lambda}{u^{0^2}}\right)\frac{\mathrm{d}u^0}{\mathrm{d}x} - \frac{1}{u^0 Fr^2} = 0. \tag{3.2.84}$$

Solving the first order ordinary differential equation (3.2.84) via the separation of variables, the following transcendental equation in u^0 is found

$$\frac{1}{2}u^{0^2} - \Lambda \log u^0 = \frac{x}{Fr^2} + \frac{1}{2}. \tag{3.2.85}$$

By differentiating (3.2.84) an expression for $\mathrm{d}^2u^0/\mathrm{d}x^2$ is obtained

$$\begin{aligned}\frac{\mathrm{d}^2u^0}{\mathrm{d}x^2} &= -\frac{\mathrm{d}u^0}{\mathrm{d}x}\left(\frac{u^{0^2} + \Lambda}{Fr^2\left(u^{0^2} - \Lambda\right)^2}\right) \\ &= -\frac{u^0\left(u^{0^2} + \Lambda\right)}{Fr^4\left(u^{0^2} - \Lambda\right)^3},\end{aligned}$$

which can be substituted into (3.2.83). Multiplying (3.2.83) through by

$$\frac{u^0}{\mathcal{R}\left(q_1 + \frac{\rho_2}{\rho_1}(1-q_1)\right)},$$

and simplifying, we obtain

$$\left(u^{0^2} - \Theta u + \Lambda\right)\frac{\mathrm{d}^2\overline{y}^0}{\mathrm{d}x^2} + \frac{1}{Fr^2}\frac{\mathrm{d}\overline{y}^0}{\mathrm{d}x} = \frac{3\Psi u^{0^3} - 2\Phi u^{0^2} - \Lambda\Psi u^0 + \Lambda\Phi}{u^0\left(u^{0^2} - \Lambda\right)^3}. \tag{3.2.86}$$

This is a first order linear ODE for $\mathrm{d}\overline{y}^0/\mathrm{d}x$, which is solved using the integrating factor method to find

$$\begin{aligned}\overline{y}^0 =& \frac{Fr^4}{2\Lambda^2}\left(\frac{c_3}{c_2}\tan^{-1}\left(\frac{u^0 - \frac{1}{2}\Theta}{c_2}\right) + (\Theta\Phi - 2\Lambda\Psi)\log\left(\frac{u^0}{\sqrt{u^{0^2} - \Theta u^0 + \Lambda}}\right)\right.\\ &\left. - \frac{\Lambda\Phi}{u^0} + c_1\Lambda^2 u^0 + \frac{1}{2}c_1\Theta\Lambda^2\log\left(u^{0^2} - \Theta u^0 + \Lambda\right) + c_4\right),\end{aligned} \tag{3.2.87}$$

where

$$\begin{aligned}c_1 &= \frac{2\Psi - \Phi}{1-\Lambda},\\ c_2 &= \sqrt{\Lambda - \frac{1}{4}\Theta^2},\\ c_3 &= \frac{1}{2}\Theta^2\Phi - \Theta\Lambda\Psi - \Lambda\Phi + c_1\Lambda^2\left(\frac{1}{2}\Theta^2 - 2\Lambda\right),\\ c_4 &= -\frac{c_3}{c_2}\tan^{-1}\left(\frac{1-\frac{1}{2}\Theta}{c_2}\right) + (2\Lambda\Psi - \Theta\Phi)\log\left(\frac{1}{\sqrt{1-\Theta+\Lambda}}\right) + \Lambda\Phi\\ &\quad - c_1\Lambda^2 - \frac{1}{2}c_1\Theta\Lambda^2\log\left(1-\Theta+\Lambda\right),\end{aligned}$$

are constants.

To summarise, we have solutions for Γ_j^0, H_j^0 and $\overline{y}^0$ given by (3.2.76), (3.2.77) and (3.2.87), and equation (3.2.85) to solve numerically to find u^0. This is done via Newton's

method and enables the plotting of example steady state profiles, for a range of different parameter values. It is again noted here that in the limiting case of no surfactant being present in either fluid layer the model of Dyson *et al.* [41] is recovered (see Appendix A).

3.2.4 Steady state plots

Figure 3.2 depicts examples of non-dimensional steady state curtains. The dashed lines represent the curtain without surfactant (in either layer), whilst the solid lines denote the surfactant laden curtain. We use typical values in the coating industry from [41] of $U = 2/3$ ms^{-1}, $\rho_1 = 1000$ kgm^{-3}, $\mu_1 = 0.1$ kgm^{-1}s^{-1}, $l = 0.1$ m, $h_0 = 10^{-4}$ m and $\sigma_{s,1} = 0.02$ Nm^{-1} to obtain the dimensionless parameters $\mathcal{R} = 0.6667$, $Ca = 3.3333$, $Fr = 0.6731$ in (a) and (b); whilst using a figure of $\sigma_{s,1} = 0.01$ Nm^{-1} to obtain the dimensionless parameters $\mathcal{R} = 0.6667$, $Ca = 6.6667$, $Fr = 0.6731$ in (c). The caption gives a full description of the parameters used.

In (a), all of the parameters in both layers are the same for the surfactant-free curtain, resulting in a perfectly vertical sheet. In the surfactant-case, with the surfactant being more effective in the first layer ($\beta_1 = 0.3$ compared to $\beta_2 = 0.1$) the surface tension of the free surface $y = h_1^0$ is reduced further than the surface tension of $y = h_2^0$. Consequently, the larger surface tension of h_2^0 'pulls' the curtain to the right, due to the Marangoni flow consequent from the difference in surface tension. It is noted here that η^0 coincides with $\overline{y}^0$ for the length of the curtain.

In (b), the flow rate of the first layer is significantly larger than than the flow rate in the second layer. By setting β_2 larger than β_1, the direction of the deflection of the curtain switches, with the higher surface tension on the free surface $y = h_1^0$ pulling the curtain to the left.

In (c), the constant surface tension of $\sigma_{s,1}$ has been set as twice the value of $\sigma_{s,2}$, resulting in a large pull to the left in the surfactant free case. In the surfactant case, we have

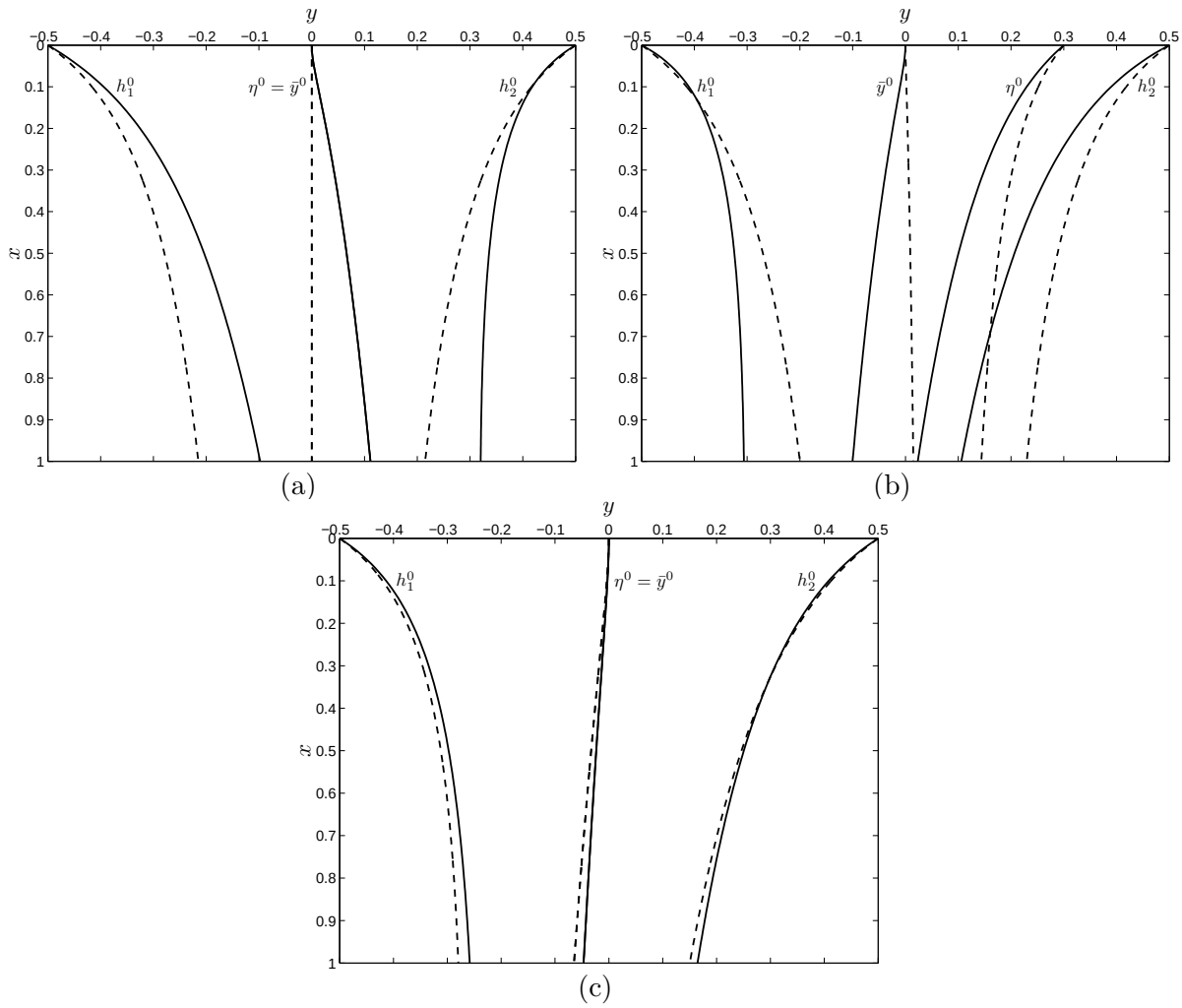

Figure 3.2: Steady state curtain profiles; the dashed curtains correspond to the case where no surfactant is present in either layer. The solid lines represent the curtain containing surfactant (in both layers).
The non-dimensional parameters are given by:
(a) $\rho_2/\rho_1 = 1$, $q_1 = 0.5$, $\sigma_{s,2}/\sigma_{s,1} = 1$, $\sigma_I/\sigma_{s,1} = 0.05$, $\beta_1 = 0.3$, $\beta_2 = 0.1$;
(b) $\rho_2/\rho_1 = 1$, $q_1 = 0.8$, $\sigma_{s,2}/\sigma_{s,1} = 1$, $\sigma_I/\sigma_{s,1} = 0.05$, $\beta_1 = 0.2$, $\beta_2 = 0.4$;
(c) $\rho_2/\rho_1 = 1$, $q_1 = 0.5$, $\sigma_{s,2}/\sigma_{s,1} = 0.5$, $\sigma_I/\sigma_{s,1} = 0.01$, $\beta_1 = \beta_2 = 0.3$.

that $\beta_1 = \beta_2$, and the curtain gets deflected to the right, compared with the surfactant-free case. The addition of surfactant to both layers with the same "effectiveness" results in the surface tension of fluid 1 not being as dominant over the surface tension of fluid 2 (though remains larger), and thus the pull to the left is not as distinctive. It is noted here that η^0 coincides with $\overline{y}^0$ for the length of the curtain.

In Figure 3.3, a more quantitative assessment of the bending effect is analysed, by plotting the change in curtain centreline of the surfactant-laden case from the surfactant-free case, $\overline{y}^0(1) - \overline{y}_s^0(1)$, against the varying parameters. Each subfigure (a)-(c) corresponds to the same parameter values as in Figure 3.2, except for the values of β_1, which are varied through 0.1, 0.2, 0.3 and 0.4 (as stated in the legend), as well as the parameter varied along the x-axis. The scale of the y-axis has been fixed in (a)-(c) to obtain a comparative viewpoint in how the parameters effect the curtain deflection. The horizontal line $\overline{y}^0(1) - \overline{y}_s^0(1) = 0$ is included in each subfigure to denote the position of no change; data above this line corresponds to the centreline being shifted to the right, whilst data below corresponds to a shift to the left. We highlight here that this shift is in comparison to the surfactant-free case, so, for example, data below the line below the line $\overline{y}^0(1) - \overline{y}_s^0(1) = 0$ might still correspond to the curtain being deflected to the right, but not to the extent as the case without surfactant.

In (a), we vary β_2 from 0.05 to 0.4. The dependence on the parameter β_2 is linear, with a negative gradient since an increase in β_2 results in the surface tension of the free surface $y = h_2^0$ being lowered, and hence a deflection in the curtain to the left. As expected, the change in the position of $\overline{y}^0(1)$ compared to $\overline{y}_s^0(1)$ is zero when $\beta_1 = \beta_2$ due to an equal surface tension along both free surfaces.

The variance of the flow rate is analysed in (b), with q_1 ranging between 0.1-0.9. It is clear to see that changing the flow rate has little impact on the difference $\overline{y}^0(1) - \overline{y}_s^0(1)$, with each case being near horizontal. Since $\beta_2 = 0.4$ in each instance, we see a shift in

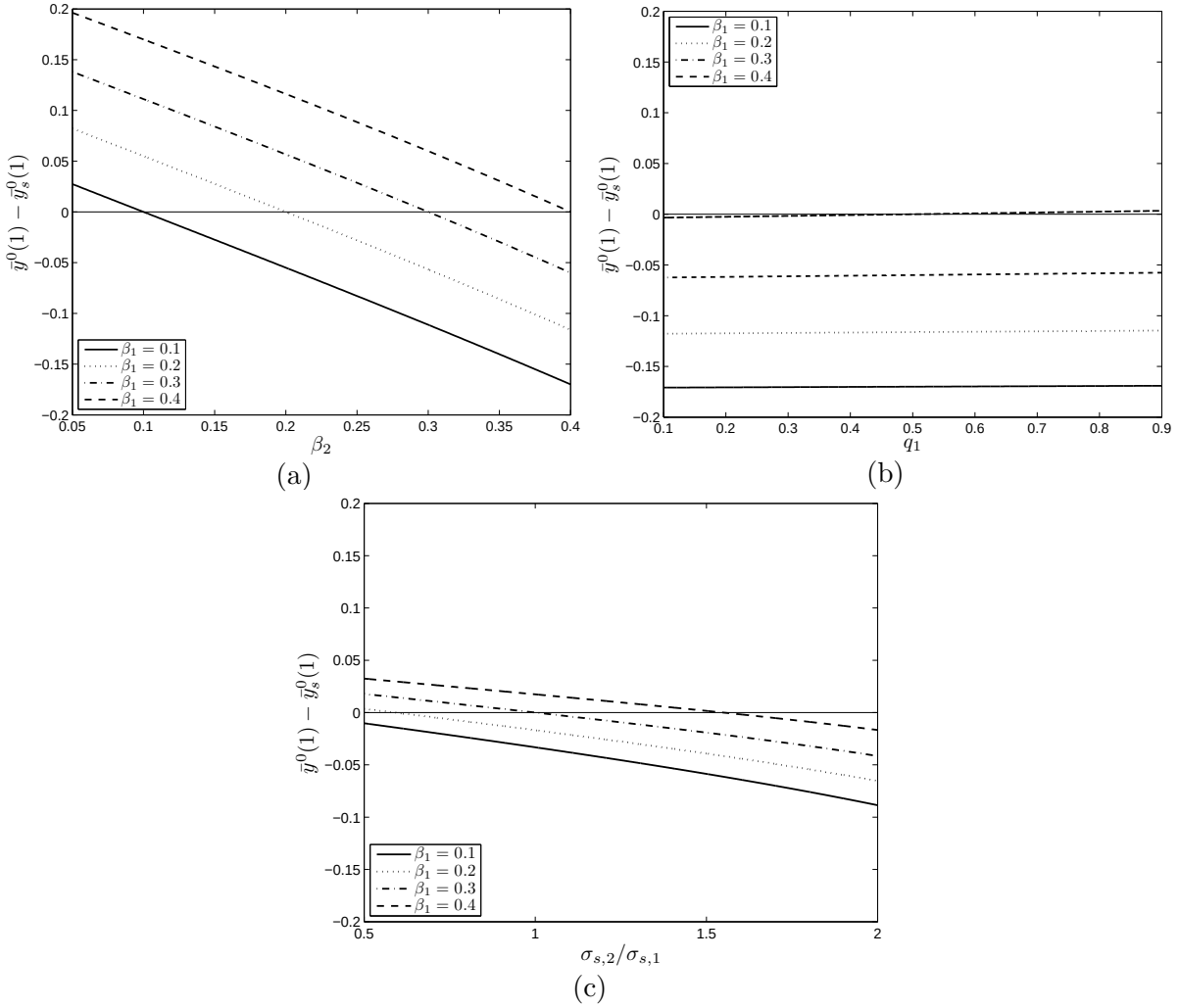

Figure 3.3: Plots showing the bending effect that surfactants have in the steady state curtain profiles. The bending is measured by taking the change in the centreline of the curtain, $\overline{y}^0$, to the surfactant-free case, $\overline{y}_s^0$, at $x = 1$, i.e. by calculating $\overline{y}^0(1) - \overline{y}_s^0(1)$. Each subfigure (a)-(c) corresponds to the same parameter values as in Figure 3.2, except for those stated on the x-axis and in the legend. The horizontal line $\overline{y}^0(1) - \overline{y}_s^0(1) = 0$ is added to each plot to signify the location of no change.

the curtain to the left in each of the cases $\beta_1 = 0.1 - 0.3$ with the higher surface tension of $y = h_1^0$. The case $\beta_1 = \beta_2 = 0.4$ shows minimal change in the curtain deflection and highlights the slight deviation from horizontal, which is evident in each case, around the horizontal line $\overline{y}^0(1) - \overline{y}_s^0(1) = 0$. When $q_1 = 0.5$, there is no change in the curtain deflection, but when q_1 is less than 0.5 there is a slight deflection to the left. This is reversed when q_1 is greater than 0.5, and demonstrates the extremely small effect the interfacial tension σ_I has on the curtain deflection; with the reduced surface tension of the free surfaces with surfactant, the value of σ_I has a larger value in proportion, and thus has a greater influence on the transverse Marangoni flow.

The dependence on the ratio $\sigma_{s,2}/\sigma_{s,1}$ is investigated in (c), where β_2 is fixed at a value of 0.3. When $\sigma_{s,2} = \sigma_{s,1}$ we have a vertical curtain in the surfactant-less case and thus we see, as expected, a deflection to the left when $\beta_1 = 0.1$ and 0.2, no deflection when $\beta_1 = 0.3$ and a deflection to the right when $\beta_1 = 0.4$ due to the corresponding changes in surface tension. As $\sigma_{s,2}$ becomes greater than $\sigma_{s,1}$, there will be a deflection in the curtain to the right, without surfactant. Adding surfactant into both layers decreases both σ_1 and σ_2 so that the higher surface tension of $y = h_2^0$ is not as dominant, resulting in a shift to the left. This is emphasised when $\beta_1 = 0.1$ (when the 'effectiveness' of surfactant in layer 2 is greater, and thus the surface tension reduced more), and interestingly even occurs when $\beta_1 = 0.4 > \beta_2$; although the curtain will still deflect to the right there is a shift to the left in comparison to the surfactant-free case.

The transverse pull of the curtain profiled in this section has been recently been demonstrated experimentally. This is documented in Appendix C.

3.3 Stability

3.3.1 Multiple scales analysis

Having obtained the steady state equations and seen examples of the steady state curtain profiles in the previous section, in this section we consider perturbations to this steady state, investigating the asymptotic stability of a two-layer curtain containing surfactants. A multiple scales approach is adopted, since disturbances along the curtain will be smaller in magnitude in comparison to the curtain length, of which $x = O(1)$. Hence, we set $\overline{x} = x/\varepsilon$ and $\overline{t} = t/\varepsilon$, and consider wave modes of the form $\exp\left(\mathrm{i}k\overline{x} + s\overline{t}\right)$, where k is the wavenumber of the disturbance and s is the complex frequency. This formulates a multiple scales problem, where $\overline{x}$ corresponds to a short length-scale associated with waves of the order of the curtain thickness, and $\overline{t}$ a short timescale associated with short wave-like disturbances of $O(\varepsilon)$. For previous examples of a multiple-scales approach in free surface stability problems see, for example, Mohsin *et al.* [86] and Wallwork *et al.* [114].

The steady state solutions found in the previous section are then disturbed slightly, by adding a small perturbation term as follows

$$\{H_j, \Gamma_j, u, \overline{y}\}(x,t) = \left\{H_j^0, \Gamma_j^0, u^0, \overline{y}^0\right\}(x) + \delta\left\{\widehat{H}_j, \widehat{\Gamma}_j, \widehat{u}, \widehat{\overline{y}}\right\} e^{\mathrm{i}k\overline{x}+s\overline{t}}, \tag{3.3.1}$$

where $0 < \delta < \varepsilon \ll 1$, with δ being a constant giving the amplitude of the wave.

We return to the leading order equations previously obtained

$$\frac{\partial H_j}{\partial t} + \frac{\partial}{\partial x}(uH_j) = 0, \tag{3.3.2}$$

$$\frac{\partial \Gamma_j}{\partial t} + \frac{\partial}{\partial x}(u\Gamma_j) = 0, \tag{3.3.3}$$

$$\mathcal{R}\left(\frac{\partial u}{\partial t}+u\frac{\partial u}{\partial x}\right)\left(H_1+\frac{\rho_2}{\rho_1}H_2\right)=\frac{\mathcal{R}}{Fr^2}\left(H_1+\frac{\rho_2}{\rho_1}H_2\right)-\frac{1}{Ca}\left(\beta_1\frac{\partial \Gamma_1}{\partial x}+\frac{\sigma_{s,2}}{\sigma_{s,1}}\frac{\Gamma_{in,1}}{\Gamma_{in,2}}\beta_2\frac{\partial \Gamma_2}{\partial x}\right), \tag{3.3.4}$$

$$\mathcal{R}\left(H_1+\frac{\rho_2}{\rho_1}H_2\right)\frac{D^2\overline{y}}{Dt^2}=\frac{1}{Ca}\left(\left(1-\beta_1\Gamma_1\right)\frac{\partial^2 h_1}{\partial x^2}+\frac{\sigma_I}{\sigma_{s,1}}\frac{\partial^2\eta}{\partial x^2}+\frac{\sigma_{s,2}}{\sigma_{s,1}}\left(1-\frac{\Gamma_{in,1}}{\Gamma_{in,2}}\beta_2\Gamma_2\right)\frac{\partial^2 h_2}{\partial x^2}\right)$$
$$-\frac{1}{Ca}\left(\beta_1\frac{\partial \Gamma_1}{\partial x}\frac{\partial h_1}{\partial x}+\frac{\sigma_{s,2}}{\sigma_{s,1}}\frac{\Gamma_{in,1}}{\Gamma_{in,2}}\beta_2\frac{\partial \Gamma_2}{\partial x}\frac{\partial h_2}{\partial x}\right), \tag{3.3.5}$$

that is, six equations in the six unknown variables $H_j(x,t)$, $\Gamma_j(x,t)$, $u(x,t)$, $\overline{y}(x,t)$. Substituting the perturbed solution (3.3.1) into (3.3.2)-(3.3.5), the steady state equations are recovered at leading order, with the equations at the next order giving us the disturbance equations.

From (3.3.2), we obtain the disturbance equation

$$\left(s+u^0\mathrm{i}k\right)\widehat{H}_j+H_j^0\mathrm{i}k\widehat{u}=0, \tag{3.3.6}$$

from (3.3.3)

$$\left(s+u^0\mathrm{i}k\right)\widehat{\Gamma}_j+\Gamma_j^0\mathrm{i}k\widehat{u}=0, \tag{3.3.7}$$

from (3.3.4)

$$\mathcal{R}\left(H_1^0+\frac{\rho_2}{\rho_1}H_2^0\right)\left(s+u^0\mathrm{i}k\right)\widehat{u}+\frac{\beta_1}{Ca}\mathrm{i}k\widehat{\Gamma_1}+\frac{\sigma_{s,2}}{\sigma_{s,1}}\frac{\Gamma_{in,1}}{\Gamma_{in,2}}\frac{\beta_2}{Ca}\mathrm{i}k\widehat{\Gamma_2}=0. \tag{3.3.8}$$

Before substituting the perturbed solution into (3.3.5), it is noted that

$$\frac{\mathrm{D}^2\overline{y}}{\mathrm{D}t^2}=\frac{\partial^2\overline{y}}{\partial t^2}+\frac{\partial u}{\partial t}\frac{\partial\overline{y}}{\partial x}+2u\frac{\partial^2\overline{y}}{\partial x\partial t}+u\frac{\partial u}{\partial x}\frac{\partial\overline{y}}{\partial x}+u^2\frac{\partial^2\overline{y}}{\partial x^2},$$

and since $\eta = h_j + (-1)^{j+1} H_j$, we have that

$$\frac{\partial^2 \eta}{\partial x^2} = \frac{\partial^2 h_j}{\partial x^2} + (-1)^{j+1} \frac{\partial^2 H_j}{\partial x^2}.$$

We then obtain the disturbance equation from (3.3.5)

$$\begin{aligned}
&\frac{1}{Ca} k^2 \Bigg(- \frac{H_1^{0^2} + 2\frac{\rho_2}{\rho_1} H_1^0 H_2^0 + \frac{\rho_2}{\rho_1} H_2^{0^2}}{2\left(H_1^0 + \frac{\rho_2}{\rho_1} H_2^0\right)^2} \left(1 + \frac{\sigma_I}{\sigma_{s,1}} + \frac{\sigma_{s,2}}{\sigma_{s,1}} - \beta_1 \Gamma_1^0 - \frac{\sigma_{s,2}}{\sigma_{s,1}} \frac{\Gamma_{in,1}}{\Gamma_{in,2}} \beta_2 \Gamma_2^0\right) \\
&\qquad + 1 - \beta_1 \Gamma_1^0 \Bigg) \widehat{H}_1 \\
&+ \frac{1}{Ca} k^2 \Bigg(\frac{\frac{\rho_2}{\rho_1}\left(H_1^{0^2} + 2 H_1^0 H_2^0 + \frac{\rho_2}{\rho_1} H_2^{0^2}\right)}{2\left(H_1^0 + \frac{\rho_2}{\rho_1} H_2^0\right)^2} \left(1 + \frac{\sigma_I}{\sigma_{s,1}} + \frac{\sigma_{s,2}}{\sigma_{s,1}} - \beta_1 \Gamma_1^0 - \frac{\sigma_{s,2}}{\sigma_{s,1}} \frac{\Gamma_{in,1}}{\Gamma_{in,2}} \beta_2 \Gamma_2^0\right) \\
&\qquad - \frac{\sigma_{s,2}}{\sigma_{s,1}} \left(1 - \frac{\Gamma_{in,1}}{\Gamma_{in,2}} \beta_2 \Gamma_2^0\right) \Bigg) \widehat{H}_2 \\
&+ \Bigg(\frac{1}{Ca} k^2 \left(\beta_1 \Gamma_1^0 + \frac{\sigma_{s,2}}{\sigma_{s,1}} \frac{\Gamma_{in,1}}{\Gamma_{in,2}} \beta_2 \Gamma_2^0 - \left(1 + \frac{\sigma_I}{\sigma_{s,1}} + \frac{\sigma_{s,2}}{\sigma_{s,1}}\right)\right) \\
&\qquad - \mathcal{R} \left(H_1^0 + \frac{\rho_2}{\rho_1} H_2^0\right) \left(s + u^0 i k\right)^2 \Bigg) \widehat{\overline{y}} = 0. \qquad (3.3.9)
\end{aligned}$$

The disturbance equations, (3.3.6)-(3.3.9), can be written in the matrix form $A\widehat{\mathbf{x}}^T = 0$, where $\widehat{\mathbf{x}} = \left(\widehat{H}_1, \widehat{H}_2, \widehat{\Gamma}_1, \widehat{\Gamma}_2, \widehat{u}, \widehat{\overline{y}}\right)$ and A is the matrix of coefficients. The dispersion relation is then obtained by setting $\det(A) = 0$, and is given by

$$\overline{s}^3 \left(\overline{s}^2 + k^2 \Lambda\right) \left(\overline{s}^2 + k^2 u^0 \Theta - k^2 \Lambda\right) = 0. \qquad (3.3.10)$$

It is noted that if the same analysis was carried out in the surfactant-free case, then the same dispersion relation (3.3.10) would be found with $\Lambda = 0$. In deriving this dispersion relation, we have utilised (3.2.75) and (3.2.76), and made the transformation $\overline{s} = s + u^0 \mathrm{i} k$. This transformation alters the wave mode form to $\exp\left[\mathrm{i}k\left(\overline{x} - u^0 \overline{t}\right) + \overline{s}\overline{t}\right]$, moving us into

a frame of reference where we travel with the steady state curtain speed u^0 in the positive $\overline{x}$ direction (direction the curtain is travelling). We let $\overline{s}$ be complex, restricting k to be real, so that $\overline{s} = \overline{s}_r + \mathrm{i}k\overline{s}_i$ where $\overline{s}_r$ and $\overline{s}_i$ are real. The wave mode is then given by $\exp\left[\mathrm{i}k\left(\overline{x} - (u^0 - \overline{s}_i)\,\overline{t}\right) + \overline{s}_r\overline{t}\right]$, a wave travelling in the positive $\overline{x}$ direction with speed $u^0 - \overline{s}_i$. Thus, if $u^0 - \overline{s}_i > 0$ the disturbance will be swept away with the flow of the curtain. However if $u^0 - \overline{s}_i < 0$, the disturbance will propagate upstream where stability may be affected. The growth of the disturbance will depend on the sign of the $\overline{s}_r$ term.

The solutions to (3.3.10) are given by

$$\overline{s} = 0, \tag{3.3.11}$$

$$\overline{s} = \pm\mathrm{i}k\sqrt{\Lambda} = \mathrm{i}k\Omega_1, \tag{3.3.12}$$

$$\overline{s} = \pm k\sqrt{\Lambda - u^0\Theta} = \mathrm{i}k\Omega_2. \tag{3.3.13}$$

The inclusion of surfactant introduces the additional eigenmodes $\widehat{\Gamma}_j$, and thus additional solutions to the dispersion relation are found (and modify already existing eigenvalues). The solution (3.3.12) is the additional eigenvalue; surface waves that correspond to Marangoni waves. Solution (3.3.13) corresponds to the already existing eigenvalue that is modified with the inclusion of surfactant.

When $\overline{s} = 0$, as in (3.3.11), the disturbance is neutral and gets swept away with the flow of curtain since the wave mode becomes of the form $\exp\left[\mathrm{i}k\left(\overline{x} - u^0 t\right)\right]$. From the definition of Λ, we have that $\Lambda \geqslant 0$, and thus $\Omega_1 = \pm\sqrt{\Lambda}$ is real. Moreover, $u^0\Theta - \Lambda > 0$, and so $\Omega_2 = \pm\sqrt{u^0\Theta - \Lambda}$ is real. To see this, we have previously shown that $0 \leqslant \beta_j < 1$, and note that $u^0 \geqslant 1$, from the boundary condition $u^0(x = 0) = 1$.

From this,

$$0 \leqslant \beta_1 + \beta_2\frac{\sigma_{s,2}}{\sigma_{s,1}} < 1 + \frac{\sigma_{s,2}}{\sigma_{s,1}}$$

and $u^0\left(1+\sigma_I/\sigma_{s,1}+\sigma_{s,2}/\sigma_{s,1}\right)>1$, with

$$\min\left[u^0\left(1+\frac{\sigma_I}{\sigma_{s,1}}+\frac{\sigma_{s,2}}{\sigma_{s,1}}\right)\right]=1+\frac{\sigma_I}{\sigma_{s,1}}+\frac{\sigma_{s,2}}{\sigma_{s,1}}.$$

Therefore

$$\begin{aligned}\min\left[u^0\left(1+\frac{\sigma_I}{\sigma_{s,1}}+\frac{\sigma_{s,2}}{\sigma_{s,1}}\right)-\left(\beta_1+\beta_2\frac{\sigma_{s,2}}{\sigma_{s,1}}\right)\right]&=1+\frac{\sigma_I}{\sigma_{s,1}}+\frac{\sigma_{s,2}}{\sigma_{s,1}}-\left(1+\frac{\sigma_{s,2}}{\sigma_{s,1}}\right)\\&=\frac{\sigma_I}{\sigma_{s,1}}>0.\end{aligned}$$

Hence

$$u^0\Theta-\Lambda=\frac{u^0\left(1+\frac{\sigma_I}{\sigma_{s,1}}+\frac{\sigma_{s,2}}{\sigma_{s,1}}\right)-\left(\beta_1+\frac{\sigma_{s,2}}{\sigma_{s,1}}\beta_2\right)}{\mathcal{R}Ca\left(q_1+\frac{\rho_2}{\rho_1}\left(1-q_1\right)\right)}$$

is always positive and thus Ω_2 is real.

3.3.2 Stability criterion

Considering both the Marangoni waves and original waves based on the local surface tension, (3.3.12) and (3.3.13), it is noted that since $\Lambda\geqslant 0$ and $u^0\Theta-\Lambda>0$, $\Omega_1=\pm\sqrt{\Lambda}$ and $\Omega_2=\pm\sqrt{u^0\Theta-\Lambda}$ are both real. Thus (3.3.12) and (3.3.13) are both of the form $\overline{s}=ik\Omega$ where Ω is real. The wave mode becomes of the form $\exp\left[\mathrm{i}k\left(\overline{x}+\left(\Omega-u^0\right)\overline{t}\right)\right]$, a wave travelling at speed $\Omega-u^0$, downstream (ensuring stability) when $\Omega-u^0<0$. Hence, when considering the negative square root from (3.3.12) and (3.3.13), both wave modes are swept downstream and the curtain is always stable. From here we only consider the cases from (3.3.12) and (3.3.13) where $\Omega_1=\sqrt{\Lambda}$ and $\Omega_2=\sqrt{u^0\Theta-\Lambda}$.

From the reasoning above, a sufficient, but not necessary, condition for curtain stability is given by $u^0-\Omega>0$; when this holds disturbances get swept away with the flow of the curtain, not propagating upstream where stability could be disrupted.

The condition $u^0 - \Omega_1 > 0$ obtained from (3.3.12) may be written as

$$\frac{u^{0^2}}{\Lambda} > 1, \tag{3.3.14}$$

and the condition $u^0 - \Omega_2 > 0$ obtained from (3.3.13) may be written as

$$\frac{u^{0^2}}{u^0\Theta - \Lambda} > 1. \tag{3.3.15}$$

To compare our new criterion with (3.1.2), we see that (3.3.14) and (3.3.15) can be written as

$$We_T > \frac{\Lambda}{\Theta u^0}, \tag{3.3.16}$$

and

$$We_T > 1 - \frac{\Lambda}{\Theta u^0}, \tag{3.3.17}$$

where $We_T = u^0/\Theta > 1$ is an equivalent of the stability criterion (3.1.2). The critical Weber number, We_c, above which the curtain is stable, comes from the two criteria (3.3.16) and (3.3.17). The larger value is taken at any given x; meaning the stability criteria can be combined into the one criterion

$$We_T > \left| \frac{\Lambda}{\Theta u^0} - \frac{1}{2} \right| + \frac{1}{2} = We_c. \tag{3.3.18}$$

In the case of no surfactant, $\Lambda = 0$ and thus (3.3.18) collapses back to criterion (3.1.2) (see Appendix A). Our new criterion (3.3.18) depends on u^0, a function of x. This means that the critical Weber number, We_c, above which the curtain is stable, will vary as we travel along the curtain.

In Figure 3.4, we plot examples of We_c against x to see how (3.3.18) compares to the constant surface tension criterion $We_T > 1$. As expected, due to the stabilizing nature of

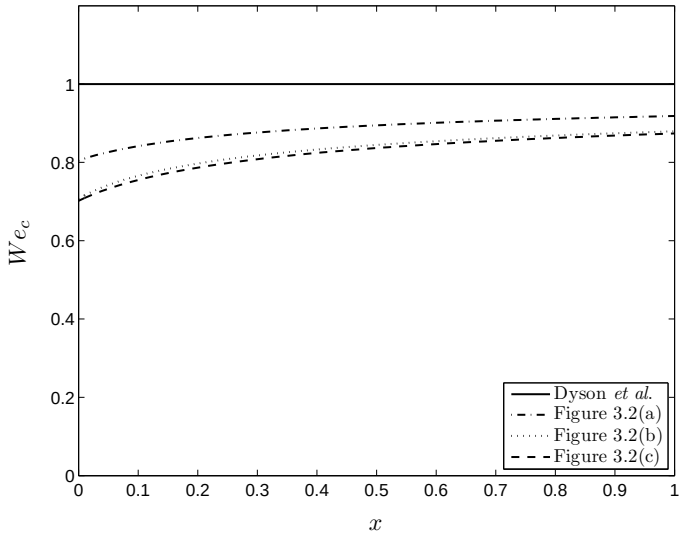

Figure 3.4: Examples of the new Weber number criterion (3.3.18) compare to the $We_T > 1$ criterion of Dyson *et al.* The parameters are the same as in Figure 3.2:
(a) $\rho_2/\rho_1 = 1$, $q_1 = 0.5$, $\sigma_{s,2}/\sigma_{s,1} = 1$, $\sigma_I/\sigma_{s,1} = 0.05$, $\beta_1 = 0.3$, $\beta_2 = 0.1$;
(b) $\rho_2/\rho_1 = 1$, $q_1 = 0.8$, $\sigma_{s,2}/\sigma_{s,1} = 1$, $\sigma_I/\sigma_{s,1} = 0.05$, $\beta_1 = 0.2$, $\beta_2 = 0.4$;
(c) $\rho_2/\rho_1 = 1$, $q_1 = 0.5$, $\sigma_{s,2}/\sigma_{s,1} = 0.5$, $\sigma_I/\sigma_{s,1} = 0.01$, $\beta_1 = \beta_2 = 0.3$.

surfactants, the new critical Weber number in all cases has decreased below unity. The increase in the parameter Λ results in the critical Weber number for Figures 3.2(b) and (c) to be reduced lower than that for Figure 3.2(a); the increase in the effectiveness of the surfactant leads to an increase in stability, as one would expect. Physically, the increase in stability can be explained by the role of the Marangoni flow that surfactant introduces. Since the surfactant concentration is greatest at the top of the curtain, and decreases along the curtain, we have that on both free surfaces the surface tension increases as going down the curtain. This gradient introduces a Marangoni flow which 'pulls' the curtain down, meaning the velocity of the curtain increases. This is confirmed in our numerical study whereby the steady state velocity, u^0, of the curtain increases with the inclusion of surfactant, and that a greater initial value of $\Gamma_{in,j}$ (i.e. a greater value of the parameter β_j) induces a greater steady state velocity u^0. The higher value of this velocity means that when a disturbance does occur, it is more likely to get flushed away with the

flow of the curtain.

Figure 3.5 provides more insight into the behaviour of We_c, by plotting the critical Weber number at $x = 1$ against the varying parameters. Again, each subfigure (a)-(c) corresponds to the same parameter values in Figure 3.2, except for the values of β_1 which vary through 0.1, 0.2, 0.3 and 0.4 (as in the legend) and the parameter being varied on the x-axis.

In (a), the dependence on β_2 is again linear, with a negative gradient; an increase in the parameter β_2 increases the stability of the curtain, with the highest value of $\beta_1 = 0.4$ showing the most stable case. Similar to Figure 3.3(b), the flow rate has no impact on $We_c(x = 1)$, with a horizontal line in each case of β_1 demonstrating no change in the critical Weber number.

In (c), with β_2 fixed at 0.3, we see that the variance of $\sigma_{s,2}/\sigma_{s,1}$ has a small influence on the We_c at $x = 1$. These results suggest that the greater the deflection of the steady state curtain from the surfactant-free case back towards vertical, the more stable the curtain becomes. When $\sigma_{s,2}/\sigma_{s,1} < 1$, the curtain will be deflected to the left in the surfactant-free case by the transverse Marangoni flow. Figure 3.3(c) shows that when $\beta_1 = 0.1$, and $\sigma_{s,2}/\sigma_{s,1} < 1$, there is a slight deflection to the left; the curtain gets pulled even further from vertical and thus we see only a small reduction from 1 in $We_c(x = 1)$. However as the ratio $\sigma_{s,2}/\sigma_{s,1}$ increases above 1, the bending in the surfactant-free case reverses to the right, and Figure 3.3(c) shows, for $\beta_1 = 0.1$, a larger deflection to the left, so that the curtain is being pulled towards vertical. As this happens Figure 3.5(c) demonstrates there is an increase in stability with $We_c(x = 1)$ decreasing. This can also be shown for the other cases of β_1.

The new stability criterion provides an interesting connection to the hypothesis made by De Luca and Meola [33], that in the case of a varying surface tension the constant surface tension in (3.1.1) should be replaced by the surface pressure. The two surface

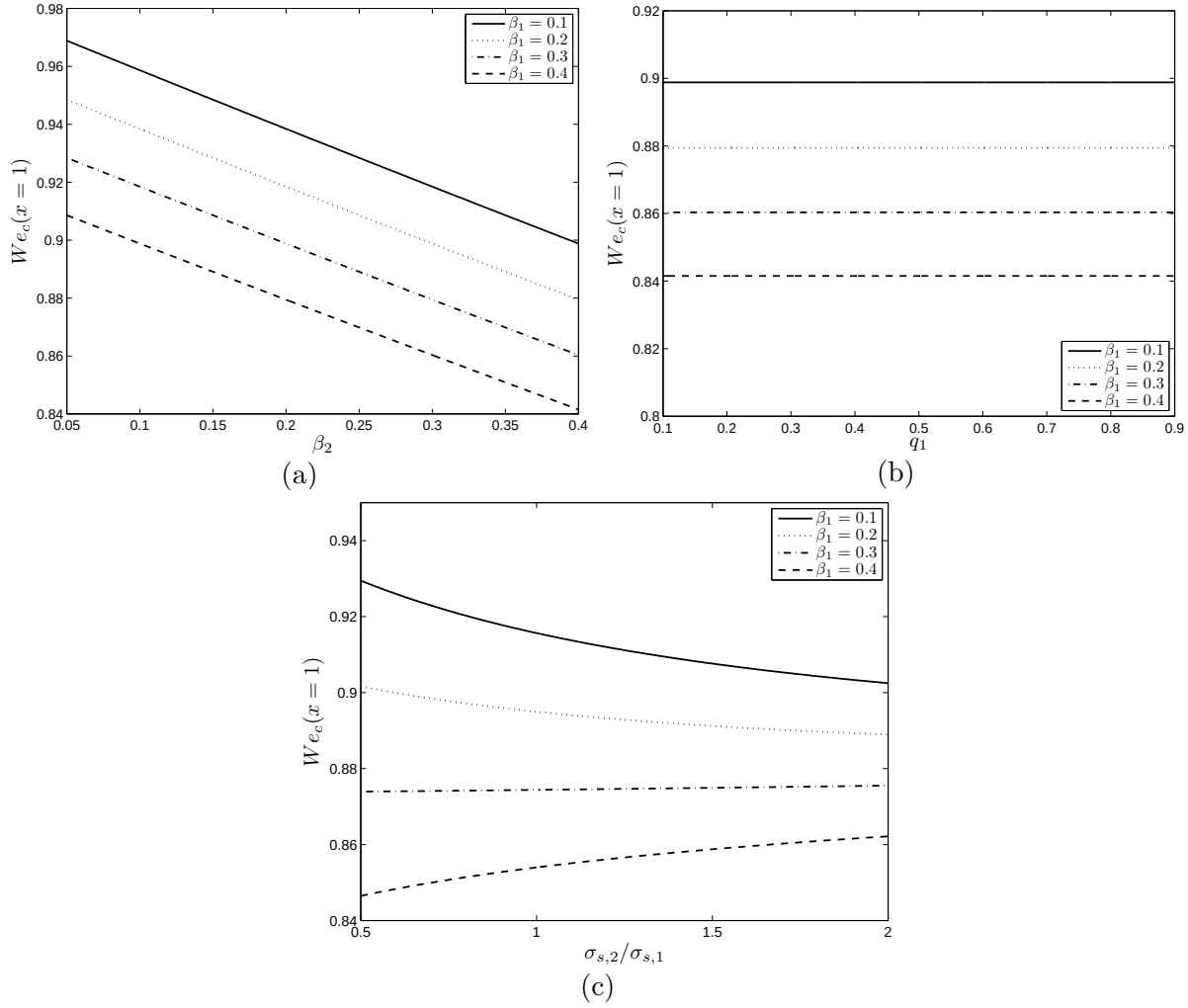

Figure 3.5: Plots showing the effect that surfactants and varying the parameter values have on We_c, given in (3.3.18), at $x = 1$. Each subfigure (a)-(c) corresponds to the same parameter values as in Figure 3.2, except for those stated on the x-axis and in the legend.

pressures, corresponding to the two free surfaces of the curtain, are defined as $\Pi_j = \sigma_{s,j} - \sigma_j = RT\Gamma_j$, having used the equation of state (3.2.39). As these equations are in dimensional form, we non-dimensionalise to obtain

$$\widehat{\Pi}_j = \frac{\sigma_{s,j} - \sigma_j}{\sigma_{s,1}} = \frac{\sigma_{s,j}}{\sigma_{s,1}} \frac{\Gamma_{in,1}}{\Gamma_{in,j}} \beta_j \Gamma_j. \tag{3.3.19}$$

Replacing the constant surface tensions in the criterion $We_T > 1$ with the surface pressures, we have

$$\frac{\mathcal{R}Ca\ u^0 \left(q_1 + \frac{\rho_2}{\rho_1}(1 - q_1)\right)}{\widehat{\Pi}_1 + \frac{\sigma_I}{\sigma_{s,1}} + \widehat{\Pi}_2} > 1. \tag{3.3.20}$$

Substituting (3.3.19) into (3.3.20), we obtain

$$\frac{\mathcal{R}Ca\ u^0 \left(q_1 + \frac{\rho_2}{\rho_1}(1 - q_1)\right)}{\left(1 + \frac{\sigma_I}{\sigma_{s,1}} + \frac{\sigma_{s,2}}{\sigma_{s,1}}\right) - \frac{\sigma_1}{\sigma_{s,1}} - \frac{\sigma_2}{\sigma_{s,1}}} > 1,$$

which can be written as

$$\frac{\mathcal{R}Ca\ u^{0^2} \left(q_1 + \frac{\rho_2}{\rho_1}(1 - q_1)\right)}{\beta_1 + \frac{\sigma_I}{\sigma_{s,1}} u^0 + \frac{\sigma_{s,2}}{\sigma_{s,1}} \beta_2} > 1, \tag{3.3.21}$$

having used the steady-solution $u^0 \Gamma_j^0 = \Gamma_{in,j}/\Gamma_{in,1}$. Interestingly, (3.3.21) is remarkably close to our new criterion (3.3.14); indeed, when $\sigma_I = 0$, (3.3.21) becomes our new condition (3.3.14).

3.3.3 Experimental comparison

In Figure 3.6 we compare the criterion established in the previous section to experimental values obtained from a previous study conducted by the author, of which the reader is referred to for details of the experimental set-up and methods [82]. In this example, a two-layer curtain comprising of two layers of a 75% glycerol (in water) solution, with 0.2%

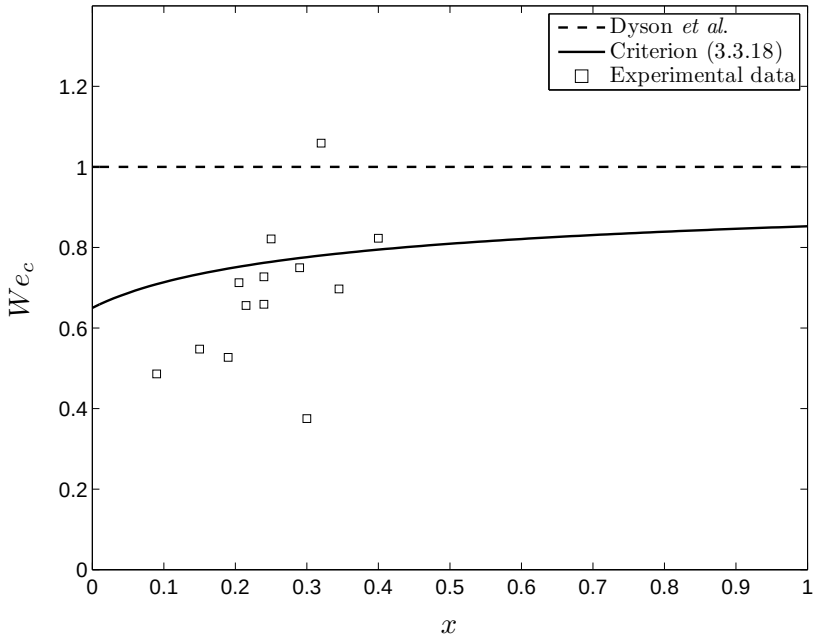

Figure 3.6: A comparison between the classic Weber number criterion (3.1.2), our criterion (3.3.18) and experimental data. A two-layer curtain where both layers are a 75% glycerol solution with 0.2% (by weight) SDS is considered, using the parameters: $\rho_1 = \rho_2 = 1200$ kgm^{-3}, $q_1 = q_2 = 0.5$, $\sigma_{s,1} = \sigma_{s,2} = 0.066$ Nm^{-1}, $\sigma_I = 0$ Nm^{-1}, $\beta_1 = \beta_2 = 0.35$. $\mathcal{R} = 17.7778$, $Ca = 0.3030$, $Fr = 0.6731$.

(by weight) of the surfactant sodium dodecyl sulfate (SDS) added in both layers.

The location of the curtain rupture, the onset of the curtain break-up, was measured as a vertical distance from the die lip and non-dimensionalised with respect to the curtain length, as in our mathematical model. The Weber number can then be calculated, obtained through a knowledge of the flow rates, the velocity of the curtain at the point of rupture (using the free-fall approximation), and the fluid properties. Thus we can then plot x against the critical Weber number for repeated experiments of the same fluid to compare against (3.1.2) and (3.3.18) [82].

The solid line represents, from our model, the critical Weber number above which the curtain is theoretically stable. The majority of break-ups, apart from one obvious outlier and two break-ups that lie just above the critical Weber number of criterion (3.3.18), occur below the line $We_c = |\Lambda/(\Theta u^0) - 1/2| + 1/2$, suggesting the criterion established

can be used as a useful extension of the classic Weber number criterion, $We_T > 1$.

3.4 Conclusions

To summarize, following a similar mathematical model to that of Dyson *et al.* [41], the flow of a vertically-falling two-layer curtain, due to gravity, has been considered with the extension of including the effect of surfactants. From this, steady state solutions were found numerically from the leading-order system, enabling the plotting of cross-sectional curtain profiles, as demonstrated in Figure 3.2. The introduction of surfactants, by lowering the surface tension, affect the 'bending' of the curtain, that is the pull to either the left or right-hand side, due to a difference in surface tension of the two free surfaces. The initial stages of experimental evidence of this pull is outlined in Appendix C.

Moreover, we have shown how the Weber number stability criterion with the assumption of constant surface tension, is affected for a two-layer curtain with surfactants. Via a multiple-scale approach, since disturbances along the curtain are typically much smaller than the length scale of the curtain itself, a new stability criterion (3.3.18) has been formulated. This emphasized the stabilizing influence of surfactants through a reduction in the critical Weber number, which varied as a function of x. As expected, the greater the 'effectiveness' of the surfactant through an increase in the parameter β, a greater reduction in We_c was achieved.

Finally, a comparison to a set of experimental data points was presented. The new criterion formulated from our model represented a better fit to the data against the criterion $We_T > 1$, with the critical Weber number reducing below unity, above which the curtain is stable; the vast majority of break-ups occurred below this new critical Weber number.

This work provides a useful study on how the transverse pull of a steady liquid cur-

tain can be controlled by the addition of surfactants and how the stability criterion is altered, despite some industrial limitations. Taking into account the transition of the fluid film from the die face to curtain formation, studying transverse disturbances, and the consideration of non-Newtonian fluids are the topics of future research.

Chapter 4

Experimental investigation of hysteresis and rupture speed in the break-up of liquid curtains

4.1 Introduction

The theoretical study of curtain stability was considered in Chapter 3, extending previous studies by considering the effect of surfactants, losing the assumption that surface tension is constant. This altered the critical Weber number, above which the curtain is stable, which corresponds to the critical flow rate at which the curtain breaks up being lowered with the addition of surfactant.

In this chapter, we investigate experimentally not only the flow rates at which curtain break-up occurred across a range of fluid properties, but also the minimum flow rate required to originally form a stable curtain, which can also vary depending on liquid properties. The difference between these flow rates formed the inspiration for this chapter; the minimum flow rate required to form a stable curtain is considerably higher than the flow rate at which break-up occurs (i.e. once a stable curtain is formed the flow rate may

be reduced, whilst the curtain remains). The capability to sustain a stable curtain at a fixed flow rate can depend on whether the flow rate has been reduced or increased to reach that flow rate, defining a hysteresis region, and is explained in further detail in Section 4.2.2.

There have been few works in the literature on the difference between these flow rates, despite the many experimental and theoretical works that have been carried out on curtain stability, of which the reader is referred to the introduction of the previous chapter for a more in-depth review. Greiller [50], in a US patent on the design of various curtain coating apparatus, noted this difference when plotting the flow rate at break-up for a range of different concentrations of gelatin solutions, stating the curtains were "first established at a high flow rate". In his experiments, a single slot-die was used to create a curtain of 11.4 cm in length. Moreover, these experiments included the use of two different surfactants (saponin and an anionic alkyl substituted aryl oxyalkylene ether) and noted the lower flow rate at which break-up occurs in both of these cases. However, there were no further reportings of the conditions required to form a stable curtain initially.

An extensive experimental study was carried out by Pritchard [93] into the different flow regimes observed when a layer of oil flows over the end of a sharp plate. Over 700 qualitatively different regimes were noted[1], with the stability of the branches of these flows investigated, by systematically changing the flux of fluid. Plotting the various configurations as a function of the Reynolds number, the hysteresis phenomenon is observed; at a fixed Reynolds number (i.e. fixed flow rate) the branch of flow depended upon the initial value of the flow rate, so that more than one configuration can be observed at an identical Reynolds number. Yet all of the flows observed in this set-up occur after break-up in our curtain coating method, without the use of edge guides to maintain the

[1]Interestingly, these different regimes even included chaotic temporal behaviour of continuous streams (i.e. liquid jets), as well as steady and periodic states. This work (the fluid flow after break-up) is investigated further in the next chapter of this thesis.

width of the liquid sheet.

Using edge guides, De Luca and Meola [34] reported findings on the break-up flow rate, noting a specific flow rate (labelled Q_{th} in their work) upon which an array of regularly spaced liquid jets formed. Moreover, they observed a range of flow rates at which break-up occurred above and below Q_{th}, which affected the regular spacing of the jets that occurred afterwards. Again, the flow rate at which one could form a curtain was not discussed.

As well as investigating the hysteresis phenomenon, this chapter also analyses the sheet behaviour *during* break-up. As described theoretically in Chapter 3, when a disturbance occurs in the liquid curtain, stability depends upon whether this is flushed with the downstream flow of the curtain or propagates upstream. Experimentally, this disturbance manifests itself as a puncture in the curtain, and grows as a hole in either case (as it gets flushed away or as it propagates upstream). Via high-speed imaging, the speed at which this hole grows can be measured and compared to past theoretical models.

Ranz [94], inspired by previous works on a liquid sheet such as Rayleigh [95], conducted experiments that concluded the film recedes at a constant speed, influenced by surface tension. Moreover, it was noted as the liquid sheet moves away from the initial point of rupture, fluid accumulates in a circular rim at the edge of the sheet. Working independently from each other, Taylor [110] and Culick [32] calculated the constant speed of the sheet retraction previously observed by Ranz, deduced by balancing the rate of change of the rim momentum with the surface tension force on the rim. This speed is known as the Taylor-Culick speed, and is given by

$$U_{TC} = \sqrt{\frac{2\sigma}{\rho H}}, \tag{4.1.1}$$

where σ is the surface tension and H the constant film thickness (away from the rim at the edge). It is noted here that these works assumed that the liquid film ahead of the rim

is stationary.

This theoretical speed matched with the experiments later conducted by McEntee and Mysels [84], when $H > 0.1$ μm, who analysed the break-up of soap films. By considering the same momentum balance, Keller [66] extended these results by considering sheets of non-uniform thickness, with the sheet thickness given as a function of the radial coordinate, r. The hole radius $R(t)$ was solved in the case when $H(r) = br^{\alpha}$, with the Taylor-Culick speed being recovered for the case $\alpha = 0$ (so that $H(r) = b$, with b being the constant film thickness). However, it was emphasised that their work should not be viewed as a precise theory, more as an indication of which parameters are influential in the hole opening process.

Two papers by Debrégeas *et al.* [35, 36] studied the high viscous limit of sheet retraction. Investigating freely suspended films of long chain polymers, two major differences to previous studies were found; firstly, the hole growth was not constant, but instead increased exponentially at a speed

$$U_{exp}(t) = R_0 \exp\left(\frac{\sigma t}{0.7\mu H}\right), \tag{4.1.2}$$

where R_0 is the initial hole size. Despite suggestions that this exponential behaviour could be a result of the viscoelastic nature of the polymer films being used, the typical shear rate was below that at which non-Newtonian behaviour would be exhibited. Secondly, it was found that no rim was formed at the receding free edge in these experiments.

Following from this observation, Brenner and Gueyffier [19] considered the different regimes effecting the shape of a retracting film, studying the conditions under which the film has a growing rim at the edge, and also the possibility of capillary waves occurring ahead of the receding edge. Further emphasising the importance of viscosity, they reasoned the existence of a rim or capillary waves depends on the size of the Ohnesorge

number, which relates viscous forces to inertial and surface tension forces, given by

$$Oh = \frac{\mu}{\sqrt{2\rho H\sigma}}. \tag{4.1.3}$$

Adopting a second order finite difference scheme, solving the lubrication equations (derived from the Navier-Stokes equations) for a thin film of thickness $H(x,t)$, they found when the Reynolds number

$$Re = \frac{\rho L U_{TC}}{\mu} = \frac{L}{H}\frac{1}{Oh}$$

is greater than 1, then there exists a growing rim at the film edge. Here, L is the axial extent of the film, considered much larger than the thickness, H. This means that there is no rim only in the high Oh limit, when the film is perfectly flat, matching with the experiments of Debrégeas *et al.* Moreover, Brenner and Gueyffier showed when the dimensionless parameter

$$\frac{\mu^2}{\rho H\sigma} = 2Oh^2$$

is smaller than 1, then capillary waves form ahead of the retracting film edge. This corresponds to the small Oh regime; as the viscosity increases, meaning an increase in Oh, first the capillary waves are damped, then the circular rim amalgamates with the bulk of the sheet. These changes are shown in Figure 4.1, taken from Savva and Bush [101]. In the first two cases (top and middle in Figure 4.1), the retraction speed follows that of Taylor and Culick given by (4.1.1), and in the high Oh case the Taylor-Culick speed would be reached in the long timescale.

In summary, viscosity does not have an effect on the final retraction speed (4.1.1), but influences how this speed is reached. This was confirmed by Sünderhauf *et al.* [108], by conducting numerical simulations of the two-dimensional Navier-Stokes equations, noting the acceleration to U_{TC} is faster for smaller values of Oh during the initial stages of

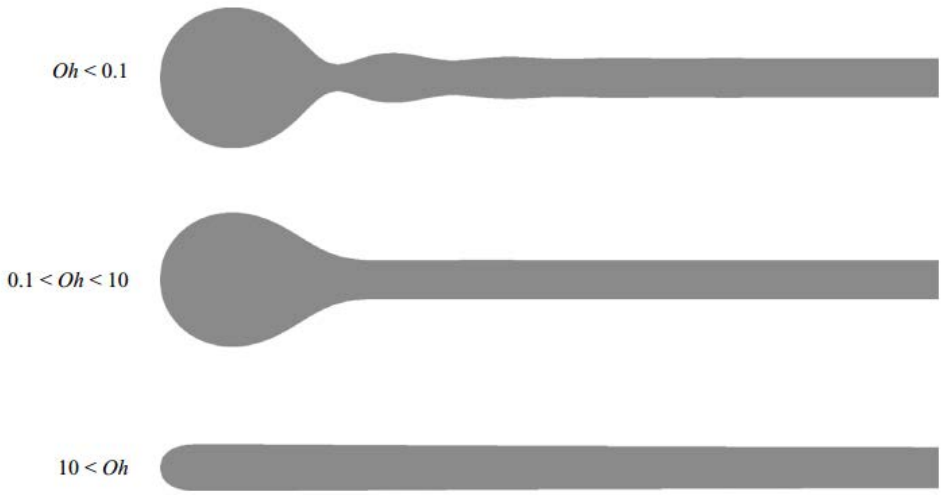

Figure 4.1: The three different regimes, dependent on the Ohnesorge number, as identified by Brenner and Gueyffier [19] of liquid sheet retraction in planar geometry; the sheet is retracting from left to right. In the low Oh case (top), capillary waves emerge ahead of the cylindrical rim at the edge of the sheet. As Oh increases, the capillary waves are lost and the rim begins to merge with the liquid sheet (middle), before becoming a flat sheet with no rim in the high Oh limit (bottom). Taken from [101].

retraction. Sünderhauf *et al.* non-dimensionalised the time t such that

$$t = \sqrt{\frac{\rho H^3}{2\sigma}}\widehat{t}, \tag{4.1.4}$$

where $\widehat{t}$ is the non-dimensional time. In the numerical simulations [108], when $Oh = 0.5$ the sheet retraction velocity had reached $0.9U_{TC}$ at $\widehat{t} = 10$; when $Oh = 33.33$ the sheet retraction velocity reached $0.9U_{TC}$ at $\widehat{t} = 30$.

More recently, Savva and Bush [101] considered the high Oh regime ($Oh \gg 10$) finding initially the film recedes according to $t^{3/2}$ in the planar geometry, and emphasised how the dynamics of retraction differ depending on the geometry considered (e.g. planar or circular), in particular for the high Oh case. Related recent works include considering the stability of the rim [98], the retraction of liquid strips on non-wetting surfaces [80], and the hole growth when two bubbles coalesce [87].

In the previous works mentioned in this section, any effect from the edge guides maintaining the width of the film is neglected. Chepushtanova and Kliakhandler [24] considered the break-up of viscous films between parallel needles, at varying distances apart, theoretically predicting the retraction velocity based upon mass accumulation at the rim as well as mass retention on the needles. In the low viscosity case, the Taylor-Culick speed (4.1.1) was recovered, and their predictions matched well with their corresponding experiments. In the experimental work that follows in this chapter, however, we consider the hole growth in the liquid curtain before reaching the edge guides, when the hole emanates from the central region of the curtain. The origin of break-up is recorded and investigated for all of the experiments conducted, however, to examine if the edge guides have a noticeable effect on the stability which has been noted by various works in the literature [85].

As commented by Schweizer *et al.* [104], due to the reduced velocity of the curtain in the vicinity of the edge guide (owing to the no-slip boundary condition at a stationary solid) and the process of wetting the guide, the curtain has lower velocity and is thinner in this region, thus proving more susceptible to break-up. The difference between the velocity in the curtain compared to at the edge results in local distortions and constrictions of the curtain edge, as highlighted in [104], with the velocity in the curtain being in accord with the free fall approximation

$$v_c = \left(v_0^2 + 2gz\right)^{1/2}, \tag{4.1.5}$$

where $v_0 = v(z = 0)$ is the velocity at the die-lip, having also been verified by a number of other studies [14, 27, 117].

Experimentally, Roche *et al.* [97] showed that the velocity (4.1.5) is well approximated by

$$v_c \approx (2gz)^{1/2}, \tag{4.1.6}$$

which is valid for $z \geqslant 2$ cm, as also discussed in [27, 104]. To calculate the velocity in the vicinity of the edge, first we consider the film thickness of a film flowing down an inclined plane, at angle θ to horizontal (as seen in Chapter 2), given by

$$h_T = \left(\frac{3Q_T \mu_1}{\rho_1 g \sin\theta} \right)^{1/3}, \tag{4.1.7}$$

with the single-layer free surface velocity given by

$$U_s = \frac{\rho g h_T^2 \sin\theta}{2\mu}. \tag{4.1.8}$$

When considering the angle of the incline to vertical, β, we see that $\sin\theta = \sin(90 - \beta) = \cos\beta$. Using this, substituting (4.1.7) into (4.1.8), we observe

$$\begin{aligned} v_{edge} &= \frac{\rho g h_T^2 \sin\theta}{2\mu} \\ &= \frac{\rho g \cos\beta}{2\mu} \left(\frac{3Q_T \mu_1}{\rho_1 g \cos\beta} \right)^{2/3} \\ &= \left(\frac{9Q_T^2 \rho g \cos\beta}{8\mu} \right)^{1/3}. \end{aligned} \tag{4.1.9}$$

In our case, β corresponds to the angle from vertical of the edge guides used, which means $\beta = 0$ when the guides are vertical. The difference in the velocities (4.1.5) and (4.1.9) can result in a reduction in curtain stability in a boundary layer at the curtain edge; to overcome this Schweizer *et al.* [104] used liquid flowing through a porous plate at the edge guides to match the velocities (4.1.5) and (4.1.9) for the entire length of the curtain. Similar patents have been filed to overcome instabilities near the edge guides, including the use of a jet of liquid adjacent to the bottom of the guides [56], and the flushing of a low-viscosity liquid at the top of the edge guide, before being extracted via suction at the bottom of the edge guides [96].

Another method to overcome the boundary-layer effects and avoid break-up at the curtain edge is to slightly taper the edge guides inwards (i.e. $\beta > 0$), so that the liquid is accelerated near the edges. In an experimental study by Becerra and Carvalho [9], angled edge guides were used which resulted in all ruptures occurring in the centre of the curtain. This chapter also investigates the difference in break-up origin when straight and angled edge guides are used. By imaging the curtain disintegrating from a stable sheet, information can be gathered on where the hole originated from, as well as it's growth to compare to the Taylor-Culick speed (4.1.1).

4.2 Experimental set-up and methods

4.2.1 Mechanical components

The apparatus used for these experiments is the same as described in Chapter 2, of which the reader is referred to for a full description, so that we only describe the key components here. A custom built 4-layer slide die (TSE Troller AG, Switzerland) was used, with a width of 12 cm and mounted at an angle of 30° from horizontal, situated on a moveable table built from aluminium profile. Located next to the table housing the slide-die was the "pumping station" which housed the fluid holding tanks (four 200-l tanks), gear pumps and electromagnetic flowmeters. The exact flow rate for each individual layer was determined by the flowmeter (Proline Promag series 50H, Switzerland), and easily converted into a flow rate per unit width (cm^2s^{-1}). Through a feed line located at the bottom of the slide die, the fluid was delivered to each layer and distributed through the width of the cavities before exiting on the top face of the die. Figure 4.2(a) shows the slide-die used, with the exit slots located on the die face labelled.

As examined in Chapter 2, the liquids then flow down the inclined plane of the die face, stacking upon each other, forming a multi-layer film. In the experiments discussed here, single and two-layer films of the same fluid were considered, so the difference is

differential motion between layers. Once the film has reached the die lip, a liquid curtain is formed (if the flow rate is suitably large enough) with the curtain width maintained using Teflon edge guides, which are mounted vertically at either side of the lip. Located at the bottom of the edge guides was a stainless steel plate, kept at a horizontal profile, as seen at the bottom of Figure 4.2(b), that would deflect the liquid into a catchpan so that the fluid could be recycled.

Angled guides

As well as using straight edge guides, shown in Figure 4.2(a), experiments were also conducted using a set of angled edge guides. The geometry of the angled edge guides are shown in Figure 4.2(b); as well as being slightly longer in length compared to the straight guides (20 cm compared to 15 cm) the angled guides are tapered such that the width of the curtain decreases in the streamwise direction, with a final width of 8 cm (compared to 12 cm) at the bottom of the curtain.

With the width of the curtain continuously decreasing downstream when using the angled guides, the flow rate per unit width becomes dependant on the vertical distance, z, from the die lip (the die lip is also labelled in Figure 4.2(a)). From the geometry of the angled guides, letting β be the inclination angle from vertical of the edge guides, we have that $\tan\beta = 0.1$. Thus, the width of the curtain at a length z cm from the die lip is given by $(12 - (2 \cdot 0.1z))$ cm $= (12 - 0.2z)$ cm. The flow rate per unit width, in cm^2s^{-1}, is then given by

$$\begin{aligned} Q(z) &= \frac{Q_{vol}}{12 - 0.2z} \\ &= \frac{\frac{Q_{vol}}{12}}{1 - \frac{z}{60}} \\ &= \frac{Q_0}{1 - \frac{z}{60}}, \end{aligned} \tag{4.2.1}$$

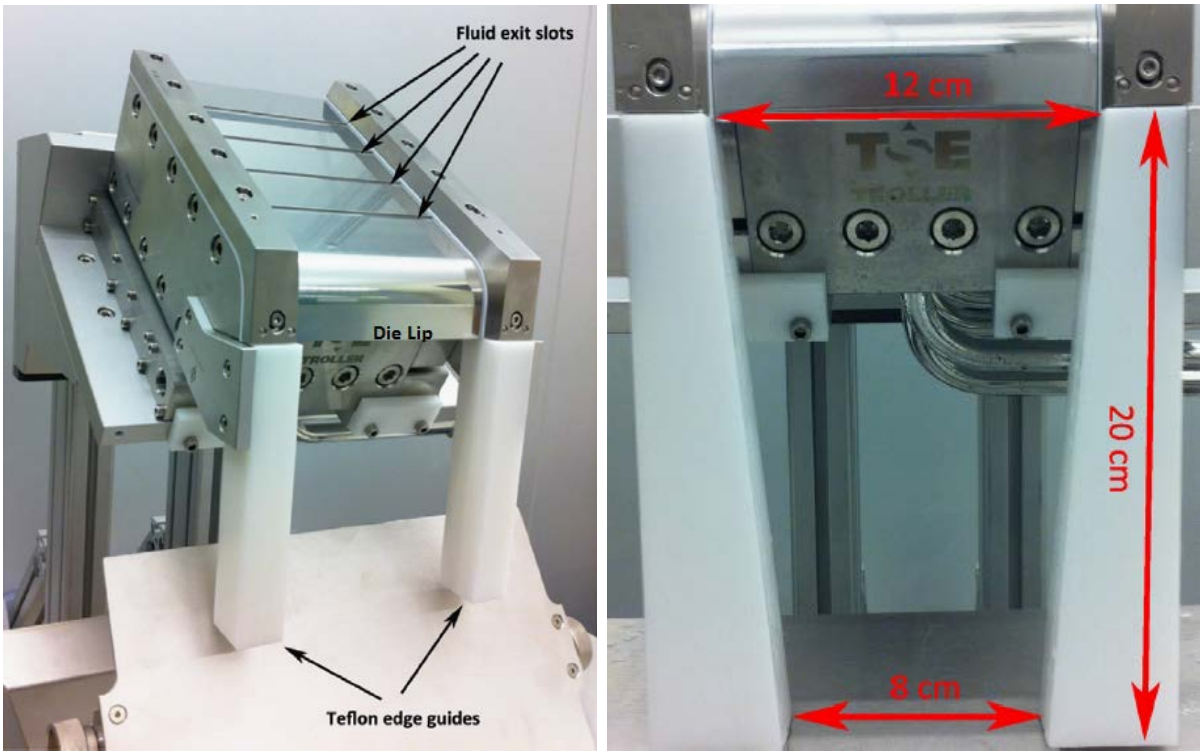

(a) (b)

Figure 4.2: Geometry of the straight and angled edge guides, both made from Teflon. In (a) the 4-layer slide die, with the fluid exit slots emanating from the die face, is shown with the straight edge guides (15 cm length) attached. In (b) the angled edge guides are attached, with the geometry labelled.

where Q_{vol} is the volumetric flow rate (in cm^3s^{-1}) at $z = 0$, and $Q_0 = Q(z = 0)$ is the flow rate per unit width at the die lip[2]. It is noted here that when discussing experiments using the angled guides, the flow rate per unit width at curtain formation is given by Q_0, and the flow rate per unit width at break-up is calculated using (4.2.1). With the straight edge guides, the flow rate per unit width is constant (Q_0), for the entire length of the curtain.

Assuming plug flow in all layers, the local curtain thickness is given by [27]:

$$H = \frac{Q_T}{v_c}, \tag{4.2.2}$$

where Q_T is the total flow rate (given by (4.2.1) in the case of angled guides) and v_c is given by (4.1.6). Figure 4.3 plots the curtain thickness against vertical distance from the die lip, to compare how the liquid sheet thickness differs when using the angled guides as opposed to the straight guides, for three different flow rates which cover the range that was used during the experiments. In this plot, the vertical distance starts at $z = 0.02$ m, from where the free-fall approximation given in (4.1.6) is valid. As expected, the curtain thickens when using the angled guides, compared to the straight guides, at a given value of z. This effect is exaggerated as the flow rate is increased. Despite (4.2.2) giving a good estimation of the curtain thickness, we note that the edge guides will affect the curtain thickness, meaning at a fixed vertical distance z from the die lip, the thickness across the width of the curtain will not be constant due to boundary layer effects. This is discussed more in Section 4.4.

[2]We note here how formula (4.2.1) changes when using the dimension metres, rather than centimetres. When using m for length and m^2s^{-1} for flow rate per unit width, the formula (4.2.1) becomes $Q(z) = Q_0/\left(1 - (5z/3)\right)$.

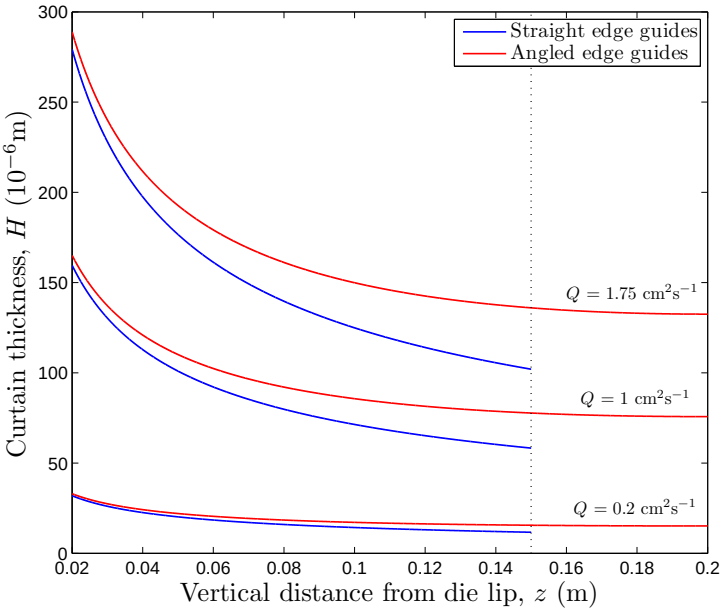

Figure 4.3: Curtain thickness as a function of vertical distance from the die lip, for three different flow rates (the flow rate corresponds to the flow rate at $z = 0$ for the angled guides).

4.2.2 Experimental procedure

Hysteresis

To observe the hysteresis phenomenon in the break-up of liquid curtains, a stable curtain must first be formed which, as explained previously, can only be done when above a certain minimum flow rate. To find this minimum flow rate, labelled Q_{min}, the flow rate was increased slowly from a low flow rate of $Q \approx 0.5$ cm^{2}s^{-1} until the curtain would either "pin" itself to the edge guides, or could be manually pinned to the edge guides using a thin plastic rod, resulting in a stable curtain as in Figure 4.4(a). The flow rate at which this occurred was recorded and taken as Q_{min}, with this method being repeated several times in order to accurately determine this value and was found to be very repeatable (discussed in more detail in Section 4.3).

After a stable curtain was formed, the flow rate was left unchanged for at least a

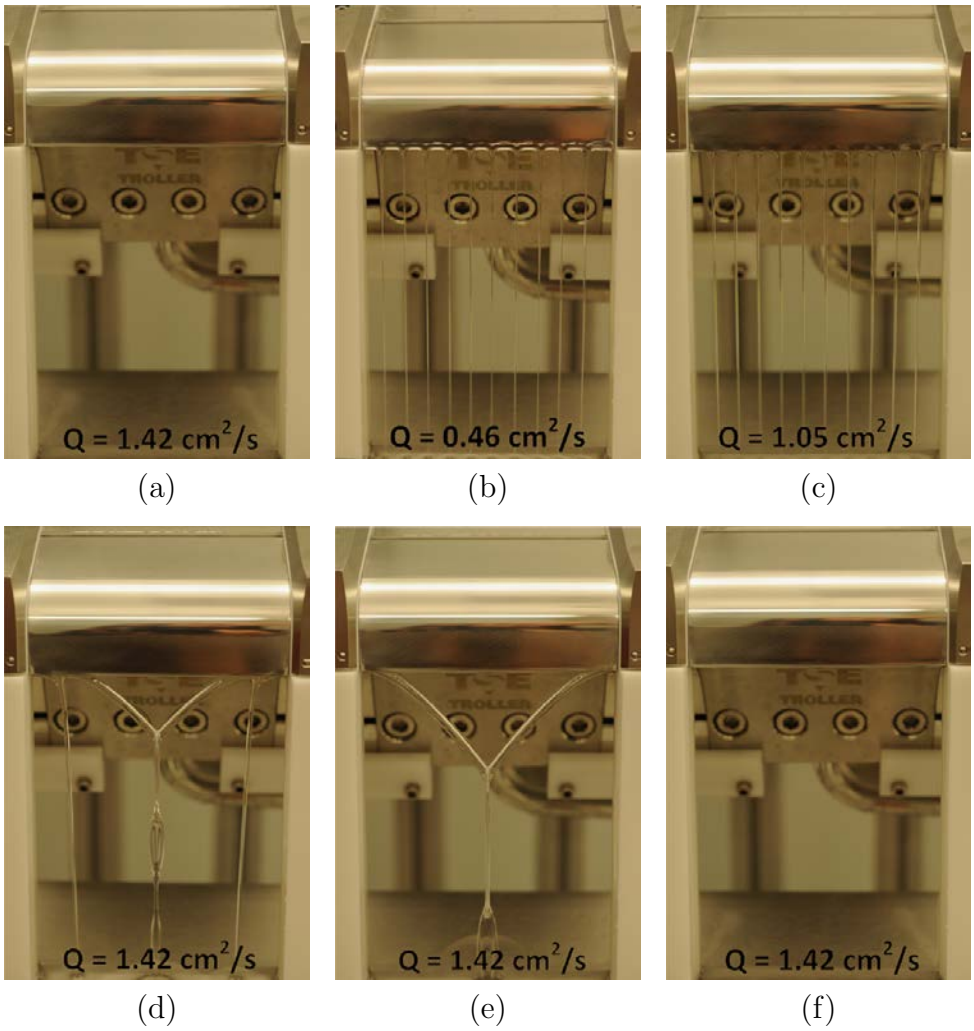

Figure 4.4: A series of photographs showing the different configurations for the liquid coming off the die, demonstrating the hysteresis phenomenon that occurs. A curtain is formed in (a) at $Q_{min} = 1.42$ cm^{2}s^{-1}, upon which the flow rate is then decreased gradually until the curtain breaks up at $Q_{thr} = 0.46$ cm^{2}s^{-1} whereby a series of liquid jets are formed, as seen in (b). Here, the flow rate is then increased, as in (c) - (f), until the curtain can be reformed again at $Q_{min} = 1.42$ cm^{2}s^{-1}. Note how images (d) - (f) show three different configurations for the same flow rate.

minute, upon which the flow rate was decreased slowly, but continuously, until break-up of the liquid curtain to a series of liquid jets occurred. This series of jets is shown in Figure 4.4(b). The curtain break-up could be observed by the naked eye, and consequently the flow rate was immediately reduced no further, recorded and labelled as Q_{thr}. For every configuration (that is, for every fluid used and for single and two-layer experiments) this procedure was repeated at least eight times in order to determine the flow rate at break-up. It is noted here that after break-up, the flow rate can be increased once more to Q_{min}, whereby several different configurations were observed, shown in Figure 4.4(c)-(f).

The true hysteresis window is thus defined as $\big(\max(Q_{thr}), \min(Q_{min})\big]$. Within this range of flow rates we can have either a stable curtain if lowering the flow rate from a value above Q_{min}, or if raising the flow rate from a value below Q_{thr} a series of liquid jets (or similar configurations, see Figure 4.4) and unable to form a stable curtain.

When performing two-layer experiments, both the flow rate of the bottom layer (i.e. the layer flowing in contact with the slide-die) Q_1, and the layer of the top layer Q_2 could be varied[3]. In our experiments, the flow rate of Q_1 was fixed at values of 0.25 cm^2s^{-1} and 0.33 cm^2s^{-1}, and the procedure just described repeated for the flow rate Q_2. Similar results would be expected if Q_2 was fixed and Q_1 was varied if each layer comprised of the same fluid. The validation of this remains the potential for future work. The minimum total flow rate at which a curtain formed is given by $Q_{T,min}$, and at which break-up occurs $Q_{T,thr}$. In the two-layer case, similar to the single-layer case, the true hysteresis window is defined as $\big(\max(Q_{T,thr}), \min(Q_{T,min})\big]$.

To be able to compare the hysteresis window size of single and two-layer curtains, we define the *normalised* hysteresis window given by

$$Q_{norm} = \frac{\min(Q_{T,min}) - \max(Q_{T,thr})}{\min(Q_{T,min})}. \tag{4.2.3}$$

[3]To clarify, a subscript T denotes the total flow rate so that $Q_T = Q_1 + Q_2$. When there is no subscript T, 1 or 2 associated with Q, the flow is strictly one-layer.

When the flow rates at which curtain formation and break-up occur are small, a change in flow rate is relatively more significant than the same change at larger flow rates. This feature is captured by defining the normalised hysteresis window as in (4.2.3), as opposed to the raw data for the hysteresis windows.

Break-up origins and rupture speed

To further analyse the break-up, a high-speed camera (Photron Fastcam SA-3) was positioned directly in front of the liquid curtain to record the hole formation and growth, operating at a frame rate of 500 fps. This meant the origin of break-up, at a vertical distance z from the die lip, could accurately be measured, within ± 1 mm. From this, the local curtain velocity at z could be calculated using (4.1.6), as well as the adjusted flow rate per unit width using (4.2.1) when using the angled guides. Knowledge of the break-up location also enables us to calculate dimensionless groups, such as the Weber, Ohnesorge and Reynolds numbers at the point of rupture, given by

$$We = \frac{v_c \rho Q_T}{2\sigma}, \quad Re = \frac{\rho Q_T}{\mu}, \tag{4.2.4}$$

with the Ohnseorge number given in (4.1.3).

Moreover, from the high-speed video sequence of the liquid curtain break-up, the development of the initial puncture in the curtain to the growth of the hole was recorded, as shown in four snapshots in Figure 4.5. After each frame following the first shot with the hole, the growth can be measured by calculating the distance between the left-most and right-most points of the hole, D_{LR}, and the top-most and bottom-most points of the hole D_{TB}. These distances are labelled in Figure 4.5(d); alongside knowing the time between each frame (1/500 s), the speed of the hole opening can be calculated and compared to the theoretical Taylor-Culick speed given in (4.1.1). This is explained fully in Section 4.4.2.

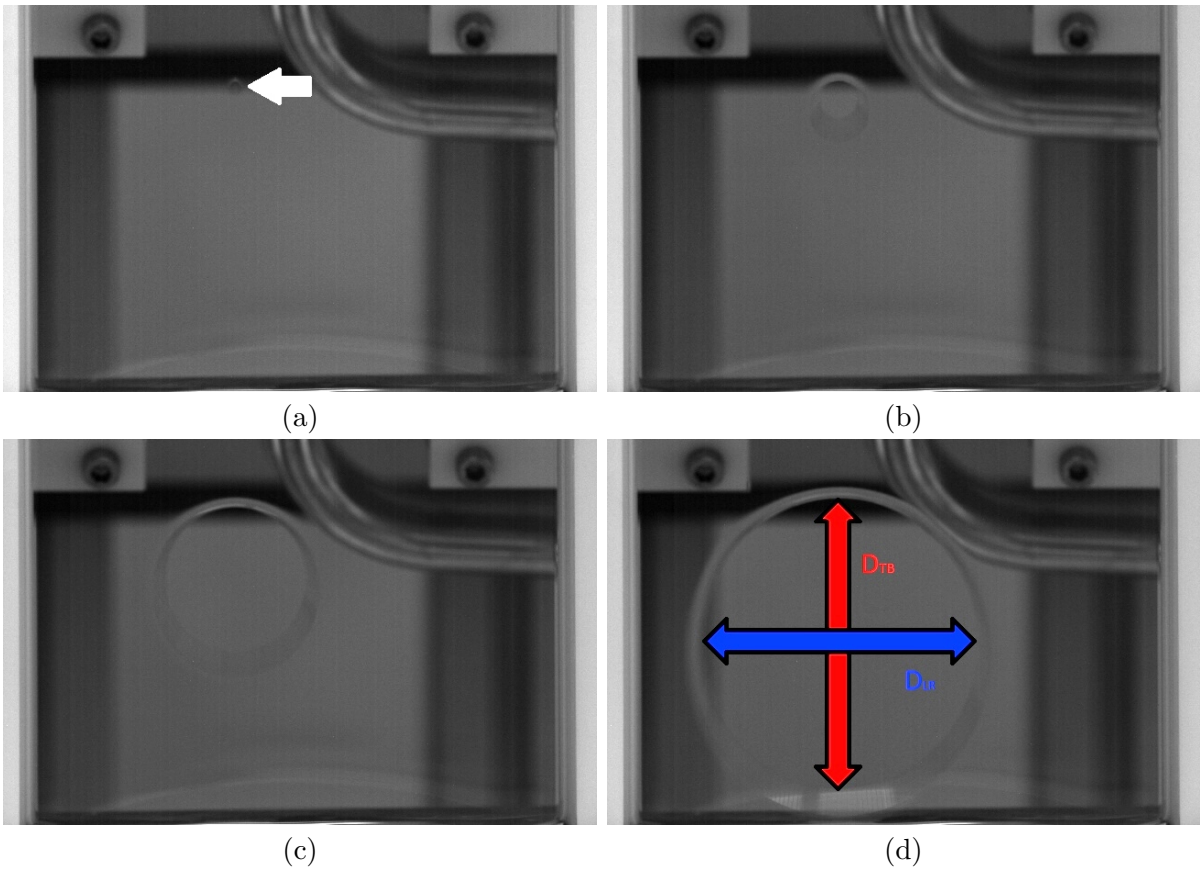

Figure 4.5: Single frame shots from a high-speed video sequence showing the origin of the curtain break-up, the white arrow in (a), and how the hole in the curtain expands in its early stages. From (a), the subsequent frames are taken at (b) $t = 4$ ms, (c) $t = 12$ ms, and (d) $t = 22$ ms. The frame in (d) shows the lengths D_{TB} (red arrow) and D_{LR} (blue arrow) used to calculate the experimental hole opening speed. Here, the fluid is 90% glycerol and the curtain is single-layer, at a flow rate $Q = 0.61$ cm^{2}s^{-1}.

Glycerol conc. ($\%_{v/v}$)	Surfactant conc. ($\%_{w/w}$)	Viscosity μ (mPa.s)	Density ρ (kg/m^3)	Surface tension σ (mN/m)
82	-	87	1224	67.2
84	-	123	1228	66.6
87	-	174	1235	66.4
90	-	262	1241	65.1
75	0.05 SDS	52.9	1207	58.3
75	0.1 SDS	52.9	1207	53.6
75	0.2 SDS	52.9	1207	43.7

Table 4.1: Physical properties of the glycerol-based fluids used in the experiments. The stated values were measured at the ambient temperature of the laboratory during the experiments (21°C).

4.2.3 Fluid properties

All of the fluids used in these experiments were water-glycerol mixtures, as shown in Table 4.1, with surfactant being added in some cases to test the effect of varying surface tension. Considering the pure water-glycerol solutions, the concentration of glycerol was varied from 82% (volume/volume) through to 90% to obtain a range of viscosities (87 - 262 mPa.s). Sodium dodecyl sulphate (SDS) surfactant was added to a 75% glycerol solution in concentrations of 0.05%, 0.1% and 0.2% (weight/weight) so that the surface tension varied from 43.7 - 58.3 mN/m for these solutions, with a maximum of 67.2 mN/m for the surfactant-free liquids.

When surfactant is added to a liquid, not only is the surface tension reduced, the surface tension becomes a variable along the free surface that is now a function of the local surfactant concentration (see previous chapters, in particular Chapter 3). The surface tension values reported in Table 4.1 are essentially *static* or *equilibrium* values, measured using a du Nouy ring or Wilhelmy plate (K100 MK2/SF/C, Kruss GmbH, Germany). This is in contrast to a method whereby the dynamic surface tension can be measured, such as bubble pressure tensiometers [43]. Viscosities were measured using a cone-and-plate geometry on a rotational rheometer (ARES-G2 TA Instruments, USA).

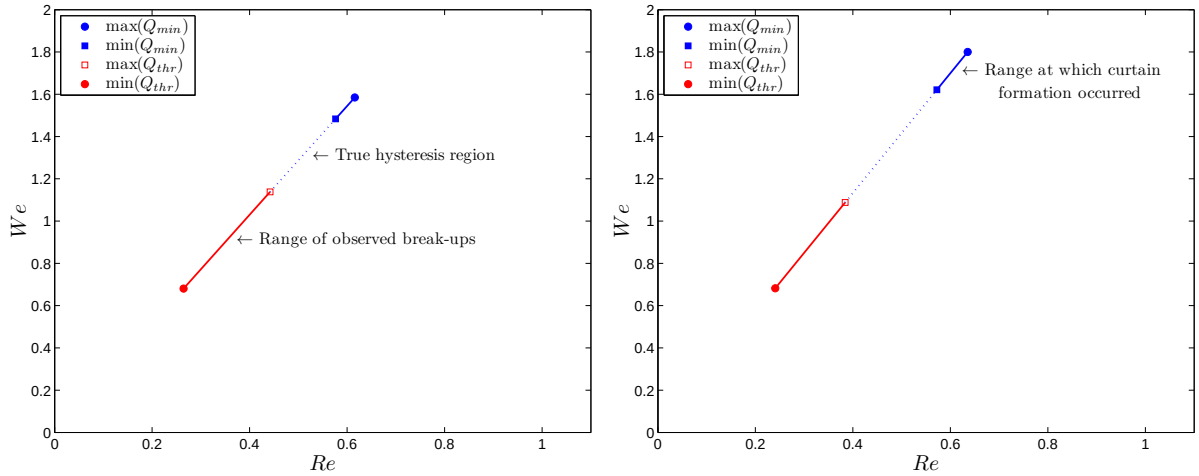

Figure 4.6: Plots of the Reynolds number against Weber number showing the hysteresis region for 90% glycerol single-layer curtains; (a) corresponds to straight edge guides and (b) corresponds to angled guides. The solid blue line represents the range of flow rates that the curtain formed whilst increasing the flow rate, the solid red line the range of flow rates at which curtain break-up occurred when decreasing the flow rate. The hysteresis region is given by the dashed blue line.

4.3 Results: hysteresis

4.3.1 Single-layer curtains

In Figure 4.6 two examples of hysteresis windows are depicted in the Re–We plane, both for 90% glycerol solutions where the (a) straight edge guides, and (b) angled edge guides are used. The values for We were calculated using a local curtain velocity of $v_c = 1.28$ ms^{-1} in (a) and $v_c = 1.41$ ms^{-1} in (b), using equation (4.1.6) based upon the average vertical distance from the die lip where break-up occurred in each case (8.3 cm and 10.1 cm, respectively). By using the average break-up, rather than the break-up location of each individual experiment, the plots in Figure 4.6 are given by a straight line, as opposed to being scattered, ensuring the hysteresis window is readily seen. For all plots after Figure 4.6, the break-up location for each individual experiment is used.

In these plots, the solid blue line represents the range of flow rates upon which

the curtain was formed, from the blue square representing $\min(Q_{min})$ to the blue circle $\max(Q_{min})$. The flow rate could then be reduced to Q_{thr} before the curtain broke-up, with the range of flow rates at which break-up occurred shown by the solid red line between the maximum, $\max(Q_{thr})$ (open red square), and minimum, $\min(Q_{thr})$ (red circle). In the examples given in Figure 4.6, $Q_{min} \in [1.22, 1.30]$ cm^{2}s^{-1} and $Q_{thr} \in [0.56, 0.93]$ cm^{2}s^{-1} in (a), and $Q_{min} \in [1.21, 1.34]$ cm^{2}s^{-1} and $Q_{thr} \in [0.51, 0.81]$ cm^{2}s^{-1} in (b). As explained previously, the hysteresis window is given by $\big(\max(Q_{thr}), \min(Q_{min})\big]$, shown by the blue dotted line in Figure 4.6. Thus, the window is given by $(0.93, 1.22]$ cm^{2}s^{-1} in (a), and $(0.81, 1.21]$ cm^{2}s^{-1} in (b). One result of note from these plots is how the range of flow rates at which curtain formation occurred was smaller than the range at which break-up occurred, a recurring feature of all these experiments. Physically, this corresponds to the repeatable nature the curtain formation compared to break-up; the complex dynamics of break-up of the liquid sheet could be due to boundary layer effects at the edge guides, and other disruptions, such as a microbubble in the liquid, to the curtain.

Figure 4.7 plots the normalised hysteresis window size against surface tension, in (a), and dynamic viscosity, in (b), for all of the single-layer experiments. There is no clear dependence on surface tension from (a), when either the straight or angled edge guides were used. This is highlighted in particular for the pure glycerol-water solutions when using the angled guides, whereby the surface tension remains centred around 66 mN/m, yet the size of the normalised hysteresis window varies over more than a tenfold increase from the lowest value of 0.03 to a maximum of 0.39. Similarly, despite not being as extreme, there is also a clear range when the straight edge guides were employed for the glycerol-water liquids.

Considering Figure 4.7(b), there is a clearer trend between viscosity and the normalised window size, that is repeated for both angled and straight guides. From the lowest viscosity fluids, the window size decreases to a minimum below 0.05 when $\mu \approx 100$ mPa.s,

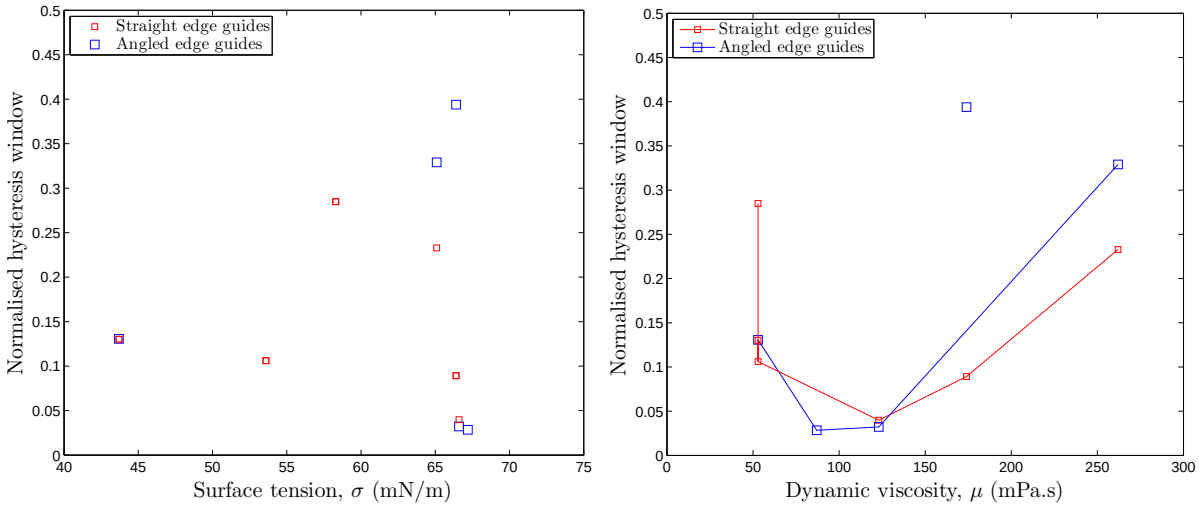

(a) (b)

Figure 4.7: Fluid properties plotted against normalised hysteresis window size; in (a) surface tension and in (b) dynamic viscosity (all single layer).

after which there is an increase in window size.

4.3.2 Two-layer curtains

To compare the two-layer experiments to their corresponding single-layer experiments (noting again, the only difference being differential motion in the two layers of the same fluid), in Figure 4.8 we have plotted Q_2 against Q_1 to show the range of flow rates at which $Q_{T,min}$ and $Q_{T,thr}$ occurred. In each of these plots, the diagonal lines correspond to the 'expected' values from the one-layer experiments. For example, the diagonal solid blue line represents the flow rate $\max(Q_{min})$, which for the single-layer 90% glycerol experiments using the straight guides was 1.30 cm^2s^{-1}. Thus in Figure 4.8(a), the solid blue line is given by $Q_1 + Q_2 = 1.30$ cm^2s^{-1}. Similarly, for the same experiments, $\min(Q_{min}) = 1.22$ cm^2s^{-1}, so that the blue diagonal dashed line in (a) is given by $Q_1 + Q_2 = 1.22$ cm^2s^{-1}. The two diagonal red lines are plotted likewise, with the dashed line corresponding to $\max(Q_{thr}) = 0.93$ cm^2s^{-1}, and the solid line to $\min(Q_{thr}) = 0.56$ cm^2s^{-1} from the single-layer experiments.

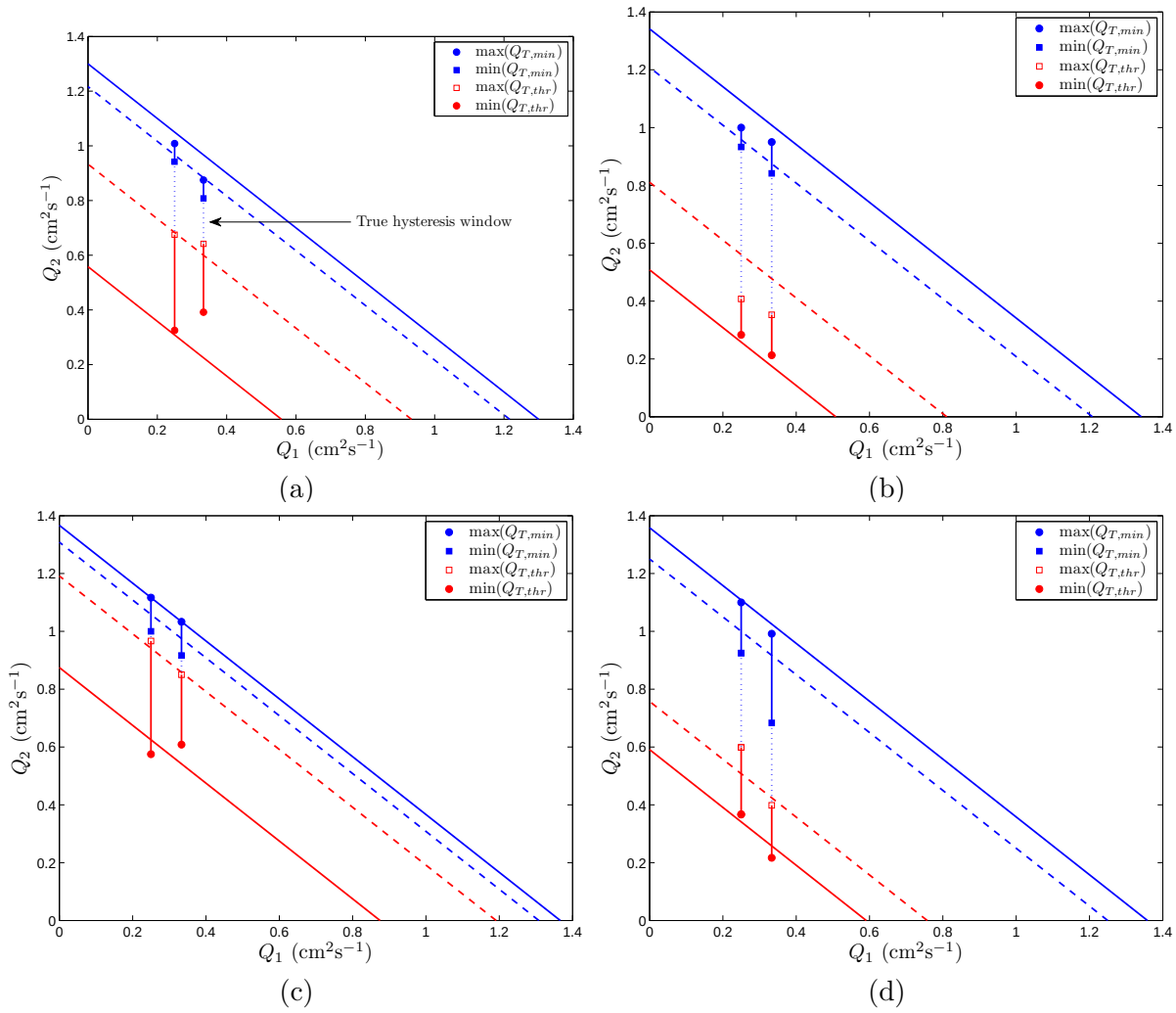

Figure 4.8: A comparison between two-layer hysteresis window size with the 'expected' window size from the corresponding single-layer experiments; both layers comprise of the same fluid in the two-layer experiments. The diagonal lines are plotted from the single-layer experiments, assuming the sum of the flow rates $Q_1 + Q_2 = Q_T$ at which curtain formation and break-up occurs in the two-layer experiments will be equal to the flow rate Q at which these phenomena occur in the single-layer experiments. Subfigures (a) and (b) are 90% glycerol experiments, (c) and (d) 87% glycerol experiments. Experiments in (a) and (c) use the straight edge guides, (b) and (d) the angled edge guides.

The diagonal lines in Figures 4.8(b)–(d) are plotted in the same way, corresponding to the single-layer experiments for (b) 90% glycerol using the angled edge guides, (c) 87% glycerol using the straight edge guides, and (d) 87% glycerol using the angled edge guides.

The vertical lines in Figure 4.8 refer to the results of the two-layer experiments, where Q_1 was fixed at values of either 0.25 or 0.33 cm^2s^{-1}, with the nature of the symbols and lines the same as in Figure 4.6. For example in Figure 4.8(a), when $Q_1 = 0.25$ cm^2s^{-1} is fixed, we obtained the data $Q_{T,min} \in [1.19, 1.26]$ cm^2s^{-1}, so that $Q_{2,min} \in [0.94, 1.01]$ cm^2s^{-1}. Thus, the blue circle representing $\max(Q_{T,min})$ is plotted at the point $(Q_1, Q_2) = (0.25, 1.01)$ cm^2s^{-1}, and similarly the blue square representing $\min(Q_{T,min})$ is plotted at the point $(Q_1, Q_2) = (0.25, 0.94)$ cm^2s^{-1}. Break-up occurred in the range $Q_{T,thr} \in [0.58, 0.93]$ cm^2s^{-1}, so that the red square representing $\max(Q_{T,thr})$ is plotted at $(Q_1, Q_2) = (0.25, 0.68)$ cm^2s^{-1} and the red circle representing $\min(Q_{T,thr})$ at $(Q_1, Q_2) = (0.25, 0.33)$ cm^2s^{-1}. This process is repeated to plot the other vertical lines in Figure 4.8, and again the blue vertical line corresponds to the range of flow rates that curtain formation occurred, the vertical red line to the range of flow rates that break-up occurred and the dashed vertical line to the true hysteresis window.

We would expect (if the two-layer curtain does indeed behave the same as the single-layer curtain) the solid blue circle to lie on the solid blue diagonal line, the solid blue square to lie on the dashed blue diagonal line, and so on. This holds true for Figure 4.8(c), where $\max(Q_{T,min}) = \max(Q_{min})$ in both cases. However, $\min(Q_{T,min}) < \min(Q_{min})$, which holds in each other subfigure (a), (b) and (d); with $\max(Q_{T,min}) < \max(Q_{min})$ in each of (a), (b) and (d) also. Thus Figure 4.8 indicates $Q_{T,min} \leqslant Q_{min}$, and physically corresponds to a two-layer curtain not requiring as high a flow rate, compared to the single-layer case, to form a stable curtain. The physical explanation for this remains the topic of future research.

Considering curtain break-up, in general we have that $\min(Q_{T,thr}) \geqslant \min(Q_{thr})$, de-

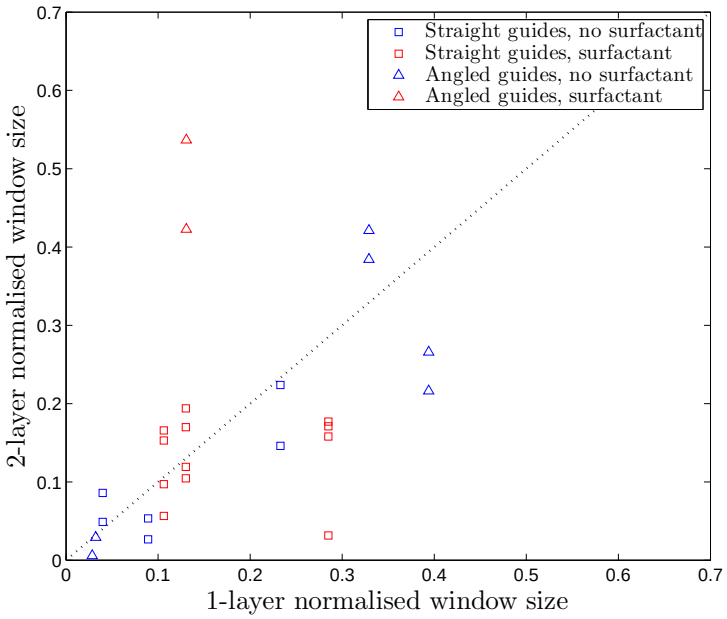

Figure 4.9: A comparison between the normalised hysteresis window size for single and two-layer curtains. The legend indicates which data points correspond to whether straight or angled edge guides were used, as well as if the fluid contained surfactant. The dashed line indicates parity.

spite a couple of red circles lying just below the diagonal red line in the cases when using 87% glycerol, in (c) and (d). We observe when using the straight edge guides, in (a) and (c), that $\max(Q_{T,thr}) \approx \max(Q_{thr})$, as the open red squares are located extremely close to the dashed red line. This feature does not follow when using the angled edge guides, in (b) and (d), where $\max(Q_{T,thr})$ is found both clearly above and below the dashed red line. This discrepancy results in the two-layer hysteresis window in (b) being larger than expected from the single-layer experiments, yet the two-layer windows are smaller in each of the other subfigures.

To obtain a quantitative comparison of hysteresis window size, Figure 4.9 plots the normalised window size for the two-layer experiments against the normalised window size for the single-layer experiments. Following from Figure 4.8, despite the majority of data points lying in a vicinity close to or below the parity line, there is a distribution both above and below parity. Similar to previous results on the hysteresis phenomenon, a

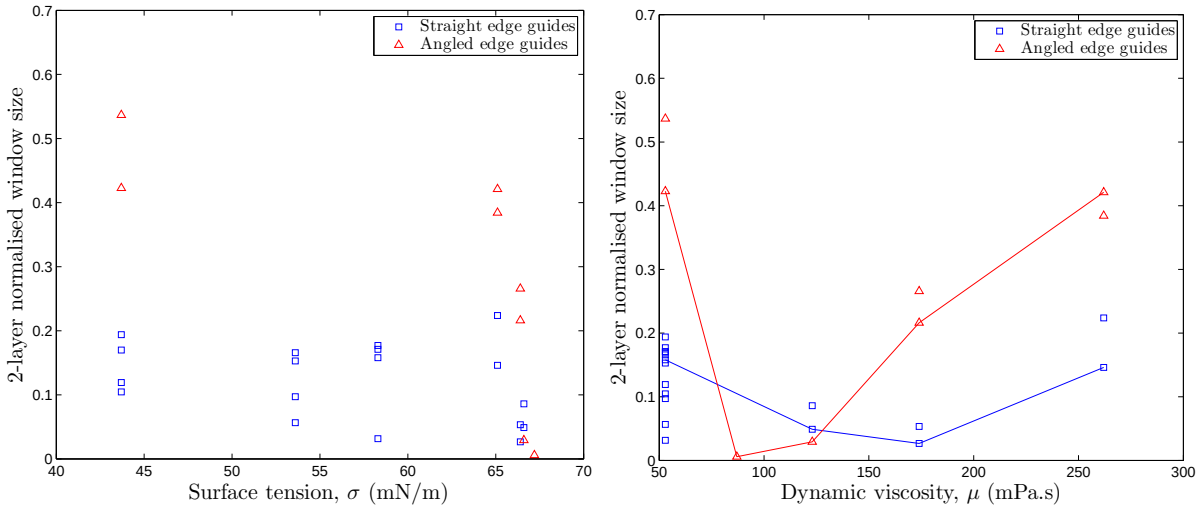

(a) (b)

Figure 4.10: Fluid properties plotted against normalised hysteresis window size; in (a) surface tension and in (b) dynamic viscosity (all two-layer).

physical explanation for the results of Figure 4.9 is the subject to future work, with this investigation providing a foundation for future studies on this topic, which is lacking in the literature.

Figure 4.10 plots the normalised window size against the (a) surface tension and (b) dynamic viscosity, for all two-layer curtain experiments. Similar to the single-layer case in Figure 4.7, surface tension has no effect on the normalised window size for two-layer curtains. In particular for experiments using the straight edge guides in Fig 4.10(a), we see for experiments at a fixed surface tension value (the change in the experiment comes from using a different fixed value of Q_1) a range in normalised window size. Moreover, in (a), the experiments using the angled guides have a larger window size, apart from a couple of anomalies; also seen in Figures 4.9 and 4.10(b). This corresponds to the flow rate at which the curtain was formed being approximately the same as with the straight guides, but the flow rate at which break-up occurred being lower due to the increased stability with the angled guides (see Section 4.4).

The same trend as the single-layer curtains is seen in Figure 4.10(b), whereby the

size of the normalised window initially decreases as viscosity increases from the least viscous fluid to a value $\mu \approx 100$ mPa.s. As the viscosity continues to increase so does the normalised window size, and continues to increase to the highest viscosity fluids; a trend that is seen more readily when the angled edge guides were used (see Section 4.4).

4.4 Results: break-up origins and rupture speed

4.4.1 Break-up origins

Boundary layer at edge guides

As discussed in Section 4.1, it is well known that using solid edge guides results in a boundary layer in the vicinity of the edge guides, with the thickness of this layer dependent on both the liquid properties and the length of the solid edge guide [102]. Following Schlichting and Gersten [102], an estimation of the boundary layer thickness δ is obtained upon balancing inertial forces and friction forces which are in equilibrium in the boundary layer, resulting in the relation

$$\frac{\rho U_\infty^2}{z} \sim \mu \frac{U_\infty}{\delta^2}. \tag{4.4.1}$$

Here, z is the vertical distance from the die-lip and U_∞ is the streamwise velocity of the flow outside of the boundary layer, which in the case of curtain flow corresponds to the local curtain velocity $v_c(z)$, given by (4.1.6).

Rearranging equation (4.4.1), and substituting the streamwise velocity of the flow outside the boundary layer U_∞ with the curtain velocity v_c, the boundary layer thickness is given by

$$\delta \sim \sqrt{\frac{\mu z}{\rho v_c}}.$$

As explained in [102], this relation becomes an equality with the inclusion of an unknown numerical factor. Using the solution of Blasius [16], a laminar boundary layer at a plate

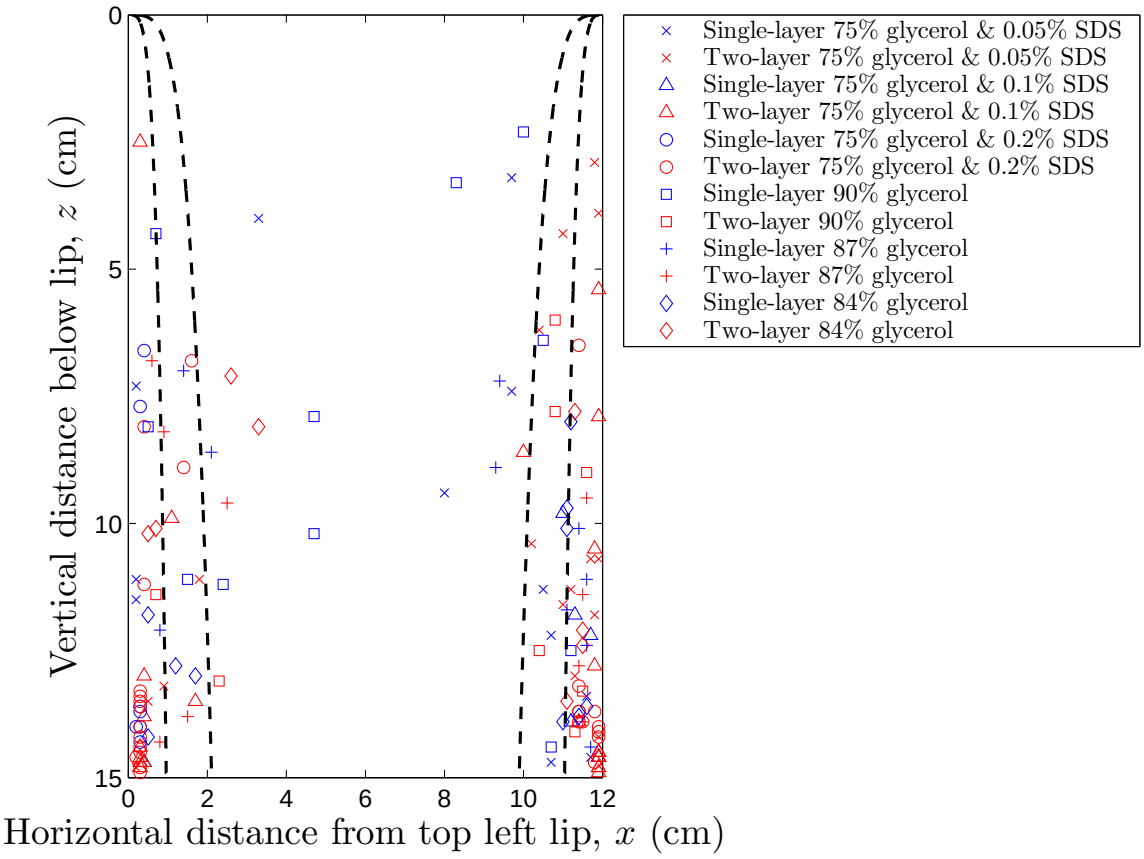

Figure 4.11: Plot showing the break-up origin of all 149 experiments, both single-layer (blue) and two-layer (red), conducted using the straight edge guides. The two dashed lines correspond to the extent of the minimum and maximum boundary layer, calculated using equation (4.4.2), that are given from the 75% glycerol (with surfactant) solutions and the 90% glycerol solutions respectively.

of zero incidence has thickness:

$$\delta \approx 4.91\sqrt{\frac{\mu z}{\rho v_c}}, \tag{4.4.2}$$

which can be used as an estimation for the boundary layer thickness when using the straight edge guides.

Figure 4.11 shows the origin of break-up for 149 experiments, for all single and two-layer experiments conducted with the straight edge guides. The dashed lines correspond to the minimum and maximum boundary layers calculated using (4.4.2). Here, the smallest boundary layer size came from the 75% glycerol (with SDS) fluids, the fluid with the

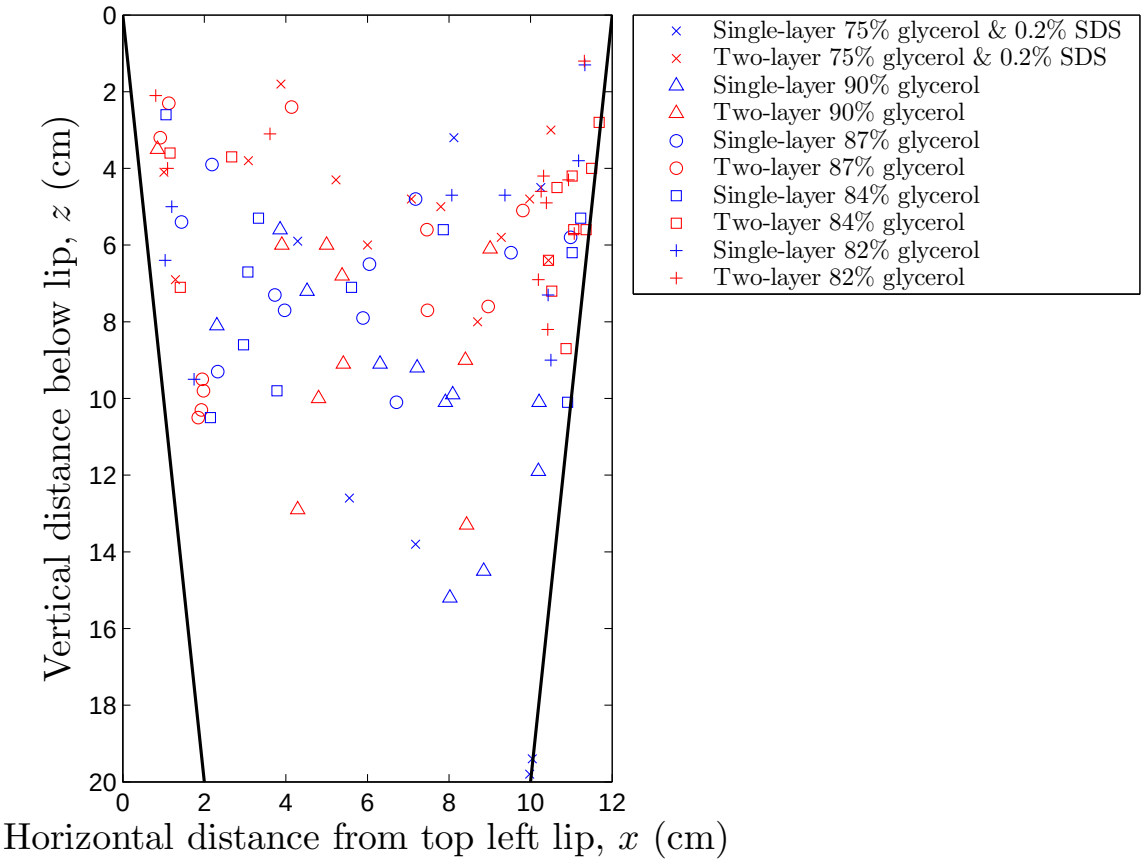

Figure 4.12: Plot showing the break-up origin of all 106 experiments, both single-layer (blue) and two-layer (red), conducted using the angled edge guides. The solid black lines correspond to the location of the edge guides.

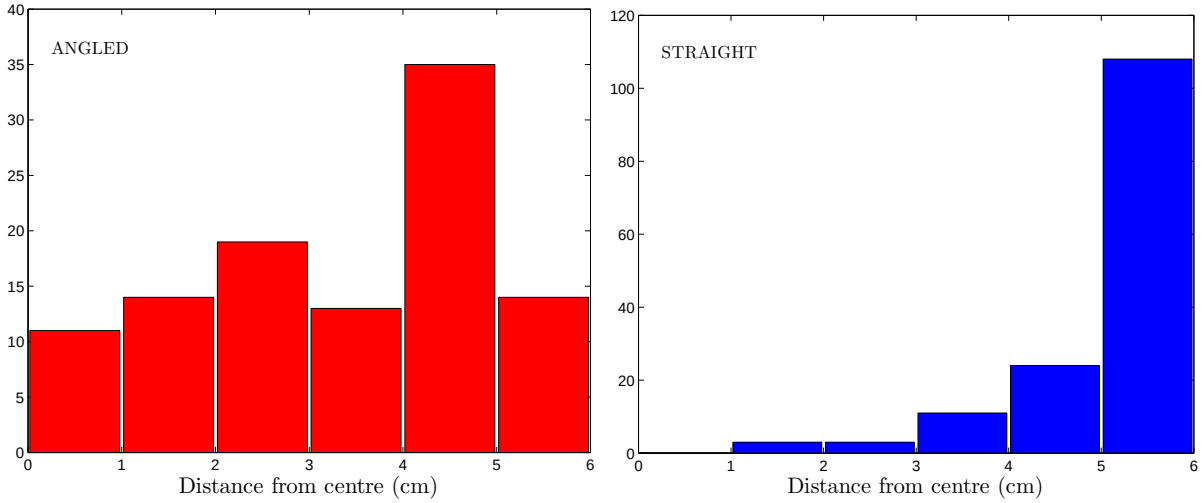

(a) (b)

Figure 4.13: Distance from the centre of the curtain that the break-up originates, for (a) straight and (b) angled guides. All 255 experiments from Figures 4.11 and 4.12 are plotted.

lowest viscosity. The largest boundary layer occurred with the 90% glycerol solution, the fluid with the largest viscosity. In general, the majority of break-ups originate from within 1–2 cm of the straight edge guides. Conversely, the break-up origins for the angled guides, shown in Figure 4.12, are more evenly distributed across the width of the curtain. This can be readily seen in Figure 4.13, where all of the experimental data from the video sequences is included. When using the straight edge guides, there is a clear bias towards the edge regions coinciding with the possible boundary layer thickness from equation (4.4.2).

When using the vertical edge guides, the flow near the edge regions has previously been explained by Miyamoto and Katagiri [85], emphasising the complicated nature of edge stability. The inherent development of a boundary layer induces lateral flow towards the centre of the curtain, creating a local thinning near the edge guides, which in addition to the slower velocities in this region, means that the curtain is more prone to break-up here compared to the central region. However, the wettability of the edge guides will also play

a role in the stability of the curtain within the boundary layer, by inducing a capillary force that draws liquid *towards* the edge region, acting to thicken the sheet here. There is then a competition between these two effects, which are both dependent on the physical properties of the liquids being used and the properties of the edge guides themselves. The complex nature of the curtain flow in close proximity to the edge guides is also discussed by Schweizer [104] in a patent designed to dampen instabilities that result from boundary layer effects.

When using a tapered guide, so that the curtain width is smaller at the bottom of the curtain, the mechanisms affecting the curtain thickness near the edge guides is altered. The free-falling liquid curtain will now 'hit' the edge guides due to the tapering inwards, meaning that the curtain acceleration is decreased close to the edge guides. This, along with capillarity effects drawing liquid towards the edge regions, results in the thinning in the curtain to be countered, increasing the stability compared to the straight guides. Conversely, the central region of the curtain is less likely to be affected as it will continue to accelerate uniformly under gravity, resulting in the curtain being at its thinnest in the centre (for any given height). Hence we would expect more break-ups to occur in the central regions for the angled guides, which we do clearly observe from Figures 4.12 and 4.13.

Moreover, it is clear from Figure 4.12 that the majority of break-ups occur in the top half of the curtain. As previously seen in Figure 4.2.2, the curtain thickness when using the angled guides remains near constant in the bottom half of the curtain, particularly at the flow rates of break up ($Q \approx 1$ cm^{2}s^{-1}). Despite this, the velocity of the curtain continues to increase in the streamwise direction, as the free-fall velocity (4.1.5). This means that in the bottom half of the curtain, a disturbance is more likely to be 'flushed' away with the flow of the curtain; resulting in a disturbance that causes break-up more likely to occur in the top half of the curtain.

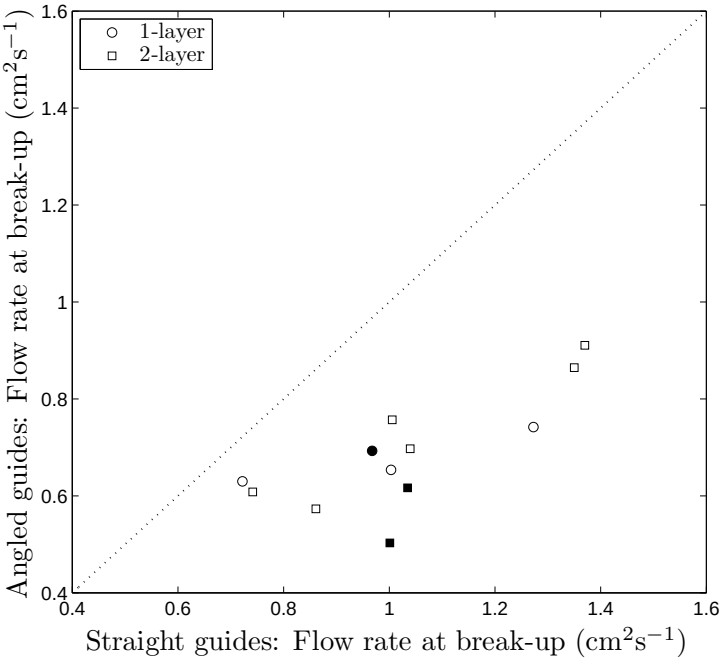

Figure 4.14: The flow rate per unit width at break-up when using straight and angled guides. The average flow rate is used for each configuration (i.e. different fluids and number of layers). The filled markers indicate the fluid contained surfactant.

Figure 4.14 plots the flow rate per unit width at break-up when the angled edge guides were used against when the straight edge guides were used. Equation (4.2.1) was used to calculate the flow rate when the angled guides were employed. The average flow rate at break-up for each configuration, that is for each different fluid when both sets of edge guides were used, and for single and two-layer experiments, is plotted. All of the data points lie below parity, clearly showing that the flow rate at break-up is lower when the angled guides were used for every case, confirming that the angled guides do indeed increase the stability of the liquid curtain.

4.4.2 Rupture speed

As previously seen, Figure 4.5 shows a series of frame snapshots of the liquid curtain puncturing, with the resulting hole growth. By measuring the hole radius against time, the speed of curtain rupture can be determined; to calculate the hole radius r, the distance

between the top-most and bottom-most part of the hole, D_{TB} was measured, as well as the distance between the left-most and right-most part of the circle, D_{LR}, as shown in Figure 4.5(d). By doing this for each subsequent frame after a hole opening, one can then plot the radius of the hole against time, using both the vertical ($r_{TB} = 0.5D_{TB}$) and horizontal ($r_{LR} = 0.5D_{LR}$) extent of the opening. This is done for four different examples in Figure 4.15, all being two-layer curtains using 87% glycerol in (a) and 75% glycerol with 0.2% SDS in (b), with both the straight and angled edge guides being employed. In both Figures 4.15 (a) and (b) there is no discernible difference between the vertical (circle markers) and horizontal (square markers) radius measurements.

There is a clear linear relationship between the measured hole radius and time, demonstrating a constant opening speed of the hole in the experiments. By using a least squares linear regression model, taking the hole radius to be zero at time $t = 0$ (i.e. the y-intercept is zero), all that needs to be found is the gradient, β, for the line of best fit. This is done using the formula

$$\beta = \frac{\sum_{i=1}^{n} (r_{i,TB} t_i) + \sum_{i=1}^{n} (r_{i,LR} t_i)}{2 \sum_{i=1}^{n} t_i^2}, \tag{4.4.3}$$

where n is the number of frames whereby the vertical and horizontal radii, $r_{i,TB}$ and $r_{i,LR}$, were measured at each time step t_i from the initial hole opening. Typically, $n \approx 10$ before the edge of the hole reached one of the edge guides, the die lip or the bottom of the curtain, corresponding to a time $t \approx 0.02$ s.

The gradient of the lines of best fit in Figure 4.15, given by (4.4.3), are used as the experimental values of the hole opening speed, to compare with the theoretical Taylor-Culick speed given in (4.1.1). As a measure of how well the line of best fit matches with the experimental data, the coefficient of determination R^2 is calculated for each example

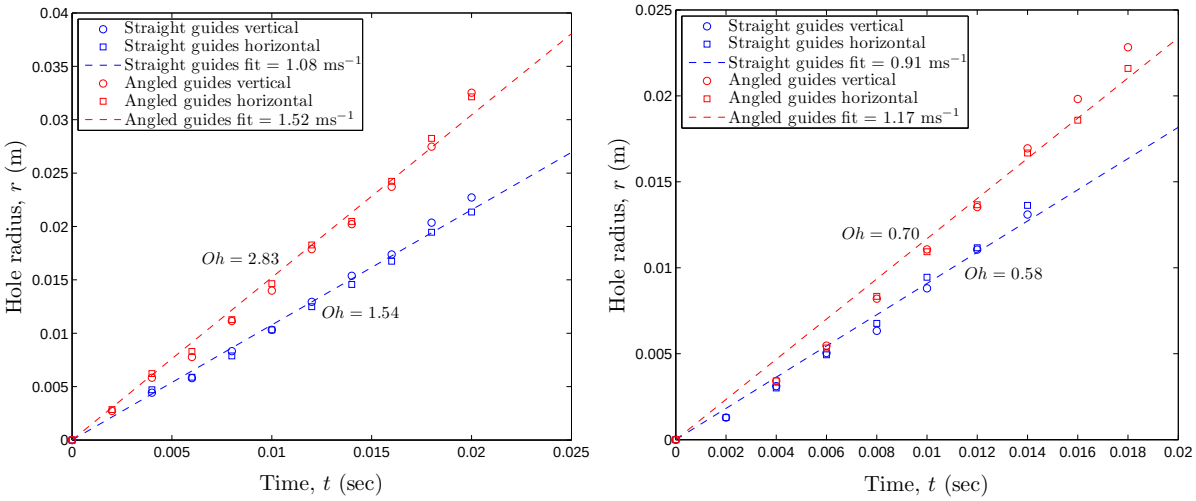

(a) 87% glycerol (b) 75% glycerol with 0.2% SDS

Figure 4.15: Hole radius against time for experiments using (a) 87% glycerol and (b) 75% glycerol with 0.2% SDS, showing the experimental speed of hole growth to compare with (4.1.1). The Ohnesorge numbers are indicated within the plots. In (a) $R^2 = 0.994$ for the straight guides and $R^2 = 0.992$ for the angled guides. In (b) $R^2 = 0.987$ for the straight guides and $R^2 = 0.981$ for the angled guides.

in Figure 4.15, and noted in the caption[4].

The Taylor-Culick speed assumes a constant thickness of the liquid sheet, H, and for this we use the local sheet thickness given by the equation $H = Q_T/v_c$, where the local curtain velocity is given by (4.1.6). In Figure 4.15(a), the Taylor-Culick speed is given by 1.18 ms^{-1} for the straight guides and 1.44 ms^{-1} for the angled guides, compared to the experimental results of 1.08 ms^{-1} and 1.52 ms^{-1}. In Figure 4.15(b), the Taylor-Culick speed is given by 0.95 ms^{-1} for the straight guides and 1.15 ms^{-1} for the angled guides, compared to the experimental results of 0.91 ms^{-1} and 1.17 ms^{-1}.

Referenced within the plots of Figure 4.15 is the Ohnesorge number in each case, calculated from (4.1.3). Considering all of the experiments carried out on the rupture speed, we have a range of $0.33 \leqslant Oh \leqslant 3.40$, within the moderate Oh regime as described

[4]The coefficient of determination is a measure of how well a line of best fit matches with given data, given as a value between 0 and 1, with 1 showing a perfect fit. It is given by the formula: $R^2 = 1 - \left[\sum_{i=1}^{n} (r_i - \beta t_i)^2 / \sum_{i=1}^{n} (r_i - (\sum_{i=1}^{n} r_i)/n)^2\right]$.

in section 5.1. Referencing back in particular to Figure 4.1, in all of our experiments the hole should experience a growing rim at the film edge, with no capillary waves preceding the rim. This indeed is the case in Figure 4.5.

An interesting figure in the work of Sünderhauf *et al.* [108] plotted the non-dimensional retraction speed, using U_{TC} from (4.1.1) as the velocity scale, against non-dimensional time, using τ from (4.1.4) as the timescale, for different values of Oh. We can compare their numerical work with our experiments. For instance, consider the angled guide experiment from Figure 4.15(a). With a knowledge of the break-up location, using (4.2.2) to calculate H at that point, we can calculate the timescale τ from (4.1.4), which in this case is given by $\tau = 3.64 \times 10^{-5}$ s. When $t^* = t/\tau = 100$, meaning when $t = 0.0036$ s, for the case $Oh = 2.83$, the retraction speed should be $0.97U_{TC}$, from [108].

Using this method, for the examples in Figure 4.15, the retraction velocities should all be at a value of at least $0.975U_{TC}$ within 0.0084 s of the initial rupture. This demonstrates that in the Oh-regime studied in these experiments, the acceleration towards U_{TC} is made quickly, and that the timescales in which we analyse the hole opening the Taylor-Culick speed should, theoretically, be very nearly reached.

An overall comparison is made in Figure 4.16, whereby the hole opening speed determined experimentally is plotted against the Taylor-Culick speed for 32 realisations. The majority of data points are clustered around the dashed line, indicating parity, showing good agreement between the experimental retraction speed and the Taylor-Culick speed. Interestingly, all of the break-ups analysed when using the straight edge guides (red markers) occurred at a speed slightly less than or equal to the Taylor-Culick speed. Apart from a few anomalies, the opposite holds for when the angled guides were employed, whereby the experimental speed is, in general, more than or equal to the Taylor-Culick speed.

This may be explained by the arguments discussed in the previous section regarding the curtain thickness; in the central regions of the curtain, where the break-ups analysed

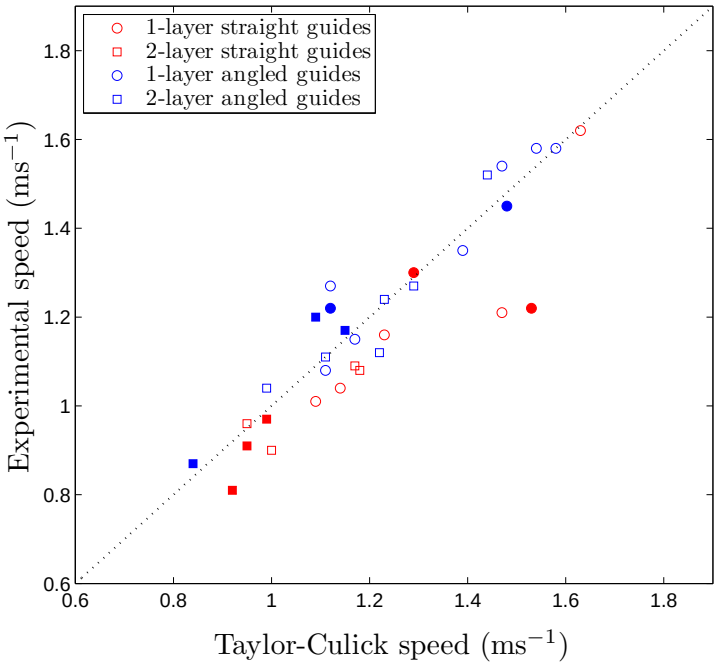

Figure 4.16: The theoretical Taylor-Culick speed plotted against the measured experimental speed of hole opening. The filled markers indicate surfactant-laden fluids, whilst the open markers contain no surfactant. The dashed line represents parity. In total, 32 experiments have been plotted.

in Figure 4.16 originated, the formula for H used to calculate U_{TC}, equation (4.2.2), will overestimate the thickness when using the straight guides and underestimate the thickness when using the angled guides. Despite the good agreement, this results in U_{TC} having a slightly larger value than expected with the straight guides, and the converse when the angled guide are employed.

4.5 Conclusion

To conclude, an experimental investigation of the formation and break-up of single and two-layer liquid curtains has been performed. Both the minimum flow rate at which a stable curtain could be formed, $Q_{T,min}$, and the flow rate at which break-up occurred, $Q_{T,thr}$, were assessed; the difference between these two flow rates defines a hysteresis window, whereby a stable curtain remains if lowering the flow rate from a value above

$Q_{T,min}$, but a curtain is unable to form if raising the flow rate from $Q_{T,thr}$.

In general, the range of flow rates for $Q_{T,min}$ was much smaller compared to $Q_{T,thr}$, attributed to the much more repeatable procedure of curtain formation as opposed to break-up, whereby the complex dynamics of the flow near the edge guides, the differential motion between layers and migration of surfactant all play a role. The normalised hysteresis window was defined, and plotted against surface tension and viscosity. Whilst there was no clear relation with surface tension, the window size decreased to a minimum when the dynamic viscosity $\mu \approx 100$ mPa.s, before increasing with increased viscosity for both single and two-layer curtains. When comparing the hysteresis window size of single and two-layer curtains comprising of the same fluid, whilst in general they are of comparable size (with the majority of data points clustered near parity in Figure 4.9), there were also certain cases whereby the window size was clearly larger or smaller than its counterpart, reasoned, again, by the complex nature of curtain break-up associated with curtain coating.

Moreover, determined from high-speed imaging, the origins of break-up were determined and found to be highly dependent on the edge guides used. The break-up origin, when using the straight guides, was normally confined to within 2 cm of the edge, coinciding with the boundary layer determined in equation (4.4.2). Also, the majority of break-ups occurred towards the bottom of the curtain, where it is at its thinnest. The converse was found when the angled guides were employed, with break-ups occurring across the full width of the curtain, and the majority in the top half of the curtain. We also confirmed that using the tapered guides increases the stability of the curtain with all flow rates reducing to a lower value (compared to the straight guides) before the curtain became unstable.

As well as the initial location of break-up, the speed at which the hole opened in the liquid curtain was analysed. The Ohnesorge number was in the range $0.33 \leqslant Oh \leqslant 3.40$

for all experiments, so that the receding film edge had a growing rim, with no capillary waves preceding it, based on previous numerical studies [101, 108]. At these values of Oh the hole opening speed also accelerates quickly to the Taylor-Culick speed U_{TC}, and within the timescale of the hole reaching an edge of the curtain in our experiments the retraction speed should be extremely close to U_{TC}. Figure 4.16 showed good agreement between the experimental speed observed and U_{TC}, with the slight differences explained by the approximation of the curtain thickness H, calculated via (4.2.2), used in the formula for the Taylor-Culick speed (4.1.1), for both the straight and angled guides.

Chapter 5

Thin film flow along an inverted inclined plane with the effect of surfactant

5.1 Introduction

In the previous chapter we investigated experimentally the free falling liquid curtain that is formed during the curtain coating process. In particular when break-up occurs, studying both the origin of the rupture, which manifests itself in the form of a hole opening, and the speed at which the hole grows, measured and compared to the Taylor-Culick speed of liquid sheet retraction. In this chapter, we examine a feature similar to which happens after break-up occurs in the liquid curtain.

As previously seen when discussing the hysteresis phenomenon in the previous chapter, once the liquid curtain disintegrates (or before forming a liquid curtain pinned to the edge guides), different formations occur as the liquid leaves the die lip (the reader is referred back to Figure 4.4). When the liquid congregates at the die lip, it is unstable with respect to gravity and, dependent on the flow rate, a series of drops or jets are formed. If the

Figure 5.1: An array of liquid jets (or columns) emanating from the die lip, with a regular spacing between the centreline of each individual jet.

flow rate is raised further, the formation of a triangular liquid sheet is formed, which can then be pinned to the edge guides to obtain the desired curtain coating set-up.

When considering the array of liquid jets that emanate from the die lip, one striking feature is the spacing between each individual jet which, under certain flow rates, is regular. This can be observed in Figure 5.1, whereby there is a series of ten liquid columns, with the consistent spacing between the jets readily seen. This spacing is due to a mechanism similar to the Rayleigh-Taylor instability, whereby the liquid film 'congregates' at the die-lip and is unstable due to the effect of gravity. Figure 5.2 depicts a schematic of the Rayleigh-Taylor instability. However, although similar, to model the jet spacing of Figure 5.1 accurately a three-dimensional model would need to be considered.

The work presented in this chapter considers a related two-dimensional model of a multi-layered liquid film flowing on the underside of an inclined plane, and thus unstable due to gravity. Despite being related, it is noted that this would not model the regular

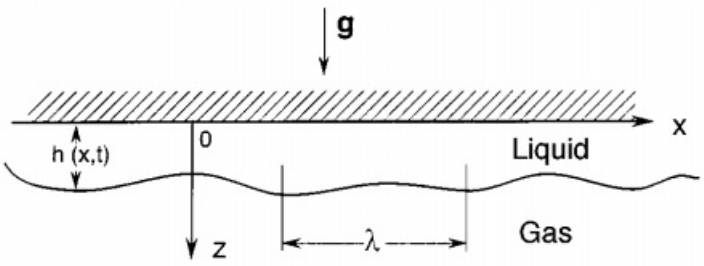

Figure 5.2: A thin liquid film, suspended beneath a horizontal solid surface, taken from Oron *et al.* [91]. The most unstable wavelength labelled λ corresponds to the Rayleigh-Taylor wavelength given by (5.1.1).

spacing of the liquid jets as shown in Figure 5.1, but provides an interesting study in its own right. By also considering the effect of surfactant, similar theoretical work from Chapter 3 is utilised, and an extension of current works in the literature is presented. Preceding that we briefly review a number of related studies in the literature, including the different formations observed from a liquid film falling due to gravity from a solid interface.

The changing formations that occur at different flow rates from the coating die in our experimental set-up have been observed and studied on numerous occasions in the past, for varying arrangements. Pritchard [93] noted experimentally over 256 different configurations of liquid flowing over the edge of a horizontal plate, including a regularly spaced array of liquid jets. It was shown how the regularity of the spacing was dependent on the flow rate, and that at certain flow rates the jets demonstrated movement in the transverse direction described as 'a complicated dance' by Pritchard, a motion that even exhibited chaotic properties. This transverse motion has been noted in experiments conducted by the author of this thesis, as described in Appendix C. De Luca and Meola [34], similarly examined the spacing of threads after liquid sheet break-up, plotting the average thread spacing against surface tension, finding good agreement with Pritchard for similar surface tension values.

Similar experiments conducted by Giorgiutti *et al.* [49], under a different experimental

set-up, had the liquid jets departing a circular geometry instead of a horizontal plate. Silicone oil was fed upwards into a vertical tube, with constant flow rate, whereby upon reaching the top, the tube overflowed and wetted the outside of a circular plastic container of 5 cm radius. At the foot of this circular container the silicone oil departed in a spatially periodic array of liquid jets. By touching a jet with a needle, Giorgiutti *et al.* forced the motion of the liquid columns forming a 'dilation wave' with a number of drifting jets moving around the perimeter. Analogous experimental work, studying a circular array of liquid columns, carried out by Counillon *et al.* [29] considered a global drift, whereby all of the jets are forced to move, initiated with the regular motion of a needle. Similar to [93], chaotic motion was also observed in this circular set-up by Brunet *et al.* [22].

Limat *et al.* [73] considered a horizontal half cylinder, made to be hollow and overflowing with silicone oil, so that the liquid would wet the outside of the half-cylinder and gather at the bottom, unstable with respect to gravity, and hence form falling drops or jets, dependent on the flow rate. The flow rate at which the dripping to jetting transition occurred was examined, and the corresponding Reynolds number; good agreement was found with the work of Pritchard [93]. The 'dancing' jets reported by Pritchard were also observed by Limat *et al.*, where liquid columns oscillated, resulting in both coalescence and nucleation of jets. Unlike the previous works mentioned studying this circular array of jets, this behaviour manifested itself unforced in the large timescale.

Limat *et al.* [73] also discussed the regular spacing between the jets when no transverse oscillations were present. The spacing was found to be close to the Rayleigh-Taylor wavelength [73]:

$$\lambda_{RT} = 2\pi\sqrt{\frac{2\sigma}{\rho g}}, \tag{5.1.1}$$

corresponding to the most unstable mode from a linear stability analysis of a thin film suspended on the underside of a horizontal surface in air. Here, σ is the constant surface tension of the interface, ρ the density of the liquid, and g the gravitational constant.

A similar study conducted by Giorgiutti *et al.* [48] controlled the flow rate at which silicone oil left a thin slot at the top of a horizontal cylinder, measured as a flow rate per unit length. Again, the silicone oil wets the surface and flows to the bottom of the cylinder, before detaching due to gravity. Giorgiutti *et al.* found below a threshold flow rate ($Q \approx 0.1$ cm^{2}s^{-1}), a number of dripping sites formed with a well-defined special periodicity extremely close to the Rayleigh-Taylor wavelength (5.1.1) of a thin layer.

Interestingly, above the threshold flow rate, liquid jets formed with a shorter spacing between each column of liquid; a decrease between 0.07-0.17 cm of the predicted distance by (5.1.1). By placing two needles in contact with the cylinder, facing vertically downwards, and changing the distance between the two, different mechanisms were observed. This included the coalescence of the liquid columns, as well as oscillations similarly witnessed previously by Pritchard [93] and Limat *et al.* [73]. Spatial-temporal diagrams were plotted, and indeed, the transverse oscillations were found to be chaotic, often followed by the nucleation of a new column after a variable time that halted the oscillations.

There has been much work in the literature on the aforementioned Rayleigh-Taylor instability, which is caused by a difference in densities at a fluid-fluid interface, with an acceleration (commonly gravity) applied from the heavier fluid into the lighter fluid [109]. This phenomenon occurs in a variety of settings, ranging from the dripping of liquid from a ceiling [23] to supernova explosions [59]. In a review of the evolution of thin films, Oron *et al.* [91] considered the case of a thin liquid film suspended underneath a horizontal surface, as shown in Figure 5.2. The cut-off wavenumber (above which all disturbances are stable) has sole dependence on the Bond number, the ratio between gravitational and surface tension forces. Gravity acts to destabilise the thin film, whilst surface tension acts to keep the film flat. Similar results were obtained by Yiantsios and Higgins [121], who performed an asymptotic analysis of a thin viscous film laying horizontally on top of a surface, above which lies a semi-infinite fluid layer with higher density.

Further theoretical and experimental investigations on the Rayleigh-Taylor instability have been conducted, for example the work of Fermigier *et al.* [44]. In this study, a drop of silicone oil was left to spread, by gravity, on top of a glass plate 30 cm in diameter, producing a thin film a fraction of a millimetre in thickness[1]. The glass plate was quickly flipped 180 degrees, with different patterns observed as the Rayleigh-Taylor instability developed; two-dimensional patterns with different symmetries, including concentric rings and hexagonal patterns. A theoretical model followed, applying the lubrication approximation to Stokes flow, with an evolution equation for the film thickness derived preceding a stability analysis, in which the Rayleigh-Taylor wavelength was recovered as the most unstable mode. Further investigations have included how to damp out the Rayleigh-Taylor instability, considering a thin film within the annulus of a cylinder [113], whereby the curvature damps out the instability, and the suppression by the Marangoni effect [7] via an uneven temperature distribution created by heating the liquid.

A similar model is derived in this chapter, examining a multi-layer film flowing along the underside of an inclined plane, and thus unstable due to the Rayleigh-Taylor instability. The model we derive in this chapter is two-dimensional, incorporating the fresh supply of liquid arriving in each liquid layer, at a pre-determined flow rate. Moreover, the effect of surfactant (introduced in detail in Chapters 2 and 3) is also considered. Surfactant decreases the surface tension of a liquid, with the surface tension no longer a constant, but a variable dependent upon the local surfactant concentration. A constant surface tension is considered in (5.1.1).

We consider inclining the horizontal surface of Figure 5.2 at a small angle θ to the horizontal, as shown in Figure 5.3. In this schematic, we can model the thin film with an incoming flow-rate for each layer, and by considering the case of a *small* angle θ, the now

[1]Due to having a low surface tension, silicone oil wets a surface extremely well. To obtain a complete spread of silicone oil over a 30 cm diameter, a drop was left for two days. In this time it was possible for solid particles (e.g. dust) to acquire at the surface, affecting the experimental results by providing an initial perturbation, as noted by the authors.

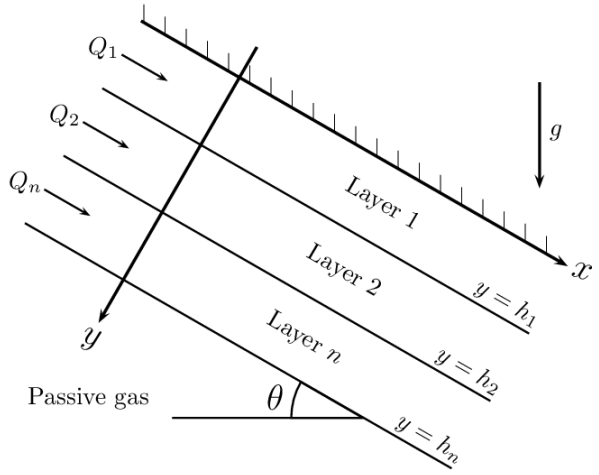

Figure 5.3: Schematic of the multi-layered film on the underside of an inclined plane. We consider a small angle θ, so that the inclined plane is near-horizontal.

inclined plane remains at near-horizontal, with the thin film flowing on the underside of the plane.

Despite the vast number of works in the literature on a falling film along an incline (the reader is referred to the introduction of Chapter 2 for a brief review) there have been less works on the inverted situation, whereby the thin liquid film is on the underside of an inclined plane as in Figure 5.3.

Lin and Kondic [77] considered the two-dimensional flow including the front of the film, encompassing the effect of a dynamic contact line to waves on the free surface. Applying the lubrication approximation and ignoring inertial effects, a capillary ridge was found to form immediately behind the film front. The same authors [78] extended this work to three dimensions, focussing on the coupling between surface instabilities and the instabilities at the front of the film (fingering instabilities in the transverse direction). Several works on rivulet flow on the underside of an inclined cylinder (for example Alekseenko *et al.* [6], Indeikina *et al.* [55]) have observed similar dripping and jetting mechanisms due to the Rayleigh-Taylor instability, with analogous results [83] when considering the fingering instability.

Brun *et al.* [21] investigated the effect of the inclination angle of a thin liquid film spread on the underside of a flat surface, from near horizontal to vertical, in both a theoretical and experimental investigation. Conducting a linear stability analysis, the flow was found to be temporally unstable for all inclination angles in this range, with the most unstable wavelength given by

$$\lambda^* = 2\pi\sqrt{\frac{2\sigma}{\rho g \cos\theta}}, \tag{5.1.2}$$

intuitively making sense with the gravity term in (5.1.1) being replaced with an effective gravity $g\cos\theta$, where the Rayleigh-Taylor wavelength (5.1.1) is recovered in the case of the solid surface being horizontal. From their linear stability analysis, one could conclude that dripping occurs at every angle except vertical, contradicting their experimental observations, whereby above a cut-off angle no dripping occurred. This contradiction was overcome by considering an absolute analysis, whereby both the wavenumber and frequency in the stability analysis was considered complex. If the plate is tilted far enough towards vertical, any disturbance is carried away by advection. When nearer horizontal, the instability overcomes the film flow; the flow is weaker in this case and has no effect on the Rayleigh-Taylor instability.

Thus the primary aim of this chapter is to model thin film flow on the underside of an inclined plane, such that the incline is close to horizontal, considering two cases: a single-layered film and a two-layered film. We incorporate the effect of an insoluble surfactant, so that the surface tension of the free surface (and the interfacial tension of the liquid-liquid interface in the two-layered case) becomes a variable, dependent on the local surfactant concentration. In Chapter 3, it was assumed that surfactant would not affect the liquid-liquid interface of the free-falling curtain. This is not assumed in the two-layer model of this chapter, as explained in more detail in the proceeding section.

Assuming the film has a much larger length compared to its width, we conduct an asymptotic analysis, solving the leading order system and finding evolution equations for the film heights and surfactant concentration along the interfaces. Perturbing these evolution equations, conducting a linear stability analysis, we obtain a dispersion relation for both the single and two-layer case, which is solved to find different properties of the stability; namely the most unstable wavenumber, cut-off wavenumber (above which all disturbances are stable) and maximum growth rate. Moreover, we investigate the effect of changing the inclination angle, as well as the effectiveness of the surfactant (changing the surface activity number), on the features of stability.

5.2 Mathematical model

As explained in Section 5.1, we consider a cross-section of both a single and two-layered film flowing on the underside of a plane inclined at an angle θ to the horizontal, as shown in the schematic Figure 5.4. Subfigure (a) shows the single-layer case and (b) the two-layer case. The coordinate system is chosen such that the inclined plane is the x-axis, with the y-axis perpendicular pointing in the direction of the free surface of the multi-layered film.

We formulate the model in the two-layer case up until Section 5.2.3, when calculating the leading order solutions, from which point on we split the work explicitly into the two separate (single and two-layer) cases. Before Section 5.2.3, the two-layer case collapses to the single-layer case with the same free surface conditions, disregarding the liquid-liquid interface conditions, and dropping any subscripts on the variables. Throughout this chapter a subscript j refers to $j \in \{1, 2\}$, where $j = 1$ corresponds to layer 1, and $j = 2$ corresponds to layer 2, shown in Figure 5.4(b).

The viscosities (μ_1 and μ_2) and densities (ρ_1 and ρ_2) in each layer are considered constant. The interfacial tensions of the liquid-liquid interface and the free surface, σ_j, are

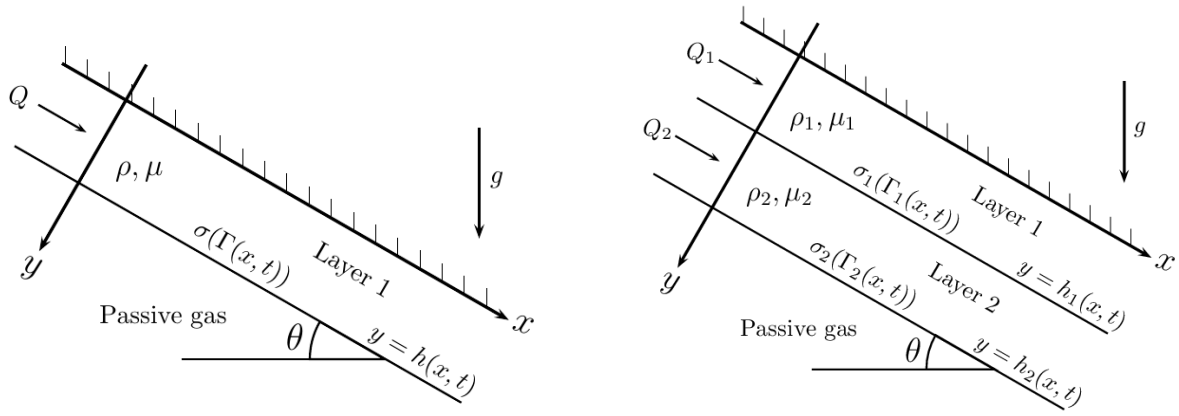

Figure 5.4: Schematics of the (a) single-layer and (b) two-layer systems considered in the mathematical model. Note the difference in notation; the variables in the single-layer case have no subscript, whereas the variables in the two-layer case either have a subscript 1 or 2, dependent on the layer.

considered as a function of the local surfactant concentration Γ_j on each of the interfaces $y = h_j$.

In the work conducted in Chapter 3, the interfacial tension of the liquid-liquid interface was considered constant; explained due to the amphipathic nature of surfactant molecules, they favour residing on the free surface as opposed to the liquid-liquid interface. In the two-layer case considered here, we assume that the insoluble surfactant in the first layer will reside at the liquid-liquid interface between the two layers, with the hydrophylic 'head' of the surfactant molecule residing in the more aqueous layer.

Due to the complex nature of surfactant adsorbtion, understanding the dynamics of surfactant at a liquid-liquid interface is a research topic in its own right (see, for example, [68, 105]). For instance, it may be more energetically favourable for the surfactant to form micelles within the bulk of the liquid film, rather than residing on the liquid-liquid interface. However, as this model assumes dilute concentrations of surfactant, it is also assumed that the surfactant will faithfully reside along the liquid-liquid interface, as opposed to forming micelles. Albeit not modelling the full complexity, we use the same

advection-diffusion equation governing surfactant concentration (and equation of state linking surface tension with surfactant concentration) as used in Chapter 3 for the liquid-liquid interface and free surface in the model presented here.

The flow is governed by the Navier-Stokes equations

$$\rho\frac{\mathrm{D}\mathbf{u}}{\mathrm{D}t} = \rho\left(\frac{\partial\mathbf{u}}{\partial t} + (\mathbf{u}\cdot\nabla)\,\mathbf{u}\right) = \nabla\cdot\mathbf{T} + \rho g\sin\theta\mathbf{i} + \rho g\cos\theta\mathbf{j}, \tag{5.2.1}$$

and the incompressible continuity equation

$$\nabla\cdot\mathbf{u} = 0. \tag{5.2.2}$$

Here, $\mathbf{u} = (u, v)$ is the velocity vector, $\mathbf{T}$ the stress tensor, g the gravitational constant, with $\mathbf{i}$ and $\mathbf{j}$ the unit vectors in the direction of increasing x and y, respectively.

Formulating the boundary conditions of the two-layered film, we need to consider the conditions at the solid boundary $y = 0$, the liquid-liquid interface located at $y = h_1(x, t)$, and the free surface at $y = h_2(x, t)$.

At the liquid-liquid interface we have the stress condition (the reader is referred to Chapter 3 for an explanation for how the introduction of surfactant affects the stress condition)

$$[\mathbf{n}_1\cdot\mathbf{T}_j]_{j=1}^{2} = \sigma_1\mathbf{n}_1\,(\nabla\cdot\mathbf{n}_1) - \nabla\sigma_1, \tag{5.2.3}$$

at $y = h_1$. At the free surface, different to condition (5.2.3) due to the passive air, we have the stress condition

$$\mathbf{n}_2\cdot\mathbf{T}_2 = -\sigma_2\mathbf{n}_2\,(\nabla\cdot\mathbf{n}_2) + \nabla\sigma_2, \tag{5.2.4}$$

at $y = h_2$, where $\mathbf{n}_j$ is the unit outward facing normal and $\mathbf{T}_j$ the stress tensor.

Determining how the surfactant concentration evolves over the changing interfaces,

the advection-diffusion equation governing the evolution of surfactant concentration is given by

$$\frac{\partial \Gamma_j}{\partial t} + \nabla_{s,j} \cdot (\Gamma_j \mathbf{u}_{s,j}) + \Gamma_j \left(\nabla_{s,j} \cdot \mathbf{n}_j\right)(\mathbf{u}_j \cdot \mathbf{n}_j) = 0, \tag{5.2.5}$$

at $y = h_j$, assuming the surfactant is insoluble and that diffusivity is small [70]. The gradient along the surface is given by $\nabla_{s,j} = (\mathrm{I} - \mathbf{n}_j \mathbf{n}_j) \cdot \nabla$, where I is the identity matrix.

To link the surface tension of each interface with the surfactant concentration, in the form $\sigma_j = \sigma_j(\Gamma_j)$, we introduce the equation of state

$$\sigma_j = \sigma_{s,j} - RT\Gamma_j, \tag{5.2.6}$$

at $y = h_j$, where $\sigma_{s,j}$ is the surface tension of the solvent, R the gas constant and T the absolute temperature. Assuming dilute concentrations of surfactant, again the reader is referred to Chapter 3 for a more in-depth discussion, equation (5.2.6) is known as the linear Frumkin equation of state [70].

The boundary conditions that are unchanged with the introduction of surfactant, to complete the mathematical model, are the kinematic condition

$$\frac{\partial h_j}{\partial t} + u_j \frac{\partial h_j}{\partial x} = v_j, \tag{5.2.7}$$

at $y = h_j$, the no-slip and impermeability condition

$$\mathbf{u} = 0, \tag{5.2.8}$$

at $y = 0$, and the continuity of velocity

$$[\mathbf{u}_j]_{j=1}^{2} = 0, \tag{5.2.9}$$

at $y = h_1$. We also have the conditions on the flow rates of each layer:

$$Q_j = \int_{h_{j-1}}^{h_j} u_j \, \mathrm{d}y, \tag{5.2.10}$$

where $j \in \{1, 2\}$, and $y = h_0$ corresponds to the solid boundary $y = 0$.

5.2.1 Non-dimensionalisation

We non-dimensionalise using the scales:

$$y = \left(\frac{\mu_1 Q_T}{\rho_1 g \sin(\theta)}\right)^{1/3} \widehat{y} = d_s \widehat{y}, \quad x = \frac{d_s}{\varepsilon}\widehat{x}, \quad u_j = \frac{Q_T}{d_s}\widehat{u}_j, \quad v_j = \frac{\varepsilon Q_T}{d_s}\widehat{v}_j,$$

$$p_j = \frac{\mu_1 Q_T}{\varepsilon d_s^2}\widehat{p}_j, \quad t = \frac{d_s^2}{\varepsilon Q_T}\widehat{t}, \quad \Gamma_j = \Gamma_{in,1}\widehat{\Gamma}_j, \quad \mathbf{T}_j = \frac{\mu_1 Q_T}{d_s^2}\widehat{\mathbf{T}}_j \tag{5.2.11}$$

where hats denote dimensionless variables. The total flow rate at $x = 0$, taken as a reference point, is given by $Q_T = Q_1 + Q_2$. The aspect ratio ε is the width of the multi-layer film divided by the length, taken as $\varepsilon \ll 1$. Moreover, $\Gamma_{in,j}$ corresponds to the concentration of surfactant on the surface $y = h_j$ at $x = 0$, considered constant, with the scale for surfactant concentration given by $\Gamma_{in,1}$.

We assume the liquid layers are Newtonian incompressible fluids, which have the constitutive equations

$$\mathbf{T}_{ij} = -p\delta_{ij} + \mu\left(\frac{\partial u_i}{\partial x_j} + \frac{\partial u_j}{\partial x_i}\right), \tag{5.2.12}$$

where, in this equation only, the subscript i and j are used as part of suffix notation. Substituting in our dimensionless variables from (5.2.11), we obtain the dimensionless

version of (5.2.12)

$$\widehat{T}_{jxx} = -\frac{1}{\varepsilon}\widehat{p}_j + 2\varepsilon\frac{\mu_j}{\mu_1}\frac{\partial\widehat{u}_j}{\partial\widehat{x}}, \tag{5.2.13}$$

$$\widehat{T}_{jxy} = \frac{\mu_j}{\mu_1}\left(\frac{\partial\widehat{u}_j}{\partial\widehat{y}} + \varepsilon^2\frac{\partial\widehat{v}_j}{\partial\widehat{x}}\right), \tag{5.2.14}$$

$$\widehat{T}_{jyy} = -\frac{1}{\varepsilon}\widehat{p}_j + 2\varepsilon\frac{\mu_j}{\mu_1}\frac{\partial\widehat{v}_j}{\partial\widehat{y}}. \tag{5.2.15}$$

Substituting our non-dimensional scales (5.2.11), as well as equations (5.2.13)–(5.2.15), into the Navier-Stokes equations (5.2.1) we obtain their non-dimensional form

$$\varepsilon\mathrm{Re}\frac{\rho_j}{\rho_1}\left(\frac{\partial\widehat{u}_j}{\partial\widehat{t}} + \widehat{u}_j\frac{\partial\widehat{u}_j}{\partial\widehat{x}} + \widehat{v}_j\frac{\partial\widehat{u}_j}{\partial\widehat{y}}\right) = -\frac{\partial\widehat{p}_j}{\partial\widehat{x}} + \frac{\mu_j}{\mu_1}\left(\varepsilon^2\frac{\partial^2\widehat{u}_j}{\partial\widehat{x}^2} + \frac{\partial^2\widehat{u}_j}{\partial\widehat{y}^2}\right) + \frac{\rho_j}{\rho_1} \tag{5.2.16}$$

$$\varepsilon^3\mathrm{Re}\frac{\rho_j}{\rho_1}\left(\frac{\partial\widehat{v}_j}{\partial\widehat{t}} + \widehat{u}_j\frac{\partial\widehat{v}_j}{\partial\widehat{x}} + \widehat{v}_j\frac{\partial\widehat{v}_j}{\partial\widehat{y}}\right) = -\frac{\partial\widehat{p}_j}{\partial\widehat{y}} + \frac{\mu_j}{\mu_1}\left(\varepsilon^4\frac{\partial^2\widehat{v}_j}{\partial\widehat{x}^2} + \varepsilon^2\frac{\partial^2\widehat{v}_j}{\partial\widehat{y}^2}\right) + \varepsilon\frac{\rho_j}{\rho_1}\cot\theta, \tag{5.2.17}$$

where we note the Reynolds number, $Re = \rho_1 Q_T/\mu_1$, is based on the properties of layer 1. The continuity equation (5.2.2) remains unchanged

$$\frac{\partial\widehat{u}_j}{\partial\widehat{x}} + \frac{\partial\widehat{v}_j}{\partial\widehat{y}} = 0. \tag{5.2.18}$$

Non-dimensionalising the boundary conditions, the stress conditions at each liquid-liquid interface (5.2.3) becomes

$$\mathrm{Ca}\left[\widehat{\mathbf{n}}_1\cdot\widehat{\mathbf{T}}_j\right]_{j=1}^2 = \frac{\sigma_1}{\sigma_{s,1}}\widehat{\mathbf{n}}_1\left(\widehat{\nabla}\cdot\widehat{\mathbf{n}}_1\right) - \widehat{\nabla}\left(\frac{\sigma_1}{\sigma_{s,1}}\right), \tag{5.2.19}$$

at $\widehat{y} = \widehat{h}_1$. The capillary number, $Ca = \mu_1 Q_T/d_s\sigma_{s,1}$, is based on the properties of the fluid in layer 1. The non-dimensional stress condition at the free surface (5.2.4) is given by

$$\mathrm{Ca}\left(\widehat{\mathbf{n}}_2\cdot\widehat{\mathbf{T}}_2\right) = -\frac{\sigma_2}{\sigma_{s,1}}\widehat{\mathbf{n}}_2\left(\widehat{\nabla}\cdot\widehat{\mathbf{n}}_2\right) + \widehat{\nabla}\left(\frac{\sigma_2}{\sigma_{s,1}}\right), \tag{5.2.20}$$

where the gradient, normal vector and curvature are given by

$$\widehat{\nabla} = \left(\varepsilon \frac{\partial}{\partial \widehat{x}}, \frac{\partial}{\partial \widehat{y}} \right),$$

$$\widehat{\mathbf{n}}_j = \frac{1}{\left(1 + \varepsilon^2 \left(\frac{\partial \widehat{h}_j}{\partial \widehat{x}} \right)^2 \right)^{1/2}} \begin{pmatrix} -\varepsilon \frac{\partial \widehat{h}_j}{\partial \widehat{x}} \\ 1 \end{pmatrix},$$

$$\widehat{\nabla} \cdot \widehat{\mathbf{n}}_j = - \frac{\varepsilon^2 \frac{\partial^2 \widehat{h}_j}{\partial \widehat{x}^2}}{\left(1 + \varepsilon^2 \left(\frac{\partial \widehat{h}_j}{\partial \widehat{x}} \right)^2 \right)^{3/2}} = \kappa_j.$$

The evolution equation for surfactant concentration (5.2.5) remains unchanged

$$\frac{\partial \widehat{\Gamma}_j}{\partial \widehat{t}} + \widehat{\nabla}_{s,j} \cdot \left(\widehat{\Gamma}_j \widehat{\mathbf{u}}_{s,j} \right) + \widehat{\Gamma}_j \left(\widehat{\nabla}_{s,j} \cdot \widehat{\mathbf{n}}_j \right) \left(\widehat{\mathbf{u}}_j \cdot \widehat{\mathbf{n}}_j \right) = 0,$$

which can be written as

$$\frac{\partial \widehat{\Gamma}_j}{\partial \widehat{t}} + \widehat{\nabla}_{s,j} \cdot \left(\widehat{\Gamma}_j \widehat{\mathbf{u}}_{s,j} \right) + \widehat{\Gamma}_j \kappa_j \left(\widehat{\mathbf{u}}_j \cdot \widehat{\mathbf{n}}_j \right) = 0. \tag{5.2.21}$$

The reader is referred to Appendix B, Section B.1, to see the terms in this equation calculated explicitly, as well as details of the non-dimensionalisation[2]. The equation of state (5.2.6) linking the surface tension to the surfactant concentration becomes

$$\frac{\sigma_j}{\sigma_{s,1}} = \frac{\sigma_{s,j}}{\sigma_{s,1}} \left(1 - \beta_j \frac{\Gamma_{in,1}}{\Gamma_{in,j}} \widehat{\Gamma}_j \right), \tag{5.2.22}$$

at $\widehat{y} = \widehat{h}_j$, where the surface activity number [106] is given by $\beta_j = RT\Gamma_{in,j}/\sigma_{s,j}$. This dimensionless number provides a measure of the sensitivity of the surface tension, σ_j, to the surfactant concentration $\widehat{\Gamma}_j$, with $0 \leqslant \beta_j < 1$. The reader is referred to Chapter 3 for

[2]At first glance, equation (5.2.21) should have an ε in front of the $\partial \widehat{\Gamma}_j / \partial \widehat{t}$ term. However, an ε occurs in each term of this equation, meaning we can divide through by ε. See Appendix B for more detail.

more details, however, it is worth re-emphasising here that the linear equation of state used is only valid for dilute concentrations of surfactant concentration, meaning a small value of β_j. Differentiating the equation of state (5.2.22) gives us the expression

$$\frac{\partial}{\partial \widehat{x}}\left(\frac{\sigma_j}{\sigma_{s,1}}\right) = -\beta_j \frac{\sigma_{s,j}}{\sigma_{s,1}} \frac{\Gamma_{in,1}}{\Gamma_{in,j}} \frac{\partial \widehat{\Gamma}_j}{\partial \widehat{x}}, \tag{5.2.23}$$

which we use for the last term on the right-hand-side of the stress conditions (5.2.19) and (5.2.20).

The kinematic condition (5.2.7), no-slip and impermeability condition (5.2.8), continuity of velocity (5.2.9), and flow rate condition (5.2.10) all remain unchanged upon non-dimensionalisation:

$$\frac{\partial \widehat{h}_j}{\partial \widehat{t}} + \widehat{u}_j \frac{\partial \widehat{h}_j}{\partial \widehat{x}} = \widehat{v}_j, \tag{5.2.24}$$

at $\widehat{y} = \widehat{h}_j$,

$$\widehat{\mathbf{u}} = \mathbf{0}, \tag{5.2.25}$$

at $\widehat{y} = 0$,

$$[\widehat{\mathbf{u}}_j]_{j=1}^{2} = \mathbf{0}, \tag{5.2.26}$$

at $\widehat{y} = \widehat{h}_1$, and

$$\widehat{Q}_j = \int_{\widehat{h}_{j-1}}^{\widehat{h}_j} \widehat{u}_j \, \mathrm{d}\widehat{y}. \tag{5.2.27}$$

Integrating the continuity equation (5.2.18) across the first layer, we obtain

$$\int_{\widehat{y}=0}^{\widehat{h}_1} \frac{\partial \widehat{u}_1}{\partial \widehat{x}} + \frac{\partial \widehat{v}_1}{\partial \widehat{y}} \, \mathrm{d}\widehat{y} = 0$$

which, using the kinematic condition (5.2.24) and the impermeability condition (5.2.25)

becomes

$$\int_{\widehat{y}=0}^{\widehat{h}_1} \frac{\partial \widehat{u}_1}{\partial \widehat{x}} \, \mathrm{d}\widehat{y} + \frac{\partial \widehat{h}_1}{\partial \widehat{t}} + \widehat{u}_1 \, \frac{\partial \widehat{h}_1}{\partial \widehat{x}} \bigg|_{\widehat{y}=\widehat{h}_1} = 0.$$

Using Leibniz's integration rule this is given by

$$\frac{\partial \widehat{h}_1}{\partial \widehat{t}} + \frac{\partial}{\partial \widehat{x}} \left(\int_{\widehat{y}=0}^{\widehat{h}_1} \widehat{u}_1 \, \mathrm{d}\widehat{y} \right) = 0,$$

which can be written as

$$\frac{\partial \widehat{h}_1}{\partial \widehat{t}} + \frac{\partial \widehat{Q}_1}{\partial \widehat{x}} = 0. \tag{5.2.28}$$

Similarly integrating (5.2.18) across the second layer, we have that

$$\frac{\partial \widehat{h}_2}{\partial \widehat{t}} - \frac{\partial \widehat{h}_1}{\partial \widehat{t}} + \frac{\partial}{\partial \widehat{x}} \left(\int_{\widehat{y}=\widehat{h}_1}^{\widehat{h}_2} \widehat{u}_2 \, \mathrm{d}\widehat{y} \right) = 0,$$

that is

$$\frac{\partial \widehat{h}_2}{\partial \widehat{t}} - \frac{\partial \widehat{h}_1}{\partial \widehat{t}} + \frac{\partial \widehat{Q}_2}{\partial \widehat{x}} = 0, \tag{5.2.29}$$

having used both the kinematic condition (5.2.24) and Leibniz's integration rule. For clarity and convenience, all hats are now dropped from non-dimensional variables.

5.2.2 Asymptotic analysis

We use the following asymptotic expansions

$$\{u_j, v_j, p_j\} = \{u_{j,0}, v_{j,0}, p_{j,0}\} + \varepsilon \{u_{j,1}, v_{j,1}, p_{j,1}\} + \varepsilon^2 \{u_{j,2}, v_{j,2}, p_{j,2}\} + \ldots,$$

and assume the following orders of magnitude

$$Re = O(1), \quad \varepsilon \cot(\theta) = \Omega(\theta) = O(1), \quad \frac{Ca}{\varepsilon^3} = \mathcal{C} = O(1), \quad \frac{\beta_j}{\varepsilon^2} = \mathcal{B}_j = O(1).$$

By taking $\cot(\theta) = O(1/\varepsilon)$ we ensure that θ is small, a condition that is desired for our model as explained in Section 5.1. This also retains the final term on the right-hand side of the y-component of the Navier-Stokes equation (5.2.17). To retain the curvature terms in the stress conditions, (5.2.19) and (5.2.20), it is necessary to have the capillary number of order ε^3. We also choose $\beta_j = O(\varepsilon^2)$, which ensures a small value of β_j for the validity of the equation of state (5.2.22), whilst retaining the terms in the stress conditions (5.2.19) and (5.2.20) associated with the gradient in surface tension. Appendix B, Section B.2, shows this explicitly.

Substituting the asymptotic expansions into the non-dimensional system, we obtain at leading order (dropping the subscript zeros immediately for clarity), from the Navier-Stokes equations (5.2.16) and (5.2.17):

$$0 = -\frac{\partial p_j}{\partial x} + \frac{\mu_j}{\mu_1}\frac{\partial^2 u_j}{\partial y^2} + \frac{\rho_j}{\rho_1}, \tag{5.2.30}$$

$$0 = -\frac{\partial p_j}{\partial y} + \frac{\rho_j}{\rho_1}\Omega(\theta). \tag{5.2.31}$$

The integrated continuity equations (5.2.28) and (5.2.29) remain unchanged at leading order:

$$\frac{\partial h_1}{\partial t} + \frac{\partial Q_1}{\partial x} = 0, \tag{5.2.32}$$

$$\frac{\partial h_2}{\partial t} - \frac{\partial h_1}{\partial t} + \frac{\partial Q_2}{\partial x} = 0. \tag{5.2.33}$$

The equation of state (5.2.22) is given by

$$\frac{\sigma_j}{\sigma_{s,1}} = \frac{\sigma_{s,j}}{\sigma_{s,1}}\left(1 - \frac{\Gamma_{in,1}}{\Gamma_{in,j}}\beta_j\Gamma_j\right) = \frac{\sigma_{s,j}}{\sigma_{s,1}}, \tag{5.2.34}$$

to leading order. Although (5.2.34) demonstrates that the surface tension does not change

to leading order, the introduction of surfactant manifests itself within the leading order system via the stress conditions at both interfaces. From the stress condition at the liquid-liquid interface (5.2.19):

$$\mathcal{C}\left(\frac{\partial h_1}{\partial x}p_2 + \frac{\mu_2}{\mu_1}\frac{\partial u_2}{\partial y} - \frac{\partial h_1}{\partial x}p_1 - \frac{\partial u_1}{\partial y}\right) = \frac{\partial^2 h_1}{\partial x^2}\frac{\partial h_1}{\partial x} + \mathcal{B}_1\frac{\partial \Gamma_1}{\partial x}, \tag{5.2.35}$$

$$\mathcal{C}\left(-p_2 + p_1\right) = -\frac{\partial^2 h_1}{\partial x^2}. \tag{5.2.36}$$

Similarly, from the stress condition at the free surface (5.2.20):

$$\mathcal{C}\left(\frac{\partial h_2}{\partial x}p_2 + \frac{\mu_2}{\mu_1}\frac{\partial u_2}{\partial y}\right) = -\frac{\sigma_{s,2}}{\sigma_{s,1}}\frac{\partial^2 h_2}{\partial x^2}\frac{\partial h_2}{\partial x} - \mathcal{B}_2\frac{\sigma_{s,2}}{\sigma_{s,1}}\frac{\Gamma_{in,1}}{\Gamma_{in,2}}\frac{\partial \Gamma_2}{\partial x}, \tag{5.2.37}$$

$$-\mathcal{C}p_2 = \frac{\sigma_{s,2}}{\sigma_{s,1}}\frac{\partial^2 h_2}{\partial x^2}. \tag{5.2.38}$$

The leading order advection-diffusion equation governing surfactant concentration (5.2.21) is given by:

$$\frac{\partial \Gamma_j}{\partial t} + \frac{\partial}{\partial x}\left(u_j\Gamma_j\right) + \Gamma_j\frac{\partial h_j}{\partial x}\frac{\partial u_j}{\partial y} = 0. \tag{5.2.39}$$

Finally, the no-slip condition (5.2.25), continuity of velocity (5.2.26), and flow rate condition (5.2.27) remain unchanged at leading order:

$$u_1 = 0 \tag{5.2.40}$$

at $y = 0$,

$$u_1 = u_2 \tag{5.2.41}$$

at $y = h_1$, and

$$Q_j = \int_{h_{j-1}}^{h_j} u_j \, \mathrm{d}y \tag{5.2.42}$$

for $j \in \{1, 2\}$, where $y = h_0$ corresponds to $y = 0$.

5.2.3 Leading order solutions

We now solve the leading order equations obtained in the previous section, considering both the single and two-layer cases explicitly.

Single-layer case

The single-layer equations are obtained from the leading order equations derived in the previous section for the two-layer case. In the one-layer case there is no liquid-liquid interface, meaning the boundary conditions (5.2.35), (5.2.36) and (5.2.41) are disregarded; similarly, the advection-diffusion equation (5.2.39) and flow rate condition (5.2.42) for the case $j = 1$ are disregarded, as is the integrated continuity equation (5.2.32). With there being no change in surface tension to leading order, the equation of state (5.2.34) can also be disregarded.

With no liquid-liquid interface, the $\partial h_1/\partial t$ term in (5.2.33) is removed. There is no stratification of liquid properties between liquid layers, so that $\mu_j/\mu_1 = \rho_j/\rho_1 = \sigma_{s,2}/\sigma_{s,1} = \Gamma_{in,1}/\Gamma_{in,2} = 1$. Finally, we remove subscripts on variables, so that $u_j = u$, $p_j = p$, $h_2 = h$, $\Gamma_j = \Gamma$, $\mathcal{B}_2 = \mathcal{B}$ and $Q_2 = Q_T = Q$ (see Figure 5.4(a) for the single-layer schematic and notation of the variables).

From the y-component of the Navier-Stokes equations, (5.2.31), after integrating with respect to y, we have

$$p = \Omega(\theta)\, y + A(x, t),$$

where A is a function that is resultant from the integration. Using the stress condition at the free surface (5.2.38) the expression for A is found, so that

$$p = \Omega(\theta)\,(y - h) - \frac{1}{\mathcal{C}}\frac{\partial^2 h}{\partial x^2}. \tag{5.2.43}$$

Substituting the solution for pressure (5.2.43) into the x-component of the Navier-Stokes equations (5.2.30), and integrating twice, we have

$$u = -\frac{1}{2}\left(\frac{1}{\mathcal{C}}\frac{\partial^3 h}{\partial x^3} + \Omega\left(\theta\right)\frac{\partial h}{\partial x} + 1\right)y^2 + B(x,t)y + C(x,t).$$

From the no-slip condition (5.2.40) we find $C = 0$, whilst from the stress condition (5.2.37) and solution for pressure (5.2.43) we can calculate the expression for $\partial u/\partial y$ at $y = h$. This is used to find B, from which the solution for velocity is given by

$$u = \left(\left(\frac{1}{\mathcal{C}}\frac{\partial^3 h}{\partial x^3} + \Omega\left(\theta\right)\frac{\partial h}{\partial x} + 1\right)\left(h - \frac{1}{2}y\right) - \frac{\mathcal{B}}{\mathcal{C}}\frac{\partial \Gamma}{\partial x}\right)y. \tag{5.2.44}$$

It will help with the mathematics in the forthcoming sections to calculate the expression for the flow rate, from equation (5.2.42). Using the solution for velocity (5.2.44), we have that

$$Q = \int_0^h u \, \mathrm{d}y = \left(\frac{1}{3}\left(\frac{1}{\mathcal{C}}\frac{\partial^3 h}{\partial x^3} + \Omega\left(\theta\right)\frac{\partial h}{\partial x} + 1\right)h - \frac{\mathcal{B}}{2\mathcal{C}}\frac{\partial \Gamma}{\partial x}\right)h^2. \tag{5.2.45}$$

2-layer case

First, we integrate the y-component of the Navier-Stokes equations (5.2.31), obtaining

$$\begin{aligned} p_1 &= \Omega\left(\theta\right)y + A(x,t), \\ p_2 &= \frac{\rho_2}{\rho_1}\Omega\left(\theta\right)y + B(x,t), \end{aligned}$$

where A and B are functions resultant of the integration. We use the stress condition (5.2.38) to find B, then the stress condition (5.2.36) to find A. Subsequently

$$p_1 = \Omega\left(\theta\right)\left(y - h_1\right) + \frac{\rho_2}{\rho_1}\Omega\left(\theta\right)\left(h_1 - h_2\right) - \frac{1}{\mathcal{C}}\left(\frac{\partial^2 h_1}{\partial x^2} + \frac{\sigma_{s,2}}{\sigma_{s,1}}\frac{\partial^2 h_2}{\partial x^2}\right), \tag{5.2.46}$$

and

$$p_2 = \frac{\rho_2}{\rho_1}\Omega(\theta)(y - h_2) - \frac{1}{\mathcal{C}}\frac{\sigma_{s,2}}{\sigma_{s,1}}\frac{\partial^2 h_2}{\partial x^2}. \tag{5.2.47}$$

Thus from the x-component of the Navier-Stokes equations (5.2.30), in the first layer:

$$\begin{aligned}\frac{\partial^2 u_1}{\partial y^2} &= \frac{\partial p_1}{\partial x} - 1, \\ &= \Omega(\theta)\left(\left(\frac{\rho_2}{\rho_1} - 1\right)\frac{\partial h_1}{\partial x} - \frac{\rho_2}{\rho_1}\frac{\partial h_2}{\partial x}\right) - \frac{1}{\mathcal{C}}\left(\frac{\partial^3 h_1}{\partial x^3} + \frac{\sigma_{s,2}}{\sigma_{s,1}}\frac{\partial^3 h_2}{\partial x^3}\right) - 1.\end{aligned}$$

Integrating this twice, we obtain

$$u_1 = \frac{1}{2}\left(\Omega(\theta)\left(\left(\frac{\rho_2}{\rho_1} - 1\right)\frac{\partial h_1}{\partial x} - \frac{\rho_2}{\rho_1}\frac{\partial h_2}{\partial x}\right) - \frac{1}{\mathcal{C}}\left(\frac{\partial^3 h_1}{\partial x^3} + \frac{\sigma_{s,2}}{\sigma_{s,1}}\frac{\partial^3 h_2}{\partial x^3}\right) - 1\right)y^2 + D(x,t)y + E(x,t).$$

Similarly, from the x-component of the Navier-Stokes equations (5.2.30), in the second layer:

$$\begin{aligned}\frac{\partial^2 u_2}{\partial y^2} &= \frac{\mu_1}{\mu_2}\left(\frac{\partial p_2}{\partial x} - \frac{\rho_2}{\rho_1}\right), \\ &= -\frac{\mu_1}{\mu_2}\left(\frac{1}{\mathcal{C}}\frac{\sigma_{s,2}}{\sigma_{s,1}}\frac{\partial^3 h_2}{\partial x^3} + \frac{\rho_2}{\rho_1}\Omega(\theta)\frac{\partial h_2}{\partial x} + \frac{\rho_2}{\rho_1}\right).\end{aligned}$$

Again, this is integrated twice

$$u_2 = -\frac{1}{2}\frac{\mu_1}{\mu_2}\left(\frac{1}{\mathcal{C}}\frac{\sigma_{s,2}}{\sigma_{s,1}}\frac{\partial^3 h_2}{\partial x^3} + \frac{\rho_2}{\rho_1}\Omega(\theta)\frac{\partial h_2}{\partial x} + \frac{\rho_2}{\rho_1}\right)y^2 + F(x,t)y + G(x,t).$$

The boundary conditions are used to find expressions for D, E, F and G. Using the no-slip condition (5.2.40), we have that $E = 0$. The stress condition at the free surface (5.2.37), using p_2 evaluated at $y = h_2$, gives the expression for $\partial u_2/\partial y$ at $y = h_2$; used to

find F:

$$F = \frac{\mu_1}{\mu_2}\left(\left(\frac{1}{\mathcal{C}} \frac{\sigma_{s,2}}{\sigma_{s,1}} \frac{\partial^3 h_2}{\partial x^3} + \frac{\rho_2}{\rho_1} \Omega(\theta) \frac{\partial h_2}{\partial x} + \frac{\rho_2}{\rho_1} \right) h_2 - \frac{\mathcal{B}_2}{\mathcal{C}} \frac{\sigma_{s,2}}{\sigma_{s,1}} \frac{\Gamma_{in,1}}{\Gamma_{in,2}} \frac{\partial \Gamma_2}{\partial x} \right).$$

The stress condition at the liquid-liquid interface (5.2.35), using p_1, p_2 and $\partial u_2/\partial y$ evaluated at $y = h_1$, gives the expression for $\partial u_1/\partial y$ at $y = h_1$. These are used to find D:

$$\begin{aligned} D = &\left(\frac{1}{\mathcal{C}} \frac{\partial^3 h_1}{\partial x^3} + \left(1 - \frac{\rho_2}{\rho_1}\right)\left(\Omega(\theta) \frac{\partial h_1}{\partial x} + 1\right) \right) h_1 + \left(\frac{1}{\mathcal{C}} \frac{\sigma_{s,2}}{\sigma_{s,1}} \frac{\partial^3 h_2}{\partial x^3} + \frac{\rho_2}{\rho_1} \Omega(\theta) \frac{\partial h_2}{\partial x} + \frac{\rho_2}{\rho_1} \right) h_2 \\ &- \frac{1}{\mathcal{C}} \left(\mathcal{B}_1 \frac{\partial \Gamma_1}{\partial x} + \mathcal{B}_2 \frac{\sigma_{s,2}}{\sigma_{s,1}} \frac{\Gamma_{in,1}}{\Gamma_{in,2}} \frac{\partial \Gamma_2}{\partial x} \right). \end{aligned}$$

Finally, we use the continuity of velocity condition (5.2.41) across the liquid-liquid interface, $u_1 = u_2$ at $y = h_1$, to find the expression for $G(x,t)$:

$$\begin{aligned} G = &\left(1 - \frac{\mu_1}{\mu_2}\right) \left(\left(\frac{1}{\mathcal{C}} \frac{\sigma_{s,2}}{\sigma_{s,1}} \frac{\partial^3 h_2}{\partial x^3} + \frac{\rho_2}{\rho_1} \Omega(\theta) \frac{\partial h_2}{\partial x} \right)\left(h_2 - \frac{1}{2} h_1\right) + \frac{\rho_2}{\rho_1} h_2 \right) h_1 \\ &+ \frac{1}{2} \left(\frac{1}{\mathcal{C}} \frac{\partial^3 h_1}{\partial x^3} + \left(1 - \frac{\rho_2}{\rho_1}\right) \Omega(\theta) \frac{\partial h_1}{\partial x} + \frac{\rho_2}{\rho_1}\left(\frac{\mu_1}{\mu_2} - 2\right) + 1 \right) h_1^2 \\ &- \left(\frac{\mathcal{B}_1}{\mathcal{C}} \frac{\partial \Gamma_1}{\partial x} + \left(1 - \frac{\mu_1}{\mu_2}\right) \frac{\mathcal{B}_2}{\mathcal{C}} \frac{\sigma_{s,2}}{\sigma_{s,1}} \frac{\Gamma_{in,1}}{\Gamma_{in,2}} \frac{\partial \Gamma_2}{\partial x} \right) h_1. \end{aligned}$$

The solutions for the velocity in the first and second layers are then given by

$$\begin{aligned} u_1 = &\left(\left(\frac{1}{\mathcal{C}} \frac{\partial^3 h_1}{\partial x^3} + \left(1 - \frac{\rho_2}{\rho_1}\right) \Omega(\theta) \frac{\partial h_1}{\partial x} + 1 \right) \left(h_1 - \frac{1}{2} y \right) \right. \\ &+ \left(\frac{1}{\mathcal{C}} \frac{\sigma_{s,2}}{\sigma_{s,1}} \frac{\partial^3 h_2}{\partial x^3} + \frac{\rho_2}{\rho_1} \Omega(\theta) \frac{\partial h_2}{\partial x} \right) \left(h_2 - \frac{1}{2} y \right) \\ &\left. - \frac{1}{\mathcal{C}} \left(\mathcal{B}_1 \frac{\partial \Gamma_1}{\partial x} + \mathcal{B}_2 \frac{\sigma_{s,2}}{\sigma_{s,1}} \frac{\Gamma_{in,1}}{\Gamma_{in,2}} \frac{\partial \Gamma_2}{\partial x} \right) - \frac{\rho_2}{\rho_1} (h_1 - h_2) \right) y, \end{aligned} \tag{5.2.48}$$

and

$$
\begin{aligned}
u_2 = \frac{\mu_1}{\mu_2}\Bigg(& \left(\frac{1}{\mathcal{C}}\frac{\sigma_{s,2}}{\sigma_{s,1}}\frac{\partial^3 h_2}{\partial x^3} + \frac{\rho_2}{\rho_1}\Omega\left(\theta\right)\frac{\partial h_2}{\partial x} + \frac{\rho_2}{\rho_1}\right)\left(h_2 - \frac{1}{2}y\right) - \frac{\mathcal{B}_2}{\mathcal{C}}\frac{\sigma_{s,2}}{\sigma_{s,1}}\frac{\Gamma_{in,1}}{\Gamma_{in,2}}\frac{\partial \Gamma_2}{\partial x}\Bigg) y \\
& + \left(1 - \frac{\mu_1}{\mu_2}\right)\Bigg(\left(\frac{1}{\mathcal{C}}\frac{\sigma_{s,2}}{\sigma_{s,1}}\frac{\partial^3 h_2}{\partial x^3} + \frac{\rho_2}{\rho_1}\Omega\left(\theta\right)\frac{\partial h_2}{\partial x}\right)\left(h_2 - \frac{1}{2}h_1\right) + \frac{\rho_2}{\rho_1}h_2\Bigg) h_1 \\
& + \frac{1}{2}\left(\frac{1}{\mathcal{C}}\frac{\partial^3 h_1}{\partial x^3} + \left(1 - \frac{\rho_2}{\rho_1}\right)\Omega\left(\theta\right)\frac{\partial h_1}{\partial x} + \frac{\rho_2}{\rho_1}\left(\frac{\mu_1}{\mu_2} - 2\right) + 1\right) h_1^2 \\
& - \left(\frac{\mathcal{B}_1}{\mathcal{C}}\frac{\partial \Gamma_1}{\partial x} + \left(1 - \frac{\mu_1}{\mu_2}\right)\frac{\mathcal{B}_2}{\mathcal{C}}\frac{\sigma_{s,2}}{\sigma_{s,1}}\frac{\Gamma_{in,1}}{\Gamma_{in,2}}\frac{\partial \Gamma_2}{\partial x}\right) h_1. \qquad (5.2.49)
\end{aligned}
$$

It will help with the mathematics in the forthcoming sections to calculate expressions for the flow rates Q_1 and Q_2, from equation (5.2.42). Using the solution for velocity (5.2.48), we have that

$$
\begin{aligned}
Q_1 &= \int_0^{h_1} u_1 \, \mathrm{d}y \\
&= \frac{1}{2}\Bigg(\frac{2}{3}\left(\frac{1}{\mathcal{C}}\frac{\partial^3 h_1}{\partial x^3} + \left(1 - \frac{\rho_2}{\rho_1}\right)\Omega\left(\theta\right)\frac{\partial h_1}{\partial x} + 1\right) h_1 + \left(\frac{1}{\mathcal{C}}\frac{\sigma_{s,2}}{\sigma_{s,1}}\frac{\partial^3 h_2}{\partial x^3} + \frac{\rho_2}{\rho_1}\Omega\left(\theta\right)\frac{\partial h_2}{\partial x}\right)\left(h_2 - \frac{1}{3}h_1\right) \\
&\quad - \frac{1}{\mathcal{C}}\left(\mathcal{B}_1\frac{\partial \Gamma_1}{\partial x} + \mathcal{B}_2\frac{\sigma_{s,2}}{\sigma_{s,1}}\frac{\Gamma_{in,1}}{\Gamma_{in,2}}\frac{\partial \Gamma_2}{\partial x}\right) - \frac{\rho_2}{\rho_1}\left(h_1 - h_2\right)\Bigg) h_1^2. \qquad (5.2.50)
\end{aligned}
$$

Using the solution for velocity (5.2.49), we have that

$$\begin{aligned}
Q_2 &= \int_{h_1}^{h_2} u_2 \, \mathrm{d}y \\
&= \left(\frac{1}{6}\frac{\mu_1}{\mu_2} \left(\frac{1}{\mathcal{C}}\frac{\sigma_{s,2}}{\sigma_{s,1}}\frac{\partial^3 h_2}{\partial x^3} + \frac{\rho_2}{\rho_1}\Omega\left(\theta\right)\frac{\partial h_2}{\partial x} + \frac{\rho_2}{\rho_1} \right) \left(2h_2^2 + 2h_1 h_2 - h_1^2 \right) \right. \\
&\quad - \frac{1}{2}\frac{\mu_1}{\mu_2}\frac{\mathcal{B}_2}{\mathcal{C}}\frac{\sigma_{s,2}}{\sigma_{s,1}}\frac{\Gamma_{in,1}}{\Gamma_{in,2}}\frac{\partial \Gamma_2}{\partial x}\left(h_1 + h_2\right) \\
&\quad + \left(1 - \frac{\mu_1}{\mu_2}\right) \left(\left(\frac{\sigma_{s,2}}{\sigma_{s,1}}\frac{1}{\mathcal{C}}\frac{\partial^3 h_2}{\partial x^3} + \frac{\rho_2}{\rho_1}\Omega\left(\theta\right)\frac{\partial h_2}{\partial x} \right)\left(h_2 - \frac{1}{2}h_1 \right) + \frac{\rho_2}{\rho_1}h_2 \right) h_1 \\
&\quad + \frac{1}{2}\left(\frac{1}{\mathcal{C}}\frac{\partial^3 h_1}{\partial x^3} + \left(1 - \frac{\rho_2}{\rho_1}\right)\Omega\left(\theta\right)\frac{\partial h_1}{\partial x} + \frac{\rho_2}{\rho_1}\left(\frac{\mu_1}{\mu_2} - 2\right) + 1 \right) h_1^2 \\
&\quad \left. - \left(\frac{\mathcal{B}_1}{\mathcal{C}}\frac{\partial \Gamma_1}{\partial x} + \left(1 - \frac{\mu_1}{\mu_2}\right)\frac{\mathcal{B}_2}{\mathcal{C}}\frac{\sigma_{s,2}}{\sigma_{s,1}}\frac{\Gamma_{in,1}}{\Gamma_{in,2}}\frac{\partial \Gamma_2}{\partial x} \right) h_1 \right) \left(h_2 - h_1\right). \qquad (5.2.51)
\end{aligned}$$

5.2.4 Steady state solutions and film heights

We now formulate the steady uni-directional solutions from the leading order solutions, used in the proceeding stability analysis, where the film heights and surfactant concentration are perturbed about this steady state. The variables in this case are denoted with a superscript zero, whereby we consider

$$v_j^0 = 0, \quad h_j^0 = \text{constant}, \quad \frac{\partial}{\partial x} = 0, \quad \frac{\partial}{\partial t} = 0,$$

again splitting the cases explicitly between the single and two-layer models.

1-layer case

We have from the solutions for pressure (5.2.43) and velocity (5.2.44), the steady state solutions

$$p^0 = \Omega\left(\theta\right)\left(y - h^0\right),$$

and

$$u^0 = \left(h^0 - \frac{1}{2}y\right) y.$$

The flow rate condition (5.2.45) in the steady state gives us the film thickness:

$$Q = 1 = \frac{1}{3}h^{0^3},$$

remembering due to the non-dimensional scales, we have that $Q_T = Q = 1$ in the single-layer case. Thus, we have the non-dimensional film height

$$h^0 = 3^{1/3}. \tag{5.2.52}$$

2-layer case

From the solution for pressure in both layers (5.2.46) and (5.2.47), the steady state pressures are

$$p_1^0 = \Omega(\theta)\left(y - h_1^0 + \frac{\rho_2}{\rho_1}\left(h_1^0 - h_2^0\right)\right),$$

$$p_2^0 = \frac{\rho_2}{\rho_1}\Omega(\theta)\left(y - h_2^0\right).$$

From (5.2.48) and (5.2.49), the steady state velocities are

$$u_1^0 = \left(h_1^0 - \frac{\rho_2}{\rho_1}\left(h_1^0 - h_2^0\right) - \frac{1}{2}y\right) y, \tag{5.2.53}$$

$$u_2^0 = \frac{\mu_1}{\mu_2}\frac{\rho_2}{\rho_1}\left(h_2^0 - \frac{1}{2}y\right) y + \left(\frac{1}{2}h_1^0 + \frac{\rho_2}{\rho_1}\frac{\mu_1}{\mu_2}\left(\frac{1}{2}h_1^0 - h_2^0\right) + \frac{\rho_2}{\rho_1}\left(h_2^0 - h_1^0\right)\right) h_1^0. \tag{5.2.54}$$

The flow rate conditions, (5.2.50) and (5.2.51), in the steady state are given by

$$Q_1 = h_1^{0^2}\left(\frac{1}{3}h_1^0 + \frac{1}{2}\frac{\rho_2}{\rho_1}\left(h_2^0 - h_1^0\right)\right), \tag{5.2.55}$$

$$Q_2 = \left(h_2^0 - h_1^0\right)\left(\frac{1}{2}h_1^{0^2} + \frac{\rho_2}{\rho_1}\left(h_2^0 - h_1^0\right)h_1^0 + \frac{1}{3}\frac{\mu_1}{\mu_2}\frac{\rho_2}{\rho_1}\left(h_2^0 - h_1^0\right)^2\right), \tag{5.2.56}$$

and are used to find the unknown film heights. Equations (5.2.55) and (5.2.56) give us two equations, with the two unknown film thicknesses, h_1^0 and h_2^0, which can be solved using Newton's method (code written and carried out in Matlab) with set parameter values for the flow rate (remembering we must have $Q_1 + Q_2 = 1$), densities and viscosities. The details of Newton's method can be found previously in Section 2.3, and so are not outlined here.

5.3 Stability

5.3.1 Evolution Equations

1-layer case

We differentiate the flow rate condition (5.2.45) with respect to x to obtain:

$$\frac{\partial Q}{\partial x} = \frac{1}{3\mathcal{C}}\frac{\partial}{\partial x}\left(\frac{\partial^3 h}{\partial x^3}h^3\right) + \frac{1}{3}\Omega(\theta)\frac{\partial}{\partial x}\left(\frac{\partial h}{\partial x}h^3\right) + \frac{1}{3}\frac{\partial}{\partial x}\left(h^3\right) - \frac{\mathcal{B}}{2\mathcal{C}}\frac{\partial}{\partial x}\left(\frac{\partial \Gamma}{\partial x}h^2\right).$$

And so from the integrated continuity equation (5.2.32), we obtain the evolution equation for the film height h:

$$\frac{\partial h}{\partial t} + \frac{1}{3\mathcal{C}}\frac{\partial}{\partial x}\left(\frac{\partial^3 h}{\partial x^3}h^3\right) + \frac{1}{3}\Omega(\theta)\frac{\partial}{\partial x}\left(\frac{\partial h}{\partial x}h^3\right) + \frac{1}{3}\frac{\partial}{\partial x}\left(h^3\right) - \frac{\mathcal{B}}{2\mathcal{C}}\frac{\partial}{\partial x}\left(\frac{\partial \Gamma}{\partial x}h^2\right) = 0. \tag{5.3.1}$$

From (5.2.44) the expression for the velocity and velocity gradient at the free surface are found. Substituting these into the evolution equation for the surfactant concentration

(5.2.39), we obtain the evolution equation for surfactant concentration

$$\frac{\partial \Gamma}{\partial t}+\frac{1}{2\mathcal{C}}\frac{\partial}{\partial x}\left(\Gamma\frac{\partial h^3}{\partial x^3}h^2\right)+\frac{1}{2}\Omega\left(\theta\right)\frac{\partial}{\partial x}\left(\Gamma\frac{\partial h}{\partial x}h^2\right)+\frac{1}{2}\frac{\partial}{\partial x}\left(\Gamma h^2\right) - \frac{\mathcal{B}}{\mathcal{C}}\frac{\partial}{\partial x}\left(\frac{\partial \Gamma}{\partial x}\Gamma h\right)-\frac{\mathcal{B}}{\mathcal{C}}\frac{\partial \Gamma}{\partial x}\Gamma\frac{\partial h}{\partial x}=0. \qquad (5.3.2)$$

2-layer case

We differentiate the flow rate conditions, (5.2.50) and (5.2.51), to obtain expressions for $\partial Q_1/\partial x$ and $\partial Q_2/\partial x$. Many of the terms in the following equations contain h_2-h_1, hence we define $H_2=h_2-h_1$ as the thickness of the second layer and substitute H_2 into the equations that follow. However, it is noted that all of the following were calculated in terms of h_1 and h_2, and H_2 has only been used to shorten terms in the equations[3]. The first two evolution equations, from the integrated continuity equations in the first and second layer layer (5.2.32) and (5.2.33), are then given by

$$\begin{aligned}&\frac{\partial h_1}{\partial t}+\frac{1}{3\mathcal{C}}\frac{\partial}{\partial x}\left(\frac{\partial^3 h_1}{\partial x^3}h_1^3\right)+\frac{1}{3}\left(1-\frac{\rho_2}{\rho_1}\right)\Omega\left(\theta\right)\frac{\partial}{\partial x}\left(\frac{\partial h_1}{\partial x}h_1^3\right)+\frac{1}{3}\frac{\partial}{\partial x}\left(h_1^3\right)\\ &+\frac{1}{2\mathcal{C}}\frac{\sigma_{s,2}}{\sigma_{s,1}}\frac{\partial}{\partial x}\left(\frac{\partial^3 h_2}{\partial x^3}h_1^2\left(h_2-\frac{1}{3}h_1\right)\right)+\frac{1}{2}\frac{\rho_2}{\rho_1}\Omega\left(\theta\right)\frac{\partial}{\partial x}\left(\frac{\partial h_2}{\partial x}h_1^2\left(h_2-\frac{1}{3}h_1\right)\right)\\ &+\frac{1}{2}\frac{\rho_2}{\rho_1}\frac{\partial}{\partial x}\left(h_1^2H_2\right)-\frac{\mathcal{B}_1}{2\mathcal{C}}\frac{\partial}{\partial x}\left(\frac{\partial \Gamma_1}{\partial x}h_1^2\right)-\frac{\mathcal{B}_2}{2\mathcal{C}}\frac{\sigma_{s,2}}{\sigma_{s,1}}\frac{\Gamma_{in,1}}{\Gamma_{in,2}}\frac{\partial}{\partial x}\left(\frac{\partial \Gamma_2}{\partial x}h_1^2\right)=0, \qquad (5.3.3)\end{aligned}$$

[3]It was attempted to formulate the problem in terms of the layer thicknesses H_1 and H_2, where $H_1=h_1$ and $H_2=h_2-h_1$, as opposed to the interface locations h_1 and h_2. Unfortunately, this did not shorten the lengthy algebra.

and

$$\frac{\partial H_2}{\partial t}+\frac{1}{6}\frac{\mu_1}{\mu_2}\frac{\partial}{\partial x}\left(\left(\frac{1}{\mathcal{C}}\frac{\sigma_{s,2}}{\sigma_{s,1}}\frac{\partial^3 h_2}{\partial x^3}h_2^3+\frac{\rho_2}{\rho_1}\Omega\left(\theta\right)\frac{\partial h_2}{\partial x}+\frac{\rho_2}{\rho_1}\right)\left(2h_2^2+2h_1h_2-h_1^2\right)H_2\right)$$
$$+\left(1-\frac{\mu_1}{\mu_2}\right)\frac{\partial}{\partial x}\left(\left(\left(\frac{1}{\mathcal{C}}\frac{\sigma_{s,2}}{\sigma_{s,1}}\frac{\partial^3 h_2}{\partial x^3}+\frac{\rho_2}{\rho_1}\Omega\left(\theta\right)\frac{\partial h_2}{\partial x}\right)\left(h_2-\frac{1}{2}h_1\right)+\frac{\rho_2}{\rho_1}h_2\right)h_1H_2\right)$$
$$+\frac{1}{2\mathcal{C}}\frac{\partial}{\partial x}\left(\frac{\partial^3 h_1}{\partial x^3}h_1^2H_2\right)+\frac{1}{2}\left(1-\frac{\rho_2}{\rho_1}\right)\Omega\left(\theta\right)\frac{\partial}{\partial x}\left(\frac{\partial h_1}{\partial x}h_1^2H_2\right)+\frac{1}{2}\left(\frac{\rho_2}{\rho_1}\left(\frac{\mu_1}{\mu_2}-2\right)+1\right)\frac{\partial}{\partial x}\left(h_1^2H_2\right)$$
$$-\frac{\mathcal{B}_1}{\mathcal{C}}\frac{\partial}{\partial x}\left(\frac{\partial \Gamma_1}{\partial x}h_1H_2\right)-\frac{\mathcal{B}_2}{\mathcal{C}}\frac{\sigma_{s,2}}{\sigma_{s,1}}\frac{\Gamma_{in,1}}{\Gamma_{in,2}}\frac{\partial}{\partial x}\left(\frac{\partial \Gamma_2}{\partial x}\left(h_1+\frac{1}{2}\frac{\mu_1}{\mu_2}H_2\right)H_2\right)=0. \tag{5.3.4}$$

Expressions for the velocity and velocity gradient at the liquid-liquid interface and the free surface are found from the leading order solutions for velocity (5.2.48) and (5.2.49). Substituting these expressions into the advection-diffusion equation (5.2.39) at $y=h_1$ and $y=h_2$, we obtain the final two evolution equations:

$$\frac{\partial \Gamma_1}{\partial t}+\frac{1}{2\mathcal{C}}\frac{\partial}{\partial x}\left(\Gamma_1\frac{\partial^3 h_1}{\partial x^3}h_1^2\right)+\frac{1}{2}\left(1-\frac{\rho_2}{\rho_1}\right)\Omega\left(\theta\right)\frac{\partial}{\partial x}\left(\Gamma_1\frac{\partial h_1}{\partial x}h_1^2\right)+\frac{1}{2}\frac{\partial}{\partial x}\left(\Gamma_1h_1^2\right)$$
$$+\frac{1}{\mathcal{C}}\frac{\sigma_{s,2}}{\sigma_{s,1}}\frac{\partial}{\partial x}\left(\Gamma_1\frac{\partial^3 h_2}{\partial x^3}\left(h_2-\frac{1}{2}h_1^2\right)h_1\right)+\frac{\rho_2}{\rho_1}\Omega\left(\theta\right)\frac{\partial}{\partial x}\left(\Gamma_1\frac{\partial h_2}{\partial x}\left(h_2-\frac{1}{2}h_1\right)h_1\right)$$
$$-\frac{\mathcal{B}_1}{\mathcal{C}}\frac{\partial}{\partial x}\left(\frac{\partial \Gamma_1}{\partial x}\Gamma_1h_1\right)-\frac{\mathcal{B}_2}{\mathcal{C}}\frac{\sigma_{s,2}}{\sigma_{s,1}}\frac{\Gamma_{in,1}}{\Gamma_{in,2}}\frac{\partial}{\partial x}\left(\frac{\partial \Gamma_2}{\partial x}\Gamma_1h_1\right)+\frac{\rho_2}{\rho_1}\frac{\partial}{\partial x}\left(\Gamma_1h_1H_2\right)$$
$$+\left(\left(\frac{1}{\mathcal{C}}\frac{\sigma_{s,2}}{\sigma_{s,1}}\frac{\partial^3 h_2}{\partial x^3}+\frac{\rho_2}{\rho_1}\Omega\left(\theta\right)\frac{\partial h_2}{\partial x}+\frac{\rho_2}{\rho_1}\right)H_2-\frac{\mathcal{B}_1}{\mathcal{C}}\frac{\partial \Gamma_1}{\partial x}-\frac{\mathcal{B}_2}{\mathcal{C}}\frac{\sigma_{s,2}}{\sigma_{s,1}}\frac{\Gamma_{in,1}}{\Gamma_{in,2}}\frac{\partial \Gamma_2}{\partial x}\right)\Gamma_1\frac{\partial h_1}{\partial x}=0, \tag{5.3.5}$$

and

$$\frac{\partial \Gamma_2}{\partial t}+\frac{1}{2}\frac{\mu_1}{\mu_2}\frac{1}{\mathcal{C}}\frac{\sigma_{s,2}}{\sigma_{s,1}}\frac{\partial}{\partial x}\left(\Gamma_2\frac{\partial^3 h_2}{\partial x^3}h_2^2\right)+\frac{1}{2}\frac{\rho_2}{\rho_1}\frac{\mu_1}{\mu_2}\frac{\partial}{\partial x}\left(\left(\Omega\left(\theta\right)\frac{\partial h_2}{\partial x}+1\right)\Gamma_2 h_2^2\right)$$
$$+\left(1-\frac{\mu_1}{\mu_2}\right)\frac{\partial}{\partial x}\left(\left(\left(\frac{1}{\mathcal{C}}\frac{\sigma_{s,2}}{\sigma_{s,1}}\frac{\partial^3 h_2}{\partial x^3}+\frac{\rho_2}{\rho_1}\Omega\left(\theta\right)\frac{\partial h_2}{\partial x}\right)\left(h_2-\frac{1}{2}h_1\right)+\frac{\rho_2}{\rho_1}h_2\right)\Gamma_2 h_1\right)$$
$$+\frac{1}{2}\left(1-\frac{\rho_2}{\rho_1}\right)\Omega\left(\theta\right)\frac{\partial}{\partial x}\left(\Gamma_2\frac{\partial h_1}{\partial x}h_1^2\right)+\frac{1}{2}\left(\frac{\rho_2}{\rho_1}\left(\frac{\mu_1}{\mu_2}-2\right)+1\right)\frac{\partial}{\partial x}\left(\Gamma_2 h_1^2\right)+\frac{1}{2\mathcal{C}}\frac{\partial}{\partial x}\left(\Gamma_2\frac{\partial^3 h_1}{\partial x^3}h_1^2\right)$$
$$-\frac{\mathcal{B}_1}{\mathcal{C}}\frac{\partial}{\partial x}\left(\frac{\partial \Gamma_1}{\partial x}\Gamma_2 h_1\right)-\frac{\mathcal{B}_2}{\mathcal{C}}\frac{\sigma_{s,2}}{\sigma_{s,1}}\frac{\Gamma_{in,1}}{\Gamma_{in,2}}\left(\frac{\partial}{\partial x}\left(\frac{\partial \Gamma_2}{\partial x}\Gamma_2\left(h_1+\frac{\mu_1}{\mu_2}H_2\right)\right)+\frac{\mu_1}{\mu_2}\frac{\partial \Gamma_2}{\partial x}\Gamma_2\frac{\partial h_2}{\partial x}\right)=0. \tag{5.3.6}$$

Perturbing the Evolution Equations

1-layer case

We perturb our evolution equations (5.3.1) and (5.3.2) using the disturbances

$$h=3^{1/3}+\delta h'\exp\left(\mathrm{i}kx+st\right),$$
$$\Gamma=1+\delta\Gamma'\exp\left(\mathrm{i}kx+st\right),$$

where $0<\delta<\varepsilon\ll 1$, with δ being a constant giving the amplitude of the wave. Substituting the disturbance into the evolution equation for film thickness (5.3.1), performing the differentiation, linearising, and cancelling the exponential terms, we obtain

$$\left(s+\frac{1}{\mathcal{C}}k^4-\Omega\left(\theta\right)k^2+3^{2/3}\mathrm{i}k\right)h'+\frac{3^{2/3}}{2}\frac{\mathcal{B}}{\mathcal{C}}k^2\Gamma'=0. \tag{5.3.7}$$

Similarly, substituting the disturbances into the evolution equation for surfactant concentration (5.3.2) we obtain

$$\left(\frac{3^{2/3}}{2}\frac{1}{\mathcal{C}}k^4 - \frac{3^{2/3}}{2}\Omega\left(\theta\right)k^2 + 3^{1/3}\mathrm{i}k\right)h' + \left(s + 3^{1/3}\frac{\mathcal{B}}{\mathcal{C}}k^2 + \frac{3^{2/3}}{2}\mathrm{i}k\right)\Gamma' = 0. \tag{5.3.8}$$

Equations (5.3.7) and (5.3.8) represent the disturbance equations, and can be written in matrix form $A\mathbf{x}' = \mathbf{0}$:

$$\begin{pmatrix} s + \frac{1}{\mathcal{C}}k^4 - \Omega\left(\theta\right)k^2 + 3^{2/3}\mathrm{i}k & \frac{3^{2/3}}{2}\frac{\mathcal{B}}{\mathcal{C}}k^2 \\ \frac{3^{2/3}}{2}\frac{1}{\mathcal{C}}k^4 - \frac{3^{2/3}}{2}\Omega\left(\theta\right)k^2 + 3^{1/3}\mathrm{i}k & s + 3^{1/3}\frac{\mathcal{B}}{\mathcal{C}}k^2 + \frac{3^{2/3}}{2}\mathrm{i}k \end{pmatrix} \cdot \begin{pmatrix} h' \\ \Gamma' \end{pmatrix} = \mathbf{0}.$$

The dispersion relation is obtained by setting $\det(A) = 0$, which is given by

$$\begin{aligned}\left(s + \frac{1}{\mathcal{C}}k^4 - \Omega\left(\theta\right)k^2 + 3^{2/3}\mathrm{i}k\right)\left(s + 3^{1/3}\frac{\mathcal{B}}{\mathcal{C}}k^2 + \frac{3^{2/3}}{2}\mathrm{i}k\right) \\ - \frac{3^{2/3}}{2}\frac{\mathcal{B}}{\mathcal{C}}k^2\left(\frac{3^{2/3}}{2}\frac{1}{\mathcal{C}}k^4 - \frac{3^{2/3}}{2}\Omega\left(\theta\right)k^2 + 3^{1/3}\mathrm{i}k\right) = 0.\end{aligned} \tag{5.3.9}$$

Before solving the dispersion relation, we make the transformation $\overline{s} = s + u_{ave}\mathrm{i}k$, where u_{ave} is the average velocity of the waveless film, given by

$$\begin{aligned} u_{ave} &= \frac{1}{h^0}\int_0^{h^0} u^0 \, \mathrm{d}y \\ &= 3^{-1/3}. \end{aligned}$$

The substitution $\overline{s} = s + 3^{-1/3}\mathrm{i}k$ alters the wave mode into the form $\exp\left[\mathrm{i}k\left(x - u_{ave}t\right) + \overline{s}t\right]$, so that we are in a reference frame moving with the average velocity of the film, in the positive x-direction. We fix the wavenumber k to be real, solving for $\overline{s}$ which can be complex; the stability of the film depends on the sign of the real part of $\overline{s}$. When the real part of $\overline{s}$ is positive perturbations will grow, and the film is unstable. Conversely, the film

is stable if the real part of $\overline{s}$ is negative. The dispersion relation (5.3.9) then becomes:

$$\overline{s}^2 + k\left(\frac{1}{\mathcal{C}}k^3 + \left(3^{1/3}\frac{\mathcal{B}}{\mathcal{C}} - \Omega\left(\theta\right)\right)k + \frac{5\cdot 3^{-1/3}}{2}\mathrm{i}\right)\overline{s} \\ + \frac{3^{-1/3}}{4}k^2\left(k\left(\frac{1}{\mathcal{C}}k^2 - \Omega\left(\theta\right)\right) + 2\cdot 3^{-1/3}\mathrm{i}\right)\left(3^{2/3}\frac{\mathcal{B}}{\mathcal{C}}k + 2\mathrm{i}\right) = 0. \quad (5.3.10)$$

Equation (5.3.10) is a quadratic in $\overline{s}$, and solved to obtain

$$\overline{s} = -\frac{k}{2}\left(\frac{1}{\mathcal{C}}k^3 + \left(3^{1/3}\frac{\mathcal{B}}{\mathcal{C}} - \Omega\left(\theta\right)\right)k + \frac{5\cdot 3^{-1/3}}{2}\mathrm{i} \pm \left(\left(\frac{1}{\mathcal{C}}k^3 + \left(3^{1/3}\frac{\mathcal{B}}{\mathcal{C}} - \Omega\left(\theta\right)\right)k + \frac{5\cdot 3^{-1/3}}{2}\mathrm{i}\right)^2 \right. \\ \left. - 3^{-1/3}\left(k\left(\frac{1}{\mathcal{C}}k^2 - \Omega\left(\theta\right)\right) + 2\cdot 3^{-1/3}\mathrm{i}\right)\left(3^{2/3}\frac{\mathcal{B}}{\mathcal{C}}k + 2\mathrm{i}\right)\right)^{1/2}\right). \quad (5.3.11)$$

This equation can be used to produce plots of the growth rate $\overline{s}$ against k, which is done in the proceeding section.

We consider here how our analysis would be affected if we disregard the effect of surfactant. In this case, we would not have the evolution equation for surfactant concentration (5.3.2), and perturbing the evolution equation for the film height (5.3.1) would lead to the dispersion relation (there being no Γ' eigenmode)

$$\overline{s} = \Omega\left(\theta\right)k^2 - \frac{1}{\mathcal{C}}k^4 - 2\cdot 3^{-1/3}\mathrm{i}k,$$

which we can re-dimensionalise:

$$\overline{s} = Q\cot\left(\theta\right)k^2 - \frac{d_s^3\sigma_{s,1}}{\mu}k^4 - \frac{2\cdot 3^{-1/3}}{d_s}Q\mathrm{i}k.$$

Whether the disturbance is stable depends upon the sign of the real part of $\overline{s}$, with the

most unstable mode given by the maximum positive value of $\overline{s}$. Since

$$\text{real}\left(\overline{s}\right) = \overline{s}_r = Q\cot\left(\theta\right)k^2 - \frac{d_s^3\sigma_{s,1}}{\mu}k^4,$$

to find the maximum of $\overline{s}_r$, we differentiate with respect to k and equate to zero:

$$\frac{\mathrm{d}\overline{s}_r}{\mathrm{d}k} = 0 \Leftrightarrow 2k\left(Q\cot\left(\theta\right) - \frac{2d_s^3\sigma_{s,1}}{\mu}k^2\right) = 0.$$

Solving for k finds the most unstable wavenumber, k^*. The solutions are $k = 0$ and

$$k^* = \sqrt{\frac{\rho g\cos\left(\theta\right)}{2\sigma_{s,1}}},$$

which gives the most unstable wavelength

$$\lambda^* = 2\pi\sqrt{\frac{2\sigma_{s,1}}{\rho g\cos\left(\theta\right)}}.$$

This matches with the linear stability analysis carried out by Brun *et al.* [21], with this wavelength being identical to (5.1.2). We can undergo this process with the solution (5.3.11) to the dispersion relation incorporating the effect of surfactant, enabling us to plot the most unstable wavelength λ^* against varying parameters, as done in the next section.

2-layer case

Similar to the single-layer case, we now perturb the evolution equations (5.3.3), (5.3.4), (5.3.5) and (5.3.6) about the steady state as follows:

$$h_1 = h_1^0 + \delta h_1' \exp\left(\mathrm{i}kx + st\right), \qquad \Gamma_1 = 1 + \delta\Gamma_1' \exp\left(\mathrm{i}kx + st\right),$$
$$h_2 = h_2^0 + \delta h_2' \exp\left(\mathrm{i}kx + st\right), \qquad \Gamma_2 = \frac{\Gamma_{in,2}}{\Gamma_{in,1}} + \delta\Gamma_2' \exp\left(\mathrm{i}kx + st\right).$$

Substituting the perturbations into the evolution equation for the liquid-liquid interface (5.3.3), performing the differentiation, linearising and cancelling the exponential terms:

$$\begin{aligned}
&\left(s + \frac{1}{3}\left(\frac{1}{\mathcal{C}}k^2 + \left(\frac{\rho_2}{\rho_1} - 1\right)\Omega\left(\theta\right)\right)h_1^{0^3}k^2 + \left(\frac{\rho_2}{\rho_1}\left(h_2^0 - \frac{3}{2}h_1^0\right) + h_1^0\right)h_1^0\mathrm{i}k\right)h_1' \\
&+\frac{1}{2}\left(\left(\frac{1}{\mathcal{C}}\frac{\sigma_{s,2}}{\sigma_{s,1}}k^2 - \frac{\rho_2}{\rho_1}\Omega\left(\theta\right)\right)\left(h_2^0 - \frac{1}{3}h_1^0\right)k^2 + \frac{\rho_2}{\rho_1}\mathrm{i}k\right)h_1^{0^2}h_2' \\
&+\frac{\mathcal{B}_1}{2\mathcal{C}}h_1^{0^2}k^2\Gamma_1' + \frac{\mathcal{B}_2}{2\mathcal{C}}\frac{\sigma_{s,2}}{\sigma_{s,1}}\frac{\Gamma_{in,1}}{\Gamma_{in,2}}h_1^{0^2}k^2\Gamma_2' = 0. \qquad (5.3.12)
\end{aligned}$$

Similarly, substituting the perturbations into the evolution equation for the free surface (5.3.4):

$$\begin{aligned}
&\left(-s + \left(\frac{1}{2}\left(\frac{1}{\mathcal{C}}k^2 - \left(1 - \frac{\rho_2}{\rho_1}\right)\Omega\left(\theta\right)\right)h_1^{0^2}k^2 - \frac{\rho_2}{\rho_1}\left(\frac{\mu_1}{\mu_2}H_2^0 + 3h_1^0 - h_2^0\right)\mathrm{i}k\right)H_2^0\right. \\
&\qquad\left. + \left(h_2^0 - \frac{3}{2}h_1^0\right)h_1^0\mathrm{i}k\right)h_1' \\
&+\left(s + \left(\left(\frac{1}{\mathcal{C}}\frac{\sigma_{s,2}}{\sigma_{s,1}}k^2 - \frac{\rho_2}{\rho_1}\Omega\left(\theta\right)\right)\left(\frac{1}{2}\left(2h_2^0 - h_1^0\right)h_1^0 + \frac{1}{3}\frac{\mu_1}{\mu_2}H_2^{0^2}\right)k^2 + \frac{\rho_2}{\rho_1}\left(\frac{\mu_1}{\mu_2}H_2^0 + 2h_1^0\right)\mathrm{i}k\right)H_2^0\right. \\
&\qquad\left. + \frac{1}{2}h_1^{0^2}\mathrm{i}k\right)h_2' + \frac{\mathcal{B}_1}{\mathcal{C}}h_1^0H_2^0k^2\Gamma_1' + \frac{\mathcal{B}_2}{\mathcal{C}}\frac{\sigma_{s,2}}{\sigma_{s,1}}\frac{\Gamma_{in,1}}{\Gamma_{in,2}}\left(h_1^0 + \frac{1}{2}\frac{\mu_1}{\mu_2}H_2^0\right)H_2^0k^2\Gamma_2' = 0. \qquad (5.3.13)
\end{aligned}$$

Substituting the perturbations into the evolution equation for the surfactant concentration along the liquid-liquid interface (5.3.5):

$$\left(\frac{1}{2}\left(\frac{1}{\mathcal{C}}k^2+\left(\frac{\rho_2}{\rho_1}-1\right)\Omega\left(\theta\right)\right)h_1^{0^2}k^2+\left(2\frac{\rho_2}{\rho_1}\left(h_2^0-\frac{3}{2}h_1^0\right)+h_1^0\right)\mathrm{i}k\right)h_1'$$
$$+\left(\left(\frac{1}{\mathcal{C}}\frac{\sigma_{s,2}}{\sigma_{s,1}}k^2-\frac{\rho_2}{\rho_1}\Omega\left(\theta\right)\right)\left(h_2^0-\frac{1}{2}h_1^0\right)h_1^0k^2+\frac{\rho_2}{\rho_1}h_1^0\mathrm{i}k\right)h_2'$$
$$+\left(s+\left(\frac{1}{2}h_1^0+\frac{\rho_2}{\rho_1}H_2^0\right)h_1^0\mathrm{i}k+\frac{\mathcal{B}_1}{\mathcal{C}}h_1^0k^2\right)\Gamma_1'+\frac{\mathcal{B}_2}{\mathcal{C}}\frac{\sigma_{s,2}}{\sigma_{s,1}}\frac{\Gamma_{in,1}}{\Gamma_{in,2}}h_1^0k^2\Gamma_2'=0. \tag{5.3.14}$$

Finally, we substitute the perturbations into the evolution equation for surfactant concentration along the free surface (5.3.6), and obtain:

$$\frac{\Gamma_{in,2}}{\Gamma_{in,1}}\left(\frac{1}{2}\left(\frac{1}{\mathcal{C}}k^2+\left(\frac{\rho_2}{\rho_1}-1\right)\Omega\left(\theta\right)\right)h_1^{0^2}k^2+\frac{\rho_2}{\rho_1}\left(h_2^0-2h_1^0-\frac{\mu_1}{\mu_2}H_2^0\right)\mathrm{i}k+h_1^0\mathrm{i}k\right)h_1'$$
$$+\frac{\Gamma_{in,2}}{\Gamma_{in,1}}\left(\left(\frac{1}{\mathcal{C}}\frac{\sigma_{s,2}}{\sigma_{s,1}}k^2-\frac{\rho_2}{\rho_1}\Omega\left(\theta\right)\right)\left(\left(h_2^0-\frac{1}{2}h_1^0\right)h_1^0+\frac{1}{2}\frac{\mu_1}{\mu_2}H_2^{0^2}\right)k^2\right.$$
$$\left.+\frac{\rho_2}{\rho_1}\left(h_1^0+\frac{\mu_1}{\mu_2}H_2^0\right)\mathrm{i}k\right)h_2'+\frac{\mathcal{B}_1}{\mathcal{C}}\frac{\Gamma_{in,2}}{\Gamma_{in,1}}h_1^0k^2\Gamma_1'$$
$$+\left(s+\frac{\rho_2}{\rho_1}\left(h_1^0+\frac{1}{2}\frac{\mu_1}{\mu_2}H_2^0\right)H_2^0\mathrm{i}k+\frac{1}{2}h_1^{0^2}\mathrm{i}k+\frac{\mathcal{B}_2}{\mathcal{C}}\frac{\sigma_{s,2}}{\sigma_{s,1}}\left(h_1^0+\frac{\mu_1}{\mu_2}H_2^0\right)k^2\right)\Gamma_2'=0. \tag{5.3.15}$$

The four disturbance equations, (5.3.12), (5.3.13), (5.3.14) and (5.3.15), can be written in matrix form, similar to the single-layer case:

$$A\cdot\begin{pmatrix}h_1'\\h_2'\\\Gamma_1'\\\Gamma_2'\end{pmatrix}=0,$$

where A is the matrix of coefficients, of size 4×4. The dispersion relation is acquired by setting by $\det(A) = 0$. The Leibniz formula for calculating the determinant of an $n \times n$ matrix M

$$\det(M) = \sum_{\sigma \in S_n} \operatorname{sgn}(\sigma) \prod_{i=1}^{n} M_{i,\sigma(i)},$$

is used. Here, S_n is the set of all permutations of the integers $\{1, 2, \ldots, n\}$, with $\operatorname{sgn}(\sigma)$ being the signature of the permutation σ, of the value -1 or 1. Finally, $\sigma(i)$ denotes the element that is in the i'th position after applying the permutation σ.

Similar to the single-layer case, we make the transformation $\overline{s} = s + u_{ave}\mathrm{i}k$, where u_{ave} is the average velocity of the film, given by

$$\begin{aligned} u_{ave} &= \frac{1}{h_2^0} \int_0^{h_2^0} u^0 \, \mathrm{d}y \\ &= \frac{1}{h_2^0} \left(\int_0^{h_1^0} u_1^0 \, \mathrm{d}y + \int_{h_1^0}^{h_2^0} u_2^0 \, \mathrm{d}y \right) \\ &= \frac{1}{h_2^0} \left(\frac{1}{3} h_1^{0^3} + \left(\frac{1}{2} \Big(1 + \frac{\rho_2}{\rho_1} \Big) h_1^0 + \frac{\rho_2}{\rho_1} H_2^0 \right) h_1^0 H_2^0 + \frac{1}{3} \frac{\rho_2}{\rho_1} \frac{\mu_1}{\mu_2} H_2^{0^3} \right). \end{aligned}$$

Having used the steady velocities from (5.2.53) and (5.2.54), and the values for the steady film thicknesses h_1^0 and h_2^0 from implementing Newton's method, explained previously.

The determinant of A is given by a quartic in $\overline{s}$. By fixing the wavenumber k, a real number, we can solve this equation using Ferrari's method.

Ferrari's method for solving quartic polynomials

We outline Ferrari's method, an exact method for solving quartic equations. The reader is referred to [39] for more detail. The quartic polynomial

$$a_4 x^4 + a_3 x^3 + a_2 x^2 + a_1 x + a_0 = 0,$$

can be transformed to the depressed quartic

$$x_d^4 + b_2 x_d^2 + b_1 x_d + b_0 = 0,$$

via the transformation $x_d = x + a_3/4a_4$, where

$$b_2 = \frac{a_2}{a_4} - \frac{3a_3^2}{8a_4^2}, \quad b_1 = \frac{a_3^3}{8a_4^3} - \frac{a_2 a_3}{2a_4^2} + \frac{a_1}{a_4}, \quad b_0 = \frac{a_0}{a_4} - \frac{3a_3^4}{256a_4^4} - \frac{a_1 a_3}{4a_4^2} + \frac{a_2 a_3^2}{16a_4^3}.$$

The depressed quartic can be written as

$$\left(x_d^2 + b_2 + y\right)^2 = \left(b_2 + 2y\right) x_d^2 - b_1 x_d + \left(y^2 + 2yb_2 + b_2^2 - b_0\right), \tag{5.3.16}$$

with the value of y arbitrary. This arbitrary value is chosen such that the right-hand side of (5.3.16) is a square. The right-hand side of (5.3.16) is a quadratic in x_d, and by setting the discriminant of this quadratic to zero, it may be written as a square. The discriminant equalling zero corresponds to

$$y^3 + \frac{5}{2} b_2 y^2 + \left(2b_2^2 - b_0\right) y + \left(\frac{b_2^3}{2} - \frac{b_2 b_0}{2} - \frac{b_1^2}{8}\right) = 0,$$

a cubic in y. The value of y is chosen to be a solution to this cubic, and makes the right-hand side a square[4]. Equation (5.3.16) can then be written as the difference of two squares, so that

$$\left(x_d^2 + b_2 + y + x_d\sqrt{b_2 + 2y} - \frac{b_1}{2\sqrt{b_2 + 2y}}\right)\left(x_d^2 + b_2 + y - x_d\sqrt{b_2 + 2y} + \frac{b_1}{2\sqrt{b_2 + 2y}}\right) = 0,$$

[4]The three solutions to the general cubic equation $ax^3 + bx^2 + cx + d = 0$ is given by a general formula. It does not matter which solution is chosen to use as the value of y. See [39] for details on the solution of a cubic equation.

the product of two quadratics, each of which can be solved via the quadratic equation. Having obtained the four solutions x_d for the depressed quartic, the solutions to the original quartic are given by $x = x_d - a_3/4a_4$. If $b_2 + 2y = 0$, this method divides by zero, however, in this case it can be shown that $b_1 = 0$. This reduces the depressed quartic into a bi-quadratic equation, which can be solved as a quadratic in x_d^2 (where the solutions to the original quartic still remain as $x = x_d - a_3/4a_4$).

5.3.2 Results and discussion

1-layer case

The two solutions (5.3.11) to the dispersion relation (5.3.9) enable us to plot the real part of the growth rate $\overline{s}$ against the wavenumber k, showing the two wave modes. Examples of this is done in Figure 5.5, where only a positive real part of $\overline{s}$ is plotted, corresponding to when the wave mode is unstable. In both subfigures (a) and (b), the parameters $\mathcal{C} = 1$ and $\Omega(\theta) = 1$ are fixed, whilst $\mathcal{B}$ is varied according to the legend, starting at a lowest value of $\mathcal{B} = 0.2$ in (a) and rising to a maximum value of $\mathcal{B} = 3$ in (b). In (a), both wave modes are unstable, and to distinguish between the two different modes, one is plotted with a solid line, the other with a dashed line (the same colour indicates the same value of $\mathcal{B}$). In (b), only one wave mode is unstable, hence only solid lines are plotted.

The two different wave modes given by the solution to the dispersion relation (5.3.11) correspond to 'original' waves based on the local surface tension (that existed without surfactant, but are modified with surfactant), and Marangoni waves that arise due to the surface tension gradients arising from introducing surfactant. Considering Figure 5.5(a), as $\mathcal{B}$ gets smaller, the solution to the wave modes plotted tend to the limiting case of no surfactant being present. In this figure, the dashed lines correspond to the original waves, and the solid lines to the Marangoni waves. In the case $\mathcal{B} = 0.2$, the black dashed line shows the original wave based on the local surface tension is the most

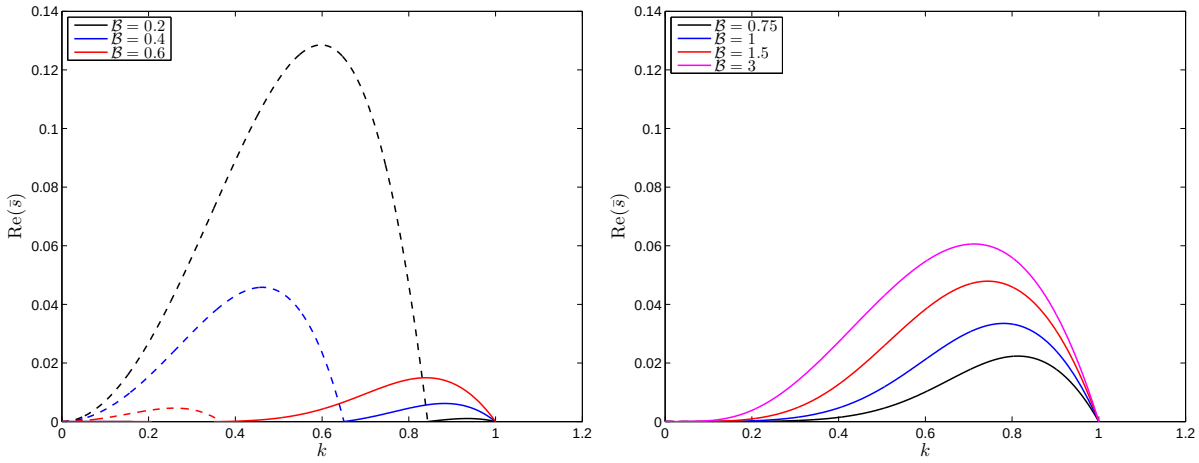

(a) (b)

Figure 5.5: Plots of the real part of $\overline{s}$ against k, from equation (5.3.11), where the parameters $\mathcal{C} = 1$ and $\Omega(\theta) = 1$ are fixed whilst $\mathcal{B}$ varies. In (a), the dashed lines distinguish between two different modes, with the same colour indicating the same value of $\mathcal{B}$.

unstable, with the Marangoni wave being unstable at larger wavenumbers, but with a small growth rate. As $\mathcal{B}$ increases, the original wave mode (dashed line) is damped out, whereas the Marangoni wave becomes increasingly unstable; suggesting that introducing surfactant initially stabilises the thin film in the respect that the growth rate is reduced (but the film remains unstable). Interestingly, the cut-off wavenumber is not affected with the inclusion of surfactant. As shown in (a), when $\mathcal{B}$ is between 0.4 and 0.6, there is a transition whereby the Marangoni wave becomes the most unstable. The parameter $\mathcal{B}$ continues to increase in subfigure (b), with the growth rate of the Marangoni wave continuing to rise. There are no dashed lines in (b), indicating the original waves are now stable.

Figure 5.6 explores the features of stability in more detail. We plot (a) the most unstable wavenumber k^*, (b) the cut-off wavenumber (above which all wavenumbers are stable) k_c and (c) the maximum growth rate $\overline{s}^*$ against $\Omega(\theta)$. We reiterate here that varying $\Omega(\theta)$ corresponds to altering the inclination angle. The parameter $\mathcal{C} = 1$ remains constant in all subfigures, whilst $\mathcal{B}$ varies as indicated in the legend. The dashed line in

Figure 5.6(a) represents where the most unstable mode switches, emphasised due to the discontinuity in k^*. Note that this switch between modes also occurs in other cases in each subfigure (a), (b) and (c), but since there is no discontinuity in the plots, no dashed line is plotted.

As $\Omega(\theta)$ increases, corresponding to a decrease in θ (that is, the inclined plane becoming more horizontal), there is an increase in the most unstable wavenumber as seen in Figure 5.6(a). This means that there is a decrease in the most unstable wavelength as the incline becomes more horizontal, in agreement with the most unstable wavelength (5.1.2) as calculated by Brun *et al.* [21]. The most unstable mode switches from the Marangoni mode to the altered 'original' mode as $\Omega(\theta)$ increases, with this value of $\Omega(\theta)$ being different for each value of $\mathcal{B}$. A decrease in the most unstable wavenumber occurs when this switch happens, and a physical explanation could be given by the gravitational force having a larger influence over surface tension as the incline becomes horizontal, resulting in gravity having more influence than the small variations in the surface tension; hence the 'original' wave becoming more prominent than the Marangoni wave. As $\mathcal{B}$ increases, this switch changes from a discontinuous drop (e.g. the case $\mathcal{B} = 0.5$), to the case where this switch is continuous and no longer visible in the plot (e.g. the case $\mathcal{B} = 3$).

Figure 5.6(b) shows that the cut-off wavenumber is not affected by the parameter $\mathcal{B}$ except in the limiting case of small $\Omega(\theta)$, where the model becomes invalid. The previous work of Oron *et al.* [91] stated that the cut-off wavenumber for the Rayleigh-Taylor instability was given by the square root of the Bond number, that is the ratio of gravitational forces to surface tension forces. In this model, despite the addition of surfactant, it is remembered at leading order there is no change in surface tension (the surface tension gradient only manifested itself in the stress boundary conditions). Thus there is no significant change in the Bond number, and we would not expect a change in k_c as predicted by Oron *et al.*

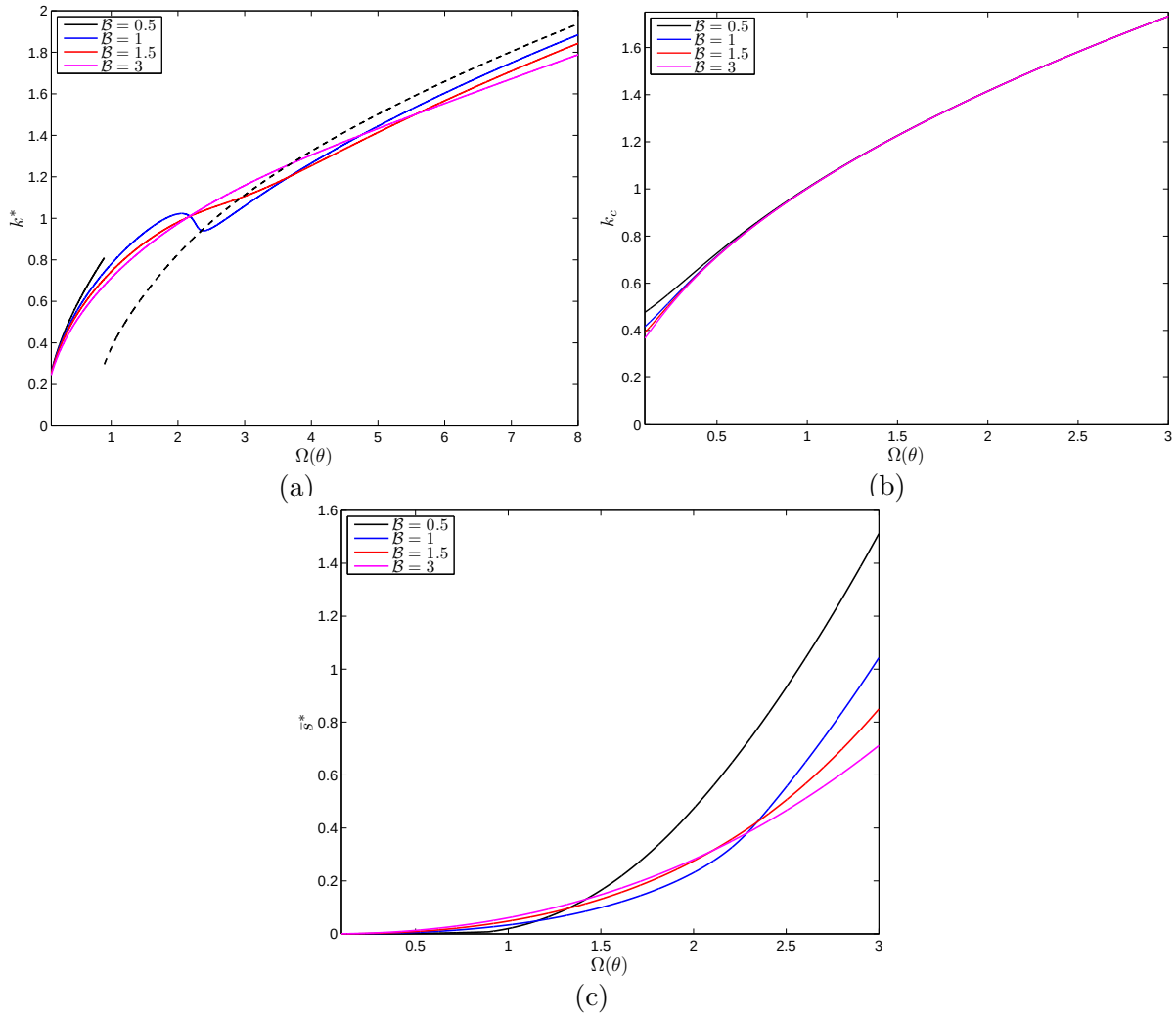

Figure 5.6: Plots of the (a) most unstable wavenumber k^*, (b) the cut-off wavenumber k_c, and (c) maximum growth rate $\overline{s}^*$ against $\Omega(\theta)$, from the solution of the dispersion relation (5.3.11). The parameter $\mathcal{B}$ varies according to the legend, whilst $\mathcal{C} = 1$ is fixed. The dashed line in (a) indicates when the most unstable wavenumber switched between modes in the $\mathcal{B} = 0.5$ case.

Figure 5.6(c) depicts the intuitive result that as the incline becomes more horizontal, the growth rate of the disturbance increases. Moreover, as $\Omega(\theta)$ gets above a certain point ($\Omega(\theta) \approx 2.3$), the increase in the effect of surfactant (increase in $\mathcal{B}$) decreases the growth rate of the most unstable mode. As explained previously, for smaller $\Omega(\theta)$ the Marangoni wave is the most unstable, and the largest value of $\mathcal{B}$ has the largest growth rate (albeit marginally). As the incline becomes more horizontal, $\Omega(\theta)$ increases, and the original wave transitions to the most unstable mode, with surfactant damping this mode, so that the smaller value of $\mathcal{B}$ has the larger growth rate.

2-layer case

Considering the case of the two-layered film, by fixing the wavenumber k as a real number we can solve (as described in the previous section) the dispersion relation $\det(A) = 0$ using Ferrari's method. Figure 5.7 plots two examples of this with the incline changing so that $\Omega(\theta) = 0.5$ in (a) and $\Omega(\theta) = 2.5$ in (b). All four modes are plotted in both cases, with the parameters listed in the caption. As expected, increasing the value of $\Omega(\theta)$ corresponds to increasing the growth rate of the disturbances, with all four modes seeing a rise in the real part of $\overline{s}$.

The features of stability whilst varying $\Omega(\theta)$ is investigated further in Figure 5.8. Subfigure (a) plots the most unstable wavelength k^*, (b) the cut-off wavenumber k_c and (c) the maximum growth rate $\overline{s}^*$ against $\Omega(\theta)$. The effectiveness of surfactant on the free surface is varied through a change in $\mathcal{B}_2$ for each of the plots, as indicated in the legends.

The results are extremely similar to the corresponding single-layer case of Figure 5.6. As seen in Figure 5.8 (a), the most unstable wavenumber increases as the inclined plane becomes more horizontal. The transition from the Marangoni wave being the most unstable for smaller values of $\Omega(\theta)$ to the 'original' wave is readily seen in each case of $\mathcal{B}_2$, with the transition occurring at a higher value of $\Omega(\theta)$ in each case.

Interestingly, the cut-off wavenumber plotted in (b) now varies depending on the value

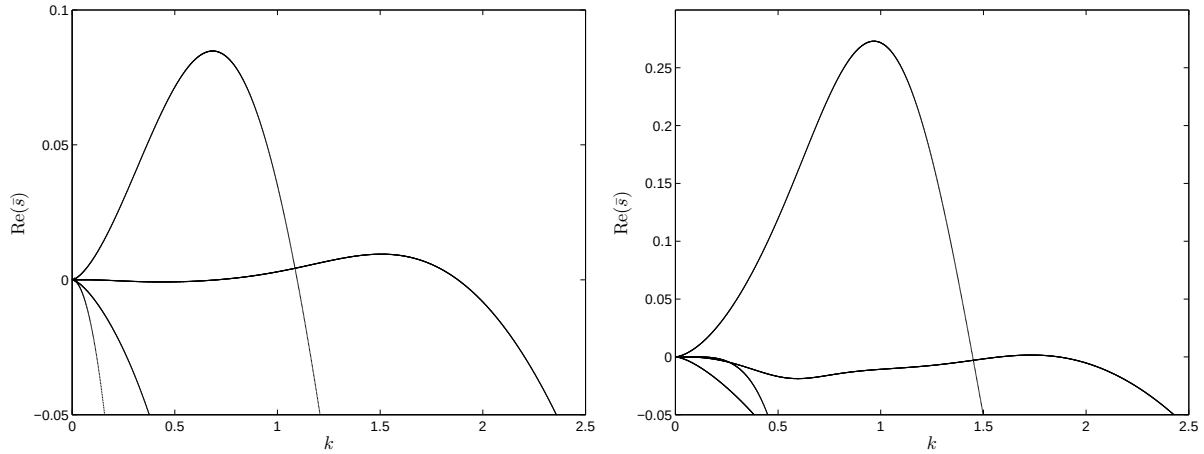

(a) (b)

Figure 5.7: Plots of the real part of $\overline{s}$ against k, from the dispersion relation $\det(A) = 0$. The parameters are fixed at $\frac{\mu_1}{\mu_2} = 1$, $\frac{\rho_2}{\rho_1} = 1$, $Q_1 = 0.5$, $\frac{\sigma_{s,2}}{\sigma_{s,1}} = 1$, $\frac{\Gamma_{in,2}}{\Gamma_{in,1}} = 1$, $\mathcal{B}_1 = 1$, $\mathcal{B}_2 = 1$, $\mathcal{C} = 1$, and (a) $\Omega(\theta) = 0.5$, (b) $\Omega(\theta) = 2.5$.

of $\mathcal{B}_2$, when $\Omega(\theta)$ is less than a value of four. Previously said to be characterised by the Bond number, by introducing a second layer and a new liquid-liquid interface into the model this no longer holds. Finally, subfigure (c) again confirms that making the inclined plane more horizontal induces a greater growth rate of the most unstable disturbance. Moreover, the maximum growth rate in the two-layer case is enlarged from the single-layer case.

5.4 Conclusions

To summarise, the aim of this chapter was to provide a two-dimensional mathematical model of a liquid film flowing along the underside of an inclined plane. This was done for two cases, both for a single-layered and two-layered film. By incorporating the effect of surfactant, an extension to recent work in the literature [21] has been carried out.

Having found the leading order and steady state solutions using a thin film approximation, evolution equations for the film height(s) and surfactant concentration(s) were then derived and perturbed through a linear stability analysis. This was followed by a study

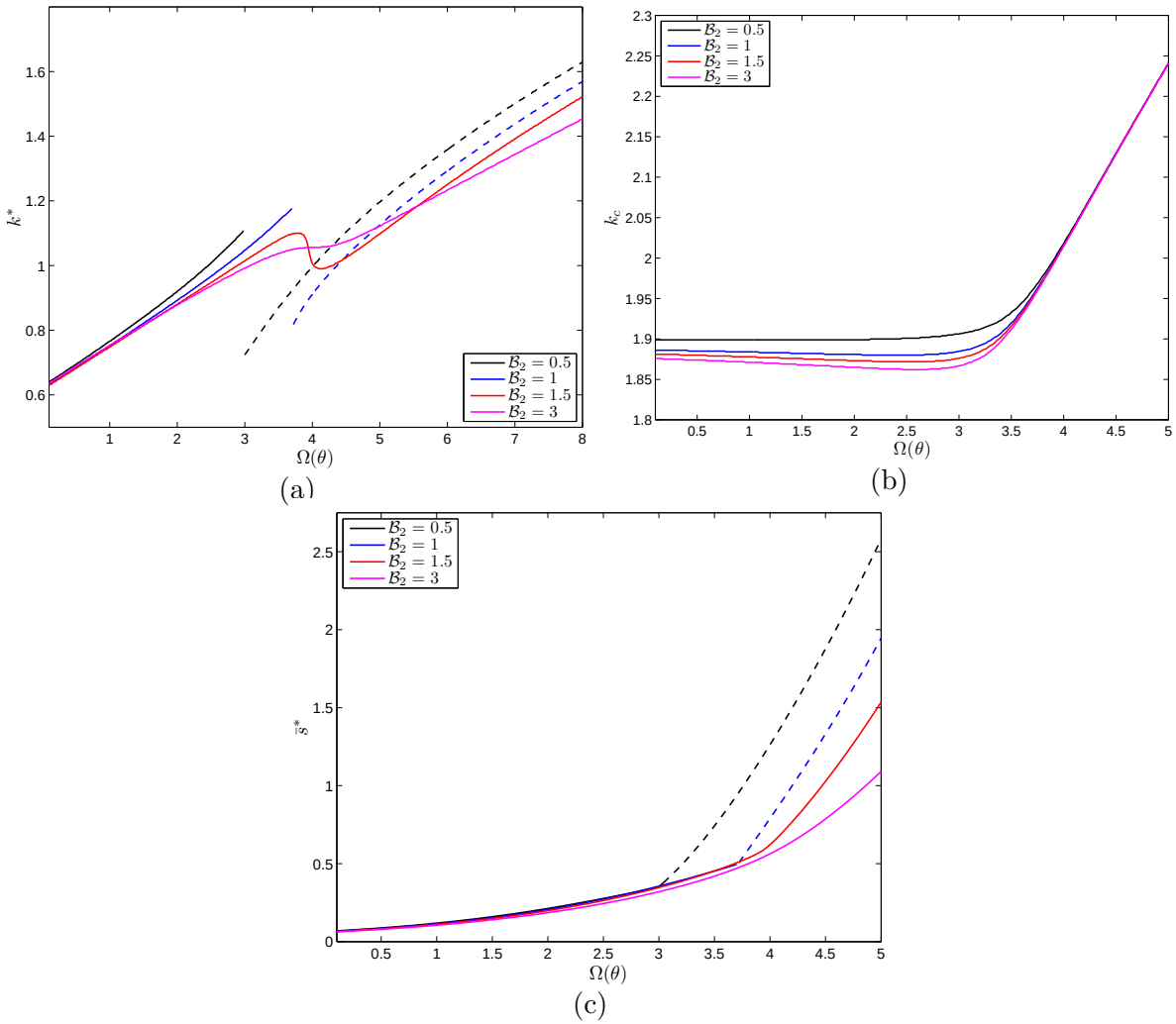

Figure 5.8: Plots of the (a) most unstable wavenumber k^*, (b) the cut-off wavenumber k_c, and (c) maximum growth rate $\overline{s}^*$ against $\Omega(\theta)$, from the dispersion relation $\det(A) = 0$. $\mathcal{B}_1$ varies according to the legend, whilst the fixed parameters are given by $\frac{\mu_1}{\mu_2} = 1$, $\frac{\rho_2}{\rho_1} = 1$, $q_1 = 0.5$, $\frac{\sigma_{s,2}}{\sigma_{s,1}} = 1$, $\frac{\Gamma_{in,2}}{\Gamma_{in,1}} = 1$, $\mathcal{B}_2 = 1$, $\mathcal{C} = 1$. The dashed lines in (a) and (c) indicate when the most unstable wavenumber and largest growth rate switched between different modes.

into the stability features of the single-layer case, examining both the effect of the inclination angle through the parameter $\Omega(\theta)$, and the effectiveness of surfactant $\mathcal{B}$. Intuitive results, such as the growth rate of disturbances increasing with the inclined plane becoming more horizontal, were confirmed. More interesting results, such as the transition of the most unstable mode from the Marangoni wave (that is produced with the inclusion of surfactant) to the altered 'original' wave (the mode that existed before the introduction of surfactant, but is modified with this alteration) were discovered. As the inclination angle became more horizontal, gravitational forces become even more dominant over the surface tension forces, resulting in the original wave (as opposed to the wave induced by surface tension gradients) becoming more prominent.

The same analysis was carried out in the two-layer case, with the dispersion relation being solved via implementing Ferrari's method. Example wave modes were plotted, and an exploration of the features of stability, similar to the single-layer case. Due to time constraints, this could not be investigated into such depth, and is the plan of future work.

Chapter 6

Conclusions

During the curtain coating method, a multi-layer film is formed and flows down the inclined plane of the die face, in preparation of the formation for a multi-layered curtain. This liquid curtain is susceptible to break-up if the flow rate of the liquid layers are lowered too far. After break-up occurs, different topological structures are possible when the liquid film leaves the die-lip, including an array of liquid jets that are uniformly spaced. This thesis has investigated, through theoretical and experimental analysis, the fluid mechanical process involved with multi-layer film formation and stability in curtain coating flows. These works have been published in peer-reviewed journals [52, 53, 82].

First, we studied the inclined plane flow that occurs along the coating die face, completing an examination of both single and multi-layer film flows. The film thicknesses and velocity profiles were analysed via two different methods; the fluorescein technique and the hydrogen bubble technique. The experimental results were compared with a mathematical model of a multi-layer film flowing down an inclined plane.

The simple "1-layer approximation" mathematical model matched identically to the multi-layer theory when all layers were composed of the same fluid. A full verification of this multi-layer model was conducted over a range of physical properties and parameters, in particular the Reynolds number ranging from $Re \approx 0.03-60$. The total film thicknesses,

location of the interface between layers and velocity profiles were all investigated. There was good agreement between the multi-layer theory and experiments for both single layer and multi-layer flows, comprising of the same fluid. As expected, when layers of different fluids were used, the multi-layer theory contrasted with the 1-layer approximation. The experimental data similarly displayed this deviation from the 1-layer approximation to corroborate the multi-layer theory.

Following on from this experimental study, the free-falling liquid curtain was modelled, extending previous work by introducing the effect of surfactants. Often used in industry, surfactant lowers the surface tension of the working fluids, and changes the surface tension from a constant to a variable. The now variable surface tension becomes another unknown in the mathematical model, dependent on the local surfactant concentration. The equation governing the evolution of surfactant concentration along the two free surfaces of the curtain, and the equation of state linking the surface tension and the surfactant concentration, were introduced. Moreover, the stress conditions were altered to compensate for the surface tension gradients that arise at the free surfaces.

The steady state equations were formulated and solved numerically, with examples of cross-sectional curtain profiles presented. The effect of changing parameters on the transverse 'pull' of the curtain was then investigated. A stability analysis was carried out via a multiple scales approach, with a new stability criterion obtained in the case of a two-layer curtain containing insoluble surfactants in both layers. As expected, surfactant increased the stability of the curtain.

The curtain stability was then investigated experimentally. The minimum flow rate required to form a curtain was found to be higher than the flow rate at which break-up occurred, defining a hysteresis region. This hysteresis region was investigated over a range of liquid properties. Moreover, the origins of break-up were recorded and found to be highly dependent on the geometry of the edge guides used. When using vertical edge

guides, boundary layer effects had a large effect on break-up. There was a remarkable difference when using edge guides that tapered inwards. In this case, break-up would occur more centrally and in the top half of the curtain.

Break-up of the curtain would occur in the form of a hole, that grew before disintegrating the liquid sheet. The speed at which this hole opened was experimentally measured. This speed matched reasonably well with the Taylor-Culick speed of liquid sheet retraction, with small discrepancies due to differences with the theory, including variations in the curtain width and not being a semi-infinite sheet.

After curtain break-up, these experiments exhibited the different formations that occur when the liquid film leaves the die-lip. One striking feature was the uniform spacing between the array of liquid jets that formed. The Rayleigh-Taylor wavelength produced an overestimate for predicting this spacing. This inspired the next theoretical model developed, aiming to improve upon the Rayleigh-Taylor wavelength for predicting the spacing. The mathematical model included the effect of insoluble surfactant, similar to the liquid curtain model. To incorporate the effect of an incoming flow rate, a thin film was modelled flowing along the underside of an inclined plane, at a small angle so the incline is near-horizontal. After a linear stability analysis, the most unstable wavelength was compared to the jet spacing observed in experiments. Although this did not succeed in predicting the liquid jet spacing, it provided an extension of previous work on inverted film flow in the literature, both in the respect of adding the effect of surfactant and considering a two-layer film. The ongoing investigation of the provisional results provided in this thesis forms a basis for future work.

Other areas for future work include the experimental study of the 'complicated dance' exhibited by the array of liquid jets, as reported by Pritchard [93]. The experiments have already been carried out by the author, and are reported in Appendix C. Further experiments already completed include the verification of the transverse 'pull' of the liquid

curtain, as reported in Chapter 3. These experiments are also transcribed in Appendix C.

There are a number of avenues for future theoretical work from that presented in this thesis. Of particular interest, again motivated from experiments, is when the flow rate is reduced further after curtain break-up occurs. In this case, the array of liquid jets formed transition from jetting to dripping. This has been of interest in the literature [8, 26]; when a drop pinches-off the remaining liquid filament 'recoils', with a velocity vertically upwards acting against gravity [42]. The results of these studies extended to the inclusion of surfactant, similar to the theoretical work presented in this thesis, would be of interest.

Investigating the capillary ridge feature seen in Chapter 2, modelling a film flowing down an incline with the inclusion of a flow rate coming through the incline would be of pertinence in the curtain coating set-up. Recent theoretical studies by Thompson *et al.* [111, 112] investigated the stability of a falling film on an incline with both suction and injection of liquid at the solid interface. This was done via a pre-determined function defining the normal velocity at the surface of the solid incline, chosen such that mass is conserved. This would not be the case in the slide-die set-up, with there being no suction. Combining these ideas with the work of liquid films meeting at a T–junction (for example, [124]) could be of potential in the context of curtain coating.

Ultimately, this could lead to the union of the cross-sectional film flowing down the inclined plane of the die, incorporating the incoming liquid layers through the slide-die, with the theoretical curtain profiles derived in Chapter 3. Unifying the two profiles, using a 'matching' condition where the two profiles meet, could be carried out similar to Jung *et al.* [60]. This was done for the single-layer case. Extending this to the two-layer set-up, incorporating the effect of surfactant, would provide a significant extension.

Appendix A
Unsupported multi-layer liquid curtain without surfactants falling under gravity

In Chapter 3 we investigated a mathematical model of an unsupported two-layer liquid curtain containing surfactants in both liquids. Throughout the chapter the work of Dyson *et al.* [41] was referenced, which modelled a two-layer liquid curtain with the constant surface tension assumption, to compare to the surfactant case. In this Appendix we briefly outline the equations derived by Dyson *et al.* for the convenience of the reader. All notation is the same as in Chapter 3, noting in particular that the constant surface tension of the free surface $y = h_j$ is denoted $\sigma_{s,j}$.

A.1 Mathematical Model

The following non-dimensional scales are used

$$u_j = U\widehat{u}_j, \quad v_j = \varepsilon U\widehat{v}_j, \quad x = l\widehat{x}, \quad y = \varepsilon l\widehat{y},$$

$$t = \frac{l}{U}\widehat{t}, \quad \mathbf{T}_j = \frac{\mu_1 U}{l}\widehat{\mathbf{T}}_j, \quad p_j = \frac{\mu_1 U}{l}\widehat{p}_j,$$

with the hats denoting dimensionless variables, which are dropped immediately for clarity (all the following equations are dimensionless). The governing equations are given by the

Navier-Stokes equations

$$\begin{aligned}
\varepsilon^2 Re\left(\frac{\partial u_1}{\partial t}+u_1\frac{\partial u_1}{\partial x}+v_1\frac{\partial u_1}{\partial y}\right) &= \frac{\partial^2 u_1}{\partial y^2}+\varepsilon^2\left(\frac{\partial^2 u_1}{\partial x^2}+\frac{Re}{Fr^2}-\frac{\partial p_1}{\partial x}\right),\\
\varepsilon^2 Re\left(\frac{\partial v_1}{\partial t}+u_1\frac{\partial v_1}{\partial x}+v_1\frac{\partial v_1}{\partial y}\right) &= -\frac{\partial p_1}{\partial y}+\varepsilon^2\frac{\partial^2 v_1}{\partial x^2}+\frac{\partial^2 v_1}{\partial y^2},\\
\varepsilon^2 Re\frac{\rho_2}{\rho_1}\left(\frac{\partial u_2}{\partial t}+u_2\frac{\partial u_2}{\partial x}+v_2\frac{\partial u_2}{\partial y}\right) &= \frac{\mu_2}{\mu_1}\frac{\partial^2 u_2}{\partial y^2}+\varepsilon^2\left(\frac{\mu_2}{\mu_1}\frac{\partial^2 u_2}{\partial x^2}+\frac{\rho_2}{\rho_1}\frac{Re}{Fr^2}-\frac{\partial p_2}{\partial x}\right),\\
\varepsilon^2 Re\frac{\rho_2}{\rho_1}\left(\frac{\partial v_2}{\partial t}+u_2\frac{\partial v_2}{\partial x}+v_2\frac{\partial v_2}{\partial y}\right) &= -\frac{\partial p_2}{\partial y}+\frac{\mu_2}{\mu_1}\left(\varepsilon^2\frac{\partial^2 v_2}{\partial x^2}+\frac{\partial^2 v_2}{\partial y^2}\right),
\end{aligned}$$

and the continuity equation

$$\frac{\partial u_j}{\partial x}+\frac{\partial v_j}{\partial y}=0.$$

The boundary conditions on the free surface $y=h_j$ are given by the stress condition

$$\mathbf{T}_j\cdot\mathbf{n}_j=-\frac{1}{Ca}\frac{\sigma_{s,j}}{\sigma_{s,1}}\left(\nabla\cdot\mathbf{n}_j\right)\mathbf{n}_j,$$

and the kinematic condition

$$\frac{\partial h_j}{\partial t}+u_j\frac{\partial h_j}{\partial x}=v_j.$$

The boundary conditions on liquid-liquid interface $y=\eta(x,t)$ are given by the stress condition

$$\left[\mathbf{T}_j\cdot\mathbf{n}\right]_1^2=-\frac{1}{Ca}\frac{\sigma_I}{\sigma_{s,1}}\left(\nabla\cdot\mathbf{n}\right)\mathbf{n},$$

the kinematic condition

$$\frac{\partial\eta}{\partial t}+u\frac{\partial\eta}{\partial x}=v,$$

and the continuity of velocity

$$u_1=u_2,\qquad v_1=v_2.$$

The net-momentum balances are given by, first in the x-direction

$$\begin{aligned}
Re\left(\frac{\partial}{\partial t}\int_{h_1}^{h_2}\rho u\,\mathrm{d}y+\frac{\partial}{\partial x}\int_{h_1}^{h_2}\rho u^2\,\mathrm{d}y\right) &= \frac{Re}{Fr^2}\int_{h_1}^{h_2}\rho\,\mathrm{d}y+\frac{\partial}{\partial x}\int_{h_1}^{h_2}T_{xx}\,\mathrm{d}y\\
-\frac{\varepsilon}{Ca}\left(\frac{\frac{\partial h_1}{\partial x}\frac{\partial^2 h_1}{\partial x^2}}{\left(1+\varepsilon^2\left(\frac{\partial h_1}{\partial x}\right)^2\right)^{3/2}}+\frac{\frac{\sigma_I}{\sigma_{s,1}}\frac{\partial\eta}{\partial x}\frac{\partial^2\eta}{\partial x^2}}{\left(1+\varepsilon^2\left(\frac{\partial\eta}{\partial x}\right)^2\right)^{3/2}}+\frac{\frac{\sigma_{s,2}}{\sigma_{s,1}}\frac{\partial h_2}{\partial x}\frac{\partial^2 h_2}{\partial x^2}}{\left(1+\varepsilon^2\left(\frac{\partial h_2}{\partial x}\right)^2\right)^{3/2}}\right), &\qquad \text{(A.1.1)}
\end{aligned}$$

and in the y-direction

$$\varepsilon Re\left(\frac{\partial}{\partial t}\int_{h_1}^{h_2}\rho v\,\mathrm{d}y+\frac{\partial}{\partial x}\int_{h_1}^{h_2}\rho uv\,\mathrm{d}y\right)=\frac{\partial}{\partial x}\int_{h_1}^{h_2}T_{xy}\,\mathrm{d}y$$
$$+\frac{1}{Ca}\left(\frac{\frac{\partial^2 h_1}{\partial x^2}}{\left(1+\varepsilon^2\left(\frac{\partial h_1}{\partial x}\right)^2\right)^{3/2}}+\frac{\frac{\sigma_I}{\sigma_{s,1}}\frac{\partial^2\eta}{\partial x^2}}{\left(1+\varepsilon^2\left(\frac{\partial\eta}{\partial x}\right)^2\right)^{3/2}}+\frac{\frac{\sigma_{s,2}}{\sigma_{s,1}}\frac{\partial^2 h_2}{\partial x^2}}{\left(1+\varepsilon^2\left(\frac{\partial h_2}{\partial x}\right)^2\right)^{3/2}}\right). \quad \text{(A.1.2)}$$

Equations (3.2.44) and (3.2.45) collapse back to (A.1.1) and (A.1.2) in the case of no surfactant being present in either layer.

After an asymptotic analysis similar to that conducted in Chapter 3, we obtain the leading order equations and use the net-momentum balances to complete the system, giving the four equations

$$\frac{\partial H_j}{\partial t}+\frac{\partial}{\partial x}\left(uH_j\right)=0,$$
$$\frac{\partial u}{\partial t}+u\frac{\partial u}{\partial x}-\frac{1}{Fr^2}=0,$$
$$\mathcal{R}\left(H_1+\frac{\rho_2}{\rho_1}H_2\right)\frac{\mathrm{D}^2\overline{y}}{\mathrm{D}t^2}=\frac{1}{Ca}\left(\frac{\partial^2 h_1}{\partial x^2}+\frac{\sigma_I}{\sigma_{s,1}}\frac{\partial^2\eta}{\partial x^2}+\frac{\sigma_{s,2}}{\sigma_{s,1}}\frac{\partial^2 h_2}{\partial x^2}\right),$$

in the four unknowns u, H_j, and $\overline{y}$. The corresponding steady state equations are given by

$$\frac{\mathrm{d}}{\mathrm{d}x}\left(u^0H_j^0\right)=0, \quad \text{(A.1.3)}$$
$$u^0\frac{\mathrm{d}u^0}{\mathrm{d}x}-\frac{1}{Fr^2}=0, \quad \text{(A.1.4)}$$
$$\mathcal{R}\left(H_1^0+\frac{\rho_2}{\rho_1}H_2^0\right)u^0\frac{\mathrm{d}}{\mathrm{d}x}\left(u^0\frac{\mathrm{d}\overline{y}^0}{\mathrm{d}x}\right)=\frac{1}{Ca}\left(\frac{\mathrm{d}^2h_1^0}{\mathrm{d}x^2}+\frac{\sigma_I}{\sigma_{s,1}}\frac{\mathrm{d}^2\eta^0}{\mathrm{d}x^2}+\frac{\sigma_{s,2}}{\sigma_{s,1}}\frac{\mathrm{d}^2h_2^0}{\mathrm{d}x^2}\right). \quad \text{(A.1.5)}$$

Using the initial conditions (3.2.70), (A.1.3) and (A.1.4) have the solutions

$$H_j^0=\frac{q_j}{u^0}, \quad \text{(A.1.6)}$$
$$u^0=\left(\frac{2x}{Fr^2}+1\right)^{1/2}. \quad \text{(A.1.7)}$$

Considering (A.1.5), we substitute in the solutions (A.1.6) and (A.1.7), as well as the expressions for $\mathrm{d}^2h_j/\mathrm{d}x^2$ and $\mathrm{d}^2\eta/\mathrm{d}x^2$, (3.2.81) and (3.2.82), to obtain the equation

$$\left(u^{0^2}-\Theta u^0\right)\frac{\mathrm{d}^2\overline{y}}{\mathrm{d}x^2}+\frac{1}{Fr^2}\frac{\mathrm{d}\overline{y}}{\mathrm{d}x}=\frac{3\Psi}{\left(\frac{2x}{Fr^2}+1\right)^2}. \quad \text{(A.1.8)}$$

Equation (3.2.84) collapses back to (A.1.4) in the limiting case of no surfactant, since

$\Lambda = 0$ in this instance. Because of this, and that $\Phi = 0$ in the case of no surfactant, (3.2.86) collapses back to (A.1.8) when no surfactant is present.

Equation (A.1.8) can be solved analytically using the integrating factor method, to obtain the solution

$$\overline{y} = Fr^4\Psi\Bigg(\left(\frac{2x}{Fr^2}+1\right)^{1/2} - 1 + \frac{1}{\Theta}\left(1 - \frac{1}{\left(\frac{2x}{Fr^2}+1\right)^{1/2}}\right) + \frac{1}{2\Theta}\log\left(\frac{2x}{Fr^2}+1\right) + \left(\log\left(\left(\frac{2x}{Fr^2}+1\right)^{1/2} - \Theta\right) - \log\left(1-\Theta\right)\right)\Bigg).$$

A.2 Stability

The stability criterion $We_T > 1$ is given by (3.1.2), that is

$$\frac{\tilde{u}\left(\rho_1\tilde{q}_1 + \rho_2\tilde{q}_2\right)}{\sigma_{s,1} + \sigma_I + \sigma_{s,2}} > 1,$$

where the tildes denote dimensional quantities. Substituting in the non-dimensional scales $\tilde{u} = Uu$ and $\tilde{q}_j = h_0 U q_j$, this criterion becomes

$$\frac{h_0U^2u\left(\rho_1q_1 + \rho_2q_2\right)}{\sigma_{s,1} + \sigma_I + \sigma_{s,2}} > 1,$$

which is equivalent to

$$\frac{\mathcal{R}Cau\left(q_1 + \frac{\rho_2}{\rho_1}q_2\right)}{1 + \frac{\sigma_I}{\sigma_{s,1}} + \frac{\sigma_{s,2}}{\sigma_{s,2}}} > 1,$$

i.e.

$$We_T = \frac{u}{\Theta} > 1. \tag{A.2.1}$$

In the case of no surfactant being present, criterion (3.3.16) becomes $We_T > 0$, which always holds, whilst criterion (3.3.17) becomes (A.2.1).

Appendix B
Explicit derivation of terms

In Chapter 5 a mathematical model for a falling film along the underside of an inclined plane, incorporating the effect of surfactant, was derived. The derivation included much algebra, in particular during the non-dimensionalisation in Section 5.2.1 and the asymptotic analysis in Section 5.2.2, most of which was not written explicitly for the ease of reading. In Section B.1, we outline the calculations relating to the advection-diffusion equation (5.2.5) in the non-dimensionalisation and asymptotic analysis. In Section B.2, the reasoning behind the orders of magnitude for the capillary number Ca and the surface activity number β_j are discussed.

B.1 Advection-diffusion equation for surfactant concentration

The dimensional advection-diffusion equation is given by

$$\frac{\partial \Gamma_j}{\partial t} + \nabla_{s,j} \cdot (\Gamma_j \mathbf{u}_{s,j}) + \Gamma_j \left(\nabla_{s,j} \cdot \mathbf{n}_j\right)(\mathbf{u}_j \cdot \mathbf{n}_j) = 0, \tag{B.1.1}$$

at $y = h_j$, where Γ_j is the surfactant concentration, $\nabla_{s,j}$ the gradient along the surface, $\mathbf{u}_{s,j}$ the velocity along the surface, and $\mathbf{n}_j$ the unit outwards facing normal. These terms are given by

$$\nabla_{s,j} = (\mathrm{I} - \mathbf{n}_j\mathbf{n}_j) \cdot \nabla, \tag{B.1.2}$$

$$\mathbf{u}_{s,j} = (\mathrm{I} - \mathbf{n}_j\mathbf{n}_j) \cdot \mathbf{u}, \tag{B.1.3}$$

where I is the identity matrix, and

$$\mathbf{n}_j = \left(1 + \left(\frac{\partial h_j}{\partial x}\right)^2\right)^{-1/2} \begin{pmatrix} -\frac{\partial h_j}{\partial x} \\ 1 \end{pmatrix}. \tag{B.1.4}$$

We use the non-dimensional scales:

$$y = \left(\frac{\mu_1 Q_T}{\rho_1 g \sin(\theta)}\right)^{1/3} \widehat{y} = d_s \widehat{y}, \quad x = \frac{d_s}{\varepsilon}\widehat{x}, \quad u_j = \frac{Q_T}{d_s}\widehat{u}_j, \quad v_j = \frac{\varepsilon Q_T}{d_s}\widehat{v}_j,$$

$$p_j = \frac{\mu_1 Q_T}{\varepsilon d_s^2}\widehat{p}_j, \quad t = \frac{d_s^2}{\varepsilon Q_T}\widehat{t}, \quad \Gamma_j = \Gamma_{in,1}\widehat{\Gamma}_j, \quad \mathbf{T}_j = \frac{\mu_1 Q_T}{d_s^2}\widehat{\mathbf{T}}_j, \tag{B.1.5}$$

where hats denote dimensionless variables. Substituting the non-dimensional scales (B.1.5) into the advection-diffusion equation (B.1.1):

$$\varepsilon\frac{\partial\widehat{\Gamma}_j}{\partial\widehat{t}} + \widehat{\nabla}_{s,j}\cdot\left(\widehat{\Gamma}_j\widehat{\mathbf{u}}_{s,j}\right) + \widehat{\Gamma}_j\left(\widehat{\nabla}_{s,j}\cdot\widehat{\mathbf{n}}_j\right)\left(\widehat{\mathbf{u}}_j\cdot\widehat{\mathbf{n}}_j\right) = 0, \tag{B.1.6}$$

having multiplied the equation through by $d_s^2/\Gamma_{in,1}Q_T$. The terms in (B.1.6) are given by

$$\widehat{\nabla} = \left(\varepsilon\frac{\partial}{\partial\widehat{x}}, \frac{\partial}{\partial\widehat{y}}\right),$$

$$\widehat{\mathbf{n}}_j = \left(1+\varepsilon^2\left(\frac{\partial\widehat{h}_j}{\partial\widehat{x}}\right)^2\right)^{-1/2}\begin{pmatrix}-\varepsilon\frac{\partial\widehat{h}_j}{\partial\widehat{x}}\\ 1\end{pmatrix},$$

$$\widehat{\nabla}_{s,j} = (\mathrm{I}-\widehat{\mathbf{n}}_j\widehat{\mathbf{n}}_j)\cdot\widehat{\nabla},$$

$$\widehat{\mathbf{u}} = (\widehat{u}, \varepsilon\widehat{v}),$$

$$\widehat{\mathbf{u}}_{s,j} = (\mathrm{I}-\widehat{\mathbf{n}}_j\widehat{\mathbf{n}}_j)\cdot\widehat{\mathbf{u}}.$$

Therefore we have that

$$\begin{aligned}\widehat{\nabla}_{s,j} &= \begin{pmatrix}1-\varepsilon^2\left(\frac{\partial\widehat{h}_j}{\partial\widehat{x}}\right)^2\left(1+\varepsilon^2\left(\frac{\partial\widehat{h}_j}{\partial\widehat{x}}\right)^2\right)^{-1} & \varepsilon\frac{\partial\widehat{h}_j}{\partial\widehat{x}}\left(1+\varepsilon^2\left(\frac{\partial\widehat{h}_j}{\partial\widehat{x}}\right)^2\right)^{-1}\\ \varepsilon\frac{\partial\widehat{h}_j}{\partial\widehat{x}}\left(1+\varepsilon^2\left(\frac{\partial\widehat{h}_j}{\partial\widehat{x}}\right)^2\right)^{-1} & 1-\left(1+\varepsilon^2\left(\frac{\partial\widehat{h}_j}{\partial\widehat{x}}\right)^2\right)^{-1}\end{pmatrix}\cdot\begin{pmatrix}\varepsilon\frac{\partial}{\partial\widehat{x}}\\ \frac{\partial}{\partial\widehat{y}}\end{pmatrix}\\ &= \begin{pmatrix}\left(1-\varepsilon^2\left(\frac{\partial\widehat{h}_j}{\partial\widehat{x}}\right)^2\left(1+\varepsilon^2\left(\frac{\partial\widehat{h}_j}{\partial\widehat{x}}\right)^2\right)^{-1}\right)\varepsilon\frac{\partial}{\partial\widehat{x}} + \varepsilon\frac{\partial\widehat{h}_j}{\partial\widehat{x}}\left(1+\varepsilon^2\left(\frac{\partial\widehat{h}_j}{\partial\widehat{x}}\right)^2\right)^{-1}\frac{\partial}{\partial\widehat{y}}\\ \varepsilon^2\frac{\partial\widehat{h}_j}{\partial\widehat{x}}\left(1+\varepsilon^2\left(\frac{\partial\widehat{h}_j}{\partial\widehat{x}}\right)^2\right)^{-1}\frac{\partial}{\partial\widehat{x}} + \left(1-\left(1+\varepsilon^2\left(\frac{\partial\widehat{h}_j}{\partial\widehat{x}}\right)^2\right)^{-1}\right)\frac{\partial}{\partial\widehat{y}}\end{pmatrix},\end{aligned}$$

and

$$\widehat{\nabla}_{s,j}\cdot\widehat{\mathbf{n}}_j=\begin{pmatrix}\left(1-\varepsilon^2\left(\frac{\partial\widehat{h}_j}{\partial\widehat{x}}\right)^2\left(1+\varepsilon^2\left(\frac{\partial\widehat{h}_j}{\partial\widehat{x}}\right)^2\right)^{-1}\right)\varepsilon\frac{\partial}{\partial\widehat{x}}+\varepsilon\frac{\partial\widehat{h}_j}{\partial\widehat{x}}\left(1+\varepsilon^2\left(\frac{\partial\widehat{h}_j}{\partial\widehat{x}}\right)^2\right)^{-1}\frac{\partial}{\partial\widehat{y}}\\ \varepsilon^2\frac{\partial\widehat{h}_j}{\partial\widehat{x}}\left(1+\varepsilon^2\left(\frac{\partial\widehat{h}_j}{\partial\widehat{x}}\right)^2\right)^{-1}\frac{\partial}{\partial\widehat{x}}+\left(1-\left(1+\varepsilon^2\left(\frac{\partial\widehat{h}_j}{\partial\widehat{x}}\right)^2\right)^{-1}\right)\frac{\partial}{\partial\widehat{y}}\end{pmatrix}$$
$$\cdot\left(1+\varepsilon^2\left(\frac{\partial\widehat{h}_j}{\partial\widehat{x}}\right)^2\right)^{-1/2}\begin{pmatrix}-\varepsilon\frac{\partial\widehat{h}_j}{\partial\widehat{x}}\\1\end{pmatrix}$$
$$=-\frac{\varepsilon^2\frac{\partial^2\widehat{h}_j}{\partial\widehat{x}^2}}{\left(1+\varepsilon^2\left(\frac{\partial\widehat{h}_j}{\partial\widehat{x}}\right)^2\right)^{3/2}}=\kappa_j.$$

Moreover,

$$\widehat{\mathbf{u}}_{s,j}=\begin{pmatrix}1-\varepsilon^2\left(\frac{\partial\widehat{h}_j}{\partial\widehat{x}}\right)^2\left(1+\varepsilon^2\left(\frac{\partial\widehat{h}_j}{\partial\widehat{x}}\right)^2\right)^{-1} & \varepsilon\frac{\partial\widehat{h}_j}{\partial\widehat{x}}\left(1+\varepsilon^2\left(\frac{\partial\widehat{h}_j}{\partial\widehat{x}}\right)^2\right)^{-1}\\ \varepsilon\frac{\partial\widehat{h}_j}{\partial\widehat{x}}\left(1+\varepsilon^2\left(\frac{\partial\widehat{h}_j}{\partial\widehat{x}}\right)^2\right)^{-1} & 1-\left(1+\varepsilon^2\left(\frac{\partial\widehat{h}_j}{\partial\widehat{x}}\right)^2\right)^{-1}\end{pmatrix}\cdot\begin{pmatrix}\widehat{u}_j\\\varepsilon\widehat{v}_j\end{pmatrix}$$
$$=\begin{pmatrix}\widehat{u}_j\left(1-\varepsilon^2\left(\frac{\partial\widehat{h}_j}{\partial\widehat{x}}\right)^2\left(1+\varepsilon^2\left(\frac{\partial\widehat{h}_j}{\partial\widehat{x}}\right)^2\right)^{-1}\right)+\varepsilon^2\widehat{v}_j\frac{\partial\widehat{h}_j}{\partial\widehat{x}}\left(1+\varepsilon^2\left(\frac{\partial\widehat{h}_j}{\partial\widehat{x}}\right)^2\right)^{-1}\\ \varepsilon\widehat{u}_j\frac{\partial\widehat{h}_j}{\partial\widehat{x}}\left(1+\varepsilon^2\left(\frac{\partial\widehat{h}_j}{\partial\widehat{x}}\right)^2\right)^{-1}+\varepsilon\widehat{v}_j\left(1-\left(1+\varepsilon^2\left(\frac{\partial\widehat{h}_j}{\partial\widehat{x}}\right)^2\right)^{-1}\right)\end{pmatrix}$$
$$=\begin{pmatrix}\widehat{u}_{s,j}\\\widehat{v}_{s,j}\end{pmatrix}.$$

Therefore

$$\begin{aligned}\widehat{\nabla}_{s,j}\cdot\left(\widehat{\Gamma}_j\widehat{\mathbf{u}}_{s,j}\right)=\varepsilon&\left(1-\varepsilon^2\left(\frac{\partial\widehat{h}_j}{\partial\widehat{x}}\right)^2\left(1+\varepsilon^2\left(\frac{\partial\widehat{h}_j}{\partial\widehat{x}}\right)^2\right)^{-1}\right)\frac{\partial}{\partial\widehat{x}}\left(\widehat{\Gamma}_j\widehat{u}_{s,j}\right)\\&+\varepsilon\frac{\partial\widehat{h}_j}{\partial\widehat{x}}\left(1+\varepsilon^2\left(\frac{\partial\widehat{h}_j}{\partial\widehat{x}}\right)^2\right)^{-1}\frac{\partial}{\partial\widehat{y}}\left(\widehat{\Gamma}_j\widehat{u}_{s,j}\right)\\&+\varepsilon^2\frac{\partial\widehat{h}_j}{\partial\widehat{x}}\left(1+\varepsilon^2\left(\frac{\partial\widehat{h}_j}{\partial\widehat{x}}\right)^2\right)^{-1}\frac{\partial}{\partial\widehat{x}}\left(\widehat{\Gamma}_j\widehat{v}_{s,j}\right)\\&+\left(1-\left(1+\varepsilon^2\left(\frac{\partial\widehat{h}_j}{\partial\widehat{x}}\right)^2\right)^{-1}\right)\frac{\partial}{\partial\widehat{y}}\left(\widehat{\Gamma}_j\widehat{v}_{s,j}\right).\end{aligned}$$

Carrying out the differentiation

$$\begin{aligned}&\widehat{\nabla}_{s,j}\cdot\left(\widehat{\Gamma}_j\widehat{\mathbf{u}}_{s,j}\right)\\&\quad=\varepsilon\left(1+\varepsilon^2\left(\frac{\partial\widehat{h}_j}{\partial\widehat{x}}\right)^2\right)^{-3}\left(\frac{\partial}{\partial\widehat{x}}\left(\widehat{u}_j\widehat{\Gamma}_j\right)+\widehat{\Gamma}_j\frac{\partial\widehat{u}_j}{\partial\widehat{y}}\frac{\partial\widehat{h}_j}{\partial\widehat{x}}+\varepsilon^2\left(\frac{\partial\widehat{h}_j}{\partial\widehat{x}}\right)^2\frac{\partial}{\partial\widehat{x}}\left(\widehat{u}_j\widehat{\Gamma}_j\right)\right.\\&\quad-2\varepsilon^2\widehat{u}_j\widehat{\Gamma}_j\frac{\partial\widehat{h}_j}{\partial\widehat{x}}\frac{\partial^2\widehat{h}_j}{\partial\widehat{x}^2}+\varepsilon^2\frac{\partial}{\partial\widehat{x}}\left(\widehat{v}_j\Gamma_j\right)\frac{\partial\widehat{h}_j}{\partial\widehat{x}}+\varepsilon^2\widehat{v}_j\Gamma_j\frac{\partial^2\widehat{h}_j}{\partial\widehat{x}^2}+\varepsilon^2\left(\frac{\partial\widehat{h}_j}{\partial\widehat{x}}\right)^3\widehat{\Gamma}_j\frac{\partial\widehat{u}_j}{\partial\widehat{y}}\\&\quad+\varepsilon^2\widehat{\Gamma}_j\frac{\partial\widehat{v}_j}{\partial\widehat{y}}\left(\frac{\partial\widehat{h}_j}{\partial\widehat{x}}\right)^2+\varepsilon^2\frac{\partial}{\partial\widehat{x}}\left(\widehat{u}_j\Gamma_j\right)\left(\frac{\partial\widehat{h}_j}{\partial\widehat{x}}\right)^2+\varepsilon^2\widehat{u}_j\widehat{\Gamma}_j\frac{\partial\widehat{h}_j}{\partial\widehat{x}}\frac{\partial^2\widehat{h}_j}{\partial\widehat{x}^2}+\varepsilon^2\left(\frac{\partial\widehat{h}_j}{\partial\widehat{x}}\right)^3\widehat{\Gamma}_j\frac{\partial\widehat{u}_j}{\partial\widehat{y}}\\&\quad+\varepsilon^4\left(\frac{\partial\widehat{h}_j}{\partial\widehat{x}}\right)^3\frac{\partial}{\partial\widehat{x}}\left(\widehat{v}_j\widehat{\Gamma}_j\right)-\varepsilon^4\widehat{v}_j\widehat{\Gamma}_j\left(\frac{\partial\widehat{h}_j}{\partial\widehat{x}}\right)^2\frac{\partial^2\widehat{h}_j}{\partial\widehat{x}^2}+\varepsilon^4\left(\frac{\partial\widehat{h}_j}{\partial\widehat{x}}\right)^4\widehat{\Gamma}_j\frac{\partial\widehat{v}_j}{\partial\widehat{y}}\\&\quad+\varepsilon^4\frac{\partial}{\partial\widehat{x}}\left(\widehat{u}_j\widehat{\Gamma}_j\right)\left(\frac{\partial\widehat{h}_j}{\partial\widehat{x}}\right)^4-\varepsilon^4\widehat{u}_j\widehat{\Gamma}_j\left(\frac{\partial\widehat{h}_j}{\partial\widehat{x}}\right)^2\frac{\partial^2\widehat{h}_j}{\partial\widehat{x}^2}+\varepsilon^4\frac{\partial}{\partial\widehat{x}}\left(\widehat{v}_j\widehat{\Gamma}_j\right)\left(\frac{\partial\widehat{h}_j}{\partial\widehat{x}}\right)^3\\&\quad+2\varepsilon^4\widehat{v}_j\widehat{\Gamma}_j\left(\frac{\partial\widehat{h}_j}{\partial\widehat{x}}\right)^2\frac{\partial^2\widehat{h}_j}{\partial\widehat{x}^2}+\varepsilon^4\left(\frac{\partial\widehat{h}_j}{\partial\widehat{x}}\right)^4\widehat{\Gamma}_j\frac{\partial\widehat{v}_j}{\partial\widehat{y}}+\varepsilon^4\left(\frac{\partial\widehat{h}_j}{\partial\widehat{x}}\right)^5\widehat{\Gamma}_j\frac{\partial\widehat{u}_j}{\partial\widehat{y}}\\&\quad\left.+\varepsilon^6\frac{\partial}{\partial\widehat{x}}\left(\widehat{v}_j\widehat{\Gamma}_j\right)\left(\frac{\partial\widehat{h}_j}{\partial\widehat{x}}\right)^5+\varepsilon^6\left(\frac{\partial\widehat{h}_j}{\partial\widehat{x}}\right)^6\widehat{\Gamma}_j\frac{\partial\widehat{v}_j}{\partial\widehat{y}}\right).\end{aligned}$$

Finally,

$$\widehat{\mathbf{u}}_j \cdot \widehat{\mathbf{n}}_j = (\widehat{u}_j, \varepsilon\widehat{v}_j) \cdot \frac{1}{\left(1+\varepsilon^2\left(\frac{\partial \widehat{h}_j}{\partial \widehat{x}}\right)^2\right)^{1/2}} \begin{pmatrix} -\varepsilon\frac{\partial \widehat{h}_j}{\partial \widehat{x}} \\ 1 \end{pmatrix}$$
$$= \frac{\varepsilon\left(\widehat{v}_j - \widehat{u}_j\frac{\partial \widehat{h}_j}{\partial \widehat{x}}\right)}{\left(1+\varepsilon^2\left(\frac{\partial \widehat{h}_j}{\partial \widehat{x}}\right)^2\right)^{1/2}}.$$

These are the terms in equation (B.1.6) written out explicitly. Note how an ε term occurs in both the $\widehat{\nabla}_{s,j} \cdot \left(\widehat{\Gamma}_j \widehat{\mathbf{u}}_{s,j}\right)$ and $\widehat{\Gamma}_j \left(\widehat{\nabla}_{s,j} \cdot \widehat{\mathbf{n}}_j\right)(\widehat{\mathbf{u}}_j \cdot \widehat{\mathbf{n}}_j)$ terms; we divide through by ε in (B.1.6) to obtain the non-dimensional convection-diffusion equation (5.2.21) as in Chapter 5:

$$\frac{\partial \widehat{\Gamma}_j}{\partial \widehat{t}} + \widehat{\nabla}_{s,j} \cdot \left(\widehat{\Gamma}_j \widehat{\mathbf{u}}_{s,j}\right) + \widehat{\Gamma}_j \left(\widehat{\nabla}_{s,j} \cdot \widehat{\mathbf{n}}_j\right)(\widehat{\mathbf{u}}_j \cdot \widehat{\mathbf{n}}_j) = 0. \tag{B.1.7}$$

B.2 Stress conditions and orders of magnitude

The choice behind the orders of magnitude for the capillary number Ca and the surface activity number β_j are reasoned in this section. Considering the stress condition at the liquid-liquid interface (5.2.19) and the free surface (5.2.20), the terms on the left-hand side of these equations are given by (all these equations are dimensionless):

$$\mathbf{n}_1 \cdot \mathbf{T}_1 = \left(1+\varepsilon^2\left(\frac{\partial h_1}{\partial x}\right)^2\right)^{-1/2} \left(-\varepsilon\frac{\partial h_1}{\partial x}, 1\right) \cdot \begin{pmatrix} -\frac{1}{\varepsilon}p_1 + 2\varepsilon\frac{\partial u_1}{\partial x} & \varepsilon^2\frac{\partial u_1}{\partial y} + \frac{\partial v_1}{\partial x} \\ \varepsilon^2\frac{\partial u_1}{\partial y} + \frac{\partial v_1}{\partial x} & -\frac{1}{\varepsilon}p_1 + 2\varepsilon\frac{\partial v_1}{\partial y} \end{pmatrix}$$
$$= \left(1+\varepsilon^2\left(\frac{\partial h_1}{\partial x}\right)^2\right)^{-1/2} \begin{pmatrix} -\varepsilon\frac{\partial h_1}{\partial x}\left(-\frac{1}{\varepsilon}p_1 + 2\varepsilon\frac{\partial u_1}{\partial x}\right) + \frac{\partial u_1}{\partial y} + \varepsilon^2\frac{\partial v_1}{\partial x} \\ -\varepsilon\frac{\partial h_1}{\partial x}\left(\frac{\partial u_1}{\partial y} + \varepsilon^2\frac{\partial v_1}{\partial x}\right) - \frac{1}{\varepsilon}p_1 + 2\varepsilon\frac{\partial v_1}{\partial y} \end{pmatrix},$$

similarly

$$\mathbf{n}_1 \cdot \mathbf{T}_2 = \left(1+\varepsilon^2\left(\frac{\partial h_1}{\partial x}\right)^2\right)^{-1/2} \begin{pmatrix} -\varepsilon\frac{\partial h_1}{\partial x}\left(-\frac{1}{\varepsilon}p_2 + 2\varepsilon\frac{\mu_2}{\mu_1}\frac{\partial u_2}{\partial x}\right) + \frac{\mu_2}{\mu_1}\left(\frac{\partial u_2}{\partial y} + \varepsilon^2\frac{\partial v_2}{\partial x}\right) \\ -\varepsilon\frac{\mu_2}{\mu_1}\frac{\partial h_1}{\partial x}\left(\frac{\partial u_2}{\partial y} + \varepsilon^2\frac{\partial v_2}{\partial x}\right) - \frac{1}{\varepsilon}p_2 + 2\varepsilon\frac{\mu_2}{\mu_1}\frac{\partial v_2}{\partial y} \end{pmatrix}.$$

Substituting these into the stress condition at the liquid-liquid interface (5.2.19), the first equation we obtain is

$$\begin{aligned} Ca\Bigg(&-\varepsilon\frac{\partial h_1}{\partial x}\left(-\frac{1}{\varepsilon}p_2+2\varepsilon\frac{\mu_2}{\mu_1}\frac{\partial u_2}{\partial x}\right)+\frac{\mu_2}{\mu_1}\left(\frac{\partial u_2}{\partial y}+\varepsilon^2\frac{\partial v_2}{\partial x}\right)\\ &\qquad\qquad +\varepsilon\frac{\partial h_1}{\partial x}\left(-\frac{1}{\varepsilon}p_1+2\varepsilon\frac{\partial u_1}{\partial x}\right)-\frac{\partial u_1}{\partial y}-\varepsilon^2\frac{\partial v_1}{\partial x}\Bigg)\\ &=\frac{\sigma_1}{\sigma_{s,1}}\left(1+\varepsilon^2\left(\frac{\partial h_1}{\partial x}\right)^2\right)^{-3/2}\varepsilon^3\frac{\partial h_1}{\partial x}\frac{\partial^2 h_j}{\partial x^2}-\varepsilon\frac{\partial}{\partial x}\left(\frac{\sigma_1}{\sigma_{s,1}}\right), \end{aligned}$$

or

$$Ca\left(p_2\frac{\partial h_1}{\partial x}+\frac{\mu_2}{\mu_1}\frac{\partial u_2}{\partial y}-p_1\frac{\partial h_1}{\partial x}-\frac{\partial u_1}{\partial y}+O\left(\varepsilon^2\right)\right)=\varepsilon^3\underbrace{\frac{\sigma_1}{\sigma_{s,1}}}_{=1-\beta_1\Gamma_1\text{ by (5.2.22)}}\frac{\partial h_1}{\partial x}\frac{\partial^2 h_1}{\partial x^2}-\varepsilon\underbrace{\frac{\partial}{\partial x}\left(\frac{\sigma_1}{\sigma_{s,1}}\right)}_{=-\beta_1\frac{\partial\Gamma_1}{\partial x}\text{ by (5.2.23)}}. \tag{B.2.1}$$

Equation (B.2.1) demonstrates our choice for the orders of magnitude for both Ca and β_j, remembering that β_j must be small for the validity of the linear equation of state. If we choose $Ca = O(1)$, then the curvature and surface tension gradient terms on the right-hand side are lost (the surface tension term would remain if $\beta_j = O(1/\varepsilon)$, however this is clearly not small). If $Ca = O(\varepsilon)$, the surface tension gradient term remains if $\beta_j = O(1)$, again, not valid for the linear equation of state. If $Ca = O(\varepsilon^2)$, the surface tension gradient term remains if $\beta_j = O(\varepsilon)$, however the curvature term is still lost. By setting $Ca = O(\varepsilon^3)$, we retain both the curvature term and the surface tension gradient term when $\beta_j = O(\varepsilon^2)$, which also ensures the validity of the equation of state. The drawback of this choice is that the surface tension is unaltered to leading order, however, this choice ensures the largest number of terms are kept whilst retaining the validity of the equation of state.

The same argument may be carried out for the other equation that arises from the liquid-liquid stress condition (5.2.19), and also the free surface stress conditions (5.2.20).

Appendix C
Further experiments

In addition to the two experimental investigations conducted in Chapters 2 and 4, further experiments have been carried out by the author. These were not included in the main Chapters of this thesis, due to time restrictions for the experiments described in Section C.1 and C.3. The experiments in Section C.2 have been published in [82], but did not fit into the main chapters of this thesis.

C.1 Curtain deflection

In Chapter 3, a mathematical model of a two-layered liquid curtain incorporating the effect of insoluble surfactant was derived. From the steady state equations cross-sectional profiles of the liquid curtain were plotted, and varying the parameters was found to have a profound effect on the transverse 'pull' of the curtain. This was primarily due to a difference in surface tension between the two free surfaces. Experiments have recently been conducted to test this theory. However, the exact liquid properties (for example, the surface tension and viscosity) are not yet known; the liquids are currently being tested to obtain these values.

Despite this, tentative agreements between the experiments and the theoretical work can still be made. Figure C.1 depicts four still photographs taken, having a side-on view of a stable two-layer curtain. In these experiments, the previously used teflon edge guides were replaced with transparent glass edge guides, that were vertical (no tapering inwards) and 15 cm in length. The width of the edge guides are 4 cm. Due to the mechanics of the slide-die, only the bottom 10 cm of the curtain can be seen in the images.

The transverse pull is readily seen in Figure C.1. In (a) and (b), both liquid layers comprise of 50% glycerol, however one has a concentration of 0.05% SDS surfactant, whilst the other has a concentration of 0.2% SDS surfactant. In (a), the first (left-hand) layer has has the higher concentration of surfactant, resulting in a lower surface tension, and thus the curtain is deflected to the right. In (b), the liquid layers are switched. This means that the second (right-hand) layer now has a lower surface tension, resulting in the curtain pulling to the left. In both (a) and (b) the flow rates of both layers are fixed at $Q_1 = Q_2 = 1$ cm^{2}s^{-1}.

In Figure C.1(c) the first (left-hand) layer is 60% glycerol with 0.05% SDS, whilst the second (right-hand) layer is 80% glycerol with 0.05% SDS. With these two liquids, there

(a) $Q_1 = Q_2 = 1$ cm^{2}s^{-1}
First layer: 50% glycerol with 0.2% SDS
Second layer: 50% glycerol with 0.05% SDS

(b) $Q_1 = Q_2 = 1$ cm^{2}s^{-1}
First layer: 50% glycerol with 0.05% SDS
Second layer: 50% glycerol with 0.2% SDS

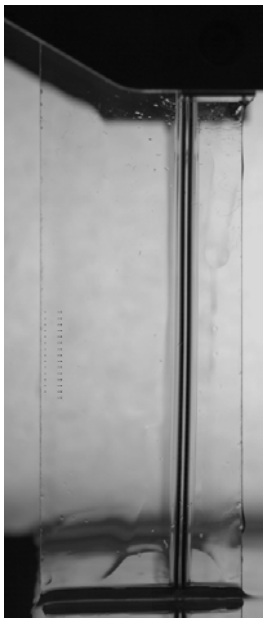

(c) $Q_1 = 1$ cm^{2}s$^{-1}, Q_2 = 2.17$ cm^{2}s^{-1}
First layer: 60% glycerol with 0.05% SDS
Second layer: 80% glycerol with 0.05% SDS

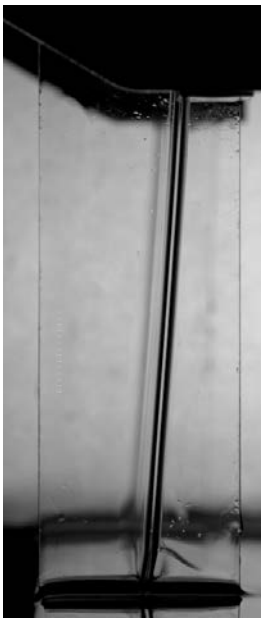

(d) $Q_1 = 1$ cm^{2}s$^{-1}, Q_2 = 2.17$ cm^{2}s^{-1}
First layer: 60% glycerol with 0.05% SDS
Second layer: 80% glycerol with 0.2% SDS

Figure C.1: Side on images of a two-layer curtain. Note the first layer is the layer on the left-hand side, the second layer is the layer on the right-hand side.

is no major difference in surface tensions, and thus the resulting profile is a near-vertical curtain. In (d), we increase the surfactant concentration of the second (right-hand) layer, so that it is now 80% glycerol with 0.2% SDS. By decreasing the surface tension of this layer, the curtain is pulled by the higher surface tension of the first layer, resulting in the curtain being deflected to the left.

Figure C.1 represents the beginnings of an experimental validation of the theory derived in Chapter 3. Once the exact liquid properties are acquired (currently the process of ongoing work) this will become a full experimental investigation.

C.2 Fluorescein experiments

Additional experiments were carried out using fluorescence imaging for the publication [82]. The aim for these experiments was to obtain qualitative features of the array of liquid jets that form after curtain break-up. In particular, to attempt to understand what happens to the multi-layer film formed on the inclined plane of the die-face once it reaches the die-lip; where does each liquid layer go upon formation of the liquid jets? Possibilities for this include the formation of compound (encapsulated) jets, whereby one liquid layer completely encapsulates the other(s).

Figure C.2 shows two still photographs taken of the array of liquid jets, with (a) showing the full width of the die lip (12 cm), and (b) a close-up image of three liquid jets leaving the die lip (3.5 cm total width). Both (a) and (b) are resultant after the break-up of a three-layered curtain, whereby only the middle layer contains fluorescein dye. Figure C.4(a) shows a cross-sectional schematic of the liquid film along the die-face, with the location of the fluorescein layer.

An interesting observation is the consistent feature of a dark triangular patch, located in the centre-line of each liquid jet, directly below the die-lip. Since the fluorescein dye is located in the middle layer, this feature indicates a localised 'squeezing' of this layer at those locations. Despite these images, it is difficult to draw any definitive conclusions.

However, Figure C.3 gives more insight into the qualitative description for the array of liquid jets after the break-up of a two-layered liquid curtain. In this figure, the first (bottom) layer contains fluorescein, as shown in the cross-sectional schematic Figure C.4(b). In these images, a single jet from the array is imaged, as the flow rate of the second (top) layer increases from left to right, whilst the flow rate of the fluorescein layer remains fixed (flow rates given in the caption).

As the flow rate of the top (fluorescein-free) layer Q_2 increases, it appears that this layer flows over and around the thread from the bottom layer and forms a compound jet. This is from the visible layer with no fluorescein on both 'sides' (of this two-dimensional image) of the central fluorescent jet. Again, due to the complex nature of this process, it is difficult to draw a definitive conclusion from these images, and provides the motivation for further work.

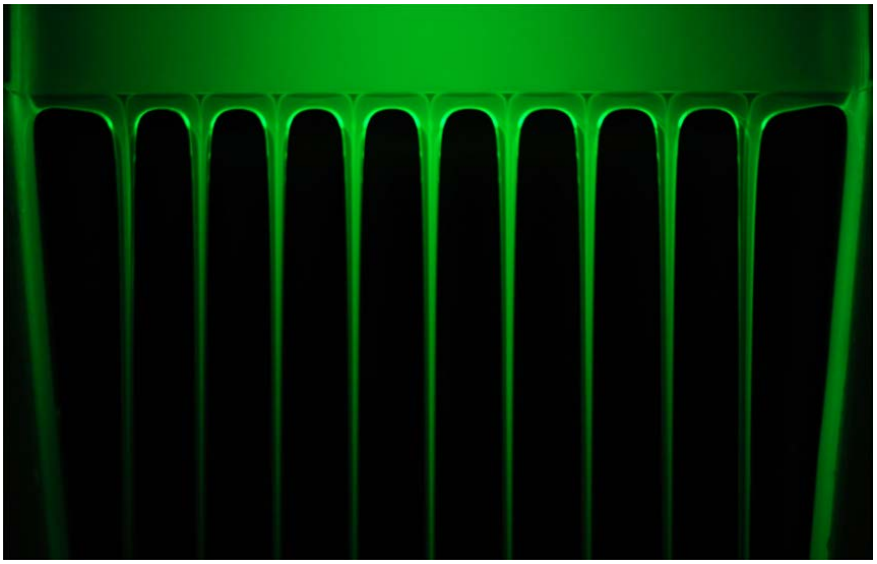

(a) Array of jets after break-up, pictured from the full length of the die lip (12 cm). The flow rates are $Q_1 = Q_3 = 0.63$ cm^{2}s^{-1}, $Q_2 = 0.22$ cm^{2}s^{-1}.

(b) Close-up of the jets, coming from the die lip. The width of the image is 3.5 cm. The flow rates are $Q_1 = Q_3 = 0.55$ cm^{2}s^{-1}, $Q_2 = 0.2$ cm^{2}s^{-1}.

Figure C.2: Fluorescence imaging of the thread structure after break-up of a three-layer curtain, where all layers are 80% glycerol with 0.2% SDS. In both subfigures, only the middle layer contains fluorescein, as depicted in Figure C.4(a) below.

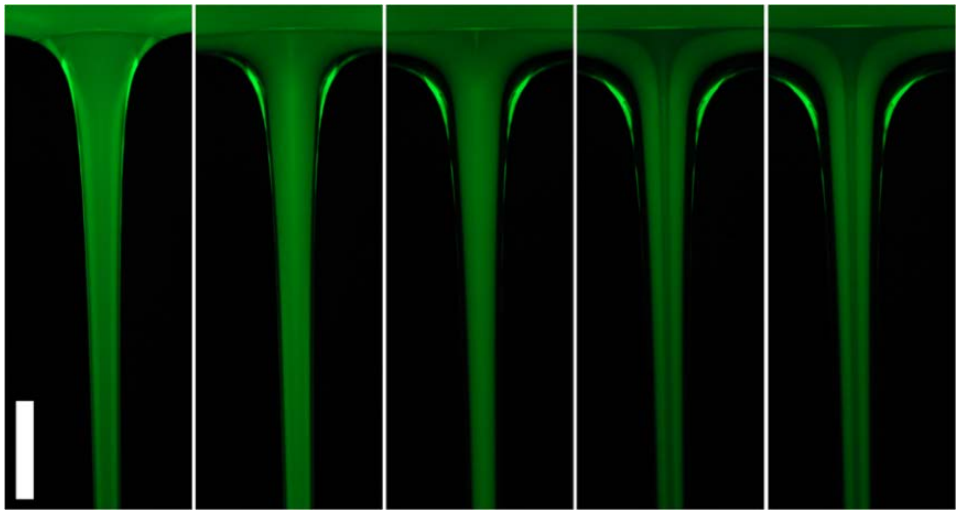

Figure C.3: Thread structure of a single jet after break-up of a two-layer curtain, where both layers are 80% glycerol with 0.2% SDS. Only the bottom layer contains fluorescein, as depicted in Figure C.4(b) below, with a flow rate fixed of $Q_1 = 0.2$ cm^{2}s^{-1}. The flow rate of the top layer increases from left to right as $Q_2 = 0.5, 0.67, 1, 1.23$ and 1.35 cm^{2}s^{-1}. The scale bar is 5 mm.

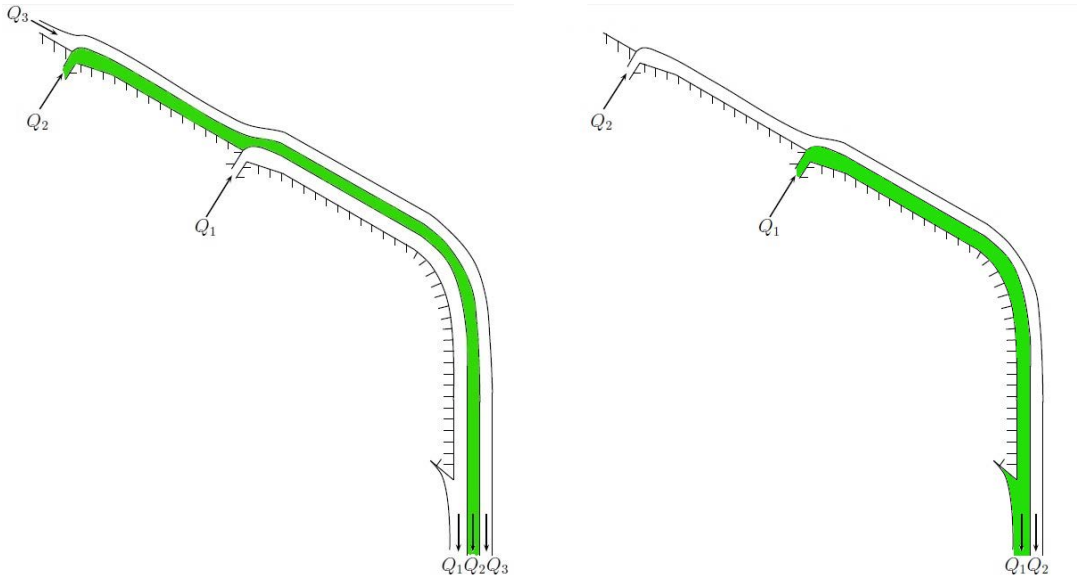

(a) (b)

Figure C.4: Schematics of the fluorescein images above. Schematic (a) corresponds to Figure C.2, whilst schematic (b) corresponds to Figure C.3.

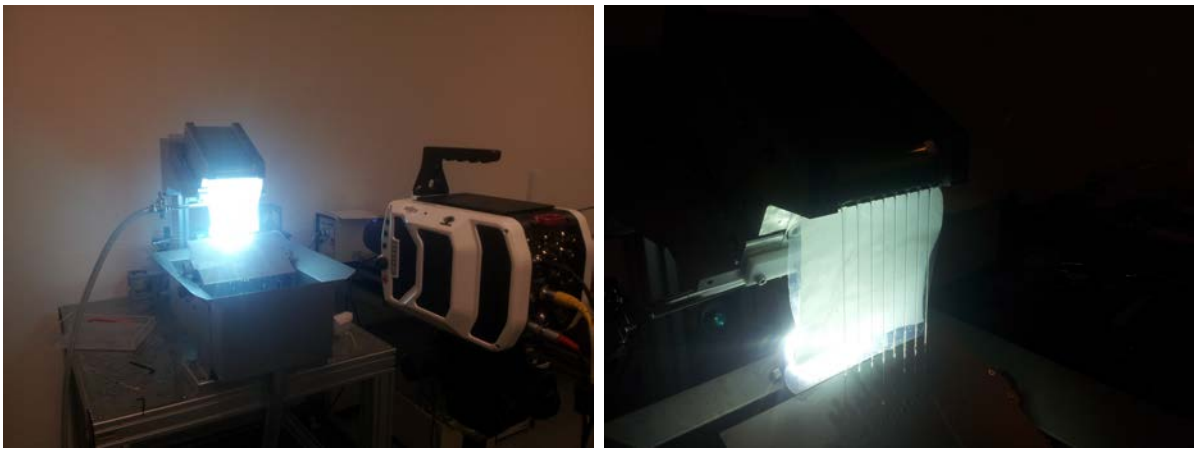

(a) (b)

Figure C.5: Experimental set-up to capture the 'dancing' jets. A white light is shone through filter paper to illuminate the jets.

C.3 Dancing jets

This work regards the beginning of an experimental investigation into the 'dance' that the array of liquid jets may undergo after liquid curtain break-up. The work presented in this section was accepted as an entry to the American Physical Society's *Gallery of Fluid Motion*, 2015.

As reported in the Introduction of Chapter 5, previous studies [73, 93] observed an array of liquid jets oscillate in the transverse direction, unforced. This phenomenon is also observed, under certain conditions, with the series of liquid jets that are formed from the die-lip in the curtain coating set-up described in this thesis. A primary aim of these experiments is to understand the conditions in which we see the series of liquid jets with regular spacing, periodic sideways movement or chaotic motion. All experiments in this section comprise of a single-layer only.

To capture the movement of the liquid jets, a white light was shone through filter paper, from behind the jets, facing a high-speed camera (Phantom v1610). This set-up is shown in Figure C.5, with resulting frames from the high-speed video shown in Figure C.6. A white rectangle has been placed above the same liquid jet in Figure C.6(a) and (b), to emphasise the sideways movement of the jets. Although the change between (a) and (b) is subtle, it is evident in (a) that the jet corresponding to the white rectangle is on the left of a 'pair' of jets (whereby the distance between this pair is smaller than the average spacing). In (b), the same jet is on the right-hand side of such a pair.

The movement of the jets at times was complex, unsurprising after the chaotic motion described in [73, 93]. Some initial results are presented in Tables C.1 and C.2, when the motion of the jets was periodic. In this case, it was possible to record the time taken for a jet, starting at an arbitrary position at time $t = 0$, to return to the initial starting

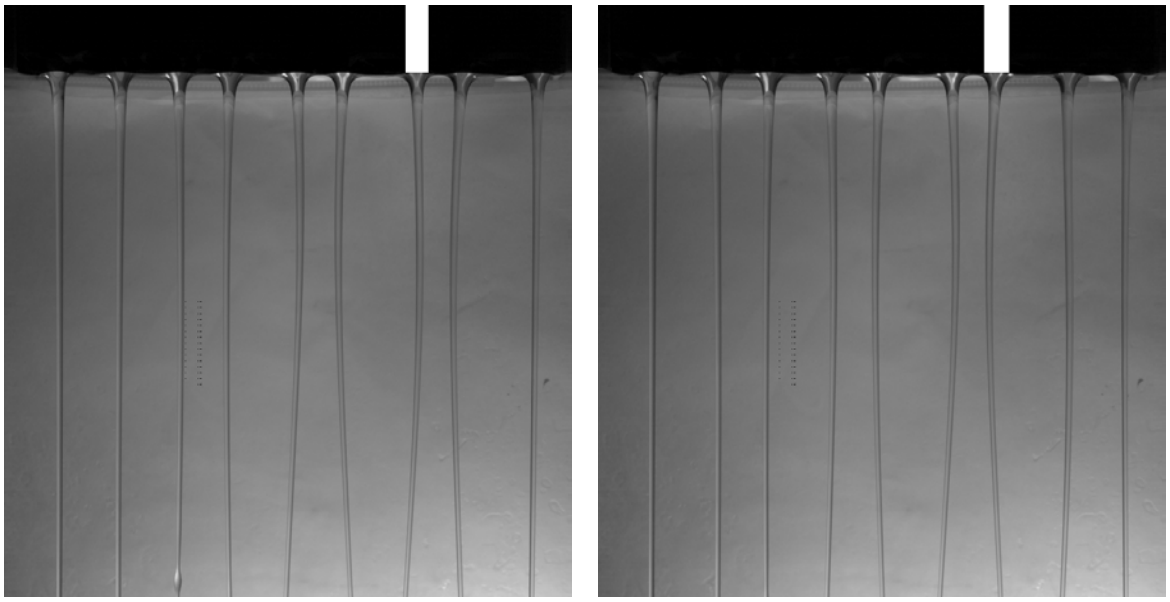

(a) (b)

Figure C.6: Two frames taken from a high-speed video of the 'dancing' liquid jets, where the white rectangle in (a) and (b) reference the same liquid jet (to emphasise the motion). Subfigure (b) is 0.14 s after (a).

Liquid	Approximate viscosity (mPa.s)	Time period of oscillation (s)
50% glycerol	8.4	0.29
60% glycerol	15.3	0.32
70% glycerol	30	0.30
80% glycerol	72	0.34

Table C.1: Time period of jet oscillations for varying glycerol solutions. The flow rate is between 0.83–1 cm^2s^{-1} in each case.

Liquid	Flow rate (cm^2s^{-1})	Time period of oscillation (s)
70% glycerol	0.83	0.30
70% glycerol	1.11	0.29
70% glycerol	1.27	0.27
70% glycerol	1.43	0.28

Table C.2: Time period of jet oscillations for varying flow rates, with each experiment using 70% glycerol.

position. This time is denoted the time period of oscillations in Tables C.1 and C.2.

Table C.1 indicates that the time period of the oscillations is independent of the viscosity of the liquid used, with there being only a small range in the time period. Similar to Section C.1, the exact liquid properties are unknown (the liquids are currently being tested to obtain values for viscosity and surface tension). In these tables, the experimental values from Chapter 2 are used as an approximation.

Table C.2 suggests that the time period of oscillations is also independent of the flow rate. In these experiments, only 70% glycerol was used, and despite the periodic oscillations occurring for a range of flow rates, there is little difference in the time period. These initial results are tentative findings into the 'dancing' jets, and the full investigation into this phenomenon is the topic of future research.

List of References

[1] A. W. Adamson and A. P. Grist. *Physical Chemistry of Surfaces*. Wiley-Interscience, 6th edition, 1997.

[2] P. Adomeit and U. Renz. Hydrodynamics of three-dimensional waves in laminar falling films. *International journal of multiphase flow*, 26(7):1183–1208, 2000.

[3] TSE Troller AG. Curtain coating in the paper industry. http://www.packaging-int.com/article/paper-curtain-coating.html. Accessed: May 2013.

[4] A. F. M Akhtaruzzaman, C. K. Wang, and S. P. Lin. Wave motion in multilayered liquid films. *J. Appl. Mech.*, 45:25–31, 1978.

[5] S. V. Alekseenko, V. A. Antipin, A. V. Bobylev, and D. M. Markovich. Application of piv to velocity measurements in a liquid film flowing down an inclined cylinder. *Experiments in Fluids*, 43(2-3):197–207, 2007.

[6] S. V. Alekseenko, D. M. Markovich, and S. I. Shtork. Wave flow of rivulets on the outer surface of an inclined cylinder. *Physics of Fluids*, 8(12):3288–3299, 1996.

[7] A. Alexeev and A. Oron. Suppression of the rayleigh-taylor instability of thin liquid films by the marangoni effect. *Physics of Fluids*, 19(8):082101, 2007.

[8] B. Ambravaneswaran, H. J. Subramani, S. D. Phillips, and O. A. Basaran. Dripping-jetting transitions in a dripping faucet. *Physical review letters*, 93(3):034501, 2004.

[9] M. Becerra and M. S. Carvalho. Stability of viscoelastic liquid curtain. *Chemical Engineering and Processing: Process Intensification*, 50(5):445–449, 2011.

[10] A. Benchabane and K. Bekkour. Rheological properties of carboxymethyl cellulose (cmc) solutions. *Colloid and Polymer Science*, 286(10):1173–1180, 2008.

[11] T. B. Benjamin. Wave formation in laminar flow down an inclined plane. *Journal of Fluid Mechanics*, 2(06):554–573, 1957.

[12] A. M. Binnie. Experiments on the onset of wave formation on a film of water flowing down a vertical plane. *Journal of Fluid Mechanics*, 2:551–553, 1957.

[13] T. D. Blake, M. Bracke, and Y. D. Shikhmurzaev. Experimental evidence of nonlocal hydrodynamic influence on the dynamic contact angle. *Physics of Fluids*, 11(8):1995–2007, 1999.

[14] T. D. Blake, A. Clarke, and K. J. Ruschak. Hydrodynamic assist of dynamic wetting. *AIChE Journal*, 40(2):229–242, 1994.

[15] T. D. Blake, R. A. Dobson, and K. J. Ruschak. Wetting at high capillary numbers. *Journal of Colloid and Interface Science*, 279(1):198 – 205, 2004.

[16] H. Blasius. Grenzschichten in flüssigkeiten mit kleiner reibung. *Z. Math. Phys.*, 56:1–37, 2009. (English translation).

[17] M. G. Blyth and C. Pozrikidis. Evolution equations for the surface concentration of an insoluble surfactant; applications to the stability of an elongating thread and a stretched interface. *Theoretical and Computational Fluid Dynamics*, 17(3):147–164, 2004.

[18] V. Bontozoglou and K. Serifi. Falling film flow along steep two-dimensional topography: The effect of inertia. *International Journal of Multiphase Flow*, 34(8):734 – 747, 2008.

[19] M. P. Brenner and D. Gueyffier. On the bursting of viscous films. *Physics of Fluids*, 11:737–739, 1999.

[20] D. Brown. A study of the behaviour of a thin sheet of moving liquid. *Journal of Fluid Mechanics*, 10:297–305, 1960.

[21] P.-T. Brun, A. Damiano, P. Rieu, G. Balestra, and F. Gallaire. Rayleigh-taylor instability under an inclined plane. *Physics of Fluids*, 27(8):084107, 2015.

[22] P. Brunet, J.-M. Flesselles, and L. Limat. Parity breaking in a one-dimensional pattern: A quantitative study with controlled wavelength. *EPL (Europhysics Letters)*, 56(2):221, 2001.

[23] J. M. Burgess, A. Juel, W. D. McCormick, J. B. Swift, and H. L. Swinney. Suppression of dripping from a ceiling. *Physical review letters*, 86(7):1203, 2001.

[24] S. V. Chepushtanova and I. L. Kliakhandler. Slow rupture of viscous films between parallel needles. *Journal of Fluid Mechanics*, 573:297–310, 2007.

[25] K. N. Christodoulou and L. E. Scriven. Lecture notes on surface tension. AIChE Annual Meeting, San Francisco, CA. Paper. 1423.

[26] C. Clanet and J. C. Lasheras. Transition from dripping to jetting. *Journal of fluid mechanics*, 383:307–326, 1999.

[27] A. Clarke, S. J. Weinstein, A. G. Moon, and E. A. Simister. Time-dependent equations governing the shape of a two-dimensional liquid curtain, part 1: Experiment. *Physics of Fluids*, 9(12):3637–3644, 1997.

[28] D. W. Clutter and A. M. O. Smith. Flow visualization by electrolysis of water. *Aerospace Engineering*, 20:24–27, 1961.

[29] C. Counillon, L. Daudet, T. Podgorski, M. C. Jullien, S. Akamatsu, and L. Limat. Global drift of a circular array of liquid columns. *EPL (Europhysics Letters)*, 40(1):37, 1997.

[30] D. J. Coyle, C. W. Macosko, and L. E. Scriven. The fluid dynamics of reverse roll coating. *AIChE Journal*, 36(2):161–174, 1990.

[31] G. D. Crapper, N. Dombrowski, and W. P. Jepson. Wave growth on thin sheets of non-newtonian liquids. *Proc. R. Soc. Lond. A*, 342:225–236, 1975.

[32] F. E. C. Culick. Comments on a ruptured soap film. *Journal of Applied Physics*, 31(6):1128–1129, 1960.

[33] L. De Luca and M. Costa. Instability of a spatially developing liquid sheet. *Journal of Fluid Mechanics*, 331:127–144, 1997.

[34] L. De Luca and C. Meola. Surfactant effects on the dynamics of a thin liquid sheet. *Journal of Fluid Mechanics*, 300:71–85, 1995.

[35] G. Debrégeas, P. G. De Gennes, and F. Brochard-Wyart. The life and death of "bare" viscous bubbles. *Science*, 279(5357):1704–1707, 1998.

[36] G. Debrégeas, P. Martin, and F. Brochard-Wyart. Viscous bursting of suspended films. *Physical review letters*, 75(21):3886, 1995.

[37] G. F. Dietze, F. Al-Sibai, and R. Kneer. Experimental study of flow separation in laminar falling liquid films. *Journal of Fluid Mechanics*, 637:73–104, 10 2009.

[38] G. F. Dietze, A. Leefken, and R. Kneer. Investigation of the backflow phenomenon in falling liquid films. *Journal of Fluid Mechanics*, 595:435–459, 1 2008.

[39] D. E. Dobbs and R. Hanks. *A modern course on the theory of equations*. Polygonal Pub House, 1992.

[40] E. I. P. Drosos, S. V. Paras, and A. J. Karabelas. Characteristics of developing free falling films at intermediate reynolds and high kapitza numbers. *International Journal of Multiphase Flow*, 30(7):853–876, 2004.

[41] R. J. Dyson, J. Brander, C. J. W. Breward, and P. D. Howell. Long-wavelength stability of an unsupported multilayer liquid film falling under gravity. *Journal of Engineering Mathematics*, 64:237–250, 2009.

[42] J. Eggers. Nonlinear dynamics and breakup of free-surface flows. *Reviews of modern physics*, 69(3):865, 1997.

[43] V. B. Fainerman, V. N. Kazakov, S. V. Lylyk, A. V. Makievski, and R. Miller. Dynamic surface tension measurements of surfactant solutions using the maximum bubble pressure method limits of applicability. *Colloids and Surfaces A: Physicochemical and Engineering Aspects*, 250(13):97 – 102, 2004.

[44] M. Fermigier, L. Limat, J. E. Wesfreid, P. Boudinet, and C. Quilliet. Two-dimensional patterns in rayleigh-taylor instability of a thin layer. *Journal of Fluid Mechanics*, 236:349–383, 1992.

[45] D. S. Finnicum, S. J. Weinstein, and K. J. Ruschak. The effect of applied pressure on the shape of a two dimensional liquid curtain falling under the influence of gravity. *Journal of Fluid Mechanics*, 255:647–665, 1993.

[46] S. J. Friedman and C. O. Miller. Liquid films in the viscous flow region. *Industrial & Engineering Chemistry*, 33(7):885–891, 1941.

[47] A. Frumkin. Die kapillarkurve der höheren fettsäuren und die zustandsgleichung der oberflächenschicht. *Z. Phys. Chem. Stoechiom. Verwandschaftsl.*, 116:466–484, 1925.

[48] F. Giorgiutti, A. Bleton, L. Limat, and J. E. Wesfreid. Dynamics of a one-dimensional array of liquid columns. *Physical Review Letters*, 74(4):538, 1995.

[49] F. Giorgiutti and L. Limat. Solitary dilation waves in a circular array of liquid columns. *Physica D: Nonlinear Phenomena*, 103(1):590–604, 1997.

[50] J. F. Greiller. Method of making photographic elements. U.S. Patent No. 3,632,374, 1972.

[51] S. S. Grimley. Liquid flow conditions in packed towers. *Trans. Inst. Chem. Eng.(London)*, 23:228–235, 1945.

[52] D. Henry, J. Uddin, J. O. Marston, and S. T. Thoroddsen. Stability of an unsupported multi-layer surfactant laden liquid curtain under gravity. *Journal of Engineering Mathematics*, 99:119–136, 2016.

[53] D. Henry, J. Uddin, J. Thompson, M. G. Blyth, S. T. Thoroddsen, and J. O. Marston. Multi-layer film flow down an inclined plane: experimental investigation. *Experiments in Fluids*, 55(12):1–14, 2014.

[54] D. J. Hughes. Method for simultaneously applying a plurality of coated layers by forming a stable multilayer free-falling vertical curtain. U.S. Patent No. 3,508,947, 1970.

[55] A. Indeikina, I. Veretennikov, and H.-C. Chang. Drop fall-off from pendent rivulets. *Journal of Fluid Mechanics*, 338:173–201, 1997.

[56] S. Ishizuka and T. Matuda. Curtain apparatus. U.S. Patent No. 4,974,533, 1990.

[57] H. Jeffreys. Lxxxiv. the flow of water in an inclined channel of rectangular section. *The London, Edinburgh, and Dublin Philosophical Magazine and Journal of Science*, 49(293):793–807, 1925.

[58] W. Y. Jiang, B. T. Helenbrook, S. P. Lin, and S. J. Weinstein. Low-reynolds-number instabilities in three-layer flow down an inclined wall. *Journal of Fluid Mechanics*, 539:387–416, 2005.

[59] B.-I. Jun, T. W. Jones, and M. L. Norman. Interaction of rayleigh-taylor fingers and circumstellar cloudlets in young supernova remnants. *The Astrophysical Journal Letters*, 468(1):L59, 1996.

[60] H. W. Jung, J. S. Lee, J. C. Hyun, S. J. Kim, L. E. Scriven, et al. Simplified modeling of slide-fed curtain coating flow. *Korea-Australia Rheology Journal*, 16(4):227–233, 2004.

[61] S. Kalliadasis, C. Bielarz, and G. M. Homsy. Steady free-surface thin film flows over topography. *Physics of Fluids*, 12(8):1889–1898, 2000.

[62] T. W. Kao. Role of the interface in the stability of stratified flow down an inclined plane. *Physics of Fluids*, 8:2190–2194, 1965.

[63] T. W. Kao. Stability of two-layer viscous stratified flow down an inclined plane. *Physics of Fluids*, 8:812–820, 1965.

[64] T. W. Kao. Role of viscosity stratification in the stability of two-layer flow down an incline. *Journal of Fluid Mechanics*, 33:561–572, 1968.

[65] P. L. Kapitza and S. P. Kapitza. Wave flow of thin viscous fluid layers. *Zh. Eksp. Teor. Fiz*, 18(3), 1948.

[66] J. B. Keller. Breaking of liquid films and threads. *Physics of Fluids*, 26(12):3451–3453, 1983.

[67] S. F. Kistler and P. M. eds Schweizer. *Liquid film coating*. Chapman & Hall, 1997.

[68] M. K. Kumar, T. Mitra, and P. Ghosh. Adsorption of ionic surfactants at liquid-liquid interfaces in the presence of salt: Application in binary coalescence of drops. *Industrial & engineering chemistry research*, 45(21):7135–7143, 2006.

[69] R. J. LaPorte. *Hydrophilic Polymer Coatings for Medical Devices: Structure/Properties, Development, Manufacture and Applications*. CRC Press, 1997.

[70] L. G. Leal. *Advanced Transport Phenomena*. Cambridge University Press, 2007.

[71] W. K. Leonard. Effects of secondary cavities, inertia, and gravity on extrusion dies. *SPE ANTEC Tech. Papers*, 31:144–148, 1985.

[72] W. K. Leonard. Inertia and gravitational effects in extrusion dies for non-newtonian fluids. *Polym. Eng. Sci.*, 25(9):570–576, 1985.

[73] L. Limat, P. Jenffer, B. Dagens, E. Touron, M. Fermigier, and J. E. Wesfreid. Gravitational instabilities of thin liquid layers: dynamics of pattern selection. *Physica D: Nonlinear Phenomena*, 61(1):166–182, 1992.

[74] S. P. Lin. Stability of a viscous liquid curtain. *Journal of Fluid Mechanics*, 104:25–32, 1981.

[75] S. P. Lin, Z. W. Lian, and B. J. Creighton. Absolute and convective instability of a liquid sheet. *Journal of Fluid Mechanics*, 220:673–689, 1990.

[76] S. P. Lin and G. Roberts. Waves in a viscous liquid curtain. *Journal of Fluid Mechanics*, 114:443–458, 1981.

[77] T.-S. Lin and L. Kondic. Thin films flowing down inverted substrates: Two dimensional flow. *Physics of Fluids*, 22(5):052105, 2010.

[78] T.-S. Lin, L. Kondic, and A. Filippov. Thin films flowing down inverted substrates: Three-dimensional flow. *Physics of Fluids*, 24(2):022105, 2012.

[79] J. Liu, J. B. Schneider, and J. P. Gollub. Three-dimensional instabilities of film flows. *Physics of Fluids*, 7(1):55–67, 1995.

[80] C. Lv, C. Clanet, and D. Quéré. Retraction of large liquid strips. *Journal of Fluid Mechanics*, 778:R6, 2015.

[81] J. O. Marston, M. J. H. Simmons, and S. P. Decent. Influence of viscosity and impingement speed on intense hydrodynamic assist in curtain coating. *Experiments in Fluids*, 42(3):483–488, 2007.

[82] J. O. Marston, S. T. Thoroddsen, J. Thompson, M. G. Blyth, D. Henry, and J. Uddin. Experimental investigation of hysteresis in the break-up of liquid curtains. *Chemical Engineering Science*, 117:248–263, 2014.

[83] L. C. Mayo, S. W. McCue, and T. J. Moroney. Gravity-driven fingering simulations for a thin liquid film flowing down the outside of a vertical cylinder. *Physical Review E*, 87(5):053018, 2013.

[84] W. R. McEntee and K. J. Mysels. Bursting of soap films. i. an experimental study. *The Journal of Physical Chemistry*, 73(9):3018–3028, 1969.

[85] K. Miyamoto and Y. Katagiri. Curtain coating. *Liquid Film Coating: Scientific principles and their technological implications*, 1997.

[86] M. Mohsin, J. Uddin, S. P. Decent, and M. F. Afzaal. Temporal instability analysis of inviscid compound jets falling under gravity. *Physics of Fluids*, 25(1), 2013.

[87] J. P. Munro, C. R. Anthony, O. A. Basaran, and J. R. Lister. Thin-sheet flow between coalescing bubbles. *Journal of Fluid Mechanics*, 773:R3, 2015.

[88] A. K. Njifenju, J. Bico, E. Andres, P. Jenffer, and M. Fermigier. Experimental investigation of liquid films in gravity-driven flows with a simple visualization technique. *Experiments in Fluids*, 54:1506, 2013.

[89] C. J. Noakes, P. H. Gaskell, H. M. Thompson, and J. B. Ikin. Streak-line defect minimization in multi-layer slide coating systems. *Chemical Engineering Research and Design*, 80(5):449–463, 2002.

[90] W. Nusselt. Die oberflachenkondensation des wasserdampfes (in german). *Z. Ver. Dt. Ing.*, 60:541–552, 1916.

[91] A. Oron, S. H. Davis, and S. G. Bankoff. Long-scale evolution of thin liquid films. *Reviews of Modern Physics*, 69(3):931–980, 1997.

[92] S. Portalski. Studies of falling liquid film flow film thickness on a smooth vertical plate. *Chemical Engineering Science*, 18(12):787–804, 1963.

[93] W. G. Pritchard. Instability and chaotic behaviour in a free-surface flow. *Journal of Fluid Mechanics*, 165:1–60, 1986.

[94] W. E. Ranz. Some experiments on the dynamics of liquid films. *Journal of Applied Physics*, 30(12):1950–1955, 1959.

[95] Lord J. W. S. Rayleigh. Some applications of photography. *Nature*, 44(1133):249–254, 1891.

[96] T. C. Reiter. Curtain coating method and apparatus. U.S. Patent No. 4,830,887, 1989.

[97] J. S. Roche, N. Le Grand, P. Brunet, L. Lebon, and L. Limat. Perturbations on a liquid curtain near break-up: Wakes and free edges. *Physics of Fluids*, 18(082101), 2006.

[98] I. V. Roisman. On the instability of a free viscous rim. *Journal of Fluid Mechanics*, 661:206–228, 2010.

[99] M. J. Rosen. *Surfactants and Interfacial Phenomena*. New York: Wiley, 1989. 2nd Edition.

[100] R. P. Salazar and E. Marschall. Time-average local thickness measurement in falling liquid film flow. *International Journal of Multiphase Flow*, 4(4):405–412, 1978.

[101] N. Savva and J. W. M. Bush. Viscous sheet retraction. *Journal of Fluid Mechanics*, 626:211–240, 5 2009.

[102] H. Schlichting and K. Gersten. *Boundary layer theory*. Springer-Verlag Berlin Heidelberg, 8th edition, 2000. (Translated by K. Mayes).

[103] P. M. Schweizer. Visualization of coating flows. *Journal of Fluid Mechanics*, 193:285–302, 1988.

[104] P. M. Schweizer and U. Troller. Method and apparatus for curtain coating providing a lateral liquid film velocity equal to the curtain falling velocity. U.S. Patent No. 6,048,582, 2000.

[105] B. Smit. Molecular-dynamics simulations of amphiphilic molecules at a liquid-liquid interface. *Physical review A*, 37(9):3431, 1988.

[106] H. A. Stone and L. G. Leal. The effects of surfactants on drop deformation and breakup. *Journal of Fluid Mechanics*, 220:161–186, 1990.

[107] T. Sullivan, S. Middleman, and R. Keunings. Use of a finite-element method to interpret rheological effects in blade coating. *AIChE Journal*, 33(12):2047–2056, 1987.

[108] G. Sünderhauf, H. Raszillier, and F. Durst. The retraction of the edge of a planar liquid sheet. *Physics of Fluids*, 14(1):198–208, 2002.

[109] G. Taylor. The instability of liquid surfaces when accelerated in a direction perpendicular to their planes. i. In *Proceedings of the Royal Society of London A: Mathematical, Physical and Engineering Sciences*, volume 201, pages 192–196, 1950.

[110] G. I. Taylor. The dynamics of thin sheets of fluid. iii. disintegration of fluid sheets. *Proc. R. Soc. Lond. A*, 253:313–321, 1957.

[111] A. B. Thompson, S. N. Gomes, G. A. Pavliotis, and D. T. Papageorgiou. Stabilising falling liquid film flows using feedback control. *Physics of Fluids*, 28(1):012107, 2016.

[112] A. B. Thompson, D. Tseluiko, and D. T. Papageorgiou. Falling liquid films with blowing and suction. *Journal of Fluid Mechanics*, 787:292–330, 2016.

[113] P. H. Trinh, H. Kim, N. Hammoud, P. D. Howell, S. J. Chapman, and H. A. Stone. Curvature suppresses the rayleigh-taylor instability. *Physics of Fluids*, 26(5):051704, 2014.

[114] I. M. Wallwork, S. P. Decent, A. C. King, and R. M. S. M. Schulkes. The trajectory and stability of a spiralling liquid jet. part 1. inviscid theory. *Journal of Fluid Mechanics*, 459:43–65, 2002.

[115] C. K. Wang, J. J. Seaborg, and S. P. Lin. Instability of multilayered liquid films. *Physics of Fluids*, 21:1669–1673, 1978.

[116] S. J. Weinstein. Wave propogation in the flow of shear-thinning fluids down an incline. *AIChE J.*, 36:1873–1889, 1990.

[117] S. J. Weinstein, A. Clarke, A. G. Moon, and E. A. Simister. Time-dependent equations governing the shape of a two-dimensional liquid curtain, part 1: Theory. *Physics of Fluids*, 9(12):3625–3636, 1997.

[118] S. J. Weinstein and K. J. Ruschak. Coating flows. *Annu. Rev. Fluid Mech.*, 36:29–53, 2004.

[119] A. Wierschem, M. Scholle, and N. Aksel. Comparison of different theoretical approaches to experiments on film flow down an inclined wavy channel. *Experiments in fluids*, 33(3):429–442, 2002.

[120] B. C. Wilson and D. J. (North American Coating Laboratories) Fiore. Anti-fingerprint coating applications for automative touchscreen displays. http://www.nacl.com/images/stories/Dansindustrial/Anti-fingerprint Accessed: May 2013.

[121] S. G. Yiantsios and B. G. Higgins. Rayleigh–taylor instability in thin viscous films. *Physics of Fluids A: Fluid Dynamics (1989-1993)*, 1(9):1484–1501, 1989.

[122] C.-S. Yih. Curtain coating. Proc. 2nd U.S. Nat. Congr. Appl. Mech. 623. American Society of Mechanical Engineers, New York.

[123] C.-S. Yih. Stability of liquid flow down an inclined plane. *Physics of Fluids*, 6(3):321–334, 1963.

[124] Y. Zhao, G. Chen, and Q. Yuan. Liquid–liquid two-phase mass transfer in the t-junction microchannels. *AIChE Journal*, 53(12):3042–3053, 2007.